Analysis of a Competitive Respiratory Disease System with Quarantine

Anna Daniel Fome

Vom Fachbereich Mathematik der
Rheinland-Pfälzischen Technischen Universität Kaiserslautern-Landau
zur Verleihung des akademischen Grades
Doktor der Naturwissenschaften (Doctor rerum naturalium, Dr. rer. nat.)
genehmigte Dissertation

Gutachter:
Prof. Dr. Axel Klar, RPTU Kaiserslautern-Landau
Prof. Dr. Thomas Götz, Universität Koblenz

RPTU Rheinland-Pfälzische Technische Universität Kaiserslautern Landau

Datum der Disputation: 17. Januar 2025

DE-386

Printed and/or published with the support of the German Academic Exchange Service.

Dedication

I wish to express my heartfelt dedication in this thesis to my mother, Christina F. Fumakule,
&
my father, Daniel P. Fome.

Declaration

I hereby declare that, except where specific reference is made to the work of others, the contents of my dissertation, titled *Analysis of a Competitive Respiratory Disease System with Quarantine*— are original and have not been submitted in whole or in part for consideration for any other degree or qualification in this or any other university. The dissertation is my own work and contains nothing that is the outcome of work done in collaboration with others, except as specified in the text and acknowledgments. Parts of this work have been submitted and published in peer-reviewed journals, and are appropriately noted in the corresponding chapters. A detailed list of these publications is included in the thesis.

Anna Daniel Fome
17 January 2025

Journal articles

This thesis incorporates the following works: the peer-reviewed journal article [45], the accepted peer-reviewed conference proceedings [47], the conference paper [46] (under review), and the preprints [49] and [44].

[44] A. D. Fome, W. Bock, **and** A. Klar. *Analysis of a competitive respiratory disease system with quarantine. arXiv preprint arXiv:2307.05044*, 2023. doi: 10.48550/arXiv.2307.05044 (see p. 27)

[45] A. D. Fome, W. Bock, **and** A. Klar. *Analysis of a competitive respiratory disease system with quarantine: Epidemic thresholds and cross-immunity effects. Applied Mathematics and Computation*, 485: 128968, 2024. doi: 10.1016/j.amc.2024.128968 (see pp. 73, 106, 108)

[46] A. D. Fome, W. Bock, **and** A. Klar. *Conditions for Backward Bifurcation in a Multi-Pathogen Model with Imperfect Quarantine and Cross-Immunity.* under-review, 2024. (see p. 73)

[47] A. D. Fome, W. Bock, **and** A. Klar. *Equilibria Dynamics in Competitive Respiratory Disease Systems with Quarantine. ECMI2023 Proceedings*, Accepted, 2024. (see p. 27)

[49] A. D. Fome, I. Rodiah, W. Bock, B. Lange, **and** A. Klar. *The Interplay of Influenza and Covid-19 in Germany, January 2020-December 2022: A Study of Competitive Disease Dynamics with Quarantine Measures and Partial Cross-Immunity. Available at SSRN 5019051*, 2024. doi: 10.2139/ssrn.5019051 (see p.)

Acknowledgements

First and foremost, I wish to express my deepest gratitude to Almighty God for His guidance and blessings throughout my PhD journey.

I am deeply grateful to Prof. Dr. Axel Klar for accepting me as a Ph.D. student and for his ongoing support and guidance. His advice and encouragement have been invaluable in shaping my research and helping me grow academically. I appreciate his patience, mentorship, and the time he has invested in my development, which has been crucial for the success of this project.

My sincere thanks go to Deutscher Akademischer Austauschdienst (DAAD) for their generous sponsorship, which has been crucial for my research. I also appreciate Ms. Parisa Asemi-Rauber, Ingrid Knapp, and Clara Horn Joya for their prompt administrative assistance, which made the process smooth and manageable.

Special thanks to Prof. Dr. Wolfgang Bock for his key contributions to study design, including methodology development and model formulation, which have greatly improved our approach to disease modeling. His guidance, collaborative efforts, and introduction to professional opportunities, such as conferences, have been invaluable. I also appreciate Dr. Berit Lange and Dr. Isti Rodiah for their virtual contributions to one of my peer-reviewed submissions.

I would like to thank the Mathematics Department, especially Dr. Triebsch, Jessica, and my MIC colleagues, for their insights on research and social life. I am also grateful to the Biomathematics group, particularly Prof. Dr. Christina Surulescu, and the Technomathematics team for their constructive feedback. My thanks extend to former members, Ms. Claudia Korb and Corinna Zurloh for their academic assistance and to the Department of International Affairs and the ISGS team for their help with accommodation. I greatly appreciate my Philippines friends, Mary Joy Togonon and Anj Gumanoy, for their support at conferences.

I owe a special debt of gratitude to my husband, Mr. Triphone Germin, and my children, Joan Triphone and Jovan Triphone, for their constant love, support and cheering throughout my project. I also thank my son, Gilbert Triphone, for his prayers during this journey.

Finally, I extend my heartfelt appreciation to my mother, Christina, my stepfather, Mr. Kalantine, my brother, Mr. Isaac, my sisters, Salome and Ester, my brother-in-law, Mr. Renatus Shinhu, and my siblings, Oliva and Pendo, for their spiritual support and encouragement. I also remember with love my late younger brother Emmanuel (may his soul rest in peace) for the support and love he gave me. Their unwavering belief in me has been a constant source of strength throughout this journey.

Abstract

The SARS-Cov2 pandemic once more showed that new respiratory diseases can be a burden for the society. On the other hand, there are long existing respiratory pathogens such as influenza or other influenza-like illnesses (ILI) in the population. This thesis studies competing a system of two competing respiratory diseases. The focus lies especially on non-pharmaceutical interventions (NPIs) effects, such as quarantine efficacy and study the long-time behavior depending on cross immunity and co-infections. Mathematically the system is investigated towards critical points, disease threshold and multi-pathogen effects in the dynamics of each strain and their co-infections. Besides, our examination includes identifying and analyzing the underlying determinants of the backward bifurcation phenomenon. We also incorporate empirical data on Influenza and SARS-CoV-2 to prove our findings in a realistic setup.

Our results suggest that effective quarantine measures are necessary for infection management, even when the quarantine reproduction numbers are below one. Under complete immunity, a strain with a quarantine reproduction number (average number of secondary cases made by an infected person under a quarantine control) of less than one may lead to extinction, while partial cross-immunity allows for its coexistence at a low level. The backward bifurcation shows the capability of the model to accommodate the simultaneousness of the disease-free equilibrium with up to four endemic equilibria. Co-infections and imperfect quarantine actions pose significant challenges in containing outbreaks, sustaining the outbreak potential even with successful control of individual virus strains. The study also emphasizes the significance of age-structured models in capturing the dynamics of influenza and SARS-CoV-2, surpassing traditional all-age group models. Again, our investigation delivers insights into the interplay between the influenza and SARS-CoV-2 transmission rates relations. This interaction remains consistently significant, especially in scenarios involving partial cross-immunity. Accordingly, our study suggests that comprehensive interventions targeting both pathogens (simultaneously) may be necessary for effectively curbing the spread of both infections in concurrent environments.

Zusammenfassung

Die SARS-CoV-2-Pandemie hat gezeigt, dass neue Atemwegserkrankungen eine Belastung für die Gesellschaft sein können. Andererseits gibt es lang bestehende Atemwegserreger wie Influenza oder andere grippeähnliche Krankheiten (ILI) in der Bevölkerung. Diese Arbeit untersucht ein System aus zwei konkurrierenden Atemwegserkrankungen. Besonders wird auf die Wirkung nicht-pharmazeutischer Interventionen (NPIs), wie die Wirksamkeit von Quarantänemaßnahmen, und das Langzeitverhalten in Abhängigkeit von Kreuzimmunität und Co-Infektionen eingegangen. Mathematisch wird das System im Hinblick auf kritische Punkte, Krankheitsschwellen und Mehrfacherreger-Effekte in der Dynamik jedes Stammes und ihrer Co-Infektionen untersucht. Darüber hinaus umfasst unsere Untersuchung die Identifizierung und Analyse der zugrunde liegenden Determinanten des Rückwärtsbifurkationsphänomens. Wir integrieren auch empirische Daten zu Influenza und SARS-CoV-2, um unser Verständnis der Dynamik der Interaktionen zwischen mehreren Stämmen zu erweitern.

Unsere Ergebnisse deuten darauf hin, dass wirksame Quarantänemaßnahmen für das Infektionsmanagement notwendig sind, selbst wenn die Quarantäne-Reproduktionszahlen unter eins liegen. Bei vollständiger Immunität kann ein Stamm mit einer Quarantäne-Reproduktionszahl von weniger als eins zur Auslöschung führen, während teilweise Kreuzimmunität seine Koexistenz auf niedrigem Niveau ermöglicht. Die Rückwärtsbifurkation zeigt die Fähigkeit des Modells, das gleichzeitige Vorhandensein des krankheitsfreien Gleichgewichts mit bis zu vier endemischen Gleichgewichten zu berücksichtigen. Dennoch stellen Co-Infektionen und unvollkommene Quarantänemaßnahmen erhebliche Herausforderungen bei der Eindämmung von Ausbrüchen dar und halten das Ausbruchspotenzial aufrecht, selbst bei erfolgreicher Kontrolle einzelner Virus-Stämme. Die Studie betont auch die Bedeutung altersstrukturierter Modelle zur Erfassung der Dynamik von Influenza und SARS-CoV-2, die herkömmliche Modelle für alle Altersgruppen übertreffen. Unsere Untersuchung liefert erneut Einblicke in das Zusammenspiel zwischen den Übertragungsraten von Influenza und SARS-CoV-2. Diese Interaktion bleibt durchweg bedeutsam, insbesondere in Szenarien mit teilweiser Kreuzimmunität. Entsprechend legt unsere Studie nahe, dass umfassende Interventionen, die auf beide Erreger gleichzeitig abzielen, notwendig sein können, um die Verbreitung beider Infektionen in gleichzeitigen Umgebungen wirksam einzudämmen.

Contents

1 Preliminaries

1.1 Overview

Acute respiratory infections, including influenza and Coronavirus Disease 2019 (COVID-19), affect the respiratory system over a short period, usually a few days to several weeks, and have a notable impact on global health [85]. The main ways influenza, caused by several influenza viruses, spreads are through respiratory droplets and contaminated surfaces. Severe consequences are more likely in vulnerable populations, including the elderly, children, pregnant women, and people with chronic diseases. Causes symptoms such as fever, headache, sore throat, runny nose, and dry cough. Strategies for managing influenza include immunization, frequent hand washing, and avoiding close contact with sick people [23, 133].

Although the ways of transmission of COVID-19 and influenza are similar, COVID-19 is caused by the novel acute respiratory syndrome coronavirus (SARS-CoV-2) and has specific symptoms such as loss of taste and smell [134]. Most COVID-19 patients have mild to moderate symptoms within 5 to 14 days. However, severe cases can cause long-term health problems called "Covid-long". Illness is characterized by symptoms such as fatigue, headache, and muscle aches that can persist for more than a month after infection. Controlling the spread of COVID-19 requires the implementation of preventive measures such as vaccination, mask use, social distancing, and adherence to health measures [15, 131].

As in previous epidemics, the global response to COVID-19 has emphasized the importance of public health and medical progress. Historical examples such as the H1N1 pandemic in 2009 and the Spanish flu in 1918 show how severe flu infections can lead to widespread illness, death, and economic hardship [85, 118]. The outbreak of SARS-CoV in 2002 highlighted the need for a public health response [103]. International cooperation and solidarity are essential in the fight against infectious diseases such as the COVID-19 pandemic, which has caused serious problems and disrupted the health system. Rapid development and widespread use of the COVID-19 vaccine is a major scientific achievement despite the difficulties of vaccine delivery. This achievement shows the need for vaccination and international cooperation to reduce the risk of epidemics [25, 69].

In addition to these medical advances, acknowledging that both SARS-CoV-2 and influenza spread primarily through respiratory droplets highlights the risk of simultaneous outbreaks and interactions between these pathogens [119]. This situation emphasizes the importance of investigating how these diseases might influence each other, including the role of non-pharmaceutical interventions (NPIs) and the long-term effects of cross-immunity and co-infections. Understand-

ing the similarities and differences between these two viruses is key to mitigating their combined impact. In Figure 1.1, the causal agents, incubation periods, severity, and social consequences of influenza and COVID-19 are compared. Although both have the same transmission route, the image highlights some significant distinctions, including the different viruses that cause each illness and the range of intensity of the symptoms. In addition, it emphasizes how vaccinations and good hygiene practices are common preventive interventions, highlighting the crucial role that NPIs play in the management of these diseases. This contrast highlights the need for additional investigation into how NPIs affect ongoing outbreaks and their ability to reduce transmission and manage the spread of respiratory diseases.

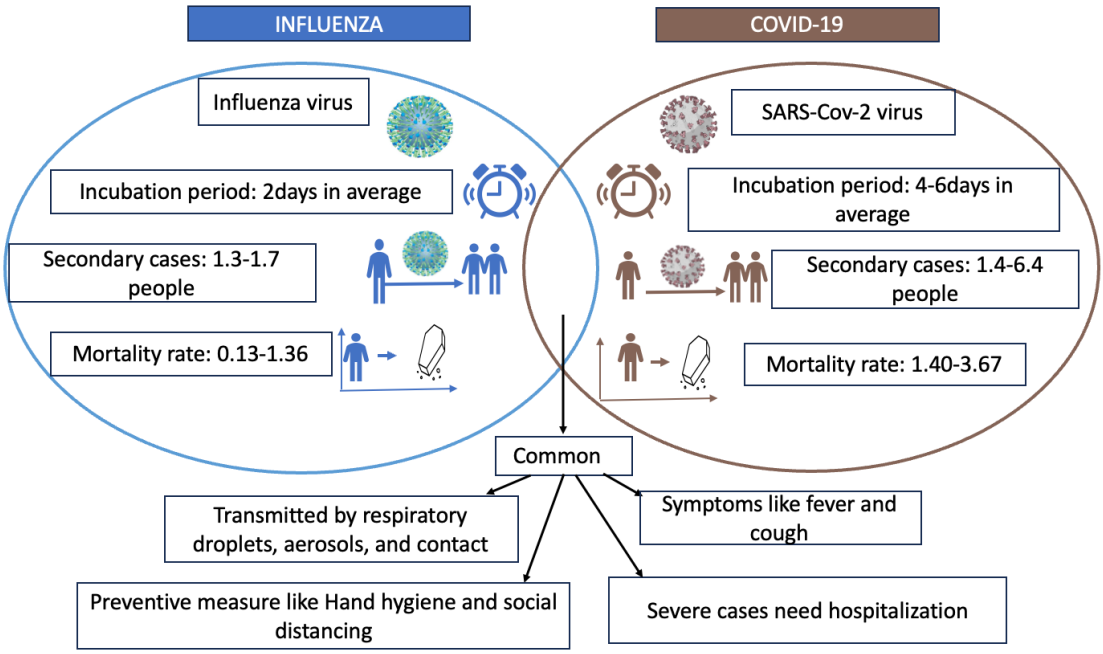

Figure 1.1: An overview highlighting how influenza and COVID-19 differ by their causative agents, incubation periods, severity, and social impacts. Again, it shows a shared mode of transmission and preventive measures. Data source [105, 134].

1.1.1 Non-pharmaceutical interventions

Non-pharmaceutical interventions (NPIs) are essential public health measures to manage infectious diseases such as influenza and COVID-19, especially when effective vaccines or antiviral treatments are not available [31]. These interventions include social distancing to minimize physical contact, personal protective measures such as mask wear and hand hygiene, and environmental hygiene practices such as frequent disinfection and proper ventilation [42]. Quarantine and isolation help contain infections by separating infected or exposed individuals, while travel restrictions aim to limit the spread of the virus between regions or countries [101].

Although NPIs have been shown to be effective in controlling individual diseases [7], their larger impact on multiple co-circulating respiratory infections is less understood. The COVID-19 pandemic provided a unique case study, demonstrating that early and strict NPIs significantly reduced infection rates and mortality in some countries [42]. Liu et al. (2023), in their study

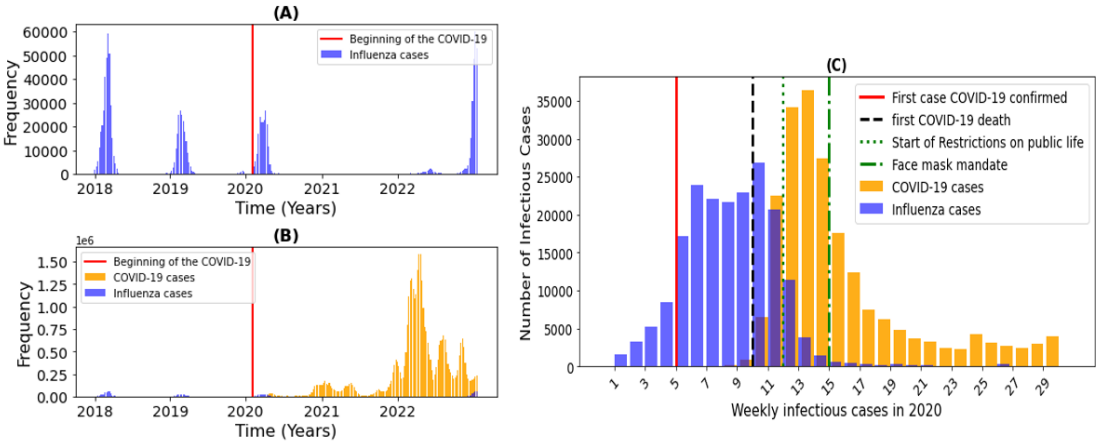

Figure 1.2: Influenza and SARS-CoV-2 trends over time in Germany (details on the data sources are provided in Section 7.3.1). Our prior analysis aims to examine and compare influenza peaks before and during the COVID-19 pandemic, as well as its overall impact. Subplot (A) presents the frequency of influenza cases from 2018 to 2022, with a red vertical line at week 5 of 2020 indicating the onset of the COVID-19 pandemic. Subplot (B) compares influenza and SARS-CoV-2 case frequencies over time, with influenza data in blue and COVID-19 data in orange, highlighting the sharp increase in COVID-19 cases. Both subplots share the x-axis, which represents time in years. Subplot (C) focuses on weekly infectious cases of COVID-19 and influenza in 2020, marking key events with vertical lines: the first confirmed COVID-19 case (week 5, red), the first COVID-19 death (week 10, black dashed), the introduction of public life restrictions (week 12, green dotted), and the face mask mandate (week 15, green dashed-dotted).

"Impact of non-pharmaceutical interventions during COVID-19 on future influenza trends in mainland China", analyzed how COVID-19 control measures influenced influenza patterns. Their findings revealed that NPIs not only reduced the incidence of influenza-like illnesses (ILIs), but also shortened the duration of infection, highlighting their role in shaping influenza transmission dynamics [82]. A similar trend is observed in Figure 1.2, suggesting that NPIs can alter interactions between respiratory viruses, ultimately influencing the overall burden of respiratory diseases. Understanding how NPIs, particularly quarantine and isolation, affect the dynamics of concurrent respiratory diseases is crucial for developing more comprehensive and effective disease control strategies.

1.1.2 Cross-immunity between Influenza and COVID-19

Cross-immunity or cross-protection occurs when exposure to one pathogen provides some degree of protection against another related pathogen. Full cross-immunity implies complete protection against a second pathogen after recovery from the first, while partial cross-immunity offers limited protection [96]. Research suggests that prior exposure to the influenza virus or influenza vaccination could trigger cross-reactive antibodies that may interact with SARS-CoV-2. Studies have shown that individuals with a history of influenza or other coronavirus infections may possess T cells capable of cross-reacting with SARS-CoV-2, potentially enhancing the immune response and aiding in viral clearance [57]. Furthermore, prior influenza infection or vaccination

can strengthen immune defenses, increasing interferon production and activating natural killer cells, which can lead to a stronger response to COVID-19 and a reduction in the severity of symptoms [60]. Some epidemiological studies suggest that influenza vaccination might lead to milder COVID-19 symptoms or reduced mortality, although these results are not definitive and may depend on factors such as access to healthcare and general health behaviors [41].

In contrast, evidence for cross-immunity from COVID-19 to influenza remains sparse. A study by Cowling et al. [26] suggested that previous SARS-CoV-2 infection might affect other respiratory viruses, including influenza, by activating immune responses. This aligns with our initial analysis, which aims to compare trends in the number of cases of influenza and COVID-19, especially focusing on seasonal peaks and the impact of the pandemic, as visualized in Figure 1.2. Our data reveal a significant decrease in seasonal influenza cases from 2020 to 2022 compared to 2018 and 2019, a pattern that supports the findings of other studies on the effect of COVID-19 on influenza in various regions [143]. Possible explanations for this decrease include increased innate immune responses or the effects of COVID-19 prevention measures, such as vaccines, which could induce broader immune responses. For example, studies in animal models have shown that macaques vaccinated against SARS-CoV-2 produced antibodies that protected against pulmonary disease [75]. Although there is no direct evidence suggesting that COVID-19 vaccination confers immunity to influenza, an enhanced immune response after COVID-19 infection or vaccination may temporarily influence the body's ability to respond to other infections [116].

Obtaining herd immunity through vaccination or natural infection can also influence the dynamics of cross-immunity. When a large portion of the population becomes immune to a disease -whether through vaccination or previous infection - the spread of the disease slows or ceases altogether [86]. In terms of cross-immunity, if a significant proportion of the population is immune to one pathogen (e.g., influenza), it may indirectly lessen the impact of a related pathogen (e.g., SARS-CoV-2) by reducing the number of susceptible hosts. This reduction in transmission can help control outbreaks and protect the community at large, underscoring the interconnected benefits of immunity to multiple pathogens. In general, the concept of cross-immunity between influenza and COVID-19 remains complex and not fully understood, which requires further research to clarify its scope and implications.

1.1.3 Influenza and COVID-19 co-infection

When a person is infected with both the influenza virus and SARS-CoV-2, they are considered co-infected with COVID-19 and influenza. In a recent study, [119] it is observed that there is a higher likelihood of co-infection during the colder months, when influenza is generally more common, and there have also been notable outbreaks of COVID-19. In addition, the main route of transmission for both pathogens, breathing, allows people to get both viruses, especially in crowded environments [119]. As the number of people who need health care increases, the coexistence of the two viruses in the population puts a strain on the health system, affecting hospitals and health care workers alike [137]. In addition to the threat provided by individual pathogenic pathogens, which we have briefly discussed in Section 1.1, there is also this. Research indicates that those with influenza and COVID-19 may have more serious consequences, such as higher hospitalization rates, admissions to intensive care units (ICU), and mortality [3, 71, 117]. In addition, because COVID-19 and influenza share many symptoms, it can be difficult

to differentiate the two diseases clinically without specific tests, which can complicate treatment plans [24, 76]. If the symptoms of co-infection worsen, they can lead to complications such as pneumonia, acute respiratory distress syndrome (ARDS), and multiorgan failure, particularly dangerous for vulnerable groups such as the elderly and people with diseases [3, 137]. In general, infected individuals show different symptoms compared to people infected with the same virus. For example, the reproduction, spread, and pathogenicity of the pathogen can be affected by its presence. Understanding these interactions is essential to predict disease outbreaks and implement effective mitigation strategies.

1.2 Study contributions

This research focuses to enhance our understanding of the interactions of two respiratory pathogens. Focus especially on the effects of non-pharmaceutical interventions (NPIs), such as quarantine efficacy, and study the long-term behavior depending on cross-immunity and co-infections. For this purpose, the research develops sophisticated mathematical model that capture the complexities of cross-immunity, between two respiratory pathogens, co-infection dynamics, as well as quarantine and isolation of individuals. Mathematically, our analysis investigates critical points, disease thresholds, stability conditions, and multipathogen interactions to guide effective quarantine strategies and enhance understanding of pathogen dynamics. We show that disease-free equilibrium can achieve local or global asymptotic stability depending on the efficacy of quarantine. Co-infections and imperfect quarantine present substantial challenges, as they can sustain outbreaks even if individual strains are controlled.

The study shows that when complete immunity is present, the pathogen with a quarantine reproduction number greater than 1 will dominate, potentially driving the pathogen with a reproduction number below 1 to extinction. Additionally, we identify conditions where diseases persist in a subcritical co-existence equilibrium and demonstrate that cross-immunity facilitates strain co-existence, highlighting the intricate dynamics between immunity and pathogens. By analyzing the efficacy of imperfect quarantine measures, the study offers valuable insights into optimizing quarantine protocols. We show that quarantine measures are effective if the recovery rate of quarantined individuals is higher than that of non-quarantined individuals. This information is essential for public health officials to tailor quarantine strategies to maximize their effectiveness in controlling disease spread. It enables the design of targeted interventions that improve recovery rates and reduce secondary transmission, ultimately improving outbreak management and public health outcomes. In addition, our examination includes identifying and analyzing the underlying determinants of the backward bifurcation phenomenon in co-existence scenarios. Our analysis underscores the importance of considering asymptomatic transmission in infectious disease modeling, as it can contribute to the phenomenon of backward bifurcation. This means that even if initial control measures are effective in reducing disease prevalence, the presence of asymptomatic carriers can lead to a situation where the disease re-emerges or persists at a high level despite efforts to control it.

We also incorporate empirical data on influenza and SARS-CoV-2 to enhance our knowledge of the dynamics of interactions between multiple strains. Specifically, we used registered data on SARS-CoV-2 and influenza diseases obtained from the Robert Koch Institute, Germany's

health institute. The study emphasizes the importance of age-structured models accounted for variations in transmission, susceptibility, and immunity between different age groups, providing a more nuanced and accurate depiction of disease spread and control measures. This contribution is vital for designing age-specific interventions and optimizing public health strategies.

1.3 Structure of the thesis

This dissertation is further divided into the following chapters:

Chapter 2 reviews existing multipathogen models based on their interactions and examines the impact of quarantine measures within these models. This chapter concludes by identifying research gaps in the current literature, setting the stage for the contributions of this thesis. Building on the identified research gaps, Chapter 3 provides the essential hypothetical and mathematical foundations required to understand, develop, and analyze the models used in this research. By introducing essential analytical tools, defining key terms, and reviewing existing theories, this chapter ensures that the research is grounded in a solid theoretical and mathematical context, thereby setting the stage for detailed modeling and analysis in subsequent chapters.

Informed by the theoretical groundwork laid out previously, Chapter 4 delves into the dynamics of a multipathogen model that incorporates the complexities of imperfect quarantine measures, cross-immunity, and co-infections. It begins with an introduction to the topic and sets the stage for the detailed design of the model. Key assumptions are outlined, followed by the formulation of the model and an analysis of the positivity and boundedness of solutions. The exploration of the Disease-Free Equilibrium (DFE) includes both local and global stability analyses. The chapter then examines the dynamics of endemic equilibria in the absence of co-infection, discussing the existence and stability of dominance and multiple endemic equilibria, as well as invasion reproduction numbers. The dynamics of multiple strains with co-infection is also explored, focusing on the invasion reproduction number in the presence of co-infection. Numerical simulations are performed to illustrate various scenarios, including the effects of quarantine, the force of infection at endemic states, and the co-circulation of pathogens. The chapter concludes with a discussion of the findings and their implications.

Following detailed model analysis, Chapter 5 examines the effectiveness of quarantine measures during the early stages of disease transmission. This chapter assesses how varying levels of quarantine compliance and capacity impact outbreak dynamics, offering evidence-based recommendations to optimize quarantine strategies. Following the discussion on quarantine measures, Chapter 6 delves into the phenomenon of subcritical co-existence, a scenario in which the reproductive number of one pathogen is less than one while that of another is greater than one. Additionally, the chapter analyses backward bifurcation, where stable disease-free and endemic equilibria coexist even when the reproduction number is below one. This chapter identifies the factors that contribute to backward bifurcation and examines its implications for disease control and public health policy, adding complexity to the understanding of disease dynamics.

To validate the theoretical models developed in the study, Chapter 7 integrates empirical data

on influenza and SARS-CoV-2. This chapter describes the calibration process and evaluates the accuracy of the models in predicting real-world dynamics, thereby strengthening the reliability of the study findings. Finally, Chapter 8 synthesizes the results of the study, discussing their implications for public health strategies and policy. This chapter highlights the practical applications of research, such as informing quarantine protocols and multipathogen management plans. It summarizes the key findings and contributions of the study, reflects on limitations, and suggests directions for future research, emphasizing the importance of continuing to explore multipathogen interactions and their implications for public health.

2 Review of Existing Multi-pathogen Models

2.1 Introduction

Multi-pathogen models are important in capturing the complex nature of real infectious diseases. Many pathogens can infect people at the same time [3] or one after another [112] and can interact in different [34] ways. Understanding these relationships is important for the development of public health policies. In addition, these models facilitate the investigation of the interactions between various diseases [77, 97], competition within populations [13, 19, 55, 66], and strategies to contain their spread [6, 112]. This chapter examines previous research comparing the dynamics of various influenza-like illnesses (ILIs). It delves into models addressing competition, coexistence, co-infection, cross-immunity, and isolation effects to elucidate how these frameworks depict the intricate interactions among multiple pathogens.

2.1.1 Early models

Mathematical modeling of infectious diseases began with the pioneering work of Kermack and McKendrick in the 1920s [70]. They introduced the susceptible-infectious-recovered (SIR) model, which divides the population into three main categories: susceptible, infectious, and recovered. The model allows analyzing how people move between these countries over time, which is important to calculate the spread of the disease and evaluate the impact of various interventions. The work of Kermack and McKendrick marked a major advance in epidemic modeling by providing a framework for understanding disease dynamics. Their original equations have greatly influenced later models and shaped the field's approach to the analysis and control of infectious diseases.
The mathematical framework for the SIR model is given by the following differential equations:

$$\frac{dS}{dt} = -\beta\frac{SI}{N}, \ \frac{dI}{dt} = \beta\frac{SI}{N} - \gamma I, \ \frac{dR}{dt} = \gamma I. \tag{2.1}$$

In these equations, N represents the total population, where $N = S + I + R$. The term $\beta\frac{SI}{N}$ represents the rate of new infections, which depends on the number of susceptible and infectious individuals and the transmission rate β. The term γI describes the rate at which infected individuals recover and transition to the recovered compartment. The following quantity is essential for understanding the dynamics of disease spread:

Definition 2.1 — Basic Reproduction Number. The basic reproduction number, R_0, quantifies the average number of secondary infections generated by a single infected individual in a fully susceptible population. In the model (2.1), it is given by $R_0 = \frac{\beta}{\gamma}$, where β is the transmission

rate and γ represents the recovery rate. If $R_0 > 1$, the infection spreads within the population, while if $R_0 < 1$, the disease eventually dies out.

Sections 3.4.1 and 3.4.2 outline methods for determining the reproduction number.

The work of Ross (1911) on malaria, especially in his paper "The Prevention of Malaria," contributed significantly to the field before that of Kermack and McKendrick [110]. This work was crucial in understanding the dynamics of vector-borne diseases. In addition, it paved the way for a better understanding of how diseases spread and are controlled, which influenced subsequent advances in epidemiological modeling.

As epidemiology science developed, researchers extended the single pathogen model to include many pathogens. Klaus Dietz's 1979 paper, "Epidemiological Overlap of Viral Populations," introduced a model that showed how competing viruses could affect each other and identified a maximum of four products with persistence [30]. Expanding on this, Castillo-Chavez and Feng (1989) developed models that incorporate age groups, integration models, and resistance components to show the effect of these variables on the dynamics of multipathogen [18]. This work advanced the field by offering a more detailed and realistic representation of how diseases spread and interact within a population. Diekmann and Heesterbeek improved our understanding of how pathogens interact by learning how they co-exist and compete with each other [29]. Their work has created models that will help us to manage and better understand diseases caused by many pathogens. It showed how the presence of multiple pathogens in a population can affect the spread and persistence of disease.

2.2 Competition, coexistence and co-infection models

Understanding complex disease dynamics in populations requires understanding models that examine competition, co-existence, and co-infection. When multiple viruses compete for a vulnerable host, *Competition* occurs, and one virus can out-compete the others. In contrast, *coexistence* refers to a stable state in which many pathogens survive in a population without completely replacing each other. *Co-Infection* models are used to recognize cases where a host is infected by more than one pathogen at the same time. Studying these processes is important for predicting how diseases will spread and developing plans to prevent them.

One principle that guides the analysis of competitive interactions is the *competitive exclusion principle*. Originating from ecology, this concept states that "Two species with similar ecological requirements cannot co-exist when resources are limited" [52]. When it comes to infectious disease modeling, this means that two diseases competing for the same vulnerable host population cannot co-exist forever; one infection will eventually out-compete the other barring the presence of other conditions. This idea depends, in epidemiological terms, on the basic reproduction number of each pathogen (R_0). The pathogen with the highest R_0 will outcompete and drive the pathogen with the lowest R_0 to extinction in a homogeneous host population [86]. This principle can be formally stated as follows:

Definition 2.2 — Competitive exclusion principle. When two pathogens compete in a population, the pathogen with the largest reproduction number out-competes the other pathogen and drives the other to extinction.

When there are several infectious agents present, the competitive exclusion principle helps in predicting the results. Through comparison of the values of the diseases R_0, scientists can anticipate which pathogen will take the lead. However, real-world complexities, such as varying host immunity, can affect these dynamics, and sometimes multiple diseases can co-exist regardless of their reproduction numbers [96]. Understanding these nuances is crucial for developing effective public health strategies.

2.2.1 Case studies

Several analyses have contributed significantly to understanding the dynamics of pathogen competition, coexistence, and coinfection. Lazebnik et al. (2022) employed an extended Susceptible-Infected-Recovered-Death (SIRD) model to examine the impact of considerable strains on pandemic dynamics, highlighting that the number of strains correlates with logarithmic increases in infection and mortality rates, which illustrates the intricate nature of multi-strain interactions [77]. In addition, Ojo et al. (2022) studied the competitive dynamics between COVID-19 and influenza through a deterministic model, indicating that a multifaceted control approach, including accompanying interventions, is more effective in addressing these co-circulating conditions than isolated strategies [97]. Bhowmick et al. (2023) developed a compartmental model to investigate the dynamics of co-infection, focusing mainly on how limited healthcare aids impact disease management and revealing the interplay between competitive and co-existence aspects in multipathogen designs [9]. Musa et al. (2023) analyzed the co-infection dynamics of COVID-19 and influenza, revealing that increased vaccination coverage and effectiveness can reduce epidemic peaks and stating that COVID-19 may have a competitive advantage over influenza in co-infection scenarios [93]. Liang et al. (2024) also donated by combining seasonal variations and multipathogen relations into their influenza model, highlighting the importance of tailored vaccination strategies [80]. Despite these improvements, there exists a need for further investigation to refine these models, particularly to better comprehend the long-term effects of co-infection, evaluate the impact of various intervention strategies in real-world settings, and address the evolving dynamics of emerging and reemerging pathogens. This ongoing research is crucial for the development of more effective public health strategies and to improve our ability to manage complex pathogen interactions.

2.3 Cross-immunity models

In the previous Section, 1.1.2, we introduced the concept of cross-immunity between influenza and SARS-CoV-2. In this section, we review models that account for cross-immunity, exploring how immunity to one pathogen can impact susceptibility to another and examining the effects of this interaction on epidemic patterns.

Studies underscore the importance of understanding multi-strain interactions and host immune responses to improve disease management and control strategies [4, 50, 96, 128]. Andreasen (1997) designed a deterministic compartmental model to study the dynamics of multiple influenza

strains with partial cross-protection. Their model, using index-set notation, shows that sufficient cross-immunity can result in sustained oscillations in disease prevalence, demonstrating how even partial immunity can significantly affect epidemic patterns and strain competition [4]. Similarly, Fudolig et al. (2020) developed a multistrain SIR model to explore the impact of selective immunity on new viral strains. Their results show that new strains can survive even when older strains remain active, highlighting how the absence of cross-immunity influences the stability and spread of emerging strains [50]. Waterlow et al. (2022) used a two-pathogen model to study cross-protection between influenza and RSV (respiratory syncetial virus), indicating that moderate or absent cross-protection affects co-infection rates and vaccination strategies. Their work also suggests that the interaction between human coronaviruses and SARS-CoV-2 warrants further study to understand the impact on susceptibility and public health strategies [128]. The dynamics of two-strain influenza with isolation and partial cross-immunity by Nuno et al. [96] are described by the following system of ordinary differential equations:

$$\begin{aligned}
\frac{dS}{dt} &= \Lambda - \sum_{i=1}^{2} \frac{\beta_i S(I_i + V_i)}{A} - \mu S, \\
\frac{dI_i}{dt} &= \frac{\beta_i S(I_i + V_i)}{A} - (\mu + \gamma_i + \delta_i) I_i, \\
\frac{dQ_i}{dt} &= \delta_i I_i - (\mu + \alpha_i) Q_i, \\
\frac{dR_i}{dt} &= \gamma_i I_i + \alpha_i Q_i - \frac{\beta_j \sigma_{ij} R_i (I_j + V_j)}{A} - \mu R_i, \quad j \neq i, \\
\frac{dV_i}{dt} &= \frac{\beta_i \sigma_{ij} R_j (I_i + V_i)}{A} - (\mu + \gamma_i) V_i, \quad j \neq i, \\
\frac{dW}{dt} &= \sum_{i=1}^{2} \gamma_i V_i - \mu W, \; A = S + W + \sum_{i=1}^{2} (I_i + V_i + R_i).
\end{aligned} \tag{2.2}$$

From Equation (2.2), S represents susceptible individuals, I_i are those infected with strain i, Q_i are isolated infected individuals, R_i are individuals recovered with partial immunity, V_i are partially immune and infected again, and W are fully immune recovered individuals. Key parameters include Λ (birth rate), β_i (transmission rate), μ (mortality rate), γ_i (recovery rate), δ_i (isolation rate), α_i (rate of leaving isolation), and σ_{ij} (cross-immunity). The study demonstrated that partial cross-immunity can slow the spread of the second strain, highlighting the importance of immune responses from prior infections. The model identified conditions under which one strain could dominate or both strains could coexist, including sub-threshold coexistence equilibrium, where $R_1 < 1$ and $R_2 > 1$. Additionally, the study outlined the impact of various parameters on the overall infection dynamics, such as transmission and recovery rates, as well as the degree of cross-immunity. However, research is still needed to address how real-world complexities, such as imperfect quarantine measures and class of asymptomatic individuals, affect these dynamics. The existing model provides a foundational understanding, but incorporating these additional factors could offer deeper insights and improve strategies for managing multi-strain infections.

2.4 Quarantine effect in multi-pathogen models

The implementation of quarantine measures plays a crucial role in controlling the spread of infectious diseases, particularly in the context of multipathogen models. Quarantine involves

the isolation of people who are infected or suspected of being infected, thereby preventing them from coming into contact with the susceptible population. In single-strain models, quarantine has been shown to significantly reduce transmission rates and effectively control outbreaks [1, 16]. This section reviews the impact of quarantine and isolation on the dynamics of multi-strain (or staged) models in controlling disease spread.

Several studies have explored the impact of quarantine on the spread of multipathogen diseases, providing valuable insights into its effectiveness. Nuno et al. (2005) investigated how isolation and quarantine influence the dynamics of two competing strains of influenza A, incorporating factors such as herd immunity and cross-immunity [96]. Their findings reveal that while quarantine can lead to periodic epidemic cycles, cross-immunity between strains can allow them to co-exist even when individual reproductive numbers are below one, highlighting the nuanced effects of quarantine on multistrain systems. Arino et al. (2007) examined the SARS outbreak and demonstrated that effective quarantine measures, including travel restrictions, could significantly reduce the number of infections and mitigate the overall impact of the epidemic [6]. This study emphasized the importance of timely and targeted quarantine interventions. Safi et al. (2011) developed a multistage model that showed that the disease-free state is globally stable if the reproduction number is below one, but if it exceeds one, the disease remains endemic [112]; their follow-up study (2013) highlighted that imperfect quarantine could lead to backward bifurcation, complicating control efforts. However, perfect quarantine measures could ensure stability if the reproduction threshold is below one [111]. These studies collectively underscore the complex role of quarantine in managing disease spread, yet further research is needed to refine quarantine strategies, particularly in multipathogen contexts, to enhance their effectiveness and better inform public health responses.

2.5 Research gaps

Existing multi-pathogen analysis, for instance [97, 102, 106, 119] fall short in addressing the complex interactions between influenza and COVID-19, particularly when considering quarantine measures, cross-immunity and co-infections. Cross protection may have unpredictable effects on vulnerability to the population [96], and individuals infected with multiple pathogens may require different isolation procedures than individuals infected with a single pathogen. Thus, the interaction of cross-immunity and co-infection in multipathogenic environments might add further complexity to quarantine and isolation procedures. Moreover, there are notable gaps in understanding how pathogens co-occurring infections impact each other, especially concerning their evolution and virulence. Possible competition and cooperation between pathogens such as influenza and SARS-CoV-2 influence disease progression and adaptation is not fully understood [97, 119]. In addition, the implications of these interactions for public health strategies, including the effectiveness of isolation measures and public information and education to facilitate effectiveness in the quarantine facility, are not well documented.

3 Mathematical Foundations

3.1 Introduction

This chapter introduces mathematical modeling as a tool, method, and technique to analyze theoretical and numerical epidemic models, estimate parameters, and compare them with experimental data. Mathematical models are important tools that provide a framework for understanding, predicting, and optimizing complex systems. They bridge the gap between theoretical concepts and real-world applications in the form of equations that describe the variation of variables over time, for instance, the epidemic model (2.1) as described in Chapter 2. In this model, dS/dt, dI/dt, and dR/dt, respectively, represent the change in the rate of susceptible, infected, and recovered individuals at time t. Consequently, the next section considers the use of ordinary differential equations (ODEs) to construct a set of n differential equations and to develop a mathematical framework to analyze the dynamics of disease in more detail.

3.2 Mathematical modeling with ODEs

We will study a collection of n differential equations as a mathematical model of the following form:

$$X' = F(X) = \begin{pmatrix} f_1(x_1, \cdots, x_n) \\ \vdots \\ f_n(x_1, \cdots, x_n) \end{pmatrix}. \tag{3.1}$$

Here, X is a vector with $(x_1, x_2, \ldots, x_n)$ variables in the n-dimensional space. $F(X)$ is vector field describes the rate of change of a state vector X. Each $f_k(x_1, x_2, \ldots, x_n)$ is a scalar function that describes the k-th component of the vector field $F(X)$ at the point $(x_1, x_2, \ldots, x_n)$. The $X' = \frac{dX}{dt}$ defines the time derivative of the k-th component of the state vector X. The system of equations (3.1) is called non-autonomous if all f_k depend on t, so the system becomes $X' = F(X, t)$. The systems (2.1) and (2.2) illustrate the use of nonlinear ordinary differential equations in disease modeling.

3.2.1 Solution of an ODEs

Definition 3.1 — Solution of an ODEs. By the solution of system (3.1), we mean a map X from some interval $I \subset \mathbb{R}$ to $\mathbb{R}^n$ which is represented as

$$X : I \to \mathbb{R}^n, \ t \mapsto X(t),$$

such that $X(t)$ satisfies the differential equations:

$$X'(t) = F(X(t)) \quad \text{for all } t \in I.$$

The vector-valued function $X(t)$ is often referred to as the **trajectory** or **solution curve** of the system. This curve describes how the state vector X evolves within the interval I following the dynamics specified by the vector field $F(X(t))$. The interval I in Definition 3.1 is called the domain or the interval of existence of the solution and can be an open interval (t_0, t_1), a closed interval $[t_0, t_1]$, an infinite interval $[t_0, \infty)$, and so on. As noted in [65], if the time is measured continuously with $t \in \mathbb{R}$, we have a continuous system.

3.2.2 Initial value problem (IVP)

Definition 3.2 — Initial value problem (IVP). Extend the formulation of a vector field representation of a dynamical system over time, as given in Equation (3.1), by including the initial condition of a variable X at the initial time $t_0 \in I$. We have:

$$\begin{cases} X' = F(X), \\ X(t_0) = X_0. \end{cases} \tag{3.2}$$

Here, $X_0 \in \mathbb{R}^n$ denote the initial states of the state vector X, and we refer to System (3.2) as an initial value problem (IVP).

In some interval I containing t_0 the problem defined by definition 3.2 solves a differential equation of n^{th} order subject to the initial condition specified at the time t_0.

3.2.3 Existence of a unique solution

When dealing with differential equations, two fundamental questions arise concerning the solutions:

i). *Does a solution to the differential equation exist?*

ii). *Is the solution to the differential equation unique?*

Understanding these aspects is crucial because it ensures that the mathematical model provides a well-defined prediction of the behavior of the system. These properties are established using the Existence and Uniqueness Theorem.

Theorem 3.3 — Existence and Uniqueness Theorem [65]. Consider the initial value problem

$$X' = F(X), \quad X(t_0) = X_0,$$

where $X_0 \in \mathbb{R}^n$ and $F : \mathbb{R}^n \to \mathbb{R}^n$ is a continuously differentiable function ($F \in C^1$). Then the following statements hold:

1. **Existence**: There exists an interval $(t_0 - a, t_0 + a) \subset I \subset \mathbb{R}$ for some $a > 0$, and a solution $X(t)$ to this initial value problem in this interval.

2. **Uniqueness**: The solution $X(t)$ is unique on this interval. More precisely, it is a map

$$X : (t_0 - a, t_0 + a) \to \mathbb{R}^n,$$

such that $X(t)$ satisfies the differential equation $X' = F(X)$ for all $t \in (t_0 - a, t_0 + a)$, and the initial condition $X(t_0) = X_0$.

The positive number a that defines the interval $(t_0 - a, t_0 + a)$ could be very small, so it is logical to assume that the solution $X(t)$ is unique in a local sense, that is, a solution defined near the point (t_0, X_0). An application of Theorem 3.3 to epidemic non-linear initial value problems is provided in Section 4.2.3.

3.2.4 Non-negativity and bounds on solutions

In this subsection, we examine the fundamental properties of the solutions to our model, specifically their non-negativity and boundedness. Ensuring that the solutions remain biologically meaningful is crucial for the validity of the model. In the following, we restate item 1 of Theorem III-5-1 in [67] in the context of our model settings.

Theorem 3.4 — Positivity of solutions. If $X(t)$ is a solution to the initial value problem

$$X' = F(X), \quad X(t_0) = X_0,$$

where $X_0 \geq 0$ and $F(X) > 0$ for all $X \in \mathbb{R}^n$, then the solution $X(t)$ remains positive for all t in the existence interval.

The theorem implies that the solution $X(t)$ will remain nonnegative for all t within the existence interval. We will apply this theorem to establish the positivity of solutions to a differential equation, as detailed in Section 4.2.4. In addition, invariant sets offer a method for predicting the long-term behavior of these solutions.

Definition 3.5 — Invariant Set. A set $\mathcal{C} \subset \mathbb{R}^n$ is a positive invariant set for the initial value problem (3.2) if any solution starting in $\mathcal{C}$ remains in $\mathcal{C}$ for all future times. Formally, this means that if $X(t_0) \in \mathcal{C}$, then $X(t) \in \mathcal{C}$ for all $t \geq t_0$.

This definition ensures that once the state $X(t)$ enters the set $\mathcal{C}$, it remains within $\mathcal{C}$ as time progresses. In Section 4.2.4, we show that the state variables are bounded for all t. These properties guarantee the model's physical realism and stability.

3.3 Tools and approaches to system analysis

This section covers key tools and methods for analyzing systems, focusing on numerical techniques, software such as MATLAB and Python, and approaches for modeling and solving differential equations. These tools help to understand system behavior and improve performance.

3.4 Analytical methods

Finding analytical solutions to dynamical systems can be challenging due to their non-linearity and complexity. However, equilibrium solutions offer a simplified, yet powerful approach to understanding the system's long-term behavior. These solutions represent steady states where the rates of change of all variables are zero, providing crucial insights into the system's dynamics over time. Mathematically,

Definition 3.6 — Equilibrium [58]. A vector $X^* \in \mathbb{R}^n$ is called an equilibrium solution or a fixed point for the system if $F(X^*) = 0$.

In the context of disease modeling, analyzing these equilibrium points allows us to predict long-term outcomes, such as whether a disease will be eradicated or continue to circulate within the population. Specifically, equilibrium analysis can identify conditions that lead to a disease-free equilibrium (indicating eradication) or an endemic equilibrium (indicating persistence in the population).

3.4.1 Local stability of linear system

We start with the formal definition of stability as follows:

Definition 3.7 — Stability of an Equilibrium [12, 58]. An equilibrium point X^* of system (3.1) is *stable* if any solution $X(t)$ that starts sufficiently close to X^* remains close to X^* for all future times. In contrast, X^* is *unstable* if there exists at least one solution that begins near X^* but eventually moves away.
More precisely, X^* is stable if, for every $\epsilon > 0$, there exists a $\delta = \delta(\epsilon) > 0$ such that for any initial condition $X(0)$ satisfying

$$\|X(0) - X^*\| < \delta,$$

the solution remains close to equilibrium for all $t \geq 0$, meaning

$$\|X(t) - X^*\| < \epsilon \quad \text{for all } t \geq 0.$$

If, in addition, $X(t)$ approaches X^* as $t \to \infty$, then X^* is said to be *asymptotically stable.*

Jacobian approach

In practice, the local behavior of the non-linear system (3.1) near an equilibrium point X^* is analyzed by linearizing the system. This involves approximating the system around X^* using the Jacobian matrix $\mathbf{J} = DF_{X^*}$, where DF_{X^*} is the derivative (Jacobian) of the vector field $F(X)$ evaluated at X^*. The linearized system is given by:

$$X' = \mathbf{J}X. \tag{3.3}$$

The linearized system offers a simplified view of the dynamics near the equilibrium point. The Jacobian matrix $\mathbf{J}$ reveals the local stability and qualitative behavior of the system. By analyzing its eigenvalues (λ), one can determine whether the equilibrium is stable, unstable, or exhibits oscillations or saddle points. The following important theorem summarizes the stability

conditions:

Theorem 3.8 — Theorem 1 in [12]. Let $X^* = X(t)$

1. The equilibrium point X^* is locally asymptotically stable if all eigenvalues of the Jacobian matrix $\mathbf{J}$ have negative real parts, i.e., $\mathrm{Re}(\lambda_i) < 0$ for all $i = 1, \ldots, n$.
2. If any eigenvalue of the Jacobian matrix $\mathbf{J}$ has a nonnegative real part, that is, $\mathrm{Re}(\lambda_i) \geq 0$, then the equilibrium point X^* is not asymptotically stable.

If Tr$\mathbf{J}$ and Det$\mathbf{J}$ denote the trace and determinant of matrix $\mathbf{J}$, we will use the following theorem for the two-dimensional case:

Theorem 3.9 — Theorem 3.2 in [86]. Assume that $\mathbf{J}$ is a matrix 2×2 with constant entries and Det$\mathbf{J} \neq 0$. Assume that $\mathbf{J}$ has been obtained as a linearization around the equilibrium (X^*).Then the equilibrium (X^*) is locally asymptotically stable if and only if Tr$\mathbf{J} < 0$ and Det$\mathbf{J} > 0$.The equilibrium (X^*) is locally unstable if and only if Tr$\mathbf{J} > 0$ or Det$\mathbf{J} < 0$.

For higher-dimensional cases that cannot be reduced to two dimensions, the Routh–Hurwitz criterion will be applied to determine the necessary and sufficient conditions for the eigenvalues to have negative real parts.

Routh–Hurwitz criterion

Let $\mathbf{I}$ be the identity matrix. The characteristic polynomial of $\mathbf{J}$ is given by

$$P(\lambda) = |\mathbf{J} - \lambda\mathbf{I}| = \lambda^n + a_1\lambda^{n-1} + \cdots + a_n = 0, \tag{3.4}$$

where $P(\lambda)$ has roots n, known as the eigenvalues (λ) of $\mathbf{J}$. The coefficients a_i, for $i = 0, 1, \ldots, n$, are real constants with $a_n \neq 0$ to ensure that the polynomial retains its full degree. If $a_n = 0$, the polynomial reduces to a lower degree equation. Furthermore, we set $a_0 = 1$, a standard normalization that simplifies the Hurwitz criterion by eliminating the need to explicitly handle the leading coefficient.

Definition 3.10 — Routh–Hurwitz criterion [92]. Routh-Hurwitz conditions is represented using determinants constructed from the coefficients of the characteristic polynomial $P(\lambda)$, defined in Equation (3.4):

$$D_1 = a_1,\ D_2 = \begin{vmatrix} a_1 & a_3 \\ 1 & a_2 \end{vmatrix},\ D_3 = \begin{vmatrix} a_1 & a_3 & a_5 \\ 1 & a_2 & a_4 \\ 0 & a_1 & a_3 \end{vmatrix}\ D_k = \begin{vmatrix} a_1 & a_3 & a_5 & \cdot & \cdot & \cdot \\ 1 & a_2 & a_4 & \cdot & \cdot & \cdot \\ 0 & a_1 & a_3 & \cdot & \cdot & \cdot \\ 0 & 1 & a_2 & \cdot & \cdot & \cdot \\ \cdot & \cdot & \cdot & \cdot & \cdot & \cdot \\ 0 & 0 & \cdot & \cdot & \cdot & a_k \end{vmatrix},\ k = 1, 2, \cdots, n. \tag{3.5}$$

Stability conditions: For the system to be stable, we require $a_n > 0$, $D_1 > 0$, $D_2 > 0$, $D_3 > 0$, …, $D_k > 0$. Specifically, for a cubic polynomial, the conditions for $\mathrm{Re}(\lambda) < 0$ are:

$$a_1 > 0, \quad a_3 > 0, \quad \text{and} \quad a_1 a_2 - a_3 > 0.$$

In Section 4.3.1, this criterion will be utilized to examine the local stability of the disease-free equilibrium. The Jacobian approach establishes conditions for disease-free stability that facilitate the derivation of reproductive numbers. In particular, when the characteristic polynomial is of degree three or higher, the reproduction number can be extracted from the constant term [86]. Furthermore, we will employ the next generation method to determine the basic reproduction number, 2.1.

3.4.2 Next Generation Matrix (NGM) Approach

In Sections 4.4.4 and 7.3.3, we have applied the next-generation matrix approach to analyze the spread of disease within the population. This method, as studied by Van den Driessche and Watmough in their work on "Reproduction numbers and subthreshold endemic equilibria for compartmental models of disease transmission" [125], allows us to categorize the population into infected and noninfected components, providing critical insights into obtaining the basic reproduction number of disease dynamics. We proceed with the key aspects of this approach as detailed in [86].

1. Model Structure: Consider a system with n infected compartments and m non-infected compartments, leading to a total of $m+n$ dependent variables. Let $X \in \mathbb{R}^n$ represent the number of individuals in the infected compartments and $Y \in \mathbb{R}^m$ represent those in the non-infected compartments. The system's dynamics are governed by the following set of ordinary differential equations, which describe the rate of change in both compartments:

$$\begin{aligned} X_i' &= f_i(X,Y), \quad i = 1,\dots,n, \\ Y_j' &= g_j(X,Y), \quad j = 1,\dots,m. \end{aligned} \tag{3.6}$$

2. Dynamics of Infected Compartments: The rate of change in the infected compartments is given by:

$$\frac{dX_i}{dt} = \mathcal{F}_i(X,Y) - \mathcal{V}_i(X,Y), \tag{3.7}$$

where $\mathcal{F}_i(X,Y)$ represents the rate of new infections in the i-th infected compartment, and $\mathcal{V}_i(X,Y)$ denotes the net rate of transfer out of that compartment. These components satisfy the following properties:

   (i). $\mathcal{F}_i(0,Y) = 0$ and $\mathcal{V}_i(0,Y) = 0$ for $Y \geq 0$ and $i = 1,2,\dots,n$, ensuring that if no infected individuals are present ($X = 0$), no new infections or transitions occur.

   (ii). $\mathcal{F}_i(X,Y) \geq 0$ for all $X, Y \geq 0$, implying that the rate of new infections in each infected compartment is always non-negative.

   (iii). $\mathcal{V}_i(X,Y) \leq 0$ whenever $x_i = 0$ for $i = 1,2,\dots,n$, meaning that if no individuals are present in the i-th infected compartment, the net outflow from that compartment is non-positive.

   (iv). $\sum_{i=1}^{n} \mathcal{V}_i(X,Y) \geq 0$ for all $X, Y \geq 0$, ensuring that the total outflow from all infected compartments is non-negative.

3. Disease-Free System: We assume that the system $Y' = g(0, Y)$ has a unique disease-free equilibrium, denoted as $DFE_Y = (0, Y_0)$. This equilibrium ensures that all solutions starting with initial conditions of the form $(0, Y)$ converge to $(0, Y_0)$ as $t \to \infty$, meaning that in the absence of infections, the population stabilizes at Y_0.

4. Linearization: We linearize the system around the DFE. This involves computing the partial derivatives of the infection, $\mathcal{F}$, and $\mathcal{V}$ and transition terms with respect to the infected compartments. Specifically, we determine the matrices:

$$F = F_{ij} = \left.\frac{\partial \mathcal{F}_i(X)}{\partial x_j}\right|_{DFE_Y}, \quad V = V_{ij} = \left.\frac{\partial \mathcal{V}_i(X)}{\partial x_j}\right|_{DFE_Y}$$

Notably, $\frac{\partial \mathcal{F}_i(0,y_0)}{\partial y_j} = \frac{\partial \mathcal{V}_i(0,y_0)}{\partial y_j} = 0$ for all i and j, indicating that the linearized equations for the infected compartments X, evaluated at the DFE, are decoupled from the other equations. Consequently, the linearized system for the infected compartments simplifies to $X' = (F - V)X$.

5. The next-generation matrix $\mathbf{K}$ is then defined as:

$$\mathbf{K} = FV^{-1}.$$

Each element K_{ij} of $\mathbf{K}$ represents the expected number of new infections in compartment i caused by an individual initially introduced into compartment j. The basic reproduction number R_0 is given by the spectral radius (i.e., the largest eigenvalue) of $\mathbf{K}$:

$$R_0 = \rho(\mathbf{K})$$

Remark 3.11 The next generation matrix (NGM) does not give the same behavior as the Jacobian. However, it gives the same threshold condition. In the NGM of a multi-strain system, there generally appear nonlinear terms related to the expressions in the Jacobian approach.

3.4.3 Bifurcation from the non-hyperbolic equilibrium

We say that an equilibrium point X^* is nonhyperbolic if at least one eigenvalue of $\mathbf{J}$ has a real part equal to zero, i.e., $\mathrm{Re}(\lambda_i) = 0$ for some i. In Section 6.3, we show that this equilibrium is often associated with bifurcations, where a small change in parameters leads to a change from stable to unstable behavior.

Theorem 4.1 (restated as Theorem 3.12 in this document) as described by [20] is not only helpful in determining the local stability of nonhyperbolic equilibria, but also addresses the question of the existence of additional equilibria. To describe it, we consider a general system of ODEs with a parameter p:

$$X' = F(X, p), F : \mathbb{R}^n \times \mathbb{R} \to \mathbb{R}^n \quad \textit{and } F \in C^2(\mathbb{R}^n \times \mathbb{R}). \tag{3.8}$$

It is assumed that zero (0) is an equilibrium for System (3.8) for all values of the parameter p, that is

$$F(0,p) \equiv 0 \text{ for all } p. \tag{3.9}$$

Theorem 3.12 — Theorem 4.1 in [20]. Assume

A1: The matrix $\mathbf{J} = DF_{X^*}(0,0)$ is the linearization matrix of the system around the equilibrium 0 with p evaluated at 0. Zero is a simple eigenvalue of $\mathbf{J}$, and all other eigenvalues of $\mathbf{J}$ have negative real parts.

A2: The matrix $\mathbf{J}$ has a non-negative right eigenvector w and a left eigenvector v corresponding to the zero eigenvalue.

Let f_k be the k-th component of F, and define the coefficients

$$\begin{aligned} a &= \sum_{k=1}^{n}\sum_{i=1}^{n}\sum_{j=1}^{n} v_k w_i w_j \frac{\partial^2 f_k}{\partial x_i \partial x_j}(0,0), \\ b &= \sum_{k=1}^{n}\sum_{i=1}^{n} v_k w_i \frac{\partial^2 f_k}{\partial x_i \partial p}(0,0). \end{aligned} \tag{3.10}$$

The local dynamics of the system around the equilibrium point at the origin are determined by the values of a and b:

(i) $a > 0, b > 0$: When $p < 0$ with $|p| \ll 1$, the equilibrium at 0 is locally asymptotically stable, and there exists a positive unstable equilibrium. When $0 < p \ll 1$, the equilibrium at 0 is unstable and there exists a negative and locally asymptotically stable equilibrium.

(ii) $a < 0, b < 0$: When $p < 0$ with $|p| \ll 1$, the equilibrium at 0 is unstable. When $0 < p \ll 1$, the equilibrium at 0 is locally asymptotically stable, and there exists a positive unstable equilibrium.

(iii) $a > 0, b < 0$: when $p < 0$ with $|p| \ll 1$, the equilibrium at 0 is unstable and there exists a locally asymptotically stable negative equilibrium. When $0 < p \ll 1$, the equilibrium at 0 is stable and a positive unstable equilibrium appears.

(iv) $a < 0, b > 0$: When p changes from negative to positive, the equilibrium at 0 changes its stability from stable to unstable. Consequently, a negative unstable equilibrium becomes positive and locally asymptotically stable.

Particularly, if $a > 0$ and $b > 0$, then a bifurcation occurs at $p = 0$ is backward.

Theorem 3.12 will be applied in Chapter 6 to examine the local stability of equilibria and identify conditions under which additional equilibria may emerge. This analysis will provide insight into how the system responds to parameter variations. Additionally, we extend our investigation to global stability, aiming to establish whether all solutions ultimately converge to a steady state, regardless of initial conditions.

3.4.4 Lyapunov Function Approach to Global Stability

The concept of Lyapunov functions, named after the Russian mathematician Aleksandr Mikhailovich Lyapunov, plays a crucial role in stability analysis. Introduced in his doctoral dissertation [81], Lyapunov functions serve as powerful tools to prove the global stability of an equilibrium [86]. A key property of these functions is that they are positive definite throughout the space, ensuring that stability can be assessed without requiring explicit solutions to the system.

Definitions and Properties

To establish the global stability of an equilibrium, we introduce key properties of functions used in the Lyapunov method. These definitions lay the groundwork for the application of Lyapunov's stability Theorem.

Definition 3.13 — Positive Definite Function [86]. A continuous scalar function $L : \mathbb{R}^n \to \mathbb{R}$ is called positive definite if: - $L(X^*) = 0$ and $L(X) > 0$ for all $X \neq X^*$, where X^* is the equilibrium.

A function satisfying this condition ensures that $L(X)$ reaches its minimum at the equilibrium and remains strictly positive elsewhere, making it useful for stability analysis.

Definition 3.14 — Radially Unbounded Function [86]. A function $L(X)$ is said to be radially unbounded if

$$L(X) \to \infty \text{ as } ||X|| \to \infty.$$

This property guarantees that $L(X)$ grows indefinitely as the system moves farther from equilibrium, ensuring that solutions do not escape to infinity.

Lyapunov's Stability Theorem

With these definitions in place, we now introduce the Lyapunov stability Theorem, which provides a sufficient condition to determine the asymptotic stability of an equilibrium.

Theorem 3.15 — Lyapunov's Stability Theorem [86]. If a function $L(X)$ is globally positive definite and radially unbounded, and its time derivative satisfies

$$L'(X) < 0 \quad \text{for all } X \neq X^*,$$

then the equilibrium X^* is asymptotically stable.

This theorem states that if we can construct a function $L(X)$ with these properties, then the system will naturally evolve toward equilibrium over time. This function is formally defined as follows.

Definition 3.16 — Lyapunov Function [86]. A function $L(X)$ satisfying the conditions of Theorem 3.15 is called a Lyapunov function.

This approach provides a rigorous framework for demonstrating global stability, as it ensures that trajectories move towards equilibrium over time. In Section 4.3.2, we will apply the Lyapunov method to establish global stability conditions for our model.

3.5 Numerical methods

Mathematical models of infectious disease dynamics often involve complex differential equations that lack analytical solutions. Numerical methods serve as essential tools to approximate these solutions, allowing investigation of the spread of the disease under varying conditions [32]. Through these computational techniques, we can efficiently analyze parameter dependencies, evaluate intervention strategies, and simulate real-world scenarios that would otherwise be intractable. This section outlines the numerical methods employed to solve the system of equations governing the interaction between two pathogens.

A widely used approach to solving ordinary differential equations (ODE) is the Euler forward method [65]. Given an equation of the form $X' = F(t, X)$ with the initial condition $X(t_0) = X_0$, this method approximates the solution by discretizing the time interval $[t_0, T]$ into equal steps N. The choice of N influences the step size and accuracy of the approximation: larger N leads to smaller step sizes and generally improves precision. The size of the step Δt is defined as:

$$\Delta t = \frac{T - t_0}{N}.$$

At each time step, the solution is iteratively updated using the formula:

$$X_{n+1} = X_n + \Delta t \cdot F(t_n, X_n). \tag{3.11}$$

The equation updates the current solution X_n by adding the product of the step size Δt and the rate of change $F(t_n, X_n)$. This provides an approximation of the solution in the next time step $t_{n+1} = t_n + \Delta t$, where $n = 0, 1, 2, \ldots, N$.

This approach is straightforward and computationally efficient. However, it has limited accuracy. The local error, which is the error introduced in a single step, is proportional to Δt^2. This implies that halving the step size Δt reduces the local error by approximately a factor of four. Meanwhile, the global error, which accumulates in multiple steps, is proportional to Δt, which means that reducing the size of the steps directly decreases the total error [32].

Despite its limitations, the forward Euler method remains widely used because of its simplicity, particularly when small time steps can be employed to maintain accuracy. However, for improved precision, higher-order methods, such as the fourth-order Runge-Kutta (RK4) method, are often preferred. The RK4 method improves accuracy by computing four different slopes (k_1, k_2, k_3, and k_4) within each time step, significantly reducing both local and global errors [32, 65]. The first slope, k_1, provides an initial estimate of the rate of change X at the current time t_n and the state X_n:

$$k_1 = F(X_n, t_n).$$

The second slope, k_2, accounts for the progression in both time and state by evaluating the rate of change at the midpoint:

$$k_2 = F\left(X_n + \frac{\Delta t}{2} k_1, t_n + \frac{\Delta t}{2}\right).$$

The third slope, k_3, refines the midpoint estimate using k_2:

$$k_3 = F\left(X_n + \frac{\Delta t}{2} k_2, t_n + \frac{\Delta t}{2}\right).$$

The fourth slope, k_4, estimates the rate of change at the end of the interval:

$$k_4 = F(X_n + \Delta t \cdot k_3, t_n + \Delta t).$$

The final approximation of X_{n+1} is then computed as:

$$X_{n+1} = X_n + \frac{\Delta t}{6}(k_1 + 2k_2 + 2k_3 + k_4).$$

RK4 is widely favored in practice due to its balance between precision and computational efficiency.

In this study, we use the MATLAB ode45 solver, which is based on an adaptive Runge-Kutta method, specifically the Dormand-Prince variant [33]. Similarly to RK4, ode45 computes intermediate steps and adjusts the step size dynamically to maintain the desired accuracy. The local error per step is $O(\Delta t^5)$, and the global error is $O(\Delta t^4)$. This adaptive approach makes ode45 particularly effective for non-stiff problems, where it efficiently handles varying rates of change. For problems with stiffness, methods like ode15s would be more appropriate, as they are designed to handle such challenges.

3.5.1 Graphical methods

Graphical approach provide visual insights into the behavior of solutions to differential equations. They are especially useful for understanding the qualitative behavior of solutions without solving the equations analytically. Here are the graphical methods used in this thesis.

Time series plots

A time series plot for a dynamic system described by the system (3.1), shows how a specific state variable, such as x_k where $k = 1, 2, \cdots, n$, evolves over time. By solving differential equations, specifically $\frac{dx_k}{dt} = f_k(x_1, \cdots, x_n)$, and plotting x_k against time t, this plot provides a visual representation of $x_1(t)$. It helps in analyzing the temporal dynamics, trends, and stability of the state variable, offering insights into how the system's behavior changes over time.

Phase plots

A phase portrait is a graphical tool used to visualize the trajectories of a dynamical system in its phase space (state space). Each trajectory in the phase portrait corresponds to a solution of the system for a particular set of initial conditions. In the context of a general dynamic system described by System (3.1), the phase plane or phase space visualizes the behavior of the system by plotting the state variables x_1, x_2, and x_3 (for 3D) or x_1 and x_2 (for 2D) against each other. In 2D, the phase plane shows trajectories representing the evolution of x_1 and x_2 over time, with fixed points indicating equilibria. In 3D, the phase space plots x_1, x_2, and x_3 to illustrate more complex dynamics and interactions. Both tools help analyze system behavior, stability, and long-term evolution by revealing the paths followed by the state variables of the system.

3.6 Sensitivity analysis

Sensitivity analysis is a method used to see how changes in a model's input affect its output. This helps identify which inputs are the most important, making it easier to improve the model and reduce uncertainty. Local sensitivity analysis looks at the effect of small changes in individual inputs on the output [62]. For example, an elementary approach of obtaining the sensitivity coefficient of the independent variable q and the dependent variable, Q can be obtained from

the partial derivative of Q to q, that is, $\partial Q/\partial q$. This approach has the attraction of being very efficient in computer time. However, it does not account for interactions between different inputs and might miss the bigger picture of how inputs work together to influence the output. On the other hand, global sensitivity analysis examines how the entire range of possible values for all inputs impacts the output [62, 114]. This approach provides complete details of the inputs that are the most influential, considering both individual effects and interactions among inputs. In the upcoming chapters, we will apply sensitivity analysis methods. Specifically, we will discuss the local sensitivity approach in Section 5.3.1 and the global sensitivity approach in Section 7.3.3.

3.7 Parameter estimation

Parameter estimation is the process of using data to approximate parameter values within a mathematical model. We employ a least-squares fitting criterion. This technique minimizes the sum of the squared differences between the observed and predicted values [32]. Let $P = (P_1, P_2, \ldots, P_l)$ be a vector of parameters. An optimal estimate P_m^* of P_m is required, with any estimate of P_m denoted $\hat{P}_m$.

$$X' = F(X, P) \tag{3.12}$$

where $X = (x_1, x_2, \ldots, x_n)$ is the vector of state variables, and F encapsulates the dynamics of the system, specifying how each state variable evolves over time.

To estimate the parameter P_m using the least squares method for the given model (3.12), we demonstrate the following steps:

The differential equation $X' = F(X, P)$ will be solved numerically using the Euler method for different values of P_m while keeping the other parameters fixed. The residuals r_i for each data point as the difference between the observed values X_{obs} and the predicted values X_{pred} are calculated using the formula

$$r_i = X_{\text{obs}}(t_i) - X_{\text{pred}}(t_i; P_m) \tag{3.13}$$

The sum of squared residuals (SSR) as a function of P_m:

$$\text{SSR}(P_m) = \sum_{i=1}^{n} \left(X_{\text{obs}}(t_i) - X_{\text{pred}}(t_i; P_m)\right)^2$$

Next, we calculate the estimated parameter value $\hat{P}_m$ that minimizes the SSR.

$$\hat{P}_m = \arg\min_{P_m} \text{SSR}(P_m) \tag{3.14}$$

This provides a set of parameter estimates at various time points. In our implementation, we utilized the 'scipy.optimize.least_squares' function with bounds to ensure that the parameters stay within realistic ranges. Finally, to determine the optimal parameter value P_m^*, the mean of $\hat{P}_m$ is calculated if the estimates are normally distributed. For non-normally distributed data, the median is used. This choice ensures robustness in deriving the central estimate of the parameter.

4 Multi-pathogen Dynamics with Quarantine, Cross-immunity, and Co-infections

4.1 Introduction

The material offered in this chapter comes from our study described in [44, 47]. We build on previous studies, as represented in Chapter 2, exploring the role of mathematical modeling in understanding multipathogen dynamics and their implications for the evolution of virulence. Specifically, we extend existing cross-immunity models [4, 50, 96] to include a class of asymptomatic individuals who, although showing no symptoms, can still spread the disease, making detection and isolation challenging. By introducing imperfect quarantine, the model reflects the reality that quarantined individuals can still transmit the pathogen, albeit at a lower rate. The model also accounts for potential inputs, such as information and educational efforts, which are crucial to enhancing the effectiveness of quarantine measures. Additionally, it includes a co-infected class to address individuals infected with multiple strains simultaneously, complicating disease progression and treatment responses. Finally, by incorporating a disease-related death rate, the model offers a more accurate representation of the disease's impact on population dynamics, aiding in the development of more effective control strategies. Thus, the chapter aims to explore the critical points (epidemic thresholds) that determine whether an outbreak will occur and to evaluate how the cross-immunity between the two pathogens affects the dynamics of each strain and the co-infections in the Susceptible-Exposed-Infected-Quarantined-Recovered ($SEIQR$) framework.

Remark 4.1 At this point, our model adopts a general framework that can be applied to different respiratory pathogens or infectious diseases within the same host. This design ensures that the model is versatile and can be used in various scenarios involving multiple strains or pathogens.

4.2 Model design

We extend the standard five compartments of the $SEIQR$ model to include thirteen (13) classes, accounting for various population groups: susceptible (S), exposed to different pathogens (E_i, E_c, E_{ic}), infectious (I_i, I_c, I_{ic}), quarantined or isolated (Q_i, Q_c, Q_{ic}), and recovered (R_i, R_c, R_{ic}). The subscripts i, c, ic, respectively, represent pathogen-i, pathogen-c, pathogen-ic (dual pathogen).

The total population N_T is given by:

$$N_T = S + E_i + E_c + E_{ic} + I_i + I_c + I_{ic} + Q_i + Q_c + Q_{ic} + R_i + R_c + R_{ic}. \tag{4.1}$$

At time t, each element in the above equation is defined in Table 4.1.

Notation	Intepretation
	Represents the number of people ...
$S(t)$	susceptible to the disease at the moment t
$E_i(t)$	exposed to pathogen-i at time t
$E_c(t)$	exposed to pathogen-c at time t
$E_{ic}(t)$	exposed to both pathogen-i and pathogen-c at time t
$I_i(t)$	infected with pathogen-i in time t
$I_c(t)$	infected with pathogen-c at time t
$I_{ic}(t)$	infected with both pathogen-i and pathogen-c at time point t
$Q_i(t)$	in quarantine due to pathogen-i infection in time t
$Q_c(t)$	in quarantine due to infection with pathogen-c at time t
$Q_{ic}(t)$	in quarantine due to infection with both pathogen-i and pathogen-c at time t
$R_i(t)$	recovered from pathogen-i at time t
$R_c(t)$	recovered from pathogen-c at time t
$R_{ic}(t)$	recovered from both pathogen-i and pathogen-c at time t
$N_T(t)$	in total

Table 4.1: Model variables at time t

4.2.1 Main assumption statements

This segment presents the key assumptions that underpin the theoretical framework of the investigation.

Remark 4.2 — Fundamental assumptions.

1. ***Vital dynamics:*** Drawing inspiration from Hethcote's argument in 1989 [64], emphasizing the significance of including birth and death rates in disease modeling, we incorporate vital dynamics into our model to mirror real-world conditions.

2. ***Transmission dynamics:*** We assume that the transmission dynamics of the two pathogens is notably distinct [24, 141].

3. ***Formation of co-infected class:*** If an individual is infected with two or more pathogens, they are considered co-infected. Hence, we posit that when a symptomatic individual with the pathogen i meets another individual infected with the pathogen c, or vice versa, a coexposed class E_{ic} is formed. However, the capacity to cause harm may differ depending on the immune response. Conversely, coexistence refers to the state or occurrence of both pathogens existing in the same population at time t.

4. ***Imperfect quarantine:*** We assumed that quarantined individuals are either recognized as a recent contact with a confirmed case or symptomatic. To be clear and

specific, we define an imperfect quarantine as any quarantine site or facility (including home) characterized by violating any guidelines, rules, and regulations to control the spread of infections. For instance

(a) *Home quarantine*: an individual may want to go out for several reasons, like shopping or getting fresh air before quarantine maturity time. In such a case, if the individual is carrying the disease, can transmit the virus (however, at a reduced rate).

(b) *Campsite quarantine*: Here, we include places such as dedicated isolation centers or government-managed quarantine facilities. In this scenario, an exposed individual, who is not currently carrying the virus, can contract the infection while camping due to movements or activities that violate quarantine rules.

5. ***Cross-immunity:*** We introduce parameters η_i^c and η_c^i, both constrained to the range [0,1], to represent the level of immune response when challenged with another strain. These parameters were derived from an epidemiological study on an epidemic caused by a virus antigenically similar to another, which was conducted in Houston [122]. The frequency of infection was estimated to range from 0% to 100%, indicating a low to high rate of infection. This range allowed us to quantify the values between 0 and 1, representing full to partial protection, respectively. When $\eta_i^c = 0$ and $\eta_c^i = 0$, it implies full cross-immunity, meaning that recovery from one strain provides complete protection against the other. In contrast, when $\eta_i^c = 1$ and $\eta_c^i = 1$, it signifies no cross-immunity, implying that prior recovery from one strain does not offer protection against the other. In addition, we make the assumption that people who have recovered from a specific strain gain permanent immunity to that particular strain.

4.2.2 Model formulation

In our formulation we assume a well-mixed population with equal contact opportunities across all classes. The model incorporates a constant inflow rate (Λ) into the susceptible class, balanced by natural deaths at a rate μ. Disease-induced deaths (δ_i, δ_c, and δ_{ic}) are rare and contribute to the stabilization of the population size over time, as observed by Martcheva et al. [87]. When susceptible individuals interact with infectious ones at transmission rates (β_i or β_c), they can transition to different exposed classes (E_i or E_c), respectively. Subsequently, progression to single infectious states (I_i or I_c) occurs at rates (ρ_i or ρ_c). When individuals in states I_i and I_c come into contact, they form a co-exposed compartment, from which individuals can develop active co-infections represented by I_{ic} at a rate ρ_{ic}. We introduce imperfect quarantine classes (Q_i, Q_c, and Q_{ic}), where individuals of the exposed classes transition to quarantine at rates α_i, α_c, and α_{ic}, respectively. Similarly, individuals in infected classes move to isolation at rates σ_i, σ_c, and σ_{ic}. Subsequently, these isolated and quarantined individuals can progress to I_i, I_c, and I_{ic} at rates τ_i, τ_c, and τ_{ic}. Furthermore, individuals progress from infected states to recovered classes at rates γ_i, γ_c, and γ_{ic}, while those in quarantine transition to recovered classes at rates ϕ_i, ϕ_c, and ϕ_{ic}. Furthermore, after recovery, individuals can only acquire a different pathogen. The degree of protection against secondary infection is indicated by η_i^c and η_c^i, where η_i^c and η_c^i are both within the range of $[0, 1]$. For example, if $\eta_c^i = 0$, people who have recovered from the

pathogen$c$ are fully protected; otherwise, they can be infected with the pathogen-i. Following these assumptions, the extended model $SEIQR$ is described by the ODE system in Equation (4.2):

$$X'(t) = F(X) \tag{4.2}$$

where $X'(t)$ represents the time derivatives of the state variables:

$$X'(t) = \Big(S'(t), E_i'(t), E_c'(t), E_{ic}'(t), I_i'(t), I_c'(t), I_{ic}'(t), Q_i'(t), Q_c'(t), Q_{ic}'(t), R_i'(t), R_c'(t), R_{ic}'(t)\Big)^T$$

and X is the state vector with components $\Big(S, E_i, E_c, E_{ic}, I_i, I_c, I_{ic}, Q_i, Q_c, Q_{ic}, R_i, R_c, R_{ic}\Big) \in \mathbb{R}^{13}$. The function $F(X) : \mathbb{R}^{13} \to \mathbb{R}^{13}$ is defined by the differential equations governing the dynamics of each state variable:

$$F(X) = \begin{pmatrix} f_1(X) \\ f_2(X) \\ f_3(X) \\ f_4(X) \\ f_5(X) \\ f_6(X) \\ f_7(X) \\ f_8(X) \\ f_9(X) \\ f_{10}(X) \\ f_{11}(X) \\ f_{12}(X) \\ f_{13}(X) \end{pmatrix} = \begin{pmatrix} \Lambda - (\xi_i + \xi_c + \mu)S \\ \xi_i S - (\alpha_i + \rho_i + \mu)E_i + \eta_c^i R_c \xi_i \\ \xi_c S - (\alpha_c + \rho_c + \mu)E_c + \eta_i^c R_i \xi_c \\ \xi_i I_c + \xi_c I_i - (\alpha_{ic} + \rho_{ic} + \mu)E_{ic} \\ \rho_i E_i + \tau_i Q_i - (\gamma_i + \sigma_i + \delta_i + \mu)I_i \\ \rho_c E_c + \tau_c Q_c - (\gamma_c + \sigma_c + \delta_c + \mu)I_c \\ \rho_{ic} E_{ic} + \tau_{ic} Q_{ic} - (\gamma_{ic} + \sigma_{ic} + \delta_{ic} + \mu)I_{ic} \\ \alpha_i E_i - (\phi_i + \tau_i + \delta_i + \mu)Q_i + \sigma_i I_i \\ \alpha_c E_c - (\phi_c + \tau_c + \delta_c + \mu)Q_c + \sigma_c I_c \\ \alpha_{ic} E_{ic} - (\phi_{ic} + \tau_{ic} + \delta_{ic} + \mu)Q_{ic} + \sigma_{ic} I_{ic} \\ \phi_i Q_i + \gamma_i I_i - \eta_i^c R_i \xi_c - \mu R_i \\ \phi_c Q_c + \gamma_c I_c - \eta_c^i R_c \xi_i - \mu R_c \\ \phi_{ic} Q_{ic} + \gamma_{ic} I_{ic} - \mu R_{ic} \end{pmatrix}, \tag{4.3}$$

where

$$\xi_i = \frac{\beta_i(I_i + I_{ic} + \Omega_i Q_i + \Omega_{ic} Q_{ic})}{N_T}, \quad \text{and} \quad \xi_c = \frac{\beta_c(I_c + I_{ic} + \Omega_c Q_c + \Omega_{ic} Q_{ic})}{N_T}. \tag{4.4}$$

At the initial time t_0, System (4.2) is equipped with strictly non-negative initial data:

$$X(t_0) = \Big(S_0, E_{i0}, E_{c0}, E_{ic0} I_{i0}, I_{c0}, I_{ic0} Q_{i0}, Q_{c0}, Q_{ic0} R_{i0}, R_{c0}, R_{ic0}\Big) \tag{4.5}$$

that sum up to the total initial population $N_T(0)$. A graphical representation that illustrates our model system is shown in Figure 4.1, with details regarding the parameters provided in Table 4.2. Furthermore, we acknowledge that all the parameters of our model are positive, as indicated in the table.

The expressions for the forces of infection, ξ_i for the pathogen-i and ξ_c for pathogen-c (refer to Equation (6.3)), highlight how these pathogens drive disease transmission in the population. A recent study, such as [109], has explored the importance of the force of infection in the dynamics of disease. Equations (in (6.3)) consider variables such as the number of infected individuals, interventions, and population size. Parameters β_i and β_c denote the transmission rates of infection. Furthermore, Ω_i, Ω_c, and Ω_{ic} serve as decreasing functions of infectiousness (as defined in

Equation (4.6)). These functions, examined by [43, 89], illustrate a reduction in disease transmission due to the implementation of control measures. We define $\Omega_k(I_k) = \Omega_k$ as a continuously differentiable function with respect to I_k, specified as:

$$\Omega_k = 1 - \omega_k I_k = \begin{cases} \to 0, & \text{if } I_k\omega_k \to 1, \\ (0,1], & \text{if } I_k\omega_k \in [0,1). \end{cases} \tag{4.6}$$

Here, the subscript k represents different pathogens: pathogen-i, pathogen-c, and pathogen-ic. The parameter ω_k quantifies the level of interventions implemented by the respective authority, such as information dissemination and education on infection dynamics [101]. A value of $\omega_k = 0$ indicates the absence of such initiatives, while values in the range $(0, 1]$ represent the varying intensities of awareness campaigns and educational efforts.

For all k, where $I_k \in (0, 1)$ and $\omega_k \in [0, 1]$, it follows that $\omega_k I_k \in (0, 1)$, ensuring that Ω_k remains nonnegative ($\Omega_k \notin \mathbb{R}^-$). This formulation assumes that I_k is normalized with respect to the total population. The function Ω_k serves to adjust the effective transmission rates according to the number of infected individuals in quarantine. To examine how Ω_k changes with respect to ω_k, we compute the derivative:

$$\frac{d\Omega_k}{d\omega_k} = -I_k.$$

This result indicates that Ω_k decreases as ω_k increases, with the rate of decline being directly proportional to I_k. The negative sign signifies an inverse relationship: increasing intervention efforts (ω_k) leads to a reduction in Ω_k. Moreover, the magnitude of this decrease depends on I_k—when I_k is large, increase in ω_k results in a significant reduction in Ω_k. The extended analysis of Equation (4.6) is given in Section 5.4.

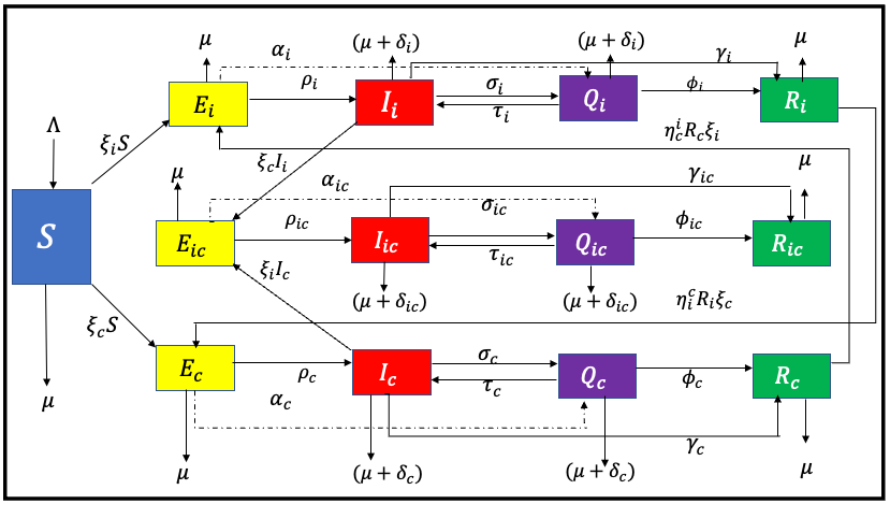

Figure 4.1: Flow diagram for the considered two-strain epidemic model with cross-immunity and co-infection

4.2.3 Existence and Uniqueness

We apply the Existence and Uniqueness Theorem 3.3 to ordinary differential equations (ODEs), as discussed in Section 3.2.3 , to verify that the model (4.2) satisfies the necessary continuity and differentiability conditions. To establish this, we prove the following key result:

Lemma 4.3 The function $F(X)$, as defined in Equation (4.2), is continuously differentiable, that is, $F \in C^1$.

Proof. Each component f_k of $F(X)$ consists of linear and rational terms involving the force of infection ξ_i and ξ_c (Equation (6.3)). Linear terms are clearly differentiable. Infection terms are ratios of differentiable functions, and their derivatives, obtained by the quotient rule, are well defined as long as $N_T > 0$, ensuring nonzero denominators. Since all f_k have continuous derivatives, $F(X)$ is continuously differentiable, that is, $F \in C^1$, satisfying the regularity conditions for the existence and uniqueness theorem. ■

Thus, $F(X)$ meets the conditions of the existence and uniqueness theorem, ensuring a unique solution to the problem of the initial value in (4.2) on an interval containing t_0. Furthermore, since F is continuously differentiable ($F \in C^1$), the solution $X(t)$ is continuous and differentiable in t, with $X'(t) = F(X(t))$ remaining continuous, highlighting the smooth dynamics of the system.

4.2.4 Positivity and boundedness of solutions

Given the dynamics of population problems, it is critical that all variables remain positive throughout $t \geq 0$ to ensure biologically meaningful interpretations. To show the limit of the solutions in the systems described by Equation (4.2), we must show that each component of $X(t)$ is located within a certain interval of all $t \geq 0$. We begin by stating the results and proving the non-negativity of the solutions.

Lemma 4.4 — Positivity of solutions. Consider the vector

$$X(t) = (S(t), E_i(t), E_c(t), E_{ic}(t), I_i(t), I_c(t), I_{ic}(t), Q_i(t), Q_c(t), Q_{ic}(t), R_i(t), R_c(t), R_{ic}(t))$$

as the solution to System (4.2). Furthermore, let

$$X_0 = (S_0, E_{i0}, E_{c0}, E_{ic0}, I_{i0}, I_{c0}, I_{ic0}, Q_{i0}, Q_{c0}, Q_{ic0}, R_{i0}, R_{c0}, R_{ic0}) \geq 0$$

denote the initial conditions of the System (4.2). Under condition $X(0) = X_0$, it is established that for $t \geq 0$, all components of $X(t)$ remain nonnegative.

Proof. By assumption at $t = 0$ we have $X(0) = X_0$, implying

$$\begin{aligned} &S(0) \geq 0,\ E_i(0) \geq 0,\ E_c(0) \geq 0,\ E_{ic}(0) \geq 0, I_i(0) \geq 0,\ I_c(0) \geq 0,\ I_{ic}(0) \geq 0, \\ &Q_i(0) \geq 0,\ Q_c(0) \geq 0, Q_{ic}(0) \geq 0,\ R_i(0) \geq 0,\ R_c(0) \geq 0, \text{ and } R_{ic}(0) \geq 0. \end{aligned} \tag{4.7}$$

Through the continuity of the solution [104], for all components $X(t)$ with positive initial values X_0 at time $t = 0$, we affirm the existence of an interval $(0, t_1)$ where $X(t) \geq 0$. Our aim is to demonstrate that $t_1 = \infty$. To ensure that each component remains nonnegative for all $t > 0$, we examine the behavior of the solution near each axis ($S = 0$, $E_i = 0$, $E_c = 0$, $E_{ic} = 0$, $I_i = 0$, $I_c = 0$, $I_{ic} = 0$, $Q_i = 0$, $Q_c = 0$, $Q_{ic} = 0$, $R_i = 0$, $R_c = 0$, $R_{ic} = 0$) while other compartments remain positive. In order to show that if we start with a nonnegative initial condition and the vector field $F(X)$ ensures a positive rate of change, the solution will never drop below zero, we

use Theorem 3.4 regarding the nonnegativity of solutions. The theorem assures that under the given conditions, the solutions of the initial value problem will always be positive,

If $S(t_2) = 0$ for $t_2 > 0$ and other solutions stay positive at $t = t_2$, then

$$\frac{dS}{dt}(t = t_2) = \Lambda > 0. \tag{4.8}$$

This implies that when the susceptible population S reaches zero, the rate of change of $S(t)$ becomes positive, suggesting that the susceptible population will begin to rise over time due to input Λ.

When $E_i(t_2) = 0$ for $t_2 > 0$ and the remaining solutions remain positive at $t = t_2$:

$$\frac{dE_i}{dt}(t = t_2) = \xi_i S + \eta_c^i R_c \xi_i \geq 0. \tag{4.9}$$

That is, the rate of change of $E_i(t)$ remains nonnegative. Similar analyses are performed for the other compartments $E_c, E_{ic}, I_i, I_c, I_{ic}, Q_i, Q_c, Q_{ic}, R_i, R_c, R_{ic}$, each ensuring non-negativity of their respective solutions if it starts at zero or are non-negative themselves. Since there are no restrictions on how large t_1 can be, continuity implies that the solution remains non-negative for all $t > 0$, or equivalently, $t_1 = \infty$. ■

Additionally, we provide results on the biologically feasible region of System (4.2) in the following lemma:

Lemma 4.5 — Invariant Region. With $X_0 \geq 0$, the set

$$\mathcal{C} = \left\{ (S, E_i, E_c, E_{ic}, I_i, I_c, I_{ic}, Q_i, Q_c, Q_{ic}, R_i, R_c, R_{ic}) \in \mathbb{R}_+^{13} : \ N_T(t) \leq \frac{\Lambda}{\mu} \right\}$$

is positively invariant for the model (4.2). Here, $N_T(t)$ is the total population at time t, and is defined in Equation (4.1).

Proof. In Equation (4.1), the total population $N_T(t)$ is defined as the sum of all compartments:

$$\begin{aligned} N_T(t) = {} & S(t) + E_i(t) + E_c(t) + E_{ic}(t) + I_i(t) + I_c(t) + I_{ic}(t) + Q_i(t) \\ & + Q_c(t) + Q_{ic}(t) + R_i(t) + R_c(t) + R_{ic}(t). \end{aligned}$$

Adding all the equations in the Model (4.2) gives the rate of change of the total population over time:

$$N_T'(t) = \Lambda - \mu N_T - (\delta_c I_c + \delta_c Q_c + \delta_i I_i + \delta_i Q_i + \delta_{ic} I_{ic} + \delta_{ic} Q_{ic}). \tag{4.10}$$

Since the terms $(\delta_c I_c + \delta_c Q_c + \delta_i I_i + \delta_i Q_i + \delta_{ic} I_{ic} + \delta_{ic} Q_{ic}) \geq 0$, it follows that:

$$N_T'(t) \leq \Lambda - \mu N_T. \tag{4.11}$$

This is a linear differential inequality with the general solution:

$$N_T(t) \leq \frac{\Lambda}{\mu} + \left(N_T(0) - \frac{\Lambda}{\mu} \right) e^{-\mu t}. \tag{4.12}$$

Given the initial condition $N_T(0) \leq \frac{\Lambda}{\mu}$, it follows directly from the solution that $N_T(t) \leq \frac{\Lambda}{\mu}$ for all $t > 0$. This is because the term $\left(N_T(0) - \frac{\Lambda}{\mu}\right)$ is nonpositive, ensuring that the solution $N_T(t)$ never exceeds $\frac{\Lambda}{\mu}$ for all $t > 0$. Since $N_T(t)$ is bounded and represents the sum of all compartments, each compartment is also bounded by $\frac{\Lambda}{\mu}$. Thus, the set

$$\mathcal{C} = \left\{ (S, E_i, E_c, E_{ic}, I_i, I_c, I_{ic}, Q_i, Q_c, Q_{ic}, R_i, R_c, R_{ic}) \in \mathbb{R}_+^{13} : \ N_T(t) \leq \frac{\Lambda}{\mu} \right\}$$

is positively invariant for the System (4.2) with $X_0 \geq 0$. ■

Remark 4.6 — Population normalization [86]. Given that $\Lambda = \mu$, the total population $N_T(t)$ approaches 1 in the long term. This value represents the normalized population size and $N_T(t)$ can therefore be treated as constant.

4.3 Exploration of the Disease-Free Equilibrium (DFE)

The equilibrium solution obtained when there is no disease in the population is known as the Disease-Free Equilibrium (DFE). The DFE for the Model (4.2), labeled as $\mathbf{E}_{ic}^0$, is defined by the following population values:

$$\begin{aligned} \mathbf{E}_{ic}^0 &= (S^0, E_i^0, E_c^0, E_{ic}^0, I_i^0, I_c^0, I_{ic}^0, Q_i^0, Q_c^0, Q_{ic}^0, R_i^0, R_c^0, R_{ic}^0) \\ &= (\Lambda/\mu, 0, 0, 0, 0, 0, 0, 0, 0, 0, 0, 0, 0)\,. \end{aligned} \tag{4.13}$$

It is generally known that the reproduction number determines the local stability of the DFE [125]. Since a quarantine class is incorporated into our model, we specify the following:

Definition 4.7 — Quarantine reproduction number. The fundamental reproduction number R_0, as stated in Definition 2.1, is changed to account for the impact of quarantine measures on the spread of the disease, and this is known as the quarantine reproduction number. It represents the typical number of secondary cases that an infected person generates under a quarantine regimen.

In the next section, we start our exploration by scrutinizing DFE stability and provide the expressions for quarantine reproduction numbers.

4.3.1 Local stability of the DFE

To assess the local stability of $\mathbf{E}_{ic}^0$, we calculate the Jacobian matrix $\mathcal{Y}$ of the system described by Equation (4.2) at the Disease-Free Equilibrium (DFE). The sequence of compartments is as follows: S, E_i, I_i, Q_i, R_i, E_c, I_c, Q_c, R_c, E_{ic}, I_{ic}, Q_{ic} and R_{ic}. The Jacobian matrix $\mathcal{Y}$ is defined

as

$$\mathcal{Y} = \begin{pmatrix} -\mu & 0 & -\beta_i & -\beta_i & 0 & 0 & -\beta_c & -\beta_c & 0 & 0 & -\beta_c-\beta_i & -\beta_c-\beta_i & 0 \\ 0 & -\mathbf{p}_i & \beta_i & \beta_i & 0 & 0 & 0 & 0 & 0 & 0 & \beta_i & \beta_i & 0 \\ 0 & \rho_i & -\mathbf{q}_i & \tau_i & 0 & 0 & 0 & 0 & 0 & 0 & 0 & 0 & 0 \\ 0 & \alpha_i & \sigma_i & -\mathbf{r}_i & 0 & 0 & 0 & 0 & 0 & 0 & 0 & 0 & 0 \\ 0 & 0 & \gamma_i & \phi_i & -\mu & 0 & 0 & 0 & 0 & 0 & 0 & 0 & 0 \\ 0 & 0 & 0 & 0 & 0 & -\mathbf{p}_c & \beta_c & \beta_c & 0 & 0 & \beta_c & \beta_c & 0 \\ 0 & 0 & 0 & 0 & 0 & \rho_c & -\mathbf{q}_c & \tau_c & 0 & 0 & 0 & 0 & 0 \\ 0 & 0 & 0 & 0 & 0 & \alpha_c & \sigma_c & -\mathbf{r}_c & 0 & 0 & 0 & 0 & 0 \\ 0 & 0 & 0 & 0 & 0 & 0 & \gamma_c & \phi_c & -\mu & 0 & 0 & 0 & 0 \\ 0 & 0 & 0 & 0 & 0 & 0 & 0 & 0 & 0 & -\mathbf{p}_{ic} & 0 & 0 & 0 \\ 0 & 0 & 0 & 0 & 0 & 0 & 0 & 0 & 0 & \rho_{ic} & -\mathbf{q}_{ic} & \tau_{ic} & 0 \\ 0 & 0 & 0 & 0 & 0 & 0 & 0 & 0 & 0 & \alpha_{ic} & \sigma_{ic} & -\mathbf{r}_{ic} & 0 \\ 0 & 0 & 0 & 0 & 0 & 0 & 0 & 0 & 0 & 0 & \gamma_{ic} & \phi_{ic} & -\mu \end{pmatrix}$$

where

$$\begin{aligned} &\mathbf{p}_i = \alpha_i + \rho_i + \mu, && \mathbf{p}_c = \alpha_c + \rho_c + \mu, && \mathbf{p}_{ic} = \alpha_{ic} + \rho_{ic} + \mu, \\ &\mathbf{q}_i = \gamma_i + \sigma_i + \delta_i + \mu, && \mathbf{q}_c = \gamma_c + \sigma_c + \delta_c + \mu, && \mathbf{q}_{ic} = \gamma_{ic} + \sigma_{ic} + \delta_{ic} + \mu, \\ &\mathbf{r}_i = \phi_i + \tau_i + \delta_i + \mu, && \mathbf{r}_c = \phi_c + \tau_c + \delta_c + \mu, && \mathbf{r}_{ic} = \phi_{ic} + \tau_{ic} + \delta_{ic} + \mu. \end{aligned}$$

Expanding the characteristic polynomial $|\mathcal{Y} - \lambda I| = 0$ along the first column, then continuing with the fifth, ninth, and thirteenth columns, we derive $\lambda_{1,2,3,4} = -\mu$. The remaining nine eigenvalues are obtained from the eigenvalues of the following matrix:

$$Y = \begin{pmatrix} Y_{11} & Y_{12} & Y_{13} \\ Y_{21} & Y_{22} & Y_{23} \\ Y_{31} & Y_{32} & Y_{33} \end{pmatrix}.$$

Each block of Y is of size 3×3, with Y_{21}, Y_{31}, and Y_{32} being zero matrices. The blocks Y_{12}, Y_{13}, and Y_{23} represent coupling terms between different compartments of the model, but do not directly contribute to the eigenvalues of Y. Instead, it is Y_{11}, Y_{22}, and Y_{33} that play a pivotal role in determining these eigenvalues. These matrices are defined as follows:

$$Y_{11} = \begin{pmatrix} -\mathbf{p}_i & \beta_i & \beta_i \\ \rho_i & -\mathbf{q}_i & \tau_i \\ \alpha_i & \sigma_i & -\mathbf{r}_i \end{pmatrix}, Y_{22} = \begin{pmatrix} -\mathbf{p}_c & \beta_c & \beta_c \\ \rho_c & -\mathbf{q}_c & \tau_c \\ \alpha_c & \sigma_c & -\mathbf{r}_c \end{pmatrix}, Y_{33} = \begin{pmatrix} -\mathbf{p}_{ic} & 0 & 0 \\ \rho_{ic} & -\mathbf{q}_{ic} & \tau_{ic} \\ \alpha_{ic} & \sigma_{ic} & -\mathbf{r}_{ic} \end{pmatrix}. \tag{4.14}$$

Now, we apply the Routh–Hurwitz conditions (as defined in Definition 3.10) to describe the criteria for Y_{11}, Y_{22}, and Y_{33} to have negative real roots. The characteristic form of Y_{11} can be expressed as $p_{11}(\lambda) = \lambda^3 + y_1\lambda^2 + y_2\lambda + y_3$, where:

$$\begin{aligned} y_1 &= (\mathbf{p}_i + \mathbf{q}_i + \mathbf{r}_i), \\ y_2 &= (-\alpha_i\beta_i + \mathbf{p}_i\mathbf{q}_i + \mathbf{p}_i\mathbf{r}_i + \mathbf{q}_i\mathbf{r}_i - \beta_i\rho_i - \sigma_i\tau_i), \\ y_3 &= -\alpha_i\beta_i\mathbf{q}_i + \mathbf{p}_i\mathbf{q}_i\mathbf{r}_i - \beta_i\mathbf{r}_i\rho_i - \beta_i\rho_i\sigma_i - \alpha_i\beta_i\tau_i - \mathbf{p}_i\sigma_i\tau_i. \end{aligned}$$

The necessary and sufficient conditions for stability are: (i) $y_1 > 0$ and $y_3 > 0$, and (ii) $y_1 y_2 > y_3$. These conditions ensure that the zeros of $p_{11}(\lambda)$ have negative real parts. It is evident that $y_1 > 0$. For three or higher-order polynomials, the quarantine reproduction number can be obtained from the constant term, where a change in sign indicates a value greater than or less than one [86]. Therefore, $y_3 > 0$ is equivalent to the inequality:

$$1 > \frac{\alpha_i\beta_i\mathbf{q}_i + \beta_i\mathbf{r}_i\rho_i + \beta_i\rho_i\sigma_i + \alpha_i\beta_i\tau_i}{\mathbf{p}_i(\dot{\mathbf{q}}_i\mathbf{r}_i + \tilde{\mathbf{r}}_i\sigma_i)} := \tilde{\mathcal{R}}_i^q. \tag{4.15}$$

Here, $\tilde{\mathbf{r}}_i = \phi_i + \delta_i + \mu$ and $\dot{\mathbf{q}}_i = \gamma_i + \delta_i + \mu$. Now, to show that $y_1 y_2 - y_3 > 0$, we note that condition $y_2 > 0$ implies $\mathbf{p}_i\mathbf{q}_i + \mathbf{p}_i\mathbf{r}_i + \mathbf{q}_i\mathbf{r}_i > \alpha_i\beta_i + \beta_i\rho_i + \sigma_i\tau_i$. Multiplying $y_1 y_2$ and rearranging the terms, we obtain $y_1 y_2 = c_1 + y_3 > c_2$.

$$\text{This implies that } y_1 y_2 - y_3 > 0 \text{ iff } c_1 > c_2. \tag{4.16}$$

Note that $c_1 = \mathbf{p}_i^2(\mathbf{q}_i + \mathbf{r}_i) + \mathbf{q}_i^2(\mathbf{p}_i + \mathbf{r}_i) + \mathbf{r}_i^2(\mathbf{p}_i + \mathbf{q}_i) + 2\mathbf{p}_i\mathbf{q}_i\mathbf{r}_i$ and $c_2 = \alpha_i\beta_i(\mathbf{p}_i + \tilde{\mathbf{r}}_i) + \beta_i\rho_i(\mathbf{p}_i + \dot{\mathbf{q}}_i) + \sigma_i\tau_i(\mathbf{q}_i + \mathbf{r}_i)$. Examining c_2, terms such as $\alpha_i\beta_i$, $\beta_i\rho_i$, and $\sigma_i\tau_i$ encapsulate various dynamics of the pathogen$i$ within the model, capturing the combined effects of quarantine, transmission, progression to symptoms, and isolation on the spread and control of infection.

Similarly, from Equation (4.14), the characteristic polynomial of Y_{22} is $p_{22}(\lambda) = \lambda^3 + y_4\lambda^2 + y_5\lambda + y_6$, where

$$\begin{aligned}
y_4 &= (\mathbf{p}_c + \mathbf{q}_c + \mathbf{r}_c)\,,\\
y_5 &= (-\alpha_c\beta_c + \mathbf{p}_c\mathbf{q}_c + \mathbf{p}_c\mathbf{r}_c + \mathbf{q}_c\mathbf{r}_c - \beta_c\rho_c - \sigma_c\tau_c)\,,\\
y_6 &= -\alpha_c\beta_c\mathbf{q}_c + \mathbf{p}_c\mathbf{q}_c\mathbf{r}_c - \beta_c\mathbf{r}_c\rho_c - \beta_c\rho_c\sigma_c - \alpha_c\beta_c\tau_c - \mathbf{p}_c\sigma_c\tau_c.
\end{aligned}$$

The necessary and sufficient conditions for stability are: i) $y_4 > 0$ and $y_6 > 0$, and ii) $y_4 y_5 > y_6$ for the zeros of $p_{22}(\lambda)$ to have negative real parts. It is evident that $y_4 > 0$. Furthermore, $y_6 > 0$ is equivalent to the inequality:

$$1 > \frac{\alpha_c\beta_c\mathbf{q}_c + \beta_c\mathbf{r}_c\rho_c + \beta_c\rho_c\sigma_c + \alpha_c\beta_c\tau_c}{\mathbf{p}_c(\dot{\mathbf{q}}_c\mathbf{r}_c + \tilde{\mathbf{r}}_c\sigma_c)} := \tilde{\mathcal{R}}_c^q. \tag{4.17}$$

Here, $\tilde{\mathbf{r}}_c = \phi_c + \delta_c + \mu$ and $\dot{\mathbf{q}}_c = \gamma_c + \delta_c + \mu$. To demonstrate that $y_4 y_5 - y_6 > 0$, we note that condition $y_5 > 0$ implies $\mathbf{p}_c\mathbf{q}_c + \mathbf{p}_c\mathbf{r}_c + \mathbf{q}_c\mathbf{r}_c > \alpha_c\beta_c + \beta_c\rho_c + \sigma_c\tau_c$. Multiplying $y_4 y_5$ and rearranging the terms, we obtain $y_4 y_5 = c_3 + y_6 > c_4$.

$$\text{This implies that } y_4 y_5 - y_6 > 0 \text{ iff } c_3 > c_4. \tag{4.18}$$

Note that $c_3 = \mathbf{p}_c^2(\mathbf{q}_c + \mathbf{r}_c) + \mathbf{q}_c^2(\mathbf{p}_c + \mathbf{r}_c) + \mathbf{r}_c^2(\mathbf{p}_c + \mathbf{q}_c) + 2\mathbf{p}_c\mathbf{q}_c\mathbf{r}_c$ and $c_4 = \alpha_c\beta_c(\mathbf{p}_c + \tilde{\mathbf{r}}_c) + \beta_c\rho_c(\mathbf{p}_c + \dot{\mathbf{q}}_c) + \sigma_c\tau_c(\mathbf{q}_c + \mathbf{r}_c)$. Analyzing c_4, terms like $\alpha_c\beta_c$, $\beta_c\rho_c$, and $\sigma_c\tau_c$ encapsulate strain-c dynamics, reflecting the combined impact of quarantine, transmission, progression of symptoms, and isolation on infection spread and control.

Finally, for Y_{33}, the polynomial equation is given by $p_{33}(\lambda) = \lambda^3 + y_7\lambda^2 + y_8\lambda + y_9$, where

$$\begin{aligned}
y_7 &= (\mathbf{p}_{ic} + \mathbf{q}_{ic} + \mathbf{r}_{ic})\,,\\
y_8 &= (\mathbf{p}_{ic}\mathbf{q}_{ic} + \mathbf{p}_{ic}\mathbf{r}_{ic} + \mathbf{q}_{ic}\mathbf{r}_{ic} - \sigma_{ic}\tau_{ic})\,,\\
y_9 &= \mathbf{p}_{ic}\mathbf{q}_{ic}\mathbf{r}_{ic} - \mathbf{p}_{ic}\sigma_{ic}\tau_{ic} = \mathbf{p}_{ic}(\dot{\mathbf{q}}_{ic}\mathbf{r}_{ic} + \tilde{\mathbf{r}}_{ic}\sigma_{ic}).
\end{aligned}$$

Here, $\tilde{\mathbf{r}}_{ic} = \phi_{ic} + \delta_{ic} + \mu$ and $\dot{\mathbf{q}}_{ic} = \gamma_{ic} + \delta_{ic} + \mu$. The necessary and sufficient conditions for stability are: i) $y_7 > 0$ and $y_9 > 0$, and ii) $y_7 y_8 > y_9$ for the zeros of $p_{33}(\lambda)$ to have negative real parts. It is evident that $y_7 > 0$ and $y_9 > 0$. Now, we demonstrate that $y_7 y_8 - y_9 > 0$. The condition $y_8 > 0$ implies $\mathbf{p}_{ic}\mathbf{q}_{ic} + \mathbf{p}_{ic}\mathbf{r}_{ic} + \mathbf{q}_{ic}\mathbf{r}_{ic} > \sigma_{ic}\tau_{ic}$. Multiplying $y_7 y_8$ and rearranging the terms, we obtain $y_7 y_8 = c_5 + y_9 > c_6$.

$$\text{This implies that } y_7 y_8 - y_9 > 0 \text{ only if } c_5 > c_6. \tag{4.19}$$

Note that $c_5 = \mathbf{p}_{ic}^2(\mathbf{q}_{ic}+\mathbf{r}_{ic}) + \mathbf{q}_{ic}^2(\mathbf{p}_{ic}+\mathbf{r}_{ic}) + \mathbf{r}_{ic}^2(\mathbf{p}_{ic}+\mathbf{q}_{ic}) + 2\mathbf{p}_{ic}\mathbf{q}_{ic}\mathbf{r}_{ic}$ and $c_6 = \sigma_{ic}\tau_{ic}(\mathbf{q}_{ic}+\mathbf{r}_{ic})$. The term $\sigma_{ic}\tau_{ic}$ underscores the crucial interplay between isolating co-infected individuals (σ_{ic}) and their progression to the infected state (τ_{ic}), emphasizing the pivotal role of timely isolation in mitigating the spread of co-infection within the model.

If Equation (4.15) and Equation (4.16) are satisfied, the eigenvalues of Y_{11} will be negative. Meeting Equation (4.17) and Equation (4.18) ensures negative eigenvalues for all of Y_{22}. Likewise, if Equation (4.19) is fulfilled, the eigenvalues of Y_{33} will also be negative. Based on the analysis conducted, Equation (4.15) and Equation (4.17) provide the quarantine reproduction numbers, $\tilde{\mathcal{R}}_i^q$ and $\tilde{\mathcal{R}}_c^q$, respectively, for the system described by Equation (4.2) pertaining to each strain. When both $\tilde{\mathcal{R}}_c^q$ and $\tilde{\mathcal{R}}_i^q$ are below one, it means that the disease lacks the ability to persist in the population. In such scenarios, infected individuals do not generate enough new infections to sustain an outbreak. The overall quarantine reproduction number is given by

$$\tilde{\mathcal{R}}^q = \max\{\tilde{\mathcal{R}}_c^q, \tilde{\mathcal{R}}_i^q\}. \tag{4.20}$$

where

$$\tilde{\mathcal{R}}_c^q = \frac{\alpha_c\beta_c\mathbf{q}_c + \beta_c\rho_c\sigma_c + \alpha_c\beta_c\tau_c + \mathbf{r}_c\beta_c\rho_c}{\mathbf{p}_c(\dot{\mathbf{q}}_c\mathbf{r}_c + \tilde{\mathbf{r}}_c\sigma_c)}, \quad \text{and,} \quad \tilde{\mathcal{R}}_i^q = \frac{\alpha_i\beta_i\mathbf{q}_i + \beta_i\rho_i\sigma_i + \alpha_i\beta_i\tau_i + \mathbf{r}_i\beta_i\rho_i}{\mathbf{p}_i(\dot{\mathbf{q}}_i\mathbf{r}_i + \tilde{\mathbf{r}}_i\sigma_i)}.$$

Now, summarizing the local stability result of the disease-free equilibrium:

Lemma 4.8 The disease-free equilibrium (DFE), $\mathbf{E}_{ic}^0$, in System (4.2), is locally asymptotically stable (LAS) if $\max\{\tilde{\mathcal{R}}_i^q, \tilde{\mathcal{R}}_c^q\} < 1$, $c_1 > c_2$, and $c_3 > c_4$. Otherwise, it is unstable, and at least one endemic equilibrium will occur.

Inequalities $c_1 > c_2$ and $c_3 > c_4$ in Lemma 4.8 are influenced by imperfect quarantine measures, as we elaborate in Section 4.3.1. They must be met for DFE stability if $\max\{\tilde{\mathcal{R}}_i^q, \tilde{\mathcal{R}}_c^q\} < 1$. The expressions for $c_1, c_2, c_3, \& c_4$ are defined in Equation (4.21).

$$\begin{aligned}
c_1 &= \mathbf{p}_i^2(\mathbf{q}_i + \mathbf{r}_i) + \mathbf{q}_i^2(\mathbf{p}_i + \mathbf{r}_i) + \mathbf{r}_i^2(\mathbf{p}_i + \mathbf{q}_i) + 2\mathbf{p}_i\mathbf{q}_i\mathbf{r}_i \\
c_2 &= \alpha_i\beta_i(\mathbf{p}_i + \tilde{\mathbf{r}}_i) + \beta_i\rho_i(\mathbf{p}_i + \dot{\mathbf{q}}_i) + \sigma_i\tau_i(\mathbf{q}_i + \mathbf{r}_i) \\
c_3 &= \mathbf{p}_c^2(\mathbf{q}_c + \mathbf{r}_c) + \mathbf{q}_c^2(\mathbf{p}_c + \mathbf{r}_c) + \mathbf{r}_c^2(\mathbf{p}_c + \mathbf{q}_c) + 2\mathbf{p}_c\mathbf{q}_c\mathbf{r}_c \\
c_4 &= \alpha_c\beta_c(\mathbf{p}_c + \tilde{\mathbf{r}}_c) + \beta_c\rho_c(\mathbf{p}_c + \dot{\mathbf{q}}_c) + \sigma_c\tau_c(\mathbf{q}_c + \mathbf{r}_c)
\end{aligned} \tag{4.21}$$

The lemma 4.8 provides the necessary conditions for the local stability of the disease-free state in the system (4.2) with imperfect quarantine. The following lemma addresses the scenario of perfect quarantine, where $\Omega_i = \Omega_c = \Omega_{ic} = 0$ and $\tau_i = \tau_c = \tau_{ic} = 0$.

Lemma 4.9 The disease-free equilibrium (DFE) in the model described by Equation (4.2) is present and locally asymptotically stable (LAS) if $\mathcal{R}_i^q < 1$ and $\mathcal{R}_c^q < 1$. Otherwise, it is unstable.

From Lemma 4.9, $\mathcal{R}_i^q$ and $\mathcal{R}_c^q$ represent secondary cases for strain-i and strain-c, respectively, if individuals in quarantine are effectively isolated and do not contribute to the force of infection. The expressions and proof of the lemma are provided in the Appendix (4.A).

4.3.2 Global stability of the DFE

In this subsection, we establish the global stability of the Disease-Free Equilibrium (DFE) using the approach outlined in [17]. To express System (4.2) in the form of equation 3.1 in [17], we define the following vectors:
Let $\mathbf{x} = (S, R_i, R_c, R_{ic})^T \in \mathbb{R}_+^4$ represent the vector of uninfected individuals. Similarly, let $\mathcal{I} = (E_i, E_c, E_{ic}, I_i, I_c, I_{ic}, Q_i, Q_c, Q_{ic})^T \in \mathbb{R}_+^9$ denote the vector of infected individuals. With this notation, the system can be rewritten as:

$$\frac{d\mathbf{x}}{dt} = F(\mathbf{x}, \mathcal{I}), \quad \frac{d\mathcal{I}}{dt} = G(\mathbf{x}, \mathcal{I}). \tag{4.22}$$

where $F(\mathbf{x}, \mathcal{I})$ describes the dynamics of uninfected individuals and $G(\mathbf{x}, \mathcal{I})$ governs the evolution of infected individuals. The Disease-Free Equilibrium (DFE) is given by:

$$\mathbf{E}_{ic}^0 = (\mathbf{x}^*, 0, 0, 0, 0, 0, 0, 0, 0, 0),$$

where $\mathbf{x}^*$ represents the equilibrium values of the uninfected compartments, satisfying $d\mathbf{x}/dt = 0$. We establish the following conditions:

H1: $F(\mathbf{x}, \mathcal{I})|_{\mathbf{x}^*}$ is globally asymptotically stable (GAS) at $\mathbf{x}^*$.

H2: $G(\mathbf{x}, \mathcal{I}) = A\mathcal{I} - \hat{G}(\mathbf{x}, \mathcal{I})$, where $\hat{G}(\mathbf{x}, \mathcal{I}) \geq 0$ for all $(\mathbf{x}, \mathcal{I}) \in \mathcal{C}$.

Here, $\mathcal{C}$ denotes the biologically feasible region, as defined in Lemma 4.5. The matrix

$$A = DG_{\mathcal{I}}(\mathbf{x}, \mathcal{I})|_{\mathbf{x}^*}$$

is the Jacobian of G with respect to $\mathcal{I}$, evaluated in equilibrium-free state. The off-diagonal entries of A are nonnegative and $A\mathcal{I}$ represent the linearized changes in the infected compartments near equilibrium. The term $\hat{G}(\mathbf{x}, \mathcal{I})$ captures the non-linear dynamics of the infected subsystem, describing deviations from the linearized system. It is given by

$$\hat{G}(\mathbf{x}, \mathcal{I}) = A\mathcal{I} - G(\mathbf{x}, \mathcal{I}). \tag{4.23}$$

The non-negativity of $\hat{G}(\mathbf{x}, \mathcal{I})$ ensures that the system follows a positive flow within the region $\mathcal{C}$. Under these conditions, we establish the following result:

Theorem 4.10 The disease-free equilibrium

$$\mathbf{E}_{ic}^0 = (\mathbf{x}^*, 0, 0, 0, 0, 0, 0, 0, 0, 0)$$

of System (4.22), equivalent to System (4.2), is globally asymptotically stable (GAS) if it is

locally asymptotically stable (LAS) and if assumptions **H1** and **H2** hold.

Proof. We refer to Lemma 4.8 for the local stability analysis of the Disease-Free Equilibrium (DFE), $\mathbf{E}_{ic}^0$. It follows that $\mathbf{E}_{ic}^0$ is locally asymptotically stable if the conditions

$$\tilde{\mathcal{R}}_i^q < 1, \quad \tilde{\mathcal{R}}_c^q < 1, \quad c_1 > c_2, \quad c_3 > c_4, \quad c_5 > c_6$$

are satisfied.

To verify **H1** we need to show that the subsystem governing the uninfected compartments is globally asymptotically stable (GAS) at $\mathbf{x}^* = (S^*, R_i^*, R_c^*, R_{ic}^*)$. This requires analyzing the subsystem:

$$\frac{d\mathbf{x}}{dt} = F(\mathbf{x}, 0),$$

where $\mathbf{x} = (S, R_i, R_c, R_{ic})^T$ represents the uninfected compartments. By setting infection terms to zero ($\mathcal{I} = 0$), we obtain the following system:

$$\begin{aligned} S'(t) &= \Lambda - \mu S, \\ R_i'(t) &= -\mu R_i, \\ R_c'(t) &= -\mu R_c, \\ R_{ic}'(t) &= -\mu R_{ic}. \end{aligned} \tag{4.24}$$

Setting derivatives to zero, we obtain the equilibrium:

$$\mathbf{x}^* = (S^*, R_i^*, R_c^*, R_{ic}^*) = \left(\frac{\Lambda}{\mu}, 0, 0, 0\right).$$

The Jacobian matrix of the system at $\mathbf{x}^*$ is:

$$\mathbf{J} = \begin{pmatrix} -\mu & 0 & 0 & 0 \\ 0 & -\mu & 0 & 0 \\ 0 & 0 & -\mu & 0 \\ 0 & 0 & 0 & -\mu \end{pmatrix}.$$

Since all eigenvalues are $-\mu$ (negative for $\mu > 0$), the equilibrium $\mathbf{x}^*$ is locally asymptotically stable. To extend this result to global stability, we apply Lyapunov's Stability Theorem. We define the Lyapunov function:

$$L(\mathbf{x}) = \frac{1}{2}(S - S^*)^2 + \frac{1}{2}(R_i - R_i^*)^2 + \frac{1}{2}(R_c - R_c^*)^2 + \frac{1}{2}(R_{ic} - R_{ic}^*)^2.$$

This function is positive definite, as $L(\mathbf{x}) > 0$ for $\mathbf{x} \neq \mathbf{x}^*$ and $L(\mathbf{x}^*) = 0$. Additionally, it is radially unbounded since it consists of squared terms, implying $L(\mathbf{x}) \to \infty$ as $\|\mathbf{x}\| \to \infty$. Computing the time derivative:

$$\frac{dL}{dt} = (S - S^*)(\Lambda - \mu S) + (R_i - R_i^*)(-\mu R_i) + (R_c - R_c^*)(-\mu R_c) + (R_{ic} - R_{ic}^*)(-\mu R_{ic}).$$

Substituting $S^* = \frac{\Lambda}{\mu}$, we get:

$$\frac{dL}{dt} = -\mu(S - S^*)^2 - \mu R_i^2 - \mu R_c^2 - \mu R_{ic}^2 < 0, \quad \text{for all } \mathbf{x} \neq \mathbf{x}^*.$$

Since $L(\mathbf{x})$ is positive definite, radially unbounded, and $\frac{dL}{dt}$ is negative definite, it follows from Lyapunov's theorem that the equilibrium $\mathbf{x}^*$ is globally asymptotically stable (GAS). Thus, assumption **H1** is verified.

To establish the validity of assumption **H2**, we apply the formula defined in Equation 4.23. Specifically, we must show that $\hat{G}(\mathbf{x}, \mathcal{I}) \geq 0$ to satisfy the global stability condition.

The system governing the infected compartments is given by:

$$\mathcal{I} = (E_i, E_c, E_{ic}, I_i, I_c, I_{ic}, Q_i, Q_c, Q_{ic})^T \in \mathbb{R}^9_+.$$

The corresponding differential equations take the form:

$$\frac{d\mathcal{I}}{dt} = G(\mathbf{x}, \mathcal{I}) = A\mathcal{I} - \hat{G}(\mathbf{x}, \mathcal{I}). \tag{4.25}$$

To analyze Equation 4.25, we compute the Jacobian of $G(\mathbf{x}, \mathcal{I})$ with respect to $\mathcal{I}$, denoted as $A = \mathbf{J}_{\mathcal{I}}$, and evaluate it at the equilibrium point $(\mathbf{x}^*, \mathcal{I} = 0)$. The resulting matrix A is:

$$A = \begin{pmatrix} -\mathbf{p}_i & 0 & 0 & \beta_i & 0 & \beta_i & \beta_i & 0 & \beta_i \\ 0 & -\mathbf{p}_c & 0 & 0 & \beta_c & \beta_c & 0 & \beta_c & \beta_c \\ 0 & 0 & -\mathbf{p}_{ic} & 0 & 0 & 0 & 0 & 0 & 0 \\ \rho_i & 0 & 0 & -\mathbf{q}_i & 0 & 0 & \tau_i & 0 & 0 \\ 0 & \rho_c & 0 & 0 & -\mathbf{q}_c & 0 & 0 & \tau_c & 0 \\ 0 & 0 & \rho_{ic} & 0 & 0 & -\mathbf{q}_{ic} & 0 & 0 & \tau_{ic} \\ \alpha_i & 0 & 0 & \sigma_i & 0 & 0 & -\mathbf{r}_i & 0 & 0 \\ 0 & \alpha_c & 0 & 0 & \sigma_c & 0 & 0 & -\mathbf{r}_c & 0 \\ 0 & 0 & \alpha_{ic} & 0 & 0 & \sigma_{ic} & 0 & 0 & -\mathbf{r}_{ic} \end{pmatrix}.$$

By computing $A\mathcal{I}$, we obtain the linearized system around the disease-free equilibrium (DFE):

$$A\mathcal{I} = \begin{pmatrix} -\mathbf{p}_i E_i + \beta_i(I_i + I_{ic} + Q_i + Q_{ic}) \\ -\mathbf{p}_c E_c + \beta_c(I_c + I_{ic} + Q_c + Q_{ic}) \\ -\mathbf{p}_{ic} E_{ic} \\ \rho_i E_i - \mathbf{q}_i I_i + \tau_i Q_i \\ \rho_c E_c - \mathbf{q}_c I_c + \tau_c Q_c \\ \rho_{ic} E_{ic} - \mathbf{q}_{ic} I_{ic} + \tau_{ic} Q_{ic} \\ \alpha_i E_i + \sigma_i I_i - \mathbf{r}_i Q_i \\ \alpha_c E_c + \sigma_c I_c - \mathbf{r}_c Q_c \\ \alpha_{ic} E_{ic} + \sigma_{ic} I_{ic} - \mathbf{r}_{ic} Q_{ic} \end{pmatrix}.$$

Using Equation 4.23, we determine the nonlinear contributions:

$$\hat{G}(\mathbf{x}, \mathcal{I}) = \begin{pmatrix} \beta_i[I_i + I_{ic}]\left(1 - \frac{S+\eta_c^i R_c}{N_T}\right) + \beta_i\left[Q_i\left(1 - \Omega_i\left(1 - \frac{S+\eta_c^i R_c}{N_T}\right)\right) + Q_{ic}\left(1 - \Omega_{ic}\left(1 - \frac{S+\eta_c^i R_c}{N_T}\right)\right)\right] \\ \beta_c[I_c + I_{ic}]\left(1 - \frac{S+\eta_i^c R_i}{N_T}\right) + \beta_c\left[Q_c\left(1 - \Omega_c\left(1 - \frac{S+\eta_i^c R_i}{N_T}\right)\right) + Q_{ic}\left(1 - \Omega_{ic}\left(1 - \frac{S+\eta_i^c R_i}{N_T}\right)\right)\right] \\ -\frac{\beta_i I_c}{N_T}\left(I_i + I_{ic} + \Omega_i Q_i + \Omega_{ic} Q_{ic}\right) - \frac{\beta_c I_i}{N_T}\left(I_c + I_{ic} + \Omega_c Q_c + \Omega_{ic} Q_{ic}\right) \\ 0 \\ 0 \\ 0 \\ 0 \\ 0 \\ 0 \end{pmatrix}.$$

Given that $\Omega_i, \Omega_c, \Omega_{ic} \in (0,1]$ and $0 < S, \eta_c^i R_c, \eta_i^c R_i < N_T \leq 1$, we analyze the sign of $\hat{G}(\mathbf{x}, \mathcal{I})$. Observing the third component of $\hat{G}(\mathbf{x}, \mathcal{I})$, we find that it is negative:

$$-\frac{\beta_i I_c}{N_T}\Big(I_i + I_{ic} + \Omega_i Q_i + \Omega_{ic} Q_{ic}\Big) - \frac{\beta_c I_i}{N_T}\Big(I_c + I_{ic} + \Omega_c Q_c + \Omega_{ic} Q_{ic}\Big) < 0.$$

Since assumption **H2** requires $\hat{G}(\mathbf{x}, \mathcal{I}) \geq 0$, but this condition is violated, **H2** fails. Consequently, the disease-free equilibrium $\mathbf{E}_{ic}^0$ is not globally asymptotically stable, as stated in Proposition 4.11.

■

Proposition 4.11 — Global instability of $\mathbf{E}_{ic}^0$. In System (4.2), the Disease-Free Equilibrium (DFE), denoted as $\mathbf{E}_{ic}^0$, does not achieve global asymptotic stability (GAS) when $\tilde{\mathcal{R}}^q < 1$.

Globally unstable DFE implies that the system's dynamics exhibits instability on a global scale, encompassing all possible initial conditions. This instability can result in oscillatory behavior, chaotic dynamics, or the eventual convergence to another equilibrium state [36, 72].

Global stability (in a special case)

From the above analysis, we observed that the negativity of $\hat{G}(\mathbf{x}, \mathcal{I})$ is influenced by row 3, which is responsible for the co-infected strain. Here, we assume no co-infections and perfect quarantine measures. The vector of uninfected individuals is$\mathbf{x} = (S, Q_i, Q_c, R_i, R_c)^T \in \mathbb{R}_+^5$ and the vector of infected individuals is $\mathcal{I} = (E_i, E_c, I_i, I_c)^T \in \mathbb{R}_+^4$. Then,

$$\hat{G}(\mathbf{x}, \mathcal{I}) = \begin{pmatrix} \beta_i I_i \left(1 - \frac{S + \eta_c^i R_c}{N_T}\right) \\ \beta_c I_c \left(1 - \frac{S + \eta_i^c R_i}{N_T}\right) \\ 0 \\ 0 \end{pmatrix}. \tag{4.26}$$

Since $0 < S, \eta_c^i R_c, \eta_i^c R_i < N_T \leq 1$, $\hat{G}(\mathbf{x}, \mathcal{I})$ is nonnegative (**H2** holds). These findings are summarized in the following proposition.

Proposition 4.12 — Global stability of $\mathbf{E}_{ic}^0$. In System (4.2), when $I_{ic} = 0$ and $\Omega_i = \Omega_c = \Omega_{ic} = 0$, the disease-free equilibrium (DFE), denoted $\mathbf{E}_{ic}^0$, achieves global asymptotic stability (GAS) when $\mathcal{R}^q = \max\{\mathcal{R}_i^q, \mathcal{R}_c^q\} < 1$.

4.4 Dynamic of endemic equilibria in the absence of co-infection

In this section, we investigate the dynamics of endemic equilibria in the absence of co-infections (I_{ic}) within the framework of the System (4.2). To aid in obtaining an analytical solution, we adopt the simplifying assumption of complete cross-protection, as denoted by $\eta_c^i = \eta_i^c = 0$. The equilibrium state of coexistence, denoted as $\tilde{\mathbf{E}}^*$, is represented as:

$$\tilde{\mathbf{E}}^* = \Big[\tilde{S}^*, \tilde{E}_i^*, \tilde{E}_c^*, 0, \tilde{I}_i^*, \tilde{I}_c^*, 0, \tilde{Q}_i^*, \tilde{Q}_c^*, 0, \tilde{R}_i^*, \tilde{R}_c^*, 0\Big].$$

The solution $\tilde{\mathbf{E}}^*$ satisfies the following equations:

$$\begin{aligned}
0 &= \Lambda - \tilde{\xi}_i^* \tilde{S}^* - \tilde{\xi}_c^* \tilde{S}^* - \mu \tilde{S}^*, \\
0 &= \tilde{\xi}_i^* \tilde{S}^* - \mathbf{p}_i \tilde{E}_i^* + \eta_c^i \tilde{R}_c^* \tilde{\xi}_i^*, \\
0 &= \tilde{\xi}_c^* \tilde{S}^* - \mathbf{p}_c \tilde{E}_c^* + \eta_i^c \tilde{R}_i^* \tilde{\xi}_c^* \\
0 &= \rho_i \tilde{E}_i^* + \tau_i \tilde{Q}_i^* - \mathbf{q}_i \tilde{I}_i^*, \\
0 &= \rho_c \tilde{E}_c^* + \tau_c \tilde{Q}_c^* - \mathbf{q}_c \tilde{E}_i^*, \\
0 &= \alpha_i \tilde{E}_i^* - \mathbf{r}_i \tilde{Q}_i^* + \sigma_i \tilde{I}_i^*, \\
0 &= \alpha_c \tilde{E}_c^* - \mathbf{r}_c \tilde{Q}_c^* + \sigma_c \tilde{I}_c^*, \\
0 &= \phi_i \tilde{Q}_i^* + \gamma_i \tilde{I}_i^* - \eta_i^c \tilde{R}_i^* \tilde{\xi}_c^* - \mu \tilde{R}_i^*, \\
0 &= \phi_c \tilde{Q}_c^* + \gamma_c \tilde{I}_c^* - \eta_c^i \tilde{R}_c^* \tilde{\xi}_i^* - \mu \tilde{R}_c^*.
\end{aligned} \tag{4.27}$$

These equations characterize the equilibrium state of coexistence, where the rates of change for each compartment are balanced, resulting in a stable configuration of the system. Solving Equation (4.27) we have:

$$\begin{aligned}
\tilde{S}^* &= \frac{\Lambda}{\tilde{\xi}_i^* + \tilde{\xi}_c^* + \mu}, & \tilde{I}_i^* &= \frac{\tilde{\xi}_i^* W_{11}}{(\tilde{\xi}_i^* + \tilde{\xi}_c^* + \mu)}, & \tilde{Q}_c^* &= \frac{\tilde{\xi}_c^* W_{44}}{(\tilde{\xi}_i^* + \tilde{\xi}_c^* + \mu)}, \\
\tilde{E}_i^* &= \frac{\tilde{\xi}_i^* \Lambda}{\mathbf{p}_i(\tilde{\xi}_i^* + \tilde{\xi}_c^* + \mu)}, & \tilde{I}_c^* &= \frac{\tilde{\xi}_c^* W_{33}}{(\tilde{\xi}_i^* + \tilde{\xi}_c^* + \mu)}, & \tilde{R}_i^* &= \frac{\phi_i}{\mu}\tilde{Q}_i^* + \frac{\gamma_i}{\mu}\tilde{Q}_i^*, \\
\tilde{E}_c^* &= \frac{\tilde{\xi}_c^* \Lambda}{\mathbf{p}_c(\tilde{\xi}_i^* + \tilde{\xi}_c^* + \mu)}, & \tilde{Q}_i^* &= \frac{\tilde{\xi}_i^* W_{22}}{(\tilde{\xi}_i^* + \tilde{\xi}_c^* + \mu)}, & \tilde{R}_c^* &= \frac{\phi_c}{\mu}\tilde{Q}_c^* + \frac{\gamma_c}{\mu}\tilde{Q}_c^*,
\end{aligned} \tag{4.28}$$

where,

$$W_{1k} = \left[\frac{\Lambda(\mathbf{r}_k \rho_k + \alpha_k \tau_k)}{\mathbf{p}_k(\dot{\mathbf{q}}_k \mathbf{r}_k + \tilde{\mathbf{r}}_k \sigma_k)}\right], \quad W_{2k} = \left[\frac{\Lambda(\mathbf{q}_k \alpha_k + \sigma_k \rho_k)}{\mathbf{p}_k(\dot{\mathbf{q}}_k \mathbf{r}_k + \tilde{\mathbf{r}}_k \sigma_k)}\right].$$

The parameter $W_{11} = W_{1k}$ when $(k = i)$, $W_{22} = W_{2k}$ when $(k = i)$, $W_{33} = W_{1k}$ when $(k = c)$ and $W_{44} = W_{2k}$ when $(k = c)$. The forces of infection in endemic $\tilde{\xi}_i^*$ and $\tilde{\xi}_c^*$, respectively, are

$$\begin{aligned}
\tilde{\xi}_i^* &= \frac{\beta_i(\tilde{I}_i^* + (1 - \omega_i \tilde{I}_i^*)\tilde{Q}_i^*)}{(\Lambda - (\delta_i(\tilde{I}_i^* + \tilde{Q}_i^*)) - \delta_c(\tilde{I}_c^* + \tilde{Q}_c{}^*))/\mu} \\
\tilde{\xi}_c^* &= \frac{\beta_c(\tilde{I}_c^* + (1 - \omega_c \tilde{I}_c^*)\tilde{Q}_c^*)}{(\Lambda - (\delta_i(\tilde{I}_i^* + \tilde{Q}_i^*)) - \delta_c(\tilde{I}_c^* + \tilde{Q}_c{}^*))/\mu}.
\end{aligned} \tag{4.29}$$

Employing Equation (4.28) we obtain, from Equation (4.29),

$$\begin{aligned}
0 = \; & \tilde{\xi}_i^* \Big[W_{55}\omega_i\beta_i\mu\tilde{\xi}_i^* + (1 - \tilde{\Phi}_c)\tilde{\xi}_c^{*2} + (1 - \tilde{\Phi}_i)\tilde{\xi}_i^{*2} + \Big[(1 - \tilde{\Phi}_c) + (1 - \tilde{\Phi}_i)\Big]\tilde{\xi}_i^*\tilde{\xi}_c^* \\
& + (1 - \tilde{\Phi}_c)\mu\tilde{\xi}_c^* + (1 - \tilde{\Phi}_i)\mu\tilde{\xi}_i^* + (1 - \tilde{\mathcal{R}}_c^q)\mu\tilde{\xi}_c^* + (1 - \tilde{\mathcal{R}}_i^q)\mu\tilde{\xi}_i + (1 - \tilde{\mathcal{R}}_i^q)\mu^2 \Big] \\
& f_1(\tilde{\xi}_c^*, \tilde{\xi}_i^*), \\
0 = \; & \tilde{\xi}_c^* \Big[W_{66}\omega_c\beta_c\mu\tilde{\xi}_c^* + (1 - \tilde{\Phi}_i)\tilde{\xi}_i^{*2} + (1 - \tilde{\Phi}_c)\tilde{\xi}_c^{*2} + \Big[(1 - \tilde{\Phi}_i) + (1 - \tilde{\Phi}_c)\Big]\tilde{\xi}_i^*\tilde{\xi}_c^* \\
& + (1 - \tilde{\Phi}_c)\mu\tilde{\xi}_c^* + (1 - \tilde{\Phi}_i)\mu\tilde{\xi}_i^* + (1 - \tilde{\mathcal{R}}_i^q)\mu\tilde{\xi}_i^* + (1 - \tilde{\mathcal{R}}_c^q)\mu\tilde{\xi}_c + (1 - \tilde{\mathcal{R}}_c^q)\mu^2 \Big] \\
& = f_2(\tilde{\xi}_c^*, \tilde{\xi}_i^*).
\end{aligned} \tag{4.30}$$

Here,

$$W_{55} = \left[\frac{\Lambda(\mathbf{r}_i \rho_i + \alpha_i \tau_i)(\mathbf{q}_i \alpha_i + \sigma_i \rho_i)}{\mathbf{p}_i(\dot{\mathbf{q}}_i \mathbf{r}_i + \tilde{\mathbf{r}}_i \sigma_i)^2}\right], \qquad W_{66} = \left[\frac{\Lambda(\mathbf{r}_c \rho_c + \alpha_c \tau_c)(\mathbf{q}_c \alpha_c + \sigma_c \rho_c)}{\mathbf{p}_c(\dot{\mathbf{q}}_c \mathbf{r}_c + \tilde{\mathbf{r}}_c \sigma_c)^2}\right],$$

$$\tilde{\Phi}_i = \left[\frac{\alpha_i\delta_i\mathbf{q}_i + \delta_i\mathbf{r}_i\rho_i + \delta_i\rho_i\sigma_i + \alpha_i\delta_i\tau_i}{\mathbf{p}_i(\dot{\mathbf{q}}_i\mathbf{r}_i + \tilde{\mathbf{r}}_i\sigma_i)}\right], \quad \tilde{\Phi}_c = \left[\frac{\alpha_c\delta_c\mathbf{q}_c + \delta_c\mathbf{r}_c\rho_c + \delta_c\rho_c\sigma_c + \alpha_c\delta_c\tau_c}{\mathbf{p}_c(\dot{\mathbf{q}}_c\mathbf{r}_c + \tilde{\mathbf{r}}_c\sigma_c)}\right].$$

In Equation (4.28) and Equation (4.30), $W_{11}, W_{22}, \cdots W_{66}$ depict how factors such as new births, disease progression, and quarantine transitions influence the dynamics of strain-i or -c. The presence of Λ in these calculations signifies the impact of new births on the behavior of the strains. Similarly, $\tilde{\Phi}_i$ and $\tilde{\Phi}_c$ provide insights into the associated mortalities with strain-i and -c, considering factors like disease progression and quarantine transitions. A detailed analysis of dominant endemic is provided in the following subsection.

To establish the necessary conditions for coexistence solutions, we set s_1, s_2, s_3, s_4, s_5 to represent equilibrium points expressed as $(\ddot{\xi}_c^*, \ddot{\xi}_i^*)$, corresponding to equations $f_1(\tilde{\xi}_c^*, \tilde{\xi}_i^*) = f_2(\tilde{\xi}_c^*, \tilde{\xi}_i^*) = 0$ as defined in equation (4.30). The solution s_1 arises when $\ddot{\xi}_c^* = \ddot{\xi}_i^* = 0$, while s_2 arises when $\ddot{\xi}_c^* = 0$ and $\ddot{\xi}_i^* \neq 0$, and s_3 arises when $\ddot{\xi}_c^* \neq 0$ and $\ddot{\xi}_i^* = 0$. The first fixed point, $s_1 = (0, 0)$, corresponds to the state in which everyone in the population is susceptible (see Sections 4.3.1 and 4.3.2 for detailed information). The solutions s_2 and s_3 represent strain-i and strain-c dominance equilibrium, respectively.

4.4.1 Existence of dominant endemic equilibrilium

A dominance equilibrium refers to a boundary equilibrium in which only one strain of infectious disease is present [86], which consequently implies the absence of co-infections as well. Let $\tilde{\mathbf{E}}_c^d$ and $\tilde{\mathbf{E}}_i^d$ represent the dominance equilibria of strain-c and strain-i, respectively, in the Model (4.2). In the case where $E_c = I_c = Q_c = R_c = 0$, we obtain the strain-$c$ dominance equilibrium, given by:

$$\tilde{\mathbf{E}}_i^d = \left[\tilde{S}_i^d, \tilde{E}_i^d, 0, 0, \tilde{I}_i^d, 0, 0, \tilde{Q}_i^d, 0, 0, \tilde{R}_i^d, 0, 0\right]. \tag{4.31}$$

The non-zero variables in Equation (4.33) correspond to the positive candidates of s_2

$$s_2 = \left(0, \frac{-b_1 \pm \sqrt{b_1^2 - 4a_1c_1}}{2a_1}\right) \tag{4.32}$$

where,

$$\begin{aligned} a_1 &= (1 - \tilde{\Phi}_i), \\ b_1 &= W_{55}\omega_i\beta_i\mu + (1 - \tilde{\mathcal{R}}_i^q)\mu + (1 - \tilde{\Phi}_i)\mu, \\ c_1 &= (1 - \tilde{\mathcal{R}}_i^q)\mu^2. \end{aligned}$$

Similarly, when $E_i = I_i = Q_i = R_i = 0$, we obtain the strain-$c$ dominance equilibrium, given by:

$$\tilde{\mathbf{E}}_c^d = \left[\tilde{S}_c^d, 0, \tilde{E}_c^d, 0, 0, \tilde{I}_c^d, 0, 0, \tilde{Q}_c^d, 0, 0, \tilde{R}_c^d, 0\right]. \tag{4.33}$$

The non-zero variables in Equation (4.31) are positive solutions of s_3 derived in (4.34).

$$s_3 = \left(\frac{-b_2 \pm \sqrt{b_2^2 - 4a_2c_2}}{2a_2}, 0\right) \tag{4.34}$$

where,

$$\begin{aligned} a_2 &= (1 - \tilde{\Phi}_c), \\ b_2 &= W_{66}\omega_c\beta_c\mu + (1 - \tilde{\mathcal{R}}_c^q)\mu + (1 - \tilde{\Phi}_c)\mu, \\ c_2 &= (1 - \tilde{\mathcal{R}}_c^q)\mu^2. \end{aligned}$$

For stability analysis, we assume $s_2 = (0, 1)$ and $s_3 = (1, 0)$ for simplification. For s_2, where $\ddot{\xi}_c^* = 0$ and $\ddot{\xi}_i^* \neq 0$, we set the infection force for strain c to zero and the strain force i to its

maximum normalized value. In contrast, for s_3, where $\ddot{\xi}_c^* \neq 0$ and $\ddot{\xi}_i^* = 0$, the infection force for strain i is zero while that for strain c is at its maximum normalized value. These assumptions are reasonable for a normalized model, as they highlight the extreme cases of infection dynamics, simplify the analysis, and provide clear insights into the system's behavior.

4.4.2 Local stability of dominant equilibrilium

We define matrix $\mathbf{M}$ as the stability matrix for Equation (4.30), given by:

$$\mathbf{M} = \begin{pmatrix} \dfrac{\partial f_1}{\partial \xi_c^*} & \dfrac{\partial f_1}{\partial \xi_i^*} \\ \\ \dfrac{\partial f_2}{\partial \xi_c^*} & \dfrac{\partial f_2}{\partial \xi_i^*} \end{pmatrix} \Bigg|_{\tilde{\xi}_c^* = \ddot{\xi}_c^*,\ \tilde{\xi}_i^* = \ddot{\xi}_i^*}. \tag{4.35}$$

We denote by $\mathrm{Tr}\mathbf{M}$ and $\mathrm{Det}\mathbf{M}$ the trace and determinant of matrix $\mathbf{M}$. To test the stability of $\mathbf{M}$, we use Theorem 3.9. The equilibrium $(\ddot{\xi}_c^*, \ddot{\xi}_i^*)$ is locally asymptotically stable if:

$$\mathrm{Tr}\mathbf{M} < 0 \quad \text{and} \quad \mathrm{Det}\mathbf{M} > 0. \tag{4.36}$$

We start with the stability conditions for the dominance equilibrium $s_2 = (\ddot{\xi}_c^*, \ddot{\xi}_i^*) = (0, 1)$. The trace and determinant of Equation (4.35) evaluated at $\ddot{\xi}_c^* = 0$ and $\ddot{\xi}_i^* = 1$ are given by:

$$\begin{aligned} \mathrm{Tr}\mathbf{M} &= -2W_{55}\beta_i\omega_i\mu - (1-\tilde{\mathcal{R}}_c^q)\mu^2 - (1-\tilde{\mathcal{R}}_i^q)(\mu^2+3\mu) - (1-\tilde{\Phi}_i)(3\mu+4), \\ \mathrm{Det}\mathbf{M} &= \Big(2W_{55}\beta_i\omega_i\mu + (1-\tilde{\mathcal{R}}_i^q)(\mu^2+2\mu) + (1-\tilde{\Phi}_i)(2\mu+3)\Big) \\ &\quad \Big((1-\tilde{\mathcal{R}}_c^q)\mu^2 + (1-\tilde{\mathcal{R}}_i^q)\mu + (1-\tilde{\Phi}_i)(\mu+1)\Big). \end{aligned} \tag{4.37}$$

For the condition $\mathrm{Det}\mathbf{M} > \mathbf{0}$ to hold, it is required that $\tilde{\mathcal{R}}_i^q > 1$ and $\tilde{\mathcal{R}}_c^q < 1$. Additionally, provided that $\tilde{\mathcal{R}}_i^q > 1$ and $\tilde{\mathcal{R}}_c^q < 1$ the $\mathrm{Tr}\mathbf{M} < \mathbf{0}$ is fulfilled if

$$(\tilde{\mathcal{R}}_i^q - 1)(\mu^2+3\mu) < 2W_{55}\beta_i\omega_i\mu + (1-\tilde{\mathcal{R}}_c^q)\mu^2 + (1-\tilde{\Phi}_i)(3\mu+4). \tag{4.38}$$

For $s_3 = (\ddot{\xi}_c^*, \ddot{\xi}_i^*)$ evaluated at $(1, 0)$ gives the trace and determinant as in Equation (4.39),

$$\begin{aligned} \mathrm{Tr}\mathbf{M} &= -2W_{66}\beta_c\omega_c\mu - (1-\tilde{\mathcal{R}}_i^q)\mu^2 - (1-\tilde{\mathcal{R}}_c^q)(\mu^2+3\mu) - (1-\tilde{\Phi}_c)(3\mu+4), \\ \mathrm{Det}\mathbf{M} &= \Big(2W_{66}\beta_c\omega_c\mu + (1-\tilde{\mathcal{R}}_c^q)(\mu^2+2\mu) + (1-\tilde{\Phi}_c)(2\mu+3)\Big) \\ &\quad \Big((1-\tilde{\mathcal{R}}_i^q)\mu^2 + (1-\tilde{\mathcal{R}}_c^q)\mu + (1-\tilde{\Phi}_c)(\mu+1)\Big). \end{aligned} \tag{4.39}$$

$\mathrm{Det}\mathbf{M} > \mathbf{0}$ is met if $\tilde{\mathcal{R}}_c^q > 1$ and $\tilde{\mathcal{R}}_i^q < 1$. In addition to this, $\mathrm{Tr}\mathbf{M} < \mathbf{0}$ holds if

$$(\tilde{\mathcal{R}}_c^q - 1)(\mu^2+3\mu) < 2W_{66}\beta_c\omega_c\mu + (1-\tilde{\mathcal{R}}_i^q)\mu^2 + (1-\tilde{\Phi}_c)(3\mu+4). \tag{4.40}$$

We summarize these results as follows:

Theorem 4.13 Under complete cross-immunity conditions, $\eta_i^c = \eta_c^i = 0$, and in the absence of co-infection, Model (4.2):

(i) If $\tilde{\mathcal{R}}_i^q > 1$ and $\tilde{\mathcal{R}}_c^q < 1$, strain-$i$ out-competes strain-c. Also, the strain-i endemic, $\tilde{\mathbf{E}}_i^q$, is locally asymptotically stable (LAS) if

$$(\tilde{\mathcal{R}}_i^q - 1)(\mu^2+3\mu) < 2W_{55}\beta_i\omega_i\mu + (1-\tilde{\mathcal{R}}_c^q)\mu^2 + (1-\tilde{\Phi}_i)(3\mu+4)$$

holds.

(ii) If $\tilde{\mathcal{R}}_c^q > 1$ and $\tilde{\mathcal{R}}_i^q < 1$, then strain-$c$ out-competes strain-i. Further, the strain-c endemic, $\tilde{\mathbf{E}}_c^d$, is LAS if

$$(\tilde{\mathcal{R}}_c^q - 1)(\mu^2 + 3\mu) < 2W_{66}\beta_c\omega_c\mu + (1 - \tilde{\mathcal{R}}_i^q)\mu^2 + (1 - \tilde{\Phi}_c)(3\mu + 4)$$

holds.

4.4.3 Existence of multiple endemic equilibria

On the other hand, when $\ddot{\xi}_c^* > 0$ and $\ddot{\xi}_i^* > 0$, we have s_4 and s_5. These solutions are explored with the following results:

Lemma 4.14 The System (4.2) demonstrates an equilibrium of endemic co-existence if the minimum number of quarantine reproduction numbers for both strains is greater than one, that is, $\min\{\tilde{\mathcal{R}}_c^q, \tilde{\mathcal{R}}_i^q\} > 1$.

Proof. By dividing each equation in (4.30) by their common factor and then adding the resulting equations, we obtain:

$$W_{55}\omega_i\beta_i\mu\ddot{\xi}_i^* - W_{66}\omega_c\beta_c\mu\ddot{\xi}_c^* + (\tilde{\mathcal{R}}_c^q - \tilde{\mathcal{R}}_i^q)\mu\ddot{\xi}_c^* + (\tilde{\mathcal{R}}_c^q - \tilde{\mathcal{R}}_i^q)\mu\ddot{\xi}_i^* + (\tilde{\mathcal{R}}_c^q - \tilde{\mathcal{R}}_i^q)\mu^2 = 0.$$

Remark 4.15 We assume that $\tilde{\mathcal{R}}_i^q = \tilde{\mathcal{R}}_c^q$.

Then, if we solve for $\ddot{\xi}_c^*$ we obtain s_4 and if we solve for $\ddot{\xi}_i^*$ we obtain s_5:

$$s_4 = \left(\frac{W_{55}\omega_i\beta_i\ddot{\xi}_i^*}{W_{66}\omega_c\beta_c}, \ddot{\xi}_i^*\right) \quad \text{and} \quad s_5 = \left(\ddot{\xi}_c^*, \frac{W_{66}\omega_c\beta_c\ddot{\xi}_c^*}{W_{55}\omega_i\beta_i}\right). \tag{4.41}$$

Utilizing Equation (4.41) and Equation (4.30), and grouping like terms, we obtain:

$$\begin{aligned} a_{11}{\ddot{\xi}_i^*}^2 + b_{11}\ddot{\xi}_i^* + c_{11} = 0, \\ a_{22}{\ddot{\xi}_c^*}^2 + b_{22}\ddot{\xi}_c^* + c_{22} = 0. \end{aligned} \tag{4.42}$$

From Equation (4.42),

$$\begin{aligned} a_{11} &= W_{66}^2\beta_c^2\omega_c^2(1 - \tilde{\Phi}_i) + W_{55}W_{66}\beta_c\beta_i\omega_c\omega_i\Big[(1 - \tilde{\Phi}_c) + (1 - \tilde{\Phi}_i)\Big] + W_{55}^2\beta_i^2\omega_i^2(1 - \tilde{\Phi}_c), \\ b_{11} &= W_{55}W_{66}^2\beta_c^2\beta_i\omega_c^2\omega_i\mu + (1 - \tilde{\Phi}_c)W_{55}W_{66}\beta_c\beta_i\omega_c\omega_i\mu + (1 - \tilde{\Phi}_i)W_{66}^2\beta_c^2\omega_c^2\mu + \\ &\quad (1 - \tilde{\mathcal{R}}_c^q)W_{55}W_{66}\beta_c\beta_i\omega_c\omega_i\mu + (1 - \tilde{\mathcal{R}}_i^q)W_{66}^2\beta_c^2\omega_c^2\mu, \\ c_{11} &= W_{66}^2\beta_c^2\omega_c^2\mu^2(1 - \tilde{\mathcal{R}}_i^q), \end{aligned}$$

besides,

$$\begin{aligned} a_{22} &= W_{55}^2\beta_i^2\omega_i^2(1 - \tilde{\Phi}_c) + W_{55}W_{66}\beta_c\beta_i\omega_c\omega_i\Big[(1 - \tilde{\Phi}_c) + (1 - \tilde{\Phi}_i)\Big] + W_{66}^2\beta_c^2\omega_c^2(1 - \tilde{\Phi}_i), \\ b_{22} &= W_{55}^2W_{66}\beta_c\beta_i^2\omega_c\omega_i^2\mu + (1 - \tilde{\Phi}_i)W_{55}W_{66}\beta_c\beta_i\omega_c\omega_i\mu + (1 - \tilde{\Phi}_c)W_{55}^2\beta_i^2\omega_i^2\mu + \\ &\quad (1 - \tilde{\mathcal{R}}_i^q)W_{55}W_{66}\beta_c\beta_i\omega_c\omega_i\mu + (1 - \tilde{\mathcal{R}}_c^q)W_{55}^2\beta_i^2\omega_i^2\mu, \\ c_{22} &= W_{55}^2\beta_i^2\omega_i^2\mu^2(1 - \tilde{\mathcal{R}}_c^q). \end{aligned}$$

The parameter $\tilde{\Phi}_i \& \tilde{\Phi}_c$ represents the total proportion of people who will die from the disease. In practical terms, not all individuals in the population will die of the disease, so $\tilde{\Phi}_c$ and $\tilde{\Phi}_i$ are within the range $[0, 1)$. This ensures that a_{11} and a_{22} are strictly positive.

From the first equation in (4.42), the positive $\ddot{\xi}_i^*$ implies

$$\frac{-b_{11} \pm \sqrt{b_{11}^2 - 4a_{11}c_{11}}}{2a_{11}} > 0 \implies b_{11}^2 - 4a_{11}c_{11} > b_{11}^2 \implies -4a_{11}c_{11} > 0. \tag{4.43}$$

We want $-4a_{11}c_{11} > 0$ in (4.43) to holds. Since $a_{11} > 0$, so $-4a_{11}c_{11} > 0$ iff $c_{11} < 0$, this is possible only when $\tilde{\mathcal{R}}_i^q > 1$. From the second equation, positive $\ddot{\xi}_c^*$ implies

$$\frac{-b_{22} \pm \sqrt{b_{22}^2 - 4a_{22}c_{22}}}{2a_{22}} > 0 \implies b_{22}^2 - 4a_{22}c_{22} > b_{22}^2 \implies -4a_{22}c_{22} > 0. \tag{4.44}$$

Similar to Equation (4.43), the condition $-4a_{22}c_{22} > 0$ in (4.44) is met iff $c_{22} < 0$. This is possible only when $\tilde{\mathcal{R}}_c^q > 1$.This concludes the proof. ■

4.4.4 Invasion Reproduction Numbers (IRNs) in the absence of co-infection

In this section, we evaluate the potential of each strain to disrupt the established endemic equilibrium of the other strain. We determine the Invasion Reproduction Number (IRN) for each strain when introduced into a population already at the endemic equilibrium. If either invasion reproduction number exceeds one, it indicates the potential for causing more than one secondary infection on average, potentially disrupting the existing endemic equilibrium.

Definition 4.16 — Invasion Reproduction Number (IRN) . Known as ${}_i\tilde{\mathcal{R}}_c^q$ and ${}_c\tilde{\mathcal{R}}_i^q$, these metrics assess the capacity of strain-i and strain-c to invade a system in the endemic equilibrium of strain-c and strain-i, respectively.

Various methods for computing IRN can be found in the literature [86, 125]. We use the next-generation approach to calculate ${}_i\tilde{\mathcal{R}}_c^q$ and ${}_c\tilde{\mathcal{R}}_i^q$. For strain-$i$ invasion reproduction number, ${}_i\tilde{\mathcal{R}}_c^q$ the infectious classes $E_i, I_i, \& Q_i$ are linearized when strain-c is resident. The vector of new infections $\mathcal{F}$ and outflow vector $\mathcal{V}$ are given by

$$\mathcal{F} = \begin{pmatrix} \xi_i S + \eta_c^i R_c \xi_i \\ 0 \\ 0 \end{pmatrix} \quad and \quad \mathcal{V} = \begin{pmatrix} \mathbf{p}_i E_i \\ \mathbf{q}_i I_i - \rho_i E_i + \tau_i Q_i \\ \mathbf{r}_i Q_i - \alpha_i E_i - \sigma_i I_i \end{pmatrix} \tag{4.45}$$

We take the derivatives of $\mathcal{F}$ and $\mathcal{V}$ and evaluate at Equation (4.33) to obtain matrices, namely:

$$F = \begin{pmatrix} 0 & \tilde{S}_c^d \beta_i + \tilde{R}_c^d \beta_i \eta_c^i & 0 \\ 0 & 0 & 0 \\ 0 & 0 & 0 \end{pmatrix} \quad and \quad V = \begin{pmatrix} \mathbf{p}_i & 0 & 0 \\ -\rho_i & \mathbf{q}_i & -\tau_i \\ -\alpha_i & -\sigma_i & \mathbf{r}_i \end{pmatrix} \tag{4.46}$$

The strain-i invasion reproduction number is then defined as ${}_i\tilde{\mathcal{R}}_c^q = \rho(FV^{-1})$ simplifies to:

$${}_i\tilde{\mathcal{R}}_c^q = \left[\tilde{S}_c^d + \tilde{R}_c^d \eta_c^i\right] \tilde{\mathcal{R}}_i^q. \tag{4.47}$$

Similarly, we define the strain-c invasion reproduction number, ${}_c\tilde{\mathcal{R}}_i^q$, assuming that strain-$i$ is the resident strain. This is expressed as:

$$ {}_c\tilde{\mathcal{R}}_i^q = \left[\tilde{S}_i^d + \tilde{R}_i^d \eta_i^c\right]\tilde{\mathcal{R}}_c^q. \tag{4.48}$$

In Equation (4.47), the term $\tilde{S}_c^d \tilde{\mathcal{R}}_i^q$ indicates the number of secondary cases that a single individual infected with strain-i can generate in the susceptible population. In contrast, the term $\tilde{R}_c^d \eta_c^i \tilde{\mathcal{R}}_i^q$ represents the secondary cases that a strain-i infected individual can produce, scaled by the number of individuals who have recovered from strain-c. The interpretation of Equation (4.48) follows a similar rationale to Equation (4.47). The following proposition outlines the scenarios when two strains compete or co-exist based on their quarantine reproduction numbers.

Theorem 4.17 Assume $j \neq k$, where k can be either c or i. If $\tilde{\mathcal{R}}_k^q > 1$ and $\tilde{\mathcal{R}}_j^q > 1$:

(i) Independent Sustenance: Both strains can be sustained in the population independently if ${}_j\tilde{\mathcal{R}}_k^q < 1$ and ${}_k\tilde{\mathcal{R}}_j^q < 1$. Here, the strain with a larger quarantine reproduction number will dominate.

(ii) Possible coexistence: If $\tilde{\mathcal{R}}_j^q = \tilde{\mathcal{R}}_k^q > 1$, this suggests a scenario in which neither strain is dominant over the other, leading to a possible coexistence.

Theorem 4.17 outlines conditions under which two infectious strains can independently sustain themselves and dominate according to their respective numbers of quarantine reproductions or coexist without one eliminating the other.

4.5 Endemic dynamics of multiple strains with co-infection

Next, we explore the conditions for the occurrence of a co-infected endemic equilibrium, denoted $\tilde{\mathbf{E}_{ic}}$. This equilibrium is defined as:

$$\tilde{\mathbf{E}_{ic}} = \left[S, E_i, E_c, E_{ic}, I_i, I_c, I_{ic}, Q_i, Q_c, Q_{ic}, R_i, R_c, R_{ic}\right].$$

Remark 4.18 As established in Lemma 4.14, the equilibrium of co-existence, denoted as $\tilde{\mathbf{E}}^*$, occurs when $\min\{\tilde{\mathcal{R}}_c^q, \tilde{\mathcal{R}}_i^q\} > 1$. **This condition is necessary for the co-existence endemic equilibrium to exist. However, a critical question arises**: *Is this condition alone sufficient for the co-infected endemic equilibrium to exist?*

In accordance with our model assumptions (3 in Remark 4.2), the straightforward answer is no. In particular, this assumption suggests that the ability to cause harm during interactions between symptomatic individuals infected with different pathogens plays a crucial role in the formation of a co-infection class. In our model, the invasion capabilities of strain-i and strain-c into each other's population are respectively quantified by ${}_i\tilde{\mathcal{R}}_c^q$ and ${}_c\tilde{\mathcal{R}}_i^q$. Now, assuming that any strain can successfully invade the population of the other strain, we state the following findings:

Theorem 4.19 If either ${}_i\tilde{\mathcal{R}}_c^q$ or ${}_c\tilde{\mathcal{R}}_i^q$ exceeds 1, and both $\tilde{\mathcal{R}}_i^q$ and $\tilde{\mathcal{R}}_c^q$ are greater than 1, the system depicted in Equation (4.2) will exhibit a co-infected endemic equilibrium.

The provable Theorem 4.19 analytically faces challenges due to the intricate mathematical relationships involved. Our results are predominantly drawn from numerical simulations, with strong support from Figure 4.5, particularly in region $\mathbf{C} = \mathbf{C1} + \mathbf{C2}$.

4.5.1 Invasion reproduction number with co-infection

After numerically demonstrating the presence of co-infected strains under certain conditions, this section delves into the measurement of their capacity to establish and propagate within a population. These quantities offer valuable insights into the dynamics of co-infected strains and their potential to invade and persist in a host population. The methodology follows the same procedures as described in Section 4.4.4, with the inclusion of infectious classes such as $E_i, E_{ic}, I_i, I_{ic}, Q_i$ and Q_{ic}. The calculated strain-i co-infected invasion reproduction number, ${}_i\tilde{\mathcal{I}}_c^q$, is:

$$ {}_i\tilde{\mathcal{I}}_c^q = S\tilde{\mathcal{R}}_i^q + I_c\tilde{\mathfrak{R}}_i^q + R_c\eta_c^i\tilde{\mathcal{R}}_i^q. \tag{4.49}$$

Analogously, the strain-c co-infected invasion reproduction number, ${}_c\tilde{\mathcal{I}}_i^q$ under the assumption that strain-i is resident, respectively, is defined as

$$ {}_c\tilde{\mathcal{I}}_i^q = S\tilde{\mathcal{R}}_c^q + I_i\tilde{\mathfrak{R}}_c^q + R_i\eta_i^c\tilde{\mathcal{R}}_c^q. \tag{4.50}$$

In Equation (4.49) and Equation (4.50), the first and last terms maintain a similar interpretation to that discussed in Section 4.4.4. The expressions for $\tilde{\mathfrak{R}}_i^q$ and $\tilde{\mathfrak{R}}_c^q$ in the second terms are defined as :

$$\tilde{\mathfrak{R}}_i^q = \frac{\beta_i(\alpha_{ic}\mathbf{q}_{ic} + \rho_{ic}\sigma_{ic} + \alpha_{ic}\tau_{ic} + \mathbf{r}_{ic}\rho_{ic})}{\mathbf{p}_{ic}(\dot{\mathbf{q}}_{ic}\mathbf{r}_{ic} + \tilde{\mathbf{r}}_{ic}\sigma_{ic})}, \tilde{\mathfrak{R}}_c^q = \frac{\beta_c(\alpha_{ic}\mathbf{q}_{ic} + \rho_{ic}\sigma_{ic} + \alpha_{ic}\tau_{ic} + \mathbf{r}_{ic}\rho_{ic})}{\mathbf{p}_{ic}(\dot{\mathbf{q}}_{ic}\mathbf{r}_{ic} + \tilde{\mathbf{r}}_{ic}\sigma_{ic})}.$$

The quantities $\tilde{\mathfrak{R}}_i^q$ and $\tilde{\mathfrak{R}}_c^q$, are co-infected quarantine reproduction numbers (CQRN) for strain-i and strain-c. These numbers of quarantine reproduction relate to the infected subpopulations indicated by I_c and I_i.. When the CQRN is less than 1, it means that a strain has a reduced potential to spread within its specific subpopulation in the context of co-infection. However, this does not conclusively imply that the co-infected strain cannot maintain itself within the overall population. Our analysis (in Chapter 6) has revealed that several other factors, such as the presence of cross-immunity and varying transmission dynamics, can play a pivotal role in determining whether a coexisting strain can persist within the population. Consequently, even when one of the strain's quarantine reproduction numbers is less than 1, we posit that the subthreshold co-infected endemic state may still endure.

4.6 Numerical analysis

4.6.1 Model parameters

The parameters for the simulation are chosen based on their relevance to the dynamics of pathogen-i and pathogen-c, with their values derived from various sources including empirical studies, model assumptions, and established literature. The birth and natural death rates (Λ

Table 4.2: Model parameters: symbols, meanings, and ranges. Specific parameter values for each simulation are shown in the figures. Any missing parameters were estimated within a reasonable range for illustration.

Symbol	Interpretation	Range	Source
$\Lambda(\mu)$	Birth (natural death) rate ($1/\Lambda(\mu)$=days)	(0, 1]	[96]
β_i	strain-i transmission rate ($1/\beta_i$=days)	(0, 2]	[96]
β_c	strain-c transmission rate ($1/\beta_c$=days)	(0, 2]	[7, 37]
ω_i	The parameter to measure the potential input in Q_i ($1/\omega_i$=days)	[0, 1]	Equation (4.6)
ω_c	The parameter to measure the potential input in Q_c ($1/\omega_c$=days)	[0, 1]	Equation (4.6)
ω_{ic}	The parameter to measure the potential input in Q_{ic} ($1/\omega_{ic}$=days)	[0, 1]	Equation (4.6)
Ω_i	Function to reduce the infection and measure the Q_i efficacy	[0, 1]	Equation (4.6)
Ω_c	Function to reduce the infection and measure the Q_c efficacy	[0, 1]	Equation (4.6)
Ω_{ic}	Function to reduce the infection and measure the Q_{ic} efficacy	[0, 1]	Equation (4.6)
ρ_i	Rate of developing strain-i symptoms ($1/\rho_i$=days)	[1/5,1/2]	[10]
ρ_c	Rate of developing strain-c symptoms($1/\rho_c$=days)	[1/14,1/2.3]	[11, 37]
ρ_{ic}	Rate of developing co-infections symptoms ($1/\rho_{ic}$=days)	[1/14,1/2]	Assumed
α_i	Quarantine rate for strain-i exposed individuals ($1/\alpha_i$=days)	[0,1]	[123]
α_c	Quarantine rate for strain-c exposed individuals ($1/\alpha_c$=days)	[0,1]	[123]
α_{ic}	Quarantine rate for co-exposed individuals ($1/\alpha_{ic}$=days)	[0,1]	Assumed
σ_i	Isolation rate for strain-i infected individuals ($1/\sigma_i$=days)	[1/6,1]	[96]
σ_c	Isolation rate for strain-c infected individuals ($1/\sigma_c$=days)	[0,1]	[37]
σ_{ic}	Isolation rate for co-infected individuals ($1/\sigma_{ic}$=days)	[0,1]	Assumed
τ_i	Rate of strain-i quarantine-exposed individuals become I_i ($1/\tau_i$=days)	(0, 0.5]	[139]
τ_c	Rate of strain-c quarantine-exposed individuals become I_c ($1/\tau_c$=days)	(0, 0.5]	[139]
τ_{ic}	Rate of strain-ic quarantine-exposed individuals become I_{ic} ($1/\tau_{ic}$=days)	(0, 0.5]	Assumed
ϕ_i	Recovery rate of strain-i quarantined individuals ($1/\phi_i$=days)	[1/15, 1]	[96]
ϕ_c	Recovery rate of strain-c quarantined individuals ($1/\phi_i$=days)	[0.08,0.14]	[123]
ϕ_{ic}	Recovery rate of strain-ic quarantined individuals ($1/\phi_{ic}$=days)	[1/15,1]	Assumed
γ_i	Recovery rate of strain-i infected individuals ($1/\gamma_i$=days)	[1/6,1/4]	[120]
γ_c	Recovery rate of strain-c infected individuals ($1/\gamma_c$=days)	[0.28,0.38]	[123]
γ_{ic}	Recovery rate of co-infected individuals ($1/\gamma_{ic}$=days)	[0.28,0.38]	Assumed
η_i^c	Cross-immunity against strain-i	[0, 1]	[96]
η_c^i	Cross-immunity against strain-c	[0, 1]	[96]
δ_i	Death rate due to strain-i ($1/\delta_i$=days)	[0.001,0.1]	[37]
δ_c	Death rate due to strain-c ($1/\delta_c$=days)	[0.001,0.1]	[37]
δ_{ic}	Death rate due to co-infection ($1/\delta_{ic}$=days)	[0.001,0.1]	Assumed

and μ) are set within a range of (0, 1] to represent the daily rate of births and natural deaths. Transmission rates (β_i and β_c) are set between (0, 2] to reflect the rate at which new infections occur. The quarantine and isolation rates (α_i, α_c, σ_i, σ_c) vary from 0 to 1, which captures the effectiveness of these interventions daily. The rates of symptom development (ρ_i, ρ_c) and the transition from quarantine to infection (τ_i, τ_c) are chosen based on incubation periods reported in the literature, with ρ_i and ρ_c set between [1/5, 1/2] and [1/14, 1/2.3] respectively, indicating a range from a fraction of a day to several days for symptoms to develop. Recovery rates (ϕ_i, ϕ_c, γ_i, γ_c) range from 0.08 to 1, corresponding to clinical recovery data on a daily scale. Cross-immunity

(η_i^c, η_c^i) and death rates (δ_i, δ_c) are selected within plausible ranges of [0, 1] and [0.001, 0.1], respectively, informed by studies on immunity and mortality. The choice of these parameters ensures that the model accurately reflects the biological and epidemiological characteristics of both diseases on realistic time scales, with each parameter representing the rate at which these processes occur on a daily basis. We provide the notation, meaning, range of values, and sources of the parameters of Model (4.2) in Table 4.2.

4.6.2 Diseases dynamics based on quarantine reproduction numbers

We analyzes the regions of disease-free state, dominance, and co-existence of diseases, focusing on their quarantine reproduction numbers. We note that the conditions in Lemma 4.8 for the local stability of disease-free equilibrium are met.

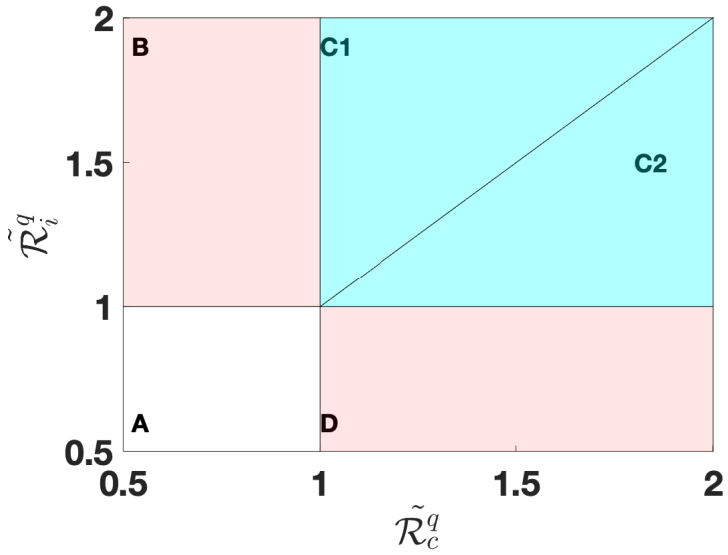

Figure 4.2: The diagram illustrates the regions of dominance, competition, and co-existence. The color-coded regions can be described as follows: Region **A** (unshaded) corresponds to the disease-free state. Regions **B** and **D**, shown in light red, indicate the persistence of one strain and the extinction of the other. The cyan areas (**C** = **C1** + **C2**) represent the coexistence of both strains.

The representation of Theorem 4.13, is depicted in Figure 4.5, with a focus on highlighting regions labeled **A**, **B** and **D**. This figure provides a comprehensive analysis and visualization of the effect of cross-immunity in the System (4.2) in the absence of co-infected strains. In particular, the model exhibits symmetry in relation to the line $\tilde{\mathcal{R}}_c^q = \tilde{\mathcal{R}}_i^q > 1$, revealing distinct regions with significant biological implications. In Region **A**, where all control reproduction numbers are less than one, both strains are expected to diminish over time, resulting in a "Lose-Lose" outcome. The region **B** signifies a "Win-Lose" scenario, where strain-i is poised to dominate and out-compete strain-c. Conversely, Region **D** suggests that strain-c is likely to prevail over strain-i, leading to another "Win-Lose" competition. Region **C**=**C1**+**C2** signifies a "Win-Win" competition, where both strains exhibit quarantine reproduction numbers greater than one. In particular, the model exhibits symmetry about the line $\tilde{\mathcal{R}}_c^q = \tilde{\mathcal{R}}_i^q > 1$, suggesting that both are

expected to persist. In **C1**, $\tilde{\mathcal{R}}_i^q > \tilde{\mathcal{R}}_c^q > 1$, this implies that strain-i is expected to dominate. In region **C2**, $\tilde{\mathcal{R}}_c^q > \tilde{\mathcal{R}}_i^q > 1$, implies strain-$c$ can dominate in a population. In this figure, we highlight the competitive advantage of pathogens with a higher number of control quarantine reproduction in environments where cross-immunity is perfect. In Section 4.6.4 we extend this analysis with the assumption of partial cross-immunity.

4.6.3 Simulation of the model without co-infections

In this section, we present simulations of the model that exclude the possibility of co-infections. This approach helps us understand the dynamics and interactions of the two pathogens, without the added complexity of individuals being infected with multiple strains simultaneously. The simulation of Model 4.30 investigates the dynamics of epidemics caused by pathogen i and pathogen c within a population. This includes estimating key metrics such as quarantine reproduction numbers, equilibrium points, and stability criteria. The model formulas and visualizations are implemented using Python code in SageMath. A streamline plot is produced to illustrate the vector field of the system, depict the flow of trajectories, and mark the equilibrium points. This visualization helps to understand the potential outcomes of the epidemic under varying parameter settings.

Figure 4.3 illustrates the impact of varying infection rates (β_i and β_c) on the stability and dynamics of the system within the normalized infection force plane for strains c and i, assuming full cross-immunity. To better understand how different factors, such as initial conditions and time, influence disease dynamics, we compared these results with the simulations shown in Figure 4.4, which explore scenarios without co-infected individuals and partial cross-immunity.

In subplot (a) of Figure 4.3, the conditions necessary for the elimination of the disease are demonstrated, which align with subplot (a) of Figure 4.4. The subplots (b) and (c) in both figures reveal that when the transmission rate of one strain exceeds 1 while that of the other is below 1, the trajectories converge towards the strain with the highest transmission rate, indicating its dominance over the weaker strain. Subplots (d) and (e) of Figure 4.3 show similar patterns when both quarantine reproduction numbers are greater than 1 but unequal, with the dominant strain continuing to prevail. Finally, subplot (f) of Figure 4.3 and subplot (d) of Figure 4.4 show strain coexistence when $\tilde{\mathcal{R}}_c^q = \tilde{\mathcal{R}}_i^q > 1$, reflecting a balanced dynamic between the two strains.

4.6.4 Simulation of co-infected model

As discussed in Section 4.6.2, in Region **C** both strains exhibit quarantine reproduction numbers greater than one. We extended the result visualized in Figure 4.2 by including the invasion reproduction numbers curves, ${}_c\tilde{\mathcal{R}}_i^q$ and ${}_i\tilde{\mathcal{R}}_c^q$, shown by black dotted and blue dashed-dotted lines, respectively. of invasion reproduction numbers defined by Equation (4.48) and Equation (4.47). The curves were plotted when ${}_c\tilde{\mathcal{R}}_i^q =_i \tilde{\mathcal{R}}_c^q = 1$. In **C1**, ${}_i\tilde{\mathcal{R}}_c^q > 1$, this implies that strain-i can invade and spread in a population where another strain-c is already present at endemic levels. In region **C2**, ${}_c\tilde{\mathcal{R}}_i^q > 1$. This suggests the ability of strain$c$ to invade and spread in a population where another strain-i is endemic. Observing the influence of the parameters of the cross-immunity, η_c^i and η_i^c, is crucial. The figure in the upper left illustrates coexistence when both rates of cross-protection are zero ($\eta_c^i = \eta_i^c = 0$). Subsequent figures result from altering parameters, such as increasing one while keeping the other at zero or simultaneously increasing both (η_c^i and η_i^c). In particular, higher values of η_i^c and η_c^i correspond to an expanded co-infected

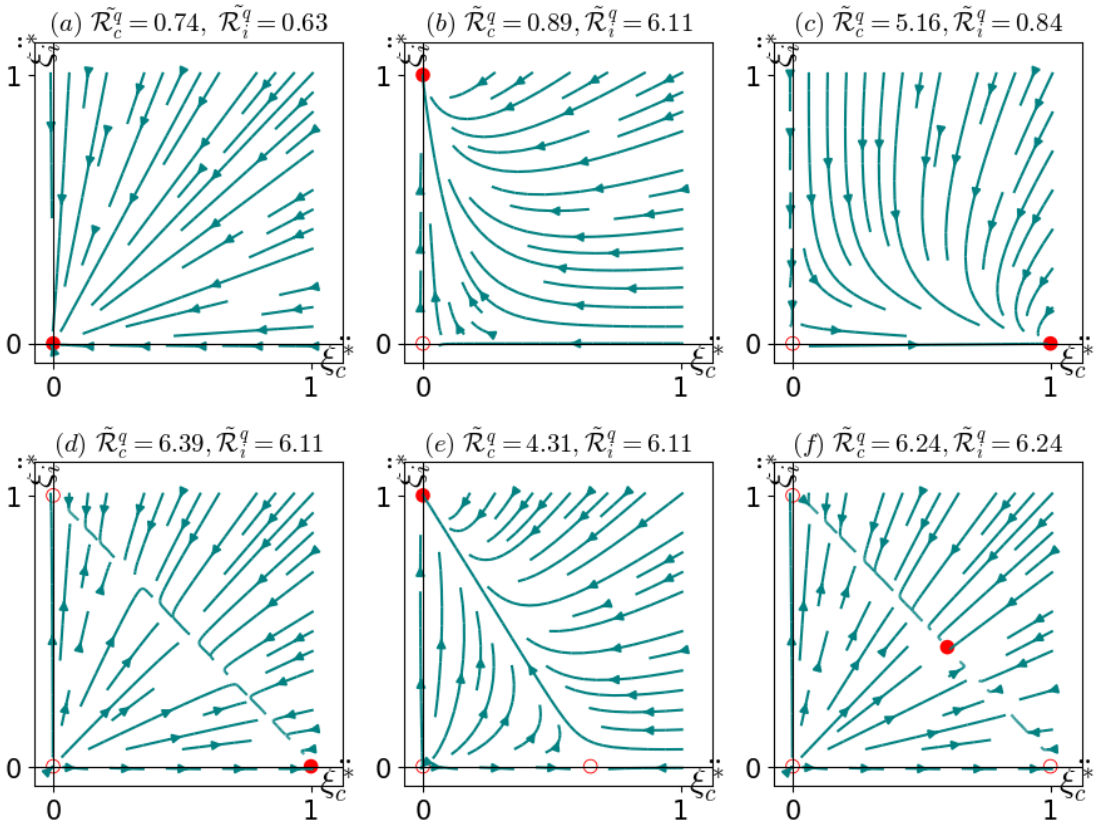

Figure 4.3: Solution behavior of System (4.30) in the $\ddot{\xi}_c^*\ddot{\xi}_i^*$-plane. Filled and unfilled dots indicate stable and unstable equilibrium states, respectively; arrows depict the direction of trajectories. Parameters: (a) $\beta_i = 0.3$, $\beta_c = 0.5$; (b) $\beta_i = 2.9$, $\beta_c = 0.6$; (c) $\beta_i = 0.4$, $\beta_c = 4.2$; (d) $\beta_i = 2.9$, $\beta_c = 4.3$; (e) $\beta_i = 2.9$, $\beta_c = 3$; (f) $\beta_i = 2.96$, $\beta_c = 4.2$. Other parameters are: $\lambda = \mu = 0.2$, $\rho_i = 0.5$, $\rho_c = 0.3$, $\tau_i = 0.4$, $\tau_c = 0.2$, $\alpha_i = 0.15$, $\alpha_c = 0.05$, $\sigma_i = 0.005$, $\sigma_c = 0.001$, $\delta_i = \delta_c = 0.00001$, $\phi_i = 0.16$, $\phi_c = 0.1$, $\gamma_i = 0.16$, $\gamma_c = 0.28$, $\omega_i = 0.4$, $\omega_c = 0.7$. The quarantine reproduction number for each case is noted in the figure titles.

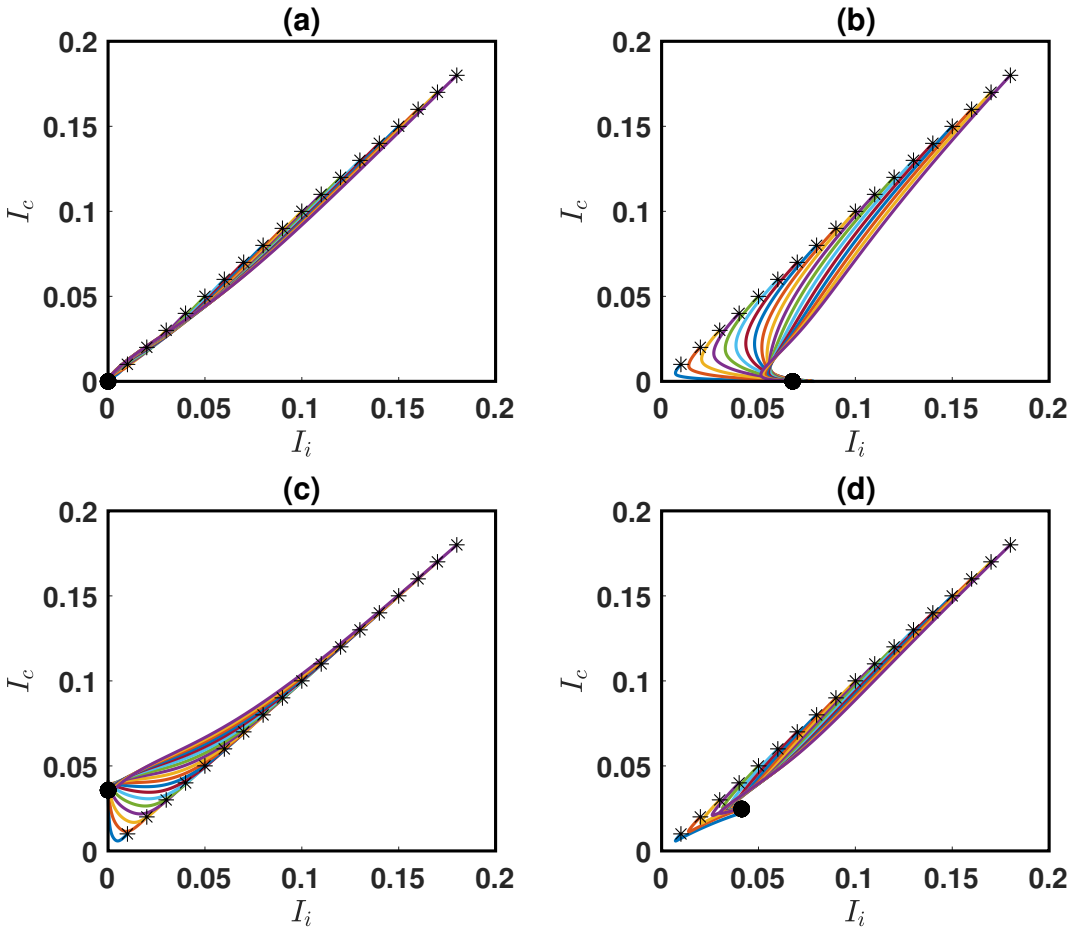

Figure 4.4: This diagram illustrates the dynamics of Disease-Free Equilibrium (DFE), strain dominance, and strain co-existence. The starting and ending points of each trajectory are marked by the start and black dots, respectively. The parameters used are: (a) $\beta_i = 0.2$, $\beta_c = 0.3$; (b) $\beta_i = 0.4$, $\beta_c = 0.3$; (c) $\beta_i = 0.2$, $\beta_c = 0.5$; (d) $\beta_i = 0.4$, $\beta_c = 0.5$. Other parameters include: $\lambda = \mu = 0.04$, $\rho_i = 0.3$, $\rho_c = 0.2$, $\eta_i = \eta_c = 0.4$, with the remaining parameters matching those in Figure 4.3. The simulation covers 600 days, with initial values $I_i(0) = I_c(0)$ starting at 0.01, ending at 0.18, and a step size of 0.01, thus $S(0) = 1 - I_i(0) - I_c(0)$. The quarantine reproduction numbers for each case are: (a) $\tilde{\mathcal{R}}_c^q = 0.79$, $\tilde{\mathcal{R}}_i^q = 0.65$; (b) $\tilde{\mathcal{R}}_c^q = 0.79$, $\tilde{\mathcal{R}}_i^q = 1.31$; (c) $\tilde{\mathcal{R}}_c^q = 1.31$, $\tilde{\mathcal{R}}_i^q = 0.65$; (d) $\tilde{\mathcal{R}}_c^q = \tilde{\mathcal{R}}_i^q = 1.31$.

region.

In our exploration of the model detailed in Equation (4.2), we conducted simulations to investigate the dynamics of co-infection. Our focus was on manipulating the cross-immunity parameters (η_i^c and η_c^i) alongside transmission rates (β_i and β_c) to understand their impact on co-infection outcomes. The results, illustrated in Figure 4.6, reveal how variations in these cross-immunity parameters influence co-infection levels. The first column of the figure depicts a bifurcation diagram, which highlights crucial parameter combinations associated with distinct infection levels. Simultaneously, the second column, presented as 3D scatter plots, provides a detailed perspective on the intricate relationship between transmission and cross-immunity rates (specifically η_i^c, η_c^i,

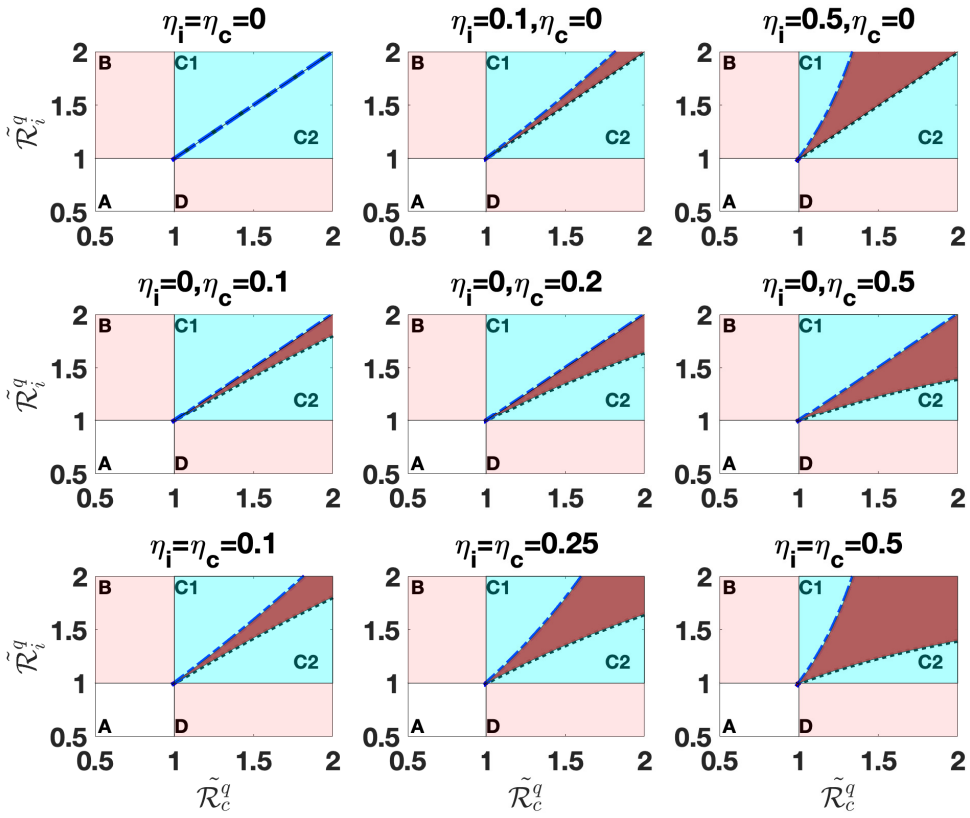

Figure 4.5: The diagram illustrates the regions of dominance, competition, and co-existence as characterized by the quarantine reproduction number under different values of cross-immunity parameters η_i^c and η_c^i. The model's remaining parameters are set as follows: $\Lambda = \mu = 0.0004$, $\beta i = 0.69$, $\beta_c \in [0.25, 1]$, $\rho_i = 0.5$, $\rho_c = 0.3$, $\alpha_i = 0.5$, $\alpha_c = 0.005$, $\sigma_i = 0.005$, $\sigma_c = 0.006$, $\tau_i = 0.05$, $\tau_c = 0.03$, $\phi_i = 0.14$, $\phi_c = 0.1$, $\gamma_i = 0.2$, $\gamma_c = 0.24$, $\eta_i^c = \eta_c^i = 0$, $\delta_i = 0.001$, $\delta_c = 0.01$. The color-coded regions are similar to Figure 4.2.

β_i and β_c) and their influence on co-infection levels.

4.7 Discussion

This chapter delves into the dynamics of multiple pathogens, shedding light on competitive exclusion, co-existence, and co-infection within populations. This investigation yields valuable information on how different diseases interact and persist when the effects of quarantine measures are taken into account to control disease transmission. We focus on understanding various epidemic scenarios, emphasizing the phenomenon of backward bifurcation, where diseases can reemerge after initial control. We explored the impact of cross-immunity, which involves interactions between different pathogens and the immune system, on disease dynamics. In addition, we discussed the stability of the Disease-Free Equilibrium in various cases.

We found that a system with co-infections does not achieve global asymptotic stability (GAS) when $\tilde{\mathcal{R}}^q < 1$. In our model, these results imply that the presence of co-infections and imperfect quarantine measures presents significant challenges in containing the outbreak. Even when we manage to slow down the spread of each virus strain individually, the presence of co-infections keeps the outbreak going. On the other hand, in the absence of co-infections, it is much easier to control the outbreak. With perfect quarantine measures, we can quickly stop the spread of the disease when $\mathcal{R}_i^q < 1$and $\mathcal{R}_c^q < 1$.

Furthermore, the analysis (in Figure 4.6) reveals the following:

- *Manifestation of Robust Cross-Immunity (Single Peak)*: In the upper diagram of Figure 4.6, a singular peak becomes evident in prevalence. This aligns with our model's premise, asserting that individuals must undergo complete recovery from one strain before encountering another. Consequently, potent cross-immunity decreases susceptibility to the second strain (refer also to Figure 4.5), leading to a predominant peak symbolizing the primary outbreak. Other studies, such as the work by Nuno et al. [96], have demonstrated robust cross-immunity, reinforcing the notion that the interaction between strains is challenging. The strain exhibiting superior invasiveness is more likely to establish dominance, potentially driving the other strain to extinction (see also [13]).

- *Weakening cross-immunity (two peaks)*: As cross-immunity weakens, the protective effect of a previous infection with one strain diminishes, making individuals more susceptible to reinfection with the other strain. Consequently, the previously suppressed strain can resurface, leading to new infections. The decline in cross-immunity results in the emergence of two peaks in the prevalence of the two strains, each corresponding to a distinct outbreak. The manifestation of these dual peaks is evident in the two middle plots of Figure 4.6, which illustrates the dynamics of co-existence under weakened cross-immunity. Similar patterns have been observed in other studies, such as [96], suggesting that the coexistence of multiple strains is more probable when the strains are antigenically distinct, indicating weak cross-immunity between them.

- *Further weakening cross-immunity (merging of peaks)*: As cross-immunity further weakens, individuals may become more susceptible to both strains simultaneously, especially when

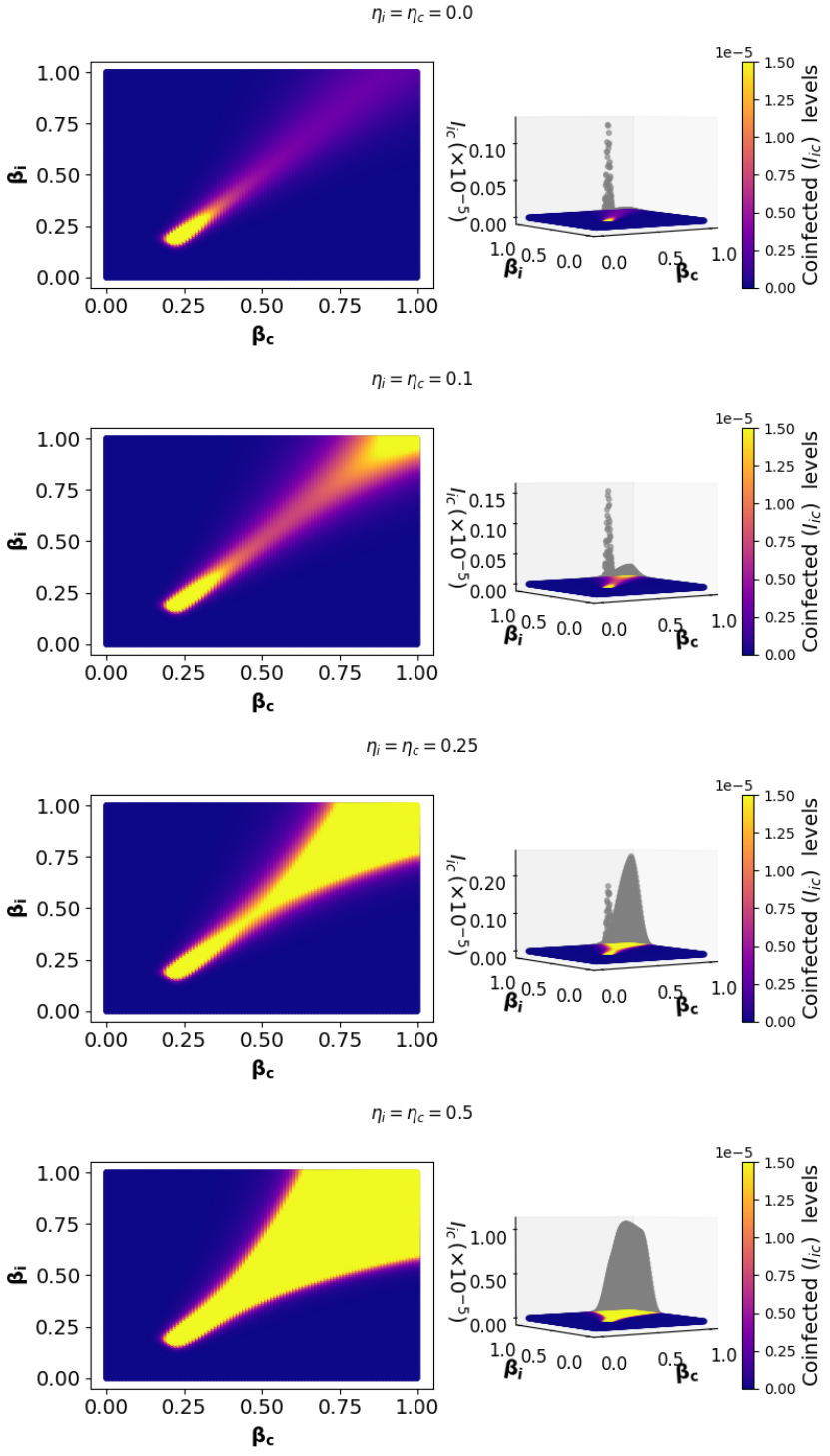

Figure 4.6: Co-infection Dynamics: Changes in co-infected individuals with varying transmission rates (β_i, β_c) and cross-immunity levels (η_i^c, η_c^i). Rows represent different cross-immunity levels: 0.00001, 0.1, 0.25, and 0.5. The color bar shows fractions of co-infected individuals at equilibrium, with peaks indicating possible outbreaks. Other parameters: $\Lambda = \mu = 0.0004$, $\rho_i = 0.3$, $\rho_c = 0.25$, $\rho_{ic} = 0.4$, $\alpha_i = 0.5$, $\alpha_c = 0.4$, $\alpha_{ic} = 0.5$, $\sigma_i = 0.5$, $\sigma_c = 0.6$, $\sigma_{ic} = 0.7$, $\tau_i = 0.05$, $\tau_c = 0.06$, $\tau_{ic} = 0.05$, $\delta_i = \delta_c = \delta_{ic} = 0.000001$, $\phi_i = 0.1$, $\phi_c = 0.14$, $\phi_{ic} = 0.07$, $\gamma_i = 0.14$, $\gamma_c = 0.28$, $\gamma_{ic} = 0.07$.

cross-immunity reaches very low levels. Under such conditions, the distinction in susceptibility between the two strains becomes less pronounced. This can lead to the eventual overlap or merging of the two separate peaks into a single peak in the prevalence of both strains, as illustrated in the bottom plot of Figure 4.6.

4.A Appendix: Local stability of DFE under perfect quarantine

We provide the proof of Lemma 4.9. Following the sequence of compartments as in Section 4.3.1, we compute the Jacobian matrix of the system described by Equation (4.2) at the Disease-Free Equilibrium (DFE) as:

$$\mathcal{Z} = \begin{pmatrix}
-\mu & 0 & -\beta_i & 0 & 0 & 0 & -\beta_c & 0 & 0 & 0 & -\beta_c-\beta_i & 0 & 0 \\
0 & -\mathbf{p}_i & \beta_i & 0 & 0 & 0 & 0 & 0 & 0 & 0 & \beta_i & 0 & 0 \\
0 & \rho_i & -\mathbf{q}_i & 0 & 0 & 0 & 0 & 0 & 0 & 0 & 0 & 0 & 0 \\
0 & \alpha_i & \sigma_i & -\tilde{\mathbf{r}}_i & 0 & 0 & 0 & 0 & 0 & 0 & 0 & 0 & 0 \\
0 & 0 & \gamma_i & \phi_i & -\mu & 0 & 0 & 0 & 0 & 0 & 0 & 0 & 0 \\
0 & 0 & 0 & 0 & 0 & -\mathbf{p}_c & \beta_c & 0 & 0 & 0 & \beta_c & 0 & 0 \\
0 & 0 & 0 & 0 & 0 & \rho_c & -\mathbf{q}_c & 0 & 0 & 0 & 0 & 0 & 0 \\
0 & 0 & 0 & 0 & 0 & \alpha_c & \sigma_c & -\tilde{\mathbf{r}}_c & 0 & 0 & 0 & 0 & 0 \\
0 & 0 & 0 & 0 & 0 & 0 & \gamma_c & \phi_c & -\mu & 0 & 0 & 0 & 0 \\
0 & 0 & 0 & 0 & 0 & 0 & 0 & 0 & 0 & -\mathbf{p}_{ic} & 0 & 0 & 0 \\
0 & 0 & 0 & 0 & 0 & 0 & 0 & 0 & 0 & \rho_{ic} & -\mathbf{q}_{ic} & 0 & 0 \\
0 & 0 & 0 & 0 & 0 & 0 & 0 & 0 & 0 & \alpha_{ic} & \sigma_{ic} & -\tilde{\mathbf{r}}_{ic} & 0 \\
0 & 0 & 0 & 0 & 0 & 0 & 0 & 0 & 0 & 0 & \gamma_{ic} & \phi_{ic} & -\mu
\end{pmatrix}$$

Expanding the characteristic polynomial $|\mathcal{Z} - \lambda I| = 0$ along the columns with only one non-zero entry, we obtained $\lambda_{1,2,3,4} = -\mu$, $\lambda_5 = \tilde{\mathbf{r}}_i$, $\lambda_6 = \tilde{\mathbf{r}}_c$, and $\lambda_7 = \tilde{\mathbf{r}}_{ic}$. The remaining six eigenvalues are obtained from the eigenvalues of the following matrix:

$$Z = \begin{pmatrix} Z_{11} & Z_{12} & Z_{13} \\ Z_{21} & Z_{22} & Z_{23} \\ Z_{31} & Z_{32} & Z_{33} \end{pmatrix} \tag{4.51}$$

Each block of Z is of size 2×2, with Z_{21}, Z_{31}, Z_{32}, and Z_{12} being zero matrices. The blocks Z_{13} and Z_{23} represent coupling terms between different compartments in the model but do not directly contribute to the eigenvalues of Z. Instead, it is Z_{11}, Z_{22}, and Z_{33} that play a pivotal role in determining these eigenvalues.

$$Z_{11} = \begin{pmatrix} -\mathbf{p}_i & \beta_i \\ \rho_i & -\mathbf{q}_i \end{pmatrix}, Z_{22} = \begin{pmatrix} -\mathbf{p}_c & \beta_c \\ \rho_c & -\mathbf{q}_c \end{pmatrix}, Z_{33} = \begin{pmatrix} -\mathbf{p}_{ic} & 0 \\ \rho_{ic} & -\mathbf{q}_{ic} \end{pmatrix}. \tag{4.52}$$

From Equation (4.51), the trace of Z_{11} is $\mathrm{Tr}(Z_{11}) = -\mathbf{p}_i - \mathbf{q}_i < 0$ and the determinant is $\mathrm{Det}(Z_{11}) = \mathbf{p}_i\mathbf{q}_i - \beta_i\rho_i$. This tells us that $\mathrm{Det}(Z_{11}) > 0$ if $1 > \beta_i\rho_i/(\mathbf{p}_i\mathbf{q}_i) = \mathcal{R}_i^q$. Similarly, the trace of Z_{22} is $\mathrm{Tr}(Z_{22}) = -\mathbf{p}_c - \mathbf{q}_c < 0$ and the determinant is $\mathrm{Det}(Z_{22}) = \mathbf{p}_c\mathbf{q}_c - \beta_c\rho_c$. Therefore, $\mathrm{Det}(Z_{22}) > 0$ if $1 > \beta_c\rho_c/(\mathbf{p}_c\mathbf{q}_c) = \mathcal{R}_c^q$. Finally, the trace of Z_{33} is $\mathrm{Tr}(Z_{33}) = -\mathbf{p}_{ic} - \mathbf{q}_{ic} < 0$ and the determinant is $\mathrm{Det}(Z_{33}) = \mathbf{p}_{ic}\mathbf{q}_{ic} > 0$. Therefore, all eigenvalues of $\mathcal{Z}$ will have negative real parts if $\mathcal{R}_i^q < 1$ and $\mathcal{R}_c^q < 1$.

5 Efficacy of Imperfect Quarantine Measure

5.1 Introduction

In the battle against infectious diseases, quarantine measures are a cornerstone of the public health strategy. However, these measures are often implemented under imperfect conditions due to various real-world challenges such as non-compliance, resource limitations, and logistical problems [84]. Understanding the effectiveness of these imperfect quarantine measures is vital for developing strategies that can effectively manage epidemics, even when ideal conditions are not met.

Central to our investigation are quarantine reproduction numbers ($\tilde{\mathcal{R}}_c^q$ and $\tilde{\mathcal{R}}_i^q$), which are crucial metrics to assess the potential spread of diseases within quarantined populations, as detailed in Equation 4.20. Given the similarity in their formula structures, we generalize our analysis using $\tilde{\mathcal{R}}_k^q$, where k denotes either the strain-(c) or strain-(i). This generalized form is expressed as:

$$\tilde{\mathcal{R}}_k^q = \frac{\alpha_k\beta_k\mathbf{q}_k + \beta_k\rho_k\sigma_k + \alpha_k\beta_k\tau_k + \mathbf{r}_k\beta_k\rho_k}{\mathbf{p}_k(\dot{\mathbf{q}}_k\mathbf{r}_k + \tilde{\mathbf{r}}_k\sigma_k)}, \tag{5.1}$$

where $\mathbf{p}_k = \alpha_k + \rho_k + \mu, \mathbf{q}_k = \gamma_k + \sigma_k + \delta_k + \mu, \mathbf{r}_k = \phi_k + \tau_k + \delta_k + \mu$, $\tilde{\mathbf{r}}_k = \phi_k + \delta_k + \mu$ and $\dot{\mathbf{q}}_k = \gamma_k + \delta_k + \mu$. The formula, $\tilde{\mathcal{R}}_k^q$ represents the secondary infections generated by an individual infected with a single pathogen-k in a population, considering the quarantine of exposed individuals (at a rate α_k) and the isolation of infected individuals (at a rate σ_k). Other parameters made up Equation (5.1) include natural death rate μ, transmission rate β_k, rates of developing symptoms ρ_k, transition from quarantine to infection τ_k, and recovery and death rates ϕ_k, γ_k, and δ_k. This comprehensive formula aids in understanding the impact of quarantine and isolation measures on disease transmission.

Definition 5.1 **Quarantine** refers to the practice of separating and restricting the movement of individuals who may have been exposed to a contagious disease but do not yet show symptoms, to prevent potential transmission of the disease to others.

Definition 5.2 **Isolation** is the separation of individuals who are confirmed to be infected with a contagious disease from healthy individuals, to prevent the spread of the disease.

This chapter explores a variety of quarantine-related parameters and scenarios to assess their impact on epidemic dynamics and public health outcomes, focusing on the early stages of disease transmission where timely and effective quarantine can significantly alter the course of an epidemic. By analyzing the incremental placement of individuals in quarantine, our aim is to

determine the benefits and limitations of these measures to control the spread of infection. In addition, we examine the critical role of informational and educational efforts in enhancing the effectiveness of quarantine measures, as these efforts are essential to improve compliance and understanding among the public, thus increasing the overall efficacy of quarantine protocols. Our analysis integrates these factors to provide a comprehensive understanding of how quarantine measures interact with public awareness and behavior to influence epidemic outcomes.

5.2 Exploring quarantine reproduction metrics

Our exploration in this section involves understanding how changes in α_k and σ_k will affect $\tilde{\mathcal{R}}_k^q$ by analyzing various mathematical formulations of the quarantine reproduction number.

Perfect quarantine

Case 1: Decreased transmission potential

We begin by investigating the limit of the control reproduction number with perfect quarantine, denoted $\mathcal{R}_k^q$, which is expressed as follows:

$$\mathcal{R}_k^q = \frac{\beta_k \rho_k}{(\alpha_k + \rho_k + \mu)(\gamma_k + \sigma_k + \delta_k + \mu)}, \tag{5.2}$$

as $\sigma_k, \alpha_k \to \infty$, the metric $\mathcal{R}_k^q \to 0$. This means that, when the isolation of exposed and infected individuals is high, the control reproduction number of the disease can drop to zero. This implies that the disease cannot spread within the population, effectively stopping the epidemic.

Remark 5.3 Although perfect quarantine is unattainable, this analysis highlights the critical role of effective quarantine measures in controlling infectious disease outbreaks and serves as a goal to achieve public health interventions, even if perfect quarantine cannot be fully realized.

Imperfect quarantine

Case 2: Increased transmission potential (when $\alpha_k = \sigma_k = 0$)

This scenario typically represents the number of reproductions at baseline without any quarantine or isolation interventions. Setting $\alpha_k = \sigma_k = 0$, the terms containing α_k and σ_k become zero, and the expression simplifies to

$$\mathcal{R}_k = \frac{\beta_k \rho_k}{(\rho_k + \mu)(\gamma_k + \delta_k + \mu)} > \tilde{\mathcal{R}}_k^q. \tag{5.3}$$

The original metric $\tilde{\mathcal{R}}_k^q$ (as given in Equation 5.1) demonstrates the potential reduction in the spread of disease due to the inclusion of α_k and σ_k. These quarantine measures act as preventive factors, reducing the transmission potential of the disease by limiting the interaction of exposed (E_k) and infected (I_k) individuals with the susceptible population. The absence of such measures ($\alpha_k = \sigma_k = 0$) signifies impact, i.e. maximizing the transmission of the disease by allowing asymptomatic and symptomatic individuals to freely interact with the rest of the population. This scenario underscores the critical role of quarantine measures in disease control.

Case 3: No isolation of exposed individuals ($\alpha_k = 0, \sigma_k \neq 0$)

The value $\alpha_k = 0$ denotes that individuals in the exposed state are permitted to pursue their regular activities without undergoing any quarantine measures. Thus, setting $\alpha_k = 0$ we have the following:

$$\tilde{\mathcal{R}}_k^q|_{\alpha_k=0} = \tilde{\mathcal{R}}_k^{\sigma_k} = \frac{\beta_k\rho_k\sigma_k + \mathbf{r}_k\beta_k\rho_k}{(\rho_k+\mu)(\dot{\mathbf{q}}_k\mathbf{r}_k + \tilde{\mathbf{r}}_k\sigma_k)} < \mathcal{R}_k. \tag{5.4}$$

The metric $\tilde{\mathcal{R}}_k^{\sigma_k}$ represents the expected number of secondary cases generated by one infected individual when there is no quarantine for exposed individuals and isolation is only applied to the infected individuals at a rate σ_k. As $\sigma_k \to \infty$, then $\tilde{\mathcal{R}}_k^{\sigma_k}$ approaches a constant $\beta_k\rho_k/(\rho_k+\mu)\tilde{\mathbf{r}}_k$ which reflects the theoretical minimal quarantine reproduction number possible under imperfect case of isolating only infected individuals.

Case 4: No isolation of infected individuals ($\sigma_k = 0, \alpha_k \neq 0$):

Without the mitigating influence of isolation ($\sigma_k = 0$), infected individuals persist in unrestricted interactions with susceptible individuals, potentially resulting in continuous transmission:

$$\tilde{\mathcal{R}}_k^q|_{\sigma_k=0} = \tilde{\mathcal{R}}_k^{\alpha_k} = \frac{\alpha_k\beta_k\dot{\mathbf{q}}_k + \alpha_k\beta_k\tau_k + \mathbf{r}_k\beta_k\rho_k}{\mathbf{p}_k\dot{\mathbf{q}}_k\mathbf{r}_k} < \mathcal{R}_k \tag{5.5}$$

$\tilde{\mathcal{R}}_k^{\alpha_k}$ describes the expected number of new cases caused by a single infected individual under the scenario where only quarantine is utilized, without isolation interventions. Here, $\tilde{\mathcal{R}}_k^{\alpha_k}$ converge to $\beta_k(\dot{\mathbf{q}}_k + \tau_k)/\dot{\mathbf{q}}_k\mathbf{r}_k$ as α_k increases. Indicating the minimum possible quarantine reproduction number when only the quarantine for exposed individuals is in practice.

Case 5: Combined impact of isolation and quarantine: ($\sigma_k \neq 0, \alpha_k \neq 0$)

Now, we explore scenarios where both isolation and quarantine parameters undergo simultaneous adjustments. For elevated values of α_k and σ_k, the limit of the imperfect quarantine reproduction number, denoted as $\tilde{\mathcal{R}}_k^q$, is given by:

$$\tilde{\mathcal{R}}_k^{lim} = \lim_{\sigma_k,\alpha_k\to\infty} \tilde{\mathcal{R}}_k^q \to \frac{\beta_k}{(\phi_k+\delta_k+\mu)} := \mathring{R}_k^q \tag{5.6}$$

The ratio $\mathring{R}_k^q$ serves as a metric to understand the dynamics of imperfect quarantine. It gives the minimum number of secondary cases generated by a single infected individual in the population where quarantine and isolation are in practice.

5.3 Effectiveness of quarantine

When quarantined individuals recover faster, quarantine measures are generally more effective because they reduce the infectious period of individuals who are separated from the general population. This can lead to a reduction in the overall number of infectious individuals in the community, thus reducing the number of quarantine reproductions.

Remark 5.4 — Hypothesis. When the quarantine-induced recovery rate ϕ_k is less than or equal to the natural recovery rate γ_k, i.e., $(\phi_k \leq \gamma_k)$, the effectiveness of quarantine in reducing the number of secondary quarantine reproductions $\tilde{\mathcal{R}}_k^q$ decreases.

5.3.1 Local sensitivity analysis approach

To provide mathematical support for the hypothesis stated in Remark 5.4, we analyze the partial derivatives of the quarantine reproduction number $\tilde{\mathcal{R}}_k^q$ with respect to the quarantine rate α_k and the isolation rate σ_k. This sensitivity analysis is essential for effective disease control, resource allocation, and policy making, as it identifies the parameters that most significantly influence the quarantine reproduction number. By understanding these sensitivities, health authorities can prioritize interventions that will have the greatest impact on reducing disease transmission. We denote $\frac{\partial \tilde{\mathcal{R}}_k^q}{\partial \sigma_k}\big|_{\alpha_k=0}$ as $\frac{\partial \tilde{\mathcal{R}}_k^q}{\partial \sigma_k}$ and $\frac{\partial \tilde{\mathcal{R}}_k^q}{\partial \alpha_k}\big|_{\sigma_k=0}$ as $\frac{\partial \tilde{\mathcal{R}}_k^q}{\partial \alpha_k}$. Applying the quotient rule for differentiation, we obtain the following:

$$\frac{\partial \tilde{\mathcal{R}}_k^q}{\partial \sigma_k} = \frac{\beta_k \rho_k \mathbf{r}_k (\gamma_k - \phi_k)}{(\rho_k + \mu)(\dot{\mathbf{q}}_k \mathbf{r}_k + \tilde{\mathbf{r}}_k \sigma_k)^2}, \quad \text{and} \quad \frac{\partial \tilde{\mathcal{R}}_k^q}{\partial \alpha_k} = \frac{\rho_k(\gamma_k - \phi_k) + \mu(\mathbf{q}_k + \tau_k)}{(\alpha + \rho_k + \mu)^2 (\dot{\mathbf{q}}_k \mathbf{r}_k)}. \tag{5.7}$$

From Equation (5.7), the expression of $\frac{\partial \tilde{\mathcal{R}}_k^q}{\partial \sigma_k}$ represents how the quarantine reproduction number $\tilde{\mathcal{R}}_k^q$ changes with respect to the isolation rate σ_k when the quarantine rate α_k is zero. Similarly, $\frac{\partial \tilde{\mathcal{R}}_k^q}{\partial \alpha_k}$ indicates how $\tilde{\mathcal{R}}_k^q$ changes with respect to the quarantine rate α_k when the isolation rate σ_k is zero. Since all parameters are positive, we state the following conditions.

Remark 5.5

1. If $\gamma_k > \phi_k$, then $\frac{\partial \tilde{\mathcal{R}}_k^q}{\partial \sigma_k} > 0$ and $\frac{\partial \tilde{\mathcal{R}}_k^q}{\partial \alpha_k} > 0$. This suggests that higher isolation or quarantine rates might unexpectedly increase the quarantine reproduction number, indicating possible inefficiencies or adverse effects of these interventions.
2. If $\gamma_k = \phi_k$, then $\frac{\partial \tilde{\mathcal{R}}_k^q}{\partial \sigma_k} = 0$ and $\frac{\partial \tilde{\mathcal{R}}_k^q}{\partial \alpha_k} = 0$. This indicates a neutral point where the isolation and quarantine rates do not influence the quarantine reproduction number, suggesting that the system is at a critical threshold.
3. If $\gamma_k < \phi_k$, then $\frac{\partial \tilde{\mathcal{R}}_k^q}{\partial \sigma_k} < 0$ and $\frac{\partial \tilde{\mathcal{R}}_k^q}{\partial \alpha_k} < 0$. This suggests that higher isolation or quarantine rates effectively reduce the quarantine reproduction number, indicating a successful intervention.

To better understand, we visualize the results presented in Remark 5.5 in Figure 5.1.

Figure 5.1 and Remark 5.5 illustrate how the effectiveness of isolation and quarantine measures depends on the recovery rates of infected versus quarantined individuals. When infected individuals recover faster than quarantined ones, increasing isolation or quarantine rates can paradoxically raise the quarantine reproduction number, reducing effectiveness. If recovery rates are equal, changing these measures has no impact on the spread of the disease. In contrast, when the recovery rate of infected individuals is lower, higher isolation or quarantine rates effectively reduce the quarantine reproduction number, indicating a successful intervention. Furthermore, $\mathring{R}_k^q$, which represents the minimum number of secondary cases generated by a single infected

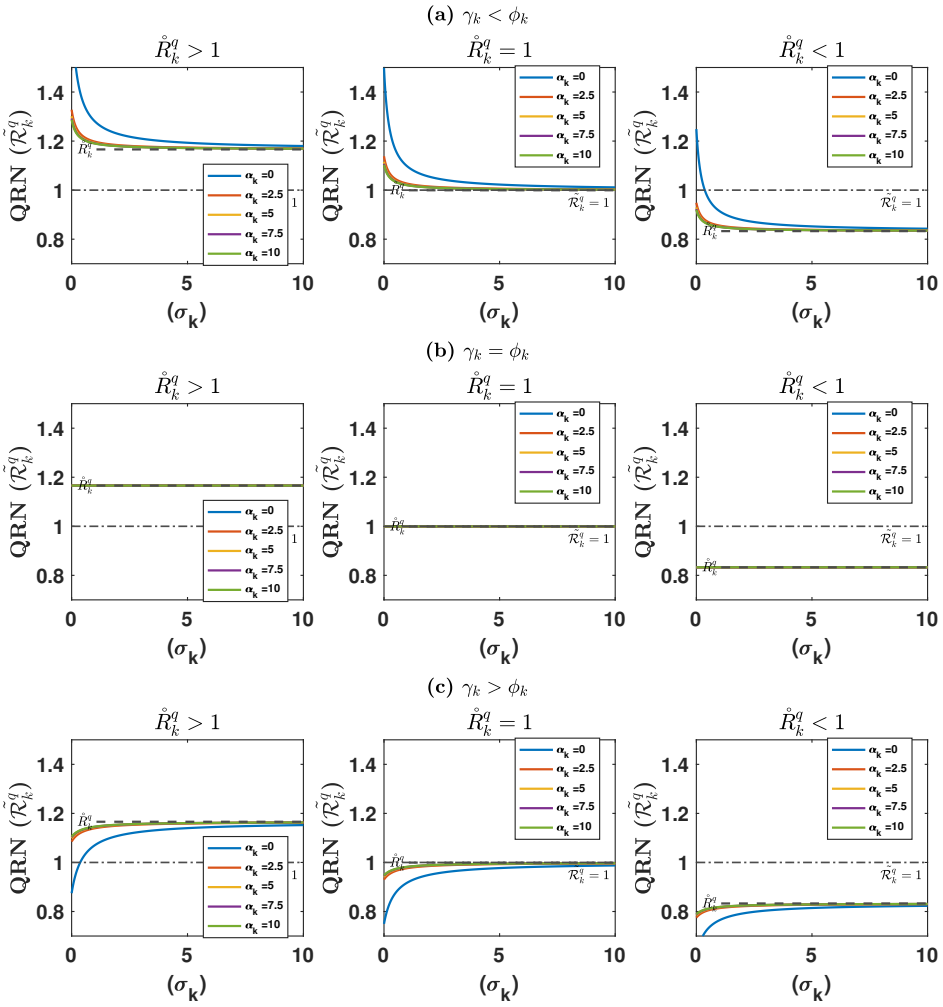

Figure 5.1: The graph shows the relationship between $\tilde{\mathcal{R}}_k^q$ and σ_k for specific α_k values. The dashed-dotted line represents the threshold $\tilde{\mathcal{R}}_k^q = 1$, while the dotted line indicates the limit $\mathring{R}_k^q$ as $\alpha_k, \sigma_k \to \infty$. Subplots: (a) $\phi_k = 0.3 > \gamma_k = 0.2$, (b) $\phi_k = \gamma_k = 0.3$, and (c) $\phi_k = 0.3 < \gamma_k = 0.4$. Transmission rates (β_k) are 0.35, 0.3, and 0.25, resulting in $\mathring{R}_k^q > 1$, $\mathring{R}_k^q = 1$, and $\mathring{R}_k^q < 1$. Changes in ϕ_k and γ_k affect quarantine reproduction number trajectories. α_k and σ_k vary between 0 and 10. Other parameters: $\rho_k = 0.3$, $\mu = 0.00001$, $\delta_k = 0.000017$, $\tau_k = 0.06$.

individual in quarantine and isolation, should ideally be less than 1 to ensure the disease declines and eventually dies out.

5.3.2 Critical levels of quarantine and isolation rates

Determining the right quarantine levels to stop an outbreak is the key to controlling epidemics. This section looks at the essential quarantine rates needed to keep the number of disease quarantine reproductions at or below one, preventing the infection from spreading.

Let α_k^* and σ_k^* be the critical quarantine and isolation rates required for imperfect quarantine. These rates are determined by solving the equation $\tilde{\mathcal{R}}_k^q = 1$ for α_k and σ_k, which gives us the following:

$$\alpha_k^* = \frac{(\tilde{\mathcal{R}}_{\alpha_k^0} - 1)\dot{\mathbf{p}}_k}{1 - \tilde{\mathcal{R}}_{\alpha_k^\infty}} \quad \text{and,} \quad \sigma_k^* = \frac{(\tilde{\mathcal{R}}_{\sigma_k^0} - 1)\dot{\mathbf{q}}_k}{1 - \tilde{\mathcal{R}}_{\sigma_k^\infty}}. \tag{5.8}$$

From Equation (5.8), as $\alpha_k \to 0$, $\tilde{\mathcal{R}}_{\alpha_k^0} = \tilde{\mathcal{R}}_k^{\alpha_k}$, and as $\alpha_k \to \infty$, $\tilde{\mathcal{R}}_{\alpha_k^\infty} = \tilde{\mathcal{R}}_k^{\alpha_k}$. Here, $\tilde{\mathcal{R}}_k^{\alpha_k}$ from Equation (5.5) represents the quarantine reproduction number when only exposed individuals are quarantined. Thus, $\tilde{\mathcal{R}}_{\alpha_k^0}$ and $\tilde{\mathcal{R}}_{\alpha_k^\infty}$ denote the maximum and minimum values of $\tilde{\mathcal{R}}_k^{\alpha_k}$, respectively. Similarly, as $\sigma_k \to 0$, $\tilde{\mathcal{R}}_{\sigma_k^0} = \tilde{\mathcal{R}}_k^{\sigma_k}$, and as $\sigma_k \to \infty$, $\tilde{\mathcal{R}}_{\sigma_k^\infty} = \tilde{\mathcal{R}}_k^{\sigma_k}$. The quantity $\tilde{\mathcal{R}}_k^{\sigma_k}$ from Equation (5.4) gives the quarantine reproduction number when only infected individuals are isolated, with $\tilde{\mathcal{R}}_{\sigma_k^0}$ and $\tilde{\mathcal{R}}_{\sigma_k^\infty}$ representing the maximum and minimum values of $\tilde{\mathcal{R}}_k^{\sigma_k}$, respectively. It is important that these terms are meaningful only if $\tilde{\mathcal{R}}_{\alpha_k^0} > 1 > \tilde{\mathcal{R}}_{\alpha_k^\infty}$ and $\tilde{\mathcal{R}}_{\sigma_k^0} > 1 > \tilde{\mathcal{R}}_{\sigma_k^\infty}$. In Figure 5.2, specifically subplots (a) and (b), we visualize the thresholds and illustrate how the quarantine reproduction numbers change with varying rates of quarantine and isolation. Subplots (c) and (d) compare these results with the outcomes of perfect quarantine. All subplots demonstrate that when $\alpha_k < \alpha_k^*$ and $\sigma_k < \sigma_k^*$, the quarantine reproduction numbers exceed one. This indicates that lower levels of quarantine and isolation are insufficient to control the disease spread, resulting in a higher number of infections.

5.3.3 Critical levels of quarantined and isolated individuals

Practicable questions, of course, are: what fractions of individuals should be restricted if we restrict

(i) exposed only ?

(ii) infected only ?

(iii) both exposed and infected individuals?

To address these questions, we define:

$$\alpha_k^q = \frac{\alpha_k}{\mathbf{r}_k}, \quad \text{and,} \quad \sigma_k^q = \frac{\sigma_k}{\mathbf{r}_k}, \tag{5.9}$$

where α_k^q and σ_k^q represent the fractions of exposed and infected individuals quarantined or isolated, respectively. By substituting α_k and σ_k from Equation (5.8) into Equation (5.9), we can determine $\boldsymbol{E}_k^{crit}$ and $\boldsymbol{I}_k^{crit}$, the critical proportions of exposed and infected individuals that

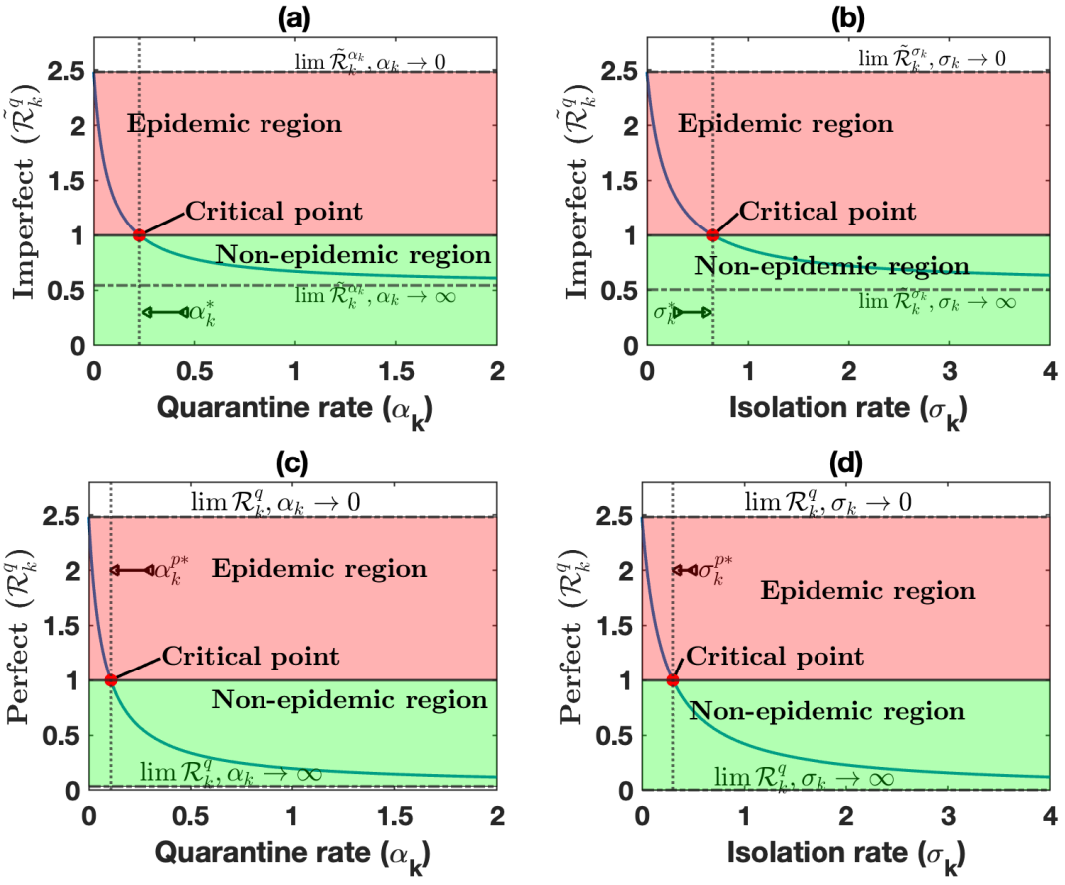

Figure 5.2: The dependence of quarantine reproduction numbers (QRN) on parameters α_k and σ_k for exposed and infected individuals. Subplots **(a)** and **(b)** show imperfect quarantine, while subplots **(c)** and **(d)** show perfect quarantine. Red dots mark the critical points where the quarantine reproduction number equals one. Vertical dotted lines indicate the critical rates. The lower dashed line shows the minimum QRN as α_k and σ_k approach large numbers, while the upper dashed line shows the maximum QRN as they approach 0, indicating the QRN in the absence of these interventions. Parameters: $\beta_k = 0.5$, $\rho_k = 0.07$, $\phi_k = 0.92$, $\tau_k = 0.015$, $\mu = 0.0001$, $\gamma = 0.2$, $\delta_k = 0.001$.

need to be restricted in the case of imperfect quarantine. These critical levels are given by:

$$\boldsymbol{E}_k^{crit} = \frac{(\tilde{\mathcal{R}}_{\alpha_k^0} - 1)\dot{\mathbf{p}}_k}{(1 - \tilde{\mathcal{R}}_{\alpha_k^\infty})\mathbf{r}_k} \quad \text{and,} \quad \boldsymbol{I}_k^{crit} = \frac{(\tilde{\mathcal{R}}_{\sigma_k^0} - 1)\dot{\mathbf{q}}_k}{(1 - \tilde{\mathcal{R}}_{\sigma_k^\infty})\mathbf{r}_k}. \tag{5.10}$$

Equations in (5.10) make sense if $\tilde{\mathcal{R}}_{\alpha_k^0} > 1 > \tilde{\mathcal{R}}_{\alpha_k^\infty}$ and $\tilde{\mathcal{R}}_{\sigma_k^0} > 1 > \tilde{\mathcal{R}}_{\sigma_k^\infty}$. Next, in Figure 5.3, we visualize the estimate of the quarantine reproduction numbers with respect to quarantine parameters to show the critical rates and levels given in Equations (5.8) and (5.10), respectively.

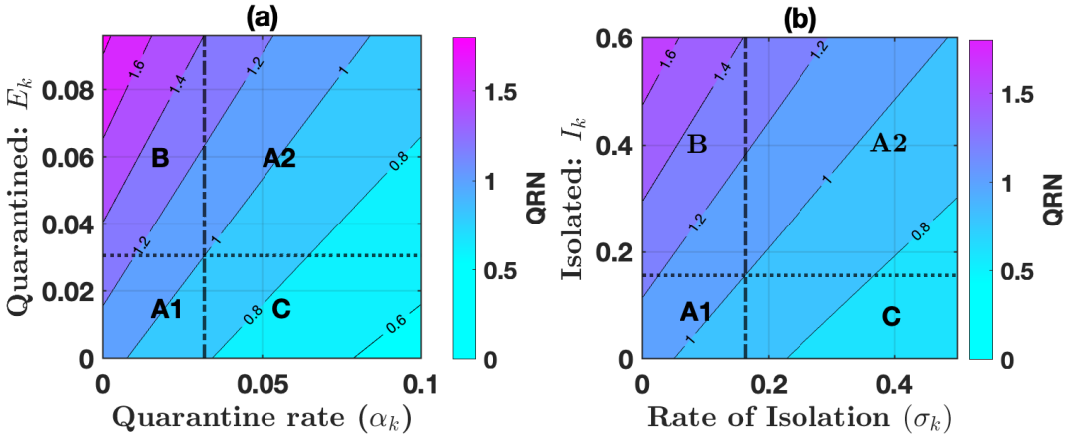

Figure 5.3: This diagram illustrates how quarantine-related parameters α_k and σ_k affect the quarantine reproduction number (QRN), with subplot (a) showing the proportion of quarantined individuals and subplot (b) showing the proportion of isolated individuals. The vertical dashed-dotted lines represent the critical levels α_k^* and σ_k^*. The horizontal dotted lines indicate the critical levels $\boldsymbol{E}_k^{crit}$ and $\boldsymbol{I}_k^{crit}$. Parameters used are $\beta_k = 0.78$, $\rho_k = 0.09$, $\tau_k = 0.0135$, $\delta_k = 0.00001$, $\phi_k = 1.02$, $\mu = 0.009$, and $\gamma_k = 0.65$.

From the subplots in Figure 5.3, we can discern the effectiveness of quarantine and isolation measures in controlling the spread of infection. In Region **A1**, both quarantine (α_k) and isolation (σ_k) rates fall below their critical thresholds (α_k^* and σ_k^*), indicating that current measures are inadequate and predicting that the quarantine reproduction number will eventually exceed one. Region **B** highlights that even with lower rates of quarantine and isolation, an overload of individuals in quarantine facilities can overwhelm the system. In Region **A2**, although quarantine and isolation rates are high, the quarantine reproduction number remains above one due to the excessive number of quarantined individuals. Region **C** illustrates the optimal scenario in which higher quarantine and isolation rates, together with the controlled number of quarantined individuals, result in a reproduction number falling below one. We make the following observation:

Remark 5.6 — Condition for possible secondary cases less than one. In addition to $\gamma_k < \phi_k$:

1. The quarantine of exposed individuals (denoted by α_k) will have a positive impact on controlling the disease only if the quarantine rate α_k is greater than or equal to the critical threshold α_k^*, and the number of quarantined exposed individuals α_k^q remains

below the critical level $\boldsymbol{E}_k^{crit}$. The left subplot in Figure (5.3) illustrates this case.

2. The isolation of infected individuals (denoted by σ_k) will have a positive impact on disease control only if the isolation rate σ_k is greater than or equal to the critical threshold σ_k^*, and the number of isolated infected individuals σ_k^q remains below the critical level $\boldsymbol{I}_k^{crit}$. See the right subplot in Figure (5.3).

3. When both exposed and infected individuals are restricted, the metric $\mathring{R}_k^q$ (as given in Equation) represents the minimum threshold for the quarantine reproduction number to be less than one. This implies that $\tilde{\mathcal{R}}_k^q \to \mathring{R}_k^q$ as $\alpha_k, \sigma_k \to \infty$. See Figure 5.1 (a).

In reality, achieving infinite quarantine or isolation rates is impractical, but this theoretical limit serves as a benchmark for the effectiveness of quarantine measures. Public health strategies should aim to maximize quarantine or isolation rates to minimize the number of reproduction of quarantines as much as possible.

5.4 Approximation of scaling function

In Chapter 4, the function $\Omega_k = 1 - \omega_k I_k$ from Equation (4.6) was introduced to scale the transmission rate within the quarantine class, where I_k represents the proportion of infected individuals and ω_k measures the impact of public information campaigns on the adherence to quarantine. Here, $\omega_k = 0$ denotes no educational efforts, while $\omega_k \in (0, 1]$ reflects the varying intensity of the campaign. The linear function $\Omega_k = 1 - \omega_k I_k$ proved to work better in the influenza model that incorporated data and fit the parameter ω_k that describes the reduction in actual transmission when applying control measures [89]. However, the choice of function was reasonable to account for the decline in infections after the implementation of quarantine measures; one could use other types of declining function could be used as mentioned in the literature. This section offers numerical approximations of this function to demonstrate how different values ω_k affect quarantine effectiveness, as detailed in Table 5.1. These approximations aim to highlight the influence of public education and adherence on controlling disease spread.

Table 5.1: Estimated degree of imperfection represented by the scaling function $\Omega_k = 1 - \omega_k I_k$.

	ω_k	I_k	$\omega_k I_k$	Ω_k	**Level of imperfection**
1.	$\omega_k \to 0$	$I_k \to 0$	$\omega_k I_k \to 0$	$\Omega_k \to 1$	High
2.	$\omega_k \to 0$	$I_k \to 1$	$\omega_k I_k \to 0$	$\Omega_k \to 1$	High
3.	$\omega_k \to 1$	$I_k \to 0$	$\omega_k I_k \to 0$	$\Omega_k \to 1$	High
4.	$\omega_k \to 1$	$I_k \to 1$	$\omega_k I_k \to 1$	$\Omega_k \to 0$	Low

We discuss the implications of these estimates in the following remark.

Remark 5.7 — Implication of results presented in Table 5.1. 1. $\omega_k \to 0$ and $I_k \to 0$ gives $\Omega_k \to 1$: This reflects a scenario where the infection rate is low, but the lack of adequate information and education can lead to a high imperfection, suggesting that more input

could further reduce the infection rates or improve preparedness.

2. $\omega_k \to 0$ and $I_k \to 1$ leads to $\Omega_k \to 1$: This highlights a critical situation where insufficient information and education efforts fail to manage the high infection rates, resulting in high imperfection.

3. $\omega_k \to 1$ and $I_k \to 0$ leads to $\Omega_k \to 1$: This suggests that the inputs provided are not being fully utilized or are unnecessary due to the low number of infections.

4. $\omega_k \to 1$ and $I_k \to 1$ leads to $\Omega_k \to 0$: This indicates that information and education efforts are effective in managing and reducing the spread of infection, resulting in a lower level of imperfection.

Moreover, we visualize the results presented in Table 5.1 along with their implications in Remark 5.7 in Figure 5.4.

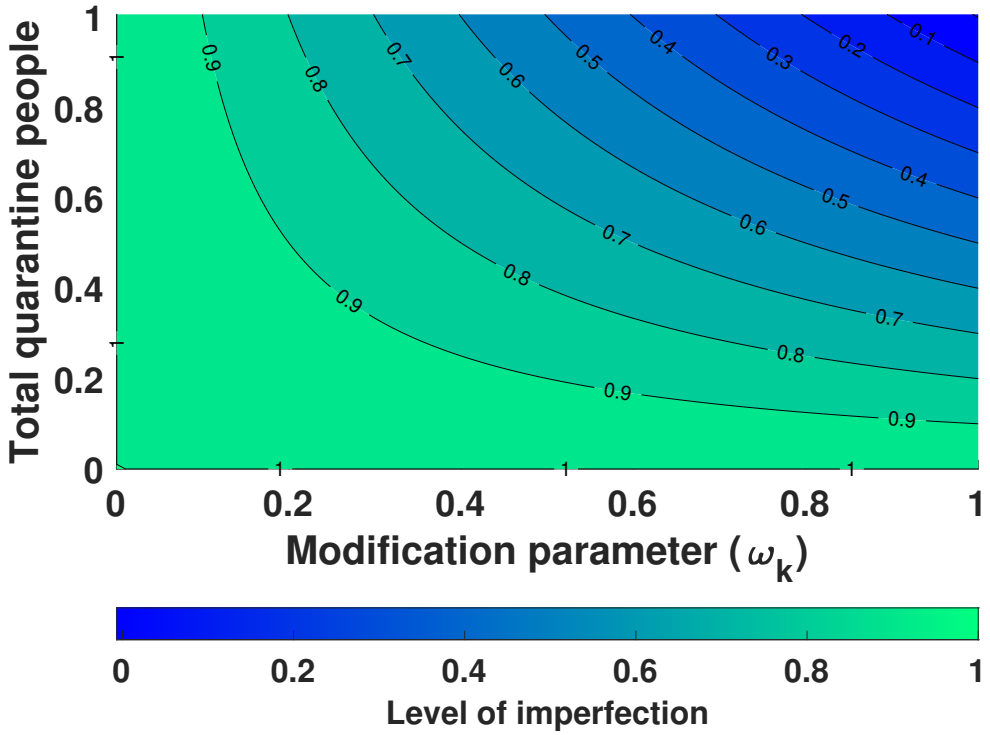

Figure 5.4: The estimates change in the level of imperfection, Ω_k, to the effort provided, ω_k, and the proportion number of individuals quarantined. Parameters are taken as in Figure 5.3.

Table 5.1 and Figure 5.4 illustrate that achieving a low level of imperfection in the management of infections requires high levels of input from the authority (information and education) and high infection rates. When the inputs are high but infections are low, or both are low, the imperfection level remains high, indicating either under-utilization of educational efforts or insufficient preparedness. High infection rates without adequate information and education also

lead to high imperfection, emphasizing the need for adequate and effective communication and education efforts to manage and reduce infections effectively.

5.4.1 Overall behavior model

Finally, we simulate and visualize the spread of a disease over time using a compartmental model (4.2) in the absence of a strain. We used combinations of different values for the parameters α_k, σ_k, and ω_k to plot the fraction of infected individuals over time. This analysis helps us understand the impact of these parameters on both the maximum height of infections and the time it takes to reach this peak, providing valuable insights to effectively mitigate disease spread.

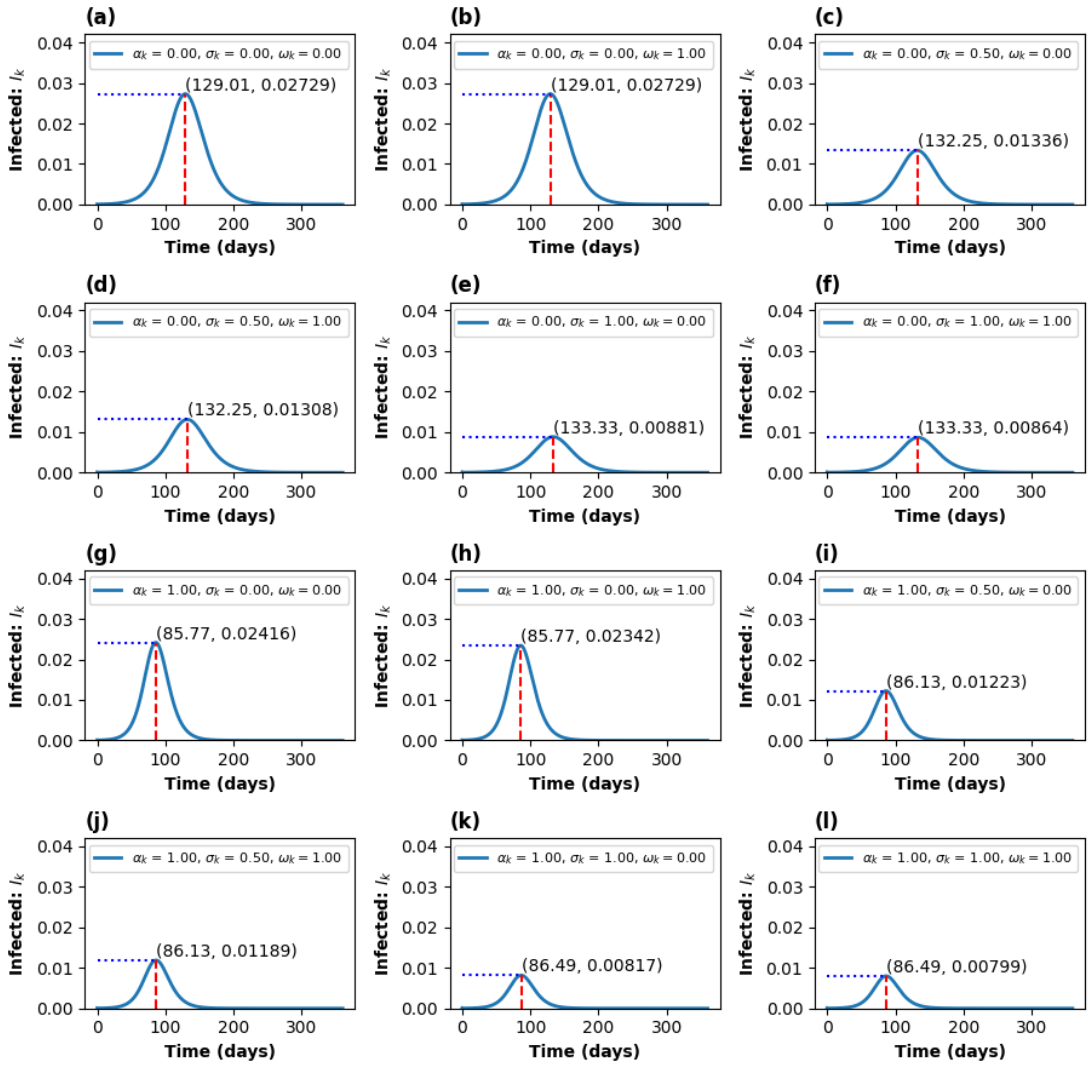

Figure 5.5: Infection dynamics I_k over 360 days for various parameter combinations α_k, σ_k, and ω_k, each ranging from 0 to 1. Each subplot illustrates the model predictions with vertical and horizontal dashed lines marking the peak times and infection values, which are annotated directly. Other parameters are fixed at $\Lambda = \mu = 0.0001$, $\beta_k = 0.4$, $\rho_k = 0.3$, $\gamma_k = 0.28$, $\phi_k = 0.3$, and $\tau_k = 0.25$. The initial conditions are $I_k(0) = 0.001$ and $S(0) = 1 - I_k(0)$.

Figure 5.5 illustrates the effects of varying parameters α_k (quarantine rate), σ_k (isolation rate), and ω_k (impact of public information campaigns) on the maximum fraction of infections and the time of this peak. Subplots (a) and (b) show that, without quarantine and isolation, the highest infection rate is 0.027286 on day 129. When isolation is introduced ($\sigma_k = 0.50$ or $\sigma_k = 1.00$), as depicted in subplots (c)-(f), the maximum infection rate decreases, with the lowest peak of 0.008638 occurring on day 133.33 when both parameters are maximized. High levels of quarantine ($\alpha_k = 1.00$) and isolation yield the lowest maximum infection rate, reaching 0.007988 on day 86.49, as seen in subplots (g)-(l). The parameter ω_k, while having a smaller impact compared to α_k and σ_k, generally contributes to the reduction of the maximum infection rates when set to non-zero values. The timing of the peak varies from 85 to 133 days depending on the parameter combinations used, underscoring that not only do these parameters affect the magnitude of the peak, but they also significantly influence the timing of the peak and the overall progression of the epidemic. Therefore, careful selection of parameters can significantly impact both the extent and timing of an epidemic's peak.

5.5 Discussion

This chapter evaluates the impact of various quarantine-related parameters on epidemic dynamics, with a focus on the early phases of disease transmission. It emphasizes the importance of timely quarantine measures and educational efforts in improving public compliance and effectiveness in controlling the spread of infection.

In the absence of quarantine and isolation, the number of reproduction is highest, which underscores the necessity of these interventions, as evidenced in Figure 5.2. Implementing perfect quarantine at the initial stages of disease transmission by isolating both exposed and infected individuals could effectively eradicate the disease. These results align with the findings on optimal and suboptimal control of the SARS model [138], which demonstrate that the maximum application of quarantine and isolation strategies in the early stage of the epidemic is critically impactful. However, in real-world situations, perfect quarantine is often unattainable [84], highlighting the need for highly effective quarantine measures.

With imperfect quarantine, the control reproduction number decreases, but not to the extent achievable with both measures. This indicates that while a single measure (either quarantine or isolation) helps reduce the infection's reproduction number, it is not as effective as using both measures together. Therefore, the combined use of quarantine and isolation is necessary to achieve a maximum reduction in the number of quarantine reproductions and to better control the spread of infection. Furthermore, as observed in Chapter 4, specifically in Lemma 4.8, when both conditions $c_1 > c_2$ and/or $c_3 > c_4$ are true, the system does not effectively contain and reduce the number of exposed and infected individuals, leading to continuous spread of infection and making the DFE unsustainable. These results align with the findings that imperfect quarantine can lead to disease persistence or recurrent outbreaks [38].

We also found that increasing the quarantine rate of exposed individuals and the isolation rate of infected individuals initially leads to a significant reduction in secondary infections. However, beyond a certain point, further increases in these rates yield progressively smaller reductions in

infection rates, as shown in Figure 5.2. This is due to the imperfect nature of these measures, which cannot completely stop transmission [139]. Thus, our findings suggest that these measures alone cannot indefinitely decrease secondary infections to zero due to inherent limitations and diminishing returns. Other complementary measures, such as testing [7], vaccination [121], public health education [43], and improved treatment protocols [98], are also necessary for effective disease control.

When ϕ_k (the quarantine-induced recovery rate) is greater than γ_k (the natural recovery rate of infected individuals who are not quarantined), it implies that quarantined individuals recover more quickly than those who are not. This condition indicates that quarantine measures are effective in accelerating the recovery process and significantly reducing the overall spread of the disease. Providing education and psychological support to individuals in quarantine is crucial to improve their adherence to quarantine measures and overall health outcomes, which can lead to faster recovery, as shown in Figure 5.1. In addition, controlled levels of quarantined individuals combined with higher rates of quarantine and isolation result in an optimal scenario where the quarantine reproduction numbers falls below one, reducing disease complications such as infection peaks as described in Figure 5.5. The figure also demonstrates that the combination of parameters influences not only the peak fraction of infections but also significantly impacts the timing of the peak and the final size of the epidemic.

6 Sub-critical Analysis: Coexistence and Bifurcation

6.1 Introduction

This chapter explores the dynamics of multipathogen systems, focusing on scenarios where the quarantine reproductive number of a pathogen (that is, $\tilde{\mathcal{R}}_i^q$ or $\tilde{\mathcal{R}}_c^q$) is less than one while the other is greater than one. This framework enables the investigation of complex co-existence scenarios where pathogens interact through mechanisms such as cross-immunity, and where the dynamics of one pathogen can significantly influence the persistence of another. Some of the content in this chapter is presented in [45, 46].

6.1.1 Background

Studies have looked at how different germs interact within a population, focusing on how they affect each other's spread and what this means for controlling diseases. Gupta et al. (1998) explored the dynamics of cross-immunity between two pathogen strains, demonstrating that a strain with reproduction number greater than 1 $R_0 > 1$ can persist in the population while a strain with $R_0 < 1$ could still impact the overall dynamics of the disease through immunological interactions [61]. Similarly, Castillo-Chavez et al. (2004) extended this understanding by revealing that the differing R_0 values of multiple pathogens can influence co-existence dynamics. They showed that while a pathogen with $R_0 > 1$ can establish an endemic equilibrium, a pathogen with $R_0 < 1$ can still affect the prevalence and stability of the more transmissible pathogen through mechanisms such as cross-immunity [20]. In their study of influenza dynamics, Nuño et al. (2005) demonstrated that cross-immunity between strains with different R_0 values can result in complex epidemiological patterns, where a less transmissible strain can modulate the dynamics of a more transmissible strain [96].

These findings emphasize that in multipathogen systems, the dynamics of one pathogen can significantly impact the presence and behavior of another, even if the second pathogen has a lower reproduction number. This interaction adds complexity that traditional disease transmission models might overlook. One such complexity is backward bifurcation, where a disease-free equilibrium and an endemic equilibrium can coexist, even if the pathogen's reproductive number R_0 is less than one. This allows the disease to persist in the population, which differs from forward bifurcation, where exceeding a critical threshold results in a shift from a disease-free state to an endemic state [20, 125].

Understanding backward bifurcation is essential for designing effective public health policies and interventions. This phenomenon underscores the importance of considering various factors

and thresholds in disease dynamics, which are not always apparent from basic models [59]. Studies have shown that mechanisms such as exogenous reinfection, imperfect vaccine efficacy, and acquired immunity can contribute to the occurrence of backward bifurcation in disease models [39, 59, 73]. For example, exogenous reinfection can maintain the presence of a disease in a population even when R_0 is less than one, while acquired immunity can create conditions where a disease can persist despite efforts to reduce transmission.

In this chapter, we explore the dynamics of multipathogen systems where the quarantine reproductive number of one pathogen is less than one while that of the other is greater than one, focusing on the conditions under which backward bifurcation occurs and providing insights into effective disease management practices. We investigate how cross-immunity and other factors contribute to disease persistence and examine the implications for public health strategies aimed at controlling multipathogen diseases. Understanding these dynamics will help us uncover how complex interactions between pathogens influence disease outcomes and guide the development of more nuanced public health interventions.

6.2 Exploring the conditions for sub-critical coexistence

In this section, we explore the dynamics and conditions that allow subcritical coexistence of pathogens, where one pathogen's quarantine reproduction number is less than one while the other is greater than one. We start by presenting the following results.

Theorem 6.1 For the scenario involving full cross-protection ($\eta_i^c = \eta_c^i = 0$) and absence of co-infections ($I_{ic} = 0$), the system described in Equation (4.2) demonstrates the presence of sub-critical coexistence equilibrium when either

i. $\tilde{\mathcal{R}}_c^q < 1$ and $\tilde{\mathcal{R}}_i^q > 1$,

ii. $\tilde{\mathcal{R}}_c^q > 1$ and $\tilde{\mathcal{R}}_i^q < 1$.

Proof. To prove Theorem 6.1, we consider the equations in System (4.42). The solutions of this system satisfy the following:

$$\ddot{\xi}^*_{i\,1,2} = \frac{-b_{11} \pm \sqrt{b_{11}^2 - 4a_{11}c_{11}}}{2a_{11}} \quad \& \quad \ddot{\xi}^*_{c\,1,2} = \frac{-b_{22} \pm \sqrt{b_{22}^2 - 4a_{22}c_{22}}}{2a_{22}}. \tag{6.1}$$

For quick reference we re-write the coefficients of $a_{11}, b_{11}, c_{11}, a_{22}, b_{22}, \ \& c_{22}$ as:

$$\begin{aligned}
a_{11} &= W_{66}^2\beta_c^2\omega_c^2(1-\tilde{\Phi}_i) + W_{55}W_{66}\beta_c\beta_i\omega_c\omega_i\Big[(1-\tilde{\Phi}_c) + (1-\tilde{\Phi}_i)\Big] + W_{55}^2\beta_i^2\omega_i^2(1-\tilde{\Phi}_c),\\
b_{11} &= W_{55}W_{66}^2\beta_c^2\beta_i\omega_c^2\omega_i\mu + (1-\tilde{\Phi}_c)W_{55}W_{66}\beta_c\beta_i\omega_c\omega_i\mu + (1-\tilde{\Phi}_i)W_{66}^2\beta_c^2\omega_c^2\mu +\\
&\quad (1-\tilde{\mathcal{R}}_c^q)W_{55}W_{66}\beta_c\beta_i\omega_c\omega_i\mu + (1-\tilde{\mathcal{R}}_i^q)W_{66}^2\beta_c^2\omega_c^2\mu,\\
c_{11} &= W_{66}^2\beta_c^2\omega_c^2\mu^2(1-\tilde{\mathcal{R}}_i^q),
\end{aligned}$$

besides,

$$
\begin{aligned}
a_{22} &= W_{55}^2\beta_i^2\omega_i^2(1-\tilde{\Phi}_c) + W_{55}W_{66}\beta_c\beta_i\omega_c\omega_i\Big[(1-\tilde{\Phi}_c)+(1-\tilde{\Phi}_i)\Big] + W_{66}^2\beta_c^2\omega_c^2(1-\tilde{\Phi}_i),\\
b_{22} &= W_{55}^2W_{66}\beta_c\beta_i^2\omega_c\omega_i^2\mu + (1-\tilde{\Phi}_i)W_{55}W_{66}\beta_c\beta_i\omega_c\omega_i\mu + (1-\tilde{\Phi}_c)W_{55}^2\beta_i^2\omega_i^2\mu +\\
&\quad (1-\tilde{\mathcal{R}}_i^q)W_{55}W_{66}\beta_c\beta_i\omega_c\omega_i\mu + (1-\tilde{\mathcal{R}}_c^q)W_{55}^2\beta_i^2\omega_i^2\mu,\\
c_{22} &= W_{55}^2\beta_i^2\omega_i^2\mu^2(1-\tilde{\mathcal{R}}_c^q).
\end{aligned}
$$

We set the discriminant $\Delta_{11} = b_{11}^2 - 4a_{11}c_{11} > 0$ and $\Delta_{22} = b_{22}^2 - 4a_{22}c_{22} > 0$ to ensure two distinct real roots for each equation. As described in Section 4.4.3, a_{11} and a_{22} are positive. For $\Delta_{11} > 0$, we need $c_{11} < 0$, which is possible if $\tilde{\mathcal{R}}_i^q > 1$. Similarly, $\Delta_{22} > 0$ if $\tilde{\mathcal{R}}_c^q > 1$. Since we want the quarantine reproduction numbers to be on opposite sides of the critical value 1, we state the following remark ensuring this condition and the positivity of solutions.

Remark 6.2 From Equation (6.1), we have $\Delta_{11} > 0$ given $\tilde{\mathcal{R}}_i^q > 1$ and $\Delta_{22} > 0$ given $\tilde{\mathcal{R}}_c^q > 1$:

i. $\ddot{\xi}_{i,1}^* = -b_{11} + \sqrt{\Delta_{11}} > 0$, and $\ddot{\xi}_{i,2}^* = -b_{11} - \sqrt{\Delta_{11}} > 0$. The first condition in Theorem 6.1 is met if $b_{11} < 0$. To achieve this, we set $\tilde{\mathcal{R}}_c^q < 1$.

ii. $\ddot{\xi}_{c,1}^* = -b_{22} + \sqrt{\Delta_{22}} > 0$, and $\ddot{\xi}_{c,2}^* = -b_{22} - \sqrt{\Delta_{22}} > 0$. The second condition in Theorem 6.1 is met if $b_{22} < 0$. To ensure subcritical co-existence, we set $\tilde{\mathcal{R}}_i^q < 1$.

It is crucial to note that we could have set both $\tilde{\mathcal{R}}_c^q > 1$ and $\tilde{\mathcal{R}}_i^q > 1$ to achieve $b_{11} < 0$ and $b_{22} < 0$, respectively, but this would result in all quarantine reproduction numbers being greater than one. This solution was discussed in Section 4.4.3. ■

Theorem 6.1 reveals that two pathogens can co-exist under certain conditions where their control reproduction numbers are divergent: one exceeding 1 and the other falling below 1. This indicates that one pathogen spreads more easily than the other under current conditions. The theorem assumes full cross-protection and no co-infections, which simplifies the model. However, in practice, varying levels of cross-immunity can greatly affect pathogen interactions and co-existence, as will be demonstrated in the numerical section 6.4.

6.3 Backward bifurcation analysis

Understanding the parameters and mechanisms that lead to backward bifurcation is crucial to designing effective public health strategies. Theorem 6.1, on the other hand, demonstrates how stable disease-free and endemic equilibria can coexist even when the quarantine reproduction number is less than one. To address this (in this section), we perform a backward bifurcation analysis to determine the conditions for such co-existence. We apply the center manifold theory as described in Theorem 4.1 of [20] recapitulated in Chapter 3.

6.3.1 Model setting

Here, we assume partial cross-immunity, that is $\eta_i^c, \eta_c^i \in (0, 1]$ and hold that there are no co-infections (i.e., $E_{ic} = I_{ic} = Q_{ic} = R_{ic} = 0$). We introduce the following notation: $S = x_1$, $E_i = x_2$, $E_c = x_3$, $I_i = x_4$, $I_c = x_5$, $Q_i = x_6$, $Q_c = x_7$, $R_i = x_8$, and $R_c = x_9$. Furthermore, let

$X'(t) = F(X) = (f_k)^T$, where $k = 1, 2, \ldots, 9$. By considering these assumptions and substituting these notations into the original model 4.2, we obtain the following:

$$\begin{aligned}
x_1'(t) &\equiv f_1 = \Lambda - \xi_i x_1 - \xi_c x_1 - \mu x_1,\\
x_2'(t) &\equiv f_2 = \xi_i x_1 - (\alpha_i + \rho_i + \mu)x_2 + \eta_c^i x_9 \xi_i,\\
x_3'(t) &\equiv f_3 = \xi_c x_1 - (\alpha_c + \rho_c + \mu)x_3 + \eta_i^c x_8 \xi_c,\\
x_4'(t) &\equiv f_4 = \rho_i x_2 + \tau_i x_6 - (\gamma_i + \sigma_i + \delta_i + \mu)x_4,\\
x_5'(t) &\equiv f_5 = \rho_c x_3 + \tau_c x_7 - (\gamma_c + \sigma_c + \delta_c + \mu)x_5,\\
x_6'(t) &\equiv f_6 = \alpha_i x_2 - (\phi_i + \tau_i + \delta_i + \mu)x_6 + \sigma_i x_4,\\
x_7'(t) &\equiv f_7 = \alpha_c x_3 - (\phi_c + \tau_c + \delta_c + \mu)x_7 + \sigma_c x_5,\\
x_8'(t) &\equiv f_8 = \phi_i x_6 + \gamma_i x_4 - \eta_i^c x_8 \xi_c - \mu x_8,\\
x_9'(t) &\equiv f_9 = \phi_c x_7 + \gamma_c x_5 - \eta_c^i x_9 \xi_i - \mu x_9,
\end{aligned} \tag{6.2}$$

where

$$\xi_i = \frac{\beta_i(x_4 + (1 - \omega_i x_4)x_6)}{T_x}, \quad \text{and} \quad \xi_c = \frac{\beta_c(x_5 + (1 - \omega_c x_5)x_7)}{T_x}. \tag{6.3}$$

At a specified time t, the total population size T_x is calculated as the sum of all compartments, given by $T_x = \sum_{i=1}^{9} x_i$.

6.3.2 Exploring bifurcation coefficients

To identify the bifurcation parameter such that $\tilde{\mathcal{R}}^q$ is at the critical value 1, it is crucial to note that $\tilde{\mathcal{R}}^q = \max\{\tilde{\mathcal{R}}_c^q, \tilde{\mathcal{R}}_i^q\}$ (the definitions of elements of the quantity $\tilde{\mathcal{R}}^q$ are given in Equation 4.20). Therefore, selecting β_c as the bifurcation parameter, we assume $\tilde{\mathcal{R}}_i^q \leq \tilde{\mathcal{R}}_c^q = 1$, so that $\tilde{\mathcal{R}}^q = 1$. Subsequently, we determine $\beta_c = \beta_c^*$ in $\tilde{\mathcal{R}}_c^q = 1$ to be:

$$\beta_c^* = \frac{\mathbf{p}_c((\gamma_c + \delta_c + \mu)\mathbf{r}_c + (\phi_c + \delta_c + \mu)\sigma_c)}{\alpha_c \mathbf{q}_c + \rho_c \sigma_c + \alpha_c \tau_c + \mathbf{r}_c \rho_c}.$$

The Jacobian of System (6.2) at the disease-free equilibrium, 4.13 is then given by:

$$J(\mathbf{E}_{ic}^0) = \begin{pmatrix}
-\mu & 0 & 0 & -\beta_i & -\beta_c^* & -\beta_i & -\beta_c^* & 0 & 0\\
0 & -\mathbf{p}_i & 0 & \beta_i & 0 & \beta_i & 0 & 0 & 0\\
0 & 0 & -\mathbf{p}_c & 0 & \beta_c^* & 0 & \beta_c^* & 0 & 0\\
0 & \rho_i & 0 & -\mathbf{q}_i & 0 & \tau_i & 0 & 0 & 0\\
0 & 0 & \rho_c & 0 & -\mathbf{q}_c & 0 & \tau_c & 0 & 0\\
0 & \alpha_i & 0 & \sigma_i & 0 & -\mathbf{r}_i & 0 & 0 & 0\\
0 & 0 & \alpha_c & 0 & \sigma_c & 0 & -\mathbf{r}_c & 0 & 0\\
0 & 0 & 0 & \gamma_i & 0 & \phi_i & 0 & -\mu & 0\\
0 & 0 & 0 & 0 & \gamma_c & 0 & \phi_c & 0 & -\mu
\end{pmatrix} \tag{6.4}$$

We consider λ as an eigenvalue of the characteristic equation $|J(\mathbf{E}_{ic}^0 - \lambda \mathbf{I})| = 0$. SageMath software was used to determine that the characteristic form has exactly one zero eigenvalue, allowing us to use the bifurcation theorem of Castillo-Chavez and Song [20]. To find a right eigenvector $w = (w_1, w_2, \ldots, w_9)^T$, we solve $J(\mathbf{E}_{ic}^0)w = 0$, which gives:

$$
\begin{aligned}
&w_1 = -\frac{\beta_i}{\mu}(w_4 + w_6) - \frac{\beta_c^*}{\mu}(w_5 + w_7),\\
&w_2 = \frac{\beta_i}{\mathbf{p}_i}(w_4 + w_6), \quad w_3 = \frac{\beta_c^*}{\mathbf{p}_c}(w_5 + w_7),\\
&w_4 = \frac{\beta_i\rho_i + \tau_i\mathbf{p}_i}{\mathbf{p}_i\mathbf{q}_i - \beta_i\rho_i}w_6, \quad w_5 = \frac{\beta_c^*\rho_c + \tau_c\mathbf{p}_c}{\mathbf{p}_c\mathbf{q}_c - \beta_c^*\rho_c}w_7, \quad w_6 = w_6 > 0, \quad w_7 = w_7 > 0,\\
&w_8 = \frac{\gamma_i}{\mu}w_4 + \frac{\phi_i}{\mu}w_6, \quad w_9 = \frac{\gamma_c}{\mu}w_5 + \frac{\phi_c}{\mu}w_7.
\end{aligned}
$$

To compute a left eigenvector $v = (v_1, v_2, \ldots, v_9)$, we analyze the equation system $v \cdot J(\mathbf{E}_{ic}^0) = 0$ to obtain:

$$
\begin{aligned}
&v_1 = v_8 = v_9 = 0, \quad v_2 = \frac{\rho_i}{\mathbf{p}_i}v_4 + \frac{\alpha_i}{\mathbf{p}_i}v_6, \quad v_3 = \frac{\rho_c}{\mathbf{p}_c}v_5 + \frac{\alpha_c}{\mathbf{p}_c}v_7,\\
&v_4 = \frac{\beta_i\alpha_i + \sigma_i\mathbf{p}_i}{\mathbf{p}_i\mathbf{q}_i - \beta_i\rho_i}v_6, \quad v_5 = \frac{\beta_c\alpha_c + \sigma_c\mathbf{p}_c}{\mathbf{p}_c\mathbf{q}_c - \beta_c^*\rho_c}v_7, \quad v_6 = v_6 > 0, \quad v_7 = v_7 > 0.
\end{aligned}
$$

We note that the variables w_6, w_7, v_6, and v_7 are unrestricted, provided that $\tilde{\mathcal{R}}_i^q = 1$. The assertion $\tilde{\mathcal{R}}_i^q = 1$ implies that all disease states are in a critical state. Consequently, we examine the behavior of the DFE under the following condition:

Remark 6.3

$$
\tilde{\mathcal{R}}^q = \max\{\tilde{\mathcal{R}}_c^q, \tilde{\mathcal{R}}_i^q\} = \max\{1, 1\} = 1. \tag{6.5}
$$

Assuming positive values for w_6, w_7, v_6, and v_7, we can see that w_4 and v_4 are nonnegative if $\mathbf{C}_1 = \mathbf{p}_i\mathbf{q}_i - \beta_i\rho_i > 0$. Similarly, w_5 and v_5 are nonnegative if $\mathbf{C}_2 = \mathbf{p}_c\mathbf{q}_c - \beta_c^*\rho_c > 0$. Therefore, the following conditions must hold:

$$
\mathbf{C}_1 > 0 \implies \frac{\mathbf{p}_i\mathbf{q}_i}{\rho_i} > \beta_i \text{ and } \mathbf{C}_2 > 0 \implies \frac{\mathbf{p}_c\mathbf{q}_c}{\rho_c} > \beta_c^*. \tag{6.6}
$$

Next, we need to determine the signs of bifurcation coefficients, a and b, using the following formula:

$$
a = \sum_{k,i,j=1}^{9} v_k w_i w_j \frac{\partial^2 f_k}{\partial x_i \partial x_j}(\mathbf{E}_{ic}^0) \text{ and } b = \sum_{k,i=1}^{9} v_k w_i \frac{\partial^2 f_k}{\partial x_i \partial \beta_c^*}(\mathbf{E}_{ic}^0) \tag{6.7}
$$

To simplify, we set all free variables to 1, yielding:

$$
\begin{aligned}
&a = a^+ - a^-,\\
&b = (z_2 + 1)\left(\frac{\alpha_c}{\mathbf{p}_c} + \frac{z_4\rho_c}{\mathbf{p}_c}\right) > 0.
\end{aligned} \tag{6.8}
$$

Here

$$
\begin{aligned}
a^+ =&\beta_i\eta_c^i\left(z_2\frac{\gamma_c}{\mu}+\frac{\phi_c}{\mu}\right)(z_1+1)+\beta_c^*\eta_i^c\left(z_1\frac{\gamma_i}{\mu}+\frac{\phi_i}{\mu}\right)(z_2+1),\\
a^- =&\left[(z_1+1)\left[\frac{{\beta_i}^2}{\mathbf{p}_i}\left(\frac{z_1{\beta_i}^2}{\mathbf{p}_i}+1\right)+\frac{\beta_c^*\beta_i}{\mathbf{p}_c}(z_2+1)+\beta_i\left(\frac{z_2\gamma_c}{\mu}+\frac{\phi_c}{\mu}\right)+\beta_i\left(\frac{z_1\gamma_i}{\mu}+\frac{\phi_i}{\mu}\right)\right.\right.\\
&\left.\left.+z_4z_2\beta_i\right]+(\beta_i\omega_i+2\beta_i)z_1+2z_1^2\beta_i+z_1\beta_i\,(z_2+1)+z_2^2\beta_i+3\,\beta_i\right]\left(\frac{\alpha_i}{\mathbf{p}_i}+z_3\frac{\rho_i}{\mathbf{p}_i}\right)\\
&+\left[(z_2+1)\left[\frac{\beta_c^*\beta_i}{\mathbf{p}_i}(z_1+1)+\frac{{\beta_c^*}^2}{\mathbf{p}_c}(z_2+1)+\beta_c^*\left(\frac{z_2\gamma_c}{\mu}+\frac{\phi_c}{\mu}\right)+\beta_c^*\left(\frac{z_1\gamma_i}{\mu}+\frac{\phi_i}{\mu}\right)\right.\right.\\
&\left.\left.+z_3z_1\beta_c^*\right]+(\beta_c^*\omega_c+2\,\beta_c^*)\,z_2+z_1\beta_c^*+4z_2^2\beta_c^*+z_2\beta_c^*\,(z_1+1)+\beta_c^*\right]\left(\frac{\alpha_c}{\mathbf{p}_c}+\frac{z_4\rho_c}{\mathbf{p}_c}\right),
\end{aligned}
\tag{6.9}
$$

where

$$
z_1=\frac{(\beta_i\rho_i+\mathbf{p}_i\tau_i)}{\mathbf{C}_1},z_2=\frac{\beta_c^*\rho_c+\mathbf{p}_c\tau_c}{\mathbf{C}_2},z_3=\frac{(\alpha_i\beta_i+\mathbf{p}_i\sigma_i)}{\mathbf{C}_1},z_4=\frac{(\alpha_c\beta_c^*+\mathbf{p}_c\sigma_c)}{\mathbf{C}_2}.
$$

Remark 6.4 Provided that the conditions in Equation(6.6) are met, then a^+ and a^- are non-negative. It follows that $a>0$ if and only if $a^+>a^-$.

We establish the following theorem regarding the System (6.2), highlighting its behavior concerning bifurcation:

Theorem 6.5 System (6.2) exhibits dual backward bifurcations near $\tilde{\mathcal{R}}_c^q=1$ and $\tilde{\mathcal{R}}_i^q=1$ if the following conditions are satisfied:

$$
\text{(a)}\quad \frac{\mathbf{p}_i\mathbf{q}_i}{\rho_i}>\beta_i,\quad \text{(b)}\quad \frac{\mathbf{p}_c\mathbf{q}_c}{\rho_c}>\beta_c^*,\quad \text{and}\quad \text{(c)}\quad a=a^+-a^->0. \tag{6.10}
$$

Dual bifurcation means that each pathogen in a two-pathogen system can independently undergo a bifurcation, potentially leading to a backward bifurcation for both pathogens under conditions in Equation (6.10).

6.4 Numerical simulation

In this section, we conduct numerical simulations to complement the theoretical findings.

6.4.1 Simulation for sub-critical coexistence

The simulation of Model (4.2) in the absence of co-infected individuals was carried out by first defining the various epidemiological parameters involved in the system and calculating the numbers of quarantine reproduction. Multiple initial conditions for the infected strain-i and strain-c populations were set. Using a forward Euler method, the state variables (susceptible, exposed, infected, quarantined, recovered) were iteratively updated over the simulation period. We created MATLAB code for this simulation and visualized the trajectories under two conditions:

full and partial cross-immunity, as depicted in Figure 6.1. Over time, the figure illustrates the potential outcomes of either the decline (in subplots (a) and (c)) or the persistence (in subplots (b) and (d)) of the strain with the lowest quarantine reproduction number.

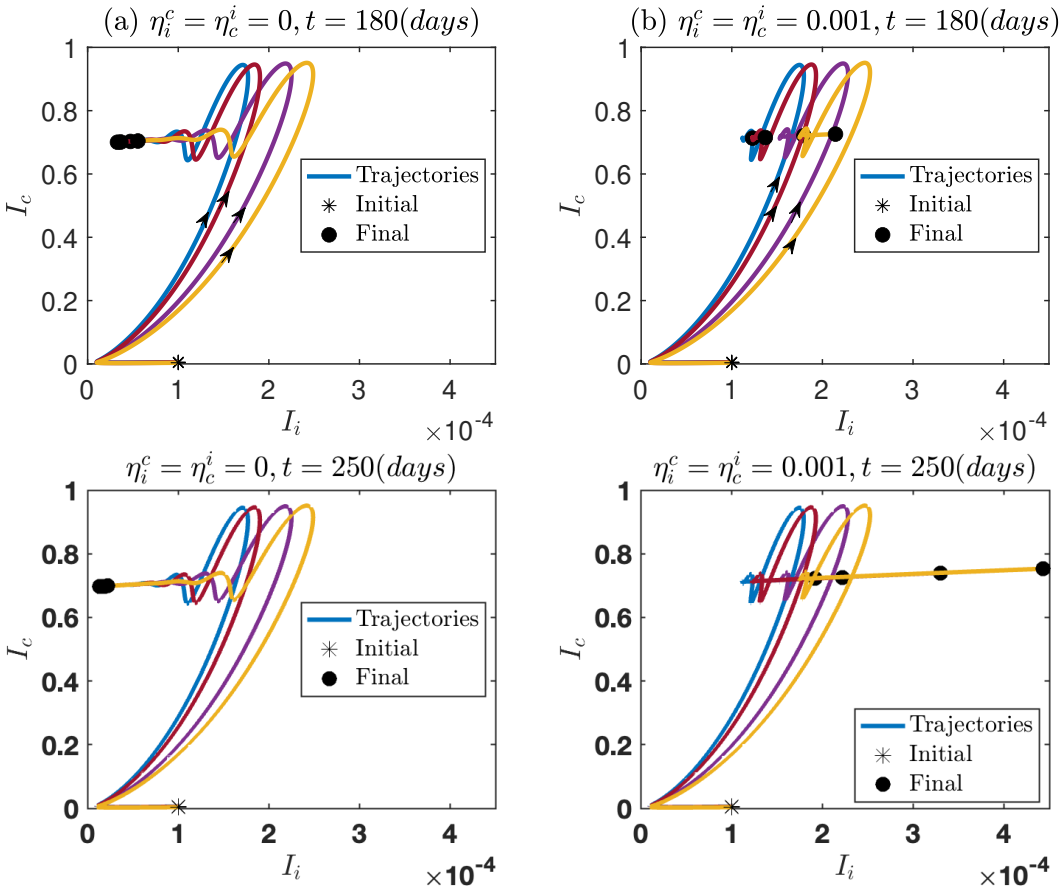

Figure 6.1: The visualization of sub-critical coexistence occurs when a specified condition, as outlined Item (ii) in Theorem 6.1 is satisfied, such that $\tilde{\mathcal{R}}_c^q = 1.24$ and $\tilde{\mathcal{R}}_i^q = 0.94$. The figures are column-wise described for the case of full cross-immunity ($\eta_c^i = \eta_i^c = 0$) and partial cross-immunity ($\eta_c^i = \eta_i^c = 0.001$). The parameter values used for generating these figures were: $\Lambda = \mu = 0.007$, $\beta_i = 0.5$, $\beta_c = 0.6$, $\omega_i = 0.2$, $\omega_c = 0.5$, $\rho_i = 0.03$, $\rho_c = 0.2$, $\alpha_i = 0.8$, $\alpha_c = 0.4$, $\sigma_i = 0.04$, $\sigma_c = 0.006$, $\tau_i = 0.0006$, $\tau_c = 0.04$, $\phi_i = 0.4$, $\phi_c = 0.6$, $\gamma_i = 0.2$, $\gamma_c = 0.25$, $\delta_i = 0.1$, and $\delta_c = 0.001$. The non-zero initial conditions were: $I_i(0) = 2 \times 10^{-4}$, $I_c(0) = [0.0035, 0.004, 0.005, 0.0055]$, and $S(0) = 1 - I_i(0) - I_c(0)$.

When the control reproduction number of one pathogen surpasses 1 while the other falls below 1, Figure 6.1 suggests that, with partial cross-immunity between strains, both pathogens can co-exist within the population without one completely displacing the other. This co-existence reflects complex interactions within the system. To explore these dynamics further, we analyze scenarios where the quarantine reproduction numbers for both pathogens exceed 1. In Figure 6.2, three cases are presented: In subplot (a), the full cross-immunity leads to the strain with the highest quarantine reproduction number dominating and driving the other to extinction. In subplots (b) and (c), with partial cross-immunity, more intricate dynamics emerge, including

the potential for multiple stable endemic equilibria and alternating dominance. These insights reveal how pathogens interact under varying levels of cross-immunity and highlight the impact of public health interventions on the long-term coexistence or control of both diseases.

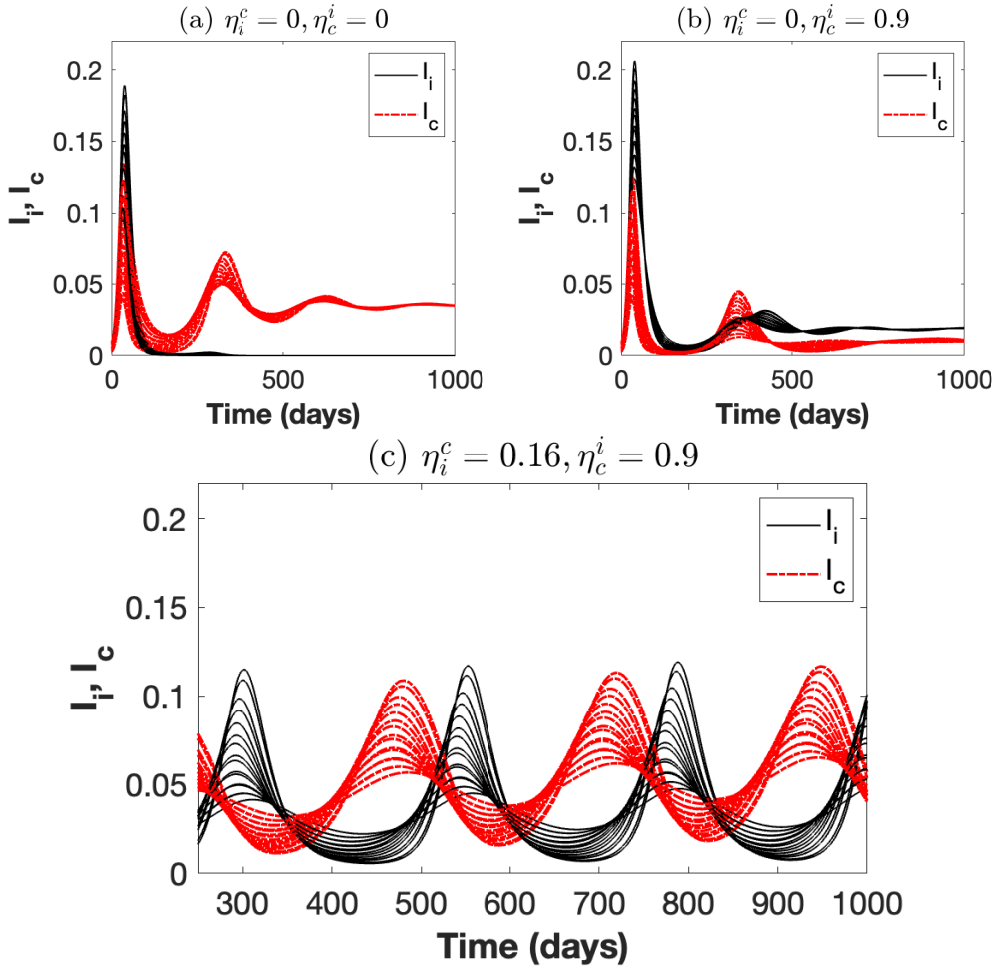

Figure 6.2: Pathogen dynamics under varying cross-immunity and initial conditions over time. (a) With full cross-immunity, the strain with the higher quarantine reproduction number dominates. (b) and (c) Partial cross-immunity leads to complex interactions, including coexistence and alternating dominance. The cross-immunity parameter values are indicated in each subplot title. Other parameters: $\Lambda = \mu = 0.002$, $\beta_i = 0.38$, $\beta_c = 0.28$, $\omega_i = 0.2$, $\omega_c = 0.5$, $\rho_i = 0.33$, $\rho_c = 0.43$, $\alpha_i = 0.06$, $\alpha_c = 0.05$, $\sigma_i = 0.005$, $\sigma_c = 0.001$, $\tau_i = 0.26$, $\tau_c = 0.34$, $\phi_i = 0.4$, $\phi_c = 0.16$, $\gamma_i = 0.12$, $\gamma_c = 0.07$, $\delta_i = 0.0001$, $\delta_c = 0.00001$.

6.4.2 Simulation of backward bifurcation

Building on the findings of Section 6.4.1, Theorem 6.1 demonstrates that Model (4.2) can accommodate both a disease-free equilibrium and up to four endemic equilibria, provided the conditions outlined in Remark 6.2 are met. Figure 6.3 illustrates these equilibria and reveals that each strain in the model can exhibit a backward bifurcation within specific parameter ranges. Specifically, when $\tilde{\mathcal{R}}_c^q \leq 1$, the strain-$i$ undergoes a backward bifurcation if $\tilde{\mathcal{R}}_i^{q*} < \tilde{\mathcal{R}}_i^q \leq 1$ (shown in the left

plot). In contrast, strain-c experiences a backward bifurcation when $\tilde{\mathcal{R}}_c^{q*} < \tilde{\mathcal{R}}_c^q \leq 1$ and $\tilde{\mathcal{R}}_i^q \leq 1$ (shown in the right plot). This behavior highlights a complex dynamic structure in which both strains can persist under certain conditions, emphasizing the critical role of quarantine measures in disease control. The critical quarantine reproduction numbers, $\tilde{\mathcal{R}}_i^{q*}$ and $\tilde{\mathcal{R}}_c^{q*}$, are key in determining the emergence and stability of these equilibria.

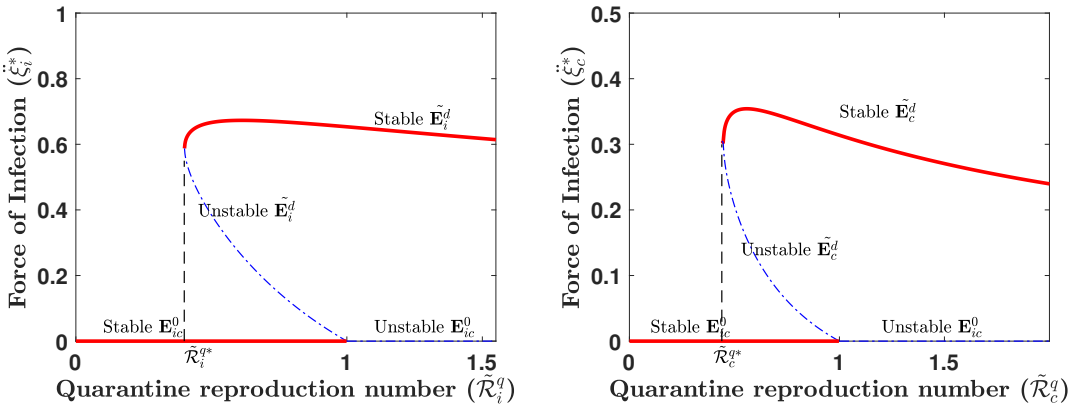

Figure 6.3: Visualization of backward bifurcation as conditions stated in Remark 6.2 are met. Here, $\tilde{\mathcal{R}}_i^{q*}$ and $\tilde{\mathcal{R}}_c^{q*}$ denote the critical quarantine reproduction numbers for $\tilde{\mathcal{R}}_i^q$ and $\tilde{\mathcal{R}}_c^q$, respectively. In the left plot: $\beta_i \in [0, 5]$ and $\beta_c = 1.5$ to ensure $\tilde{\mathcal{R}}_c^q \leq 1$, as outlined in item (i) in Remark 6.2. In the right plot: $\beta_c \in [0, 5]$ and $\beta_i = 2$ to ensure $\tilde{\mathcal{R}}_i^q \leq 1$, as specified in item (ii) in Remark 6.2. Other parameter values used: $\Lambda = \mu = 0.9$, $\omega_i = 0.7$, $\omega_c = 0.8$, $\rho_i = 0.3$, $\rho_c = 0.4$, $\alpha_i = 0.1$, $\alpha_c = 0.6$, $\sigma_i = 0.4$, $\sigma_c = 0.2$, $\tau_i = 0.01$, $\tau_c = 0.06$, $\phi_i = 0.14$, $\phi_c = 0.08$, $\gamma_i = 0.16$, $\gamma_c = 0.28$, and $\delta_i = \delta_c = 0.0001$.

The bifurcation plots shown in Figure 6.3 are based on a parameterized system. Figure 6.4 presents bifurcation diagrams depicting the dynamics of a complete two-strain disease system (Model 6.2), illustrating the phase portraits of the susceptible population $S(t)$ versus the populations of infected strains $I_c(t)$ and strain $I_i(t)$ for different initial conditions. Each subplot visualizes the system's evolution over time, highlighting the stability of equilibrium points under varying initial conditions. The analysis focuses on conditions near critical thresholds, where the quarantine reproduction numbers of the two strains ($\tilde{\mathcal{R}}_c^q$ and $\tilde{\mathcal{R}}_i^q$) approach 1. The condition $\tilde{\mathcal{R}}_c^q = 1$ implies that the strain-c is at a critical point where it can persist or be eradicated, depending on small changes in the system. Similarly, when $\tilde{\mathcal{R}}_i^q = 1$, strain-$i$ can remain endemic, but small perturbations could push the system toward eradication or persistence of the strain. This sensitivity to initial conditions underscores the complexity of the system and its potential for diverse outcomes.

The subplots (in Figures 6.4 and 6.5) reveal the presence of stable equilibria, both in disease-free and endemic scenarios. The disease-free equilibrium ($\tilde{\mathbf{E}}_{ic}^0 = (S^0, I_i^0, I_c^0) = (1, 0, 0)$) represents a scenario in which there are no infections and the entire population remains susceptible. In contrast, the strain-i endemic equilibrium ($\tilde{\mathbf{E}}_i^d$) at $(\tilde{S}, \tilde{I}_i^d, \tilde{I}_c^d) = (0.9747, 0.0007, 0)$ and the strain-c endemic equilibrium ($\tilde{\mathbf{E}}_c^d$) at $(\tilde{S}, \tilde{I}_i^d, \tilde{I}_c^d) = (0.9928, 0, 0.0003)$ indicate stable conditions where one strain remains endemic while the other is eradicated. Furthermore, the co-existence endemic equilibrium ($\tilde{\mathbf{E}}^*$) in $(\tilde{S}^*, \tilde{I_i}^*, \tilde{I_c}^*) = (0.9749, 0.0004, 0.0005)$ in Figure 6.4 shows that both infec-

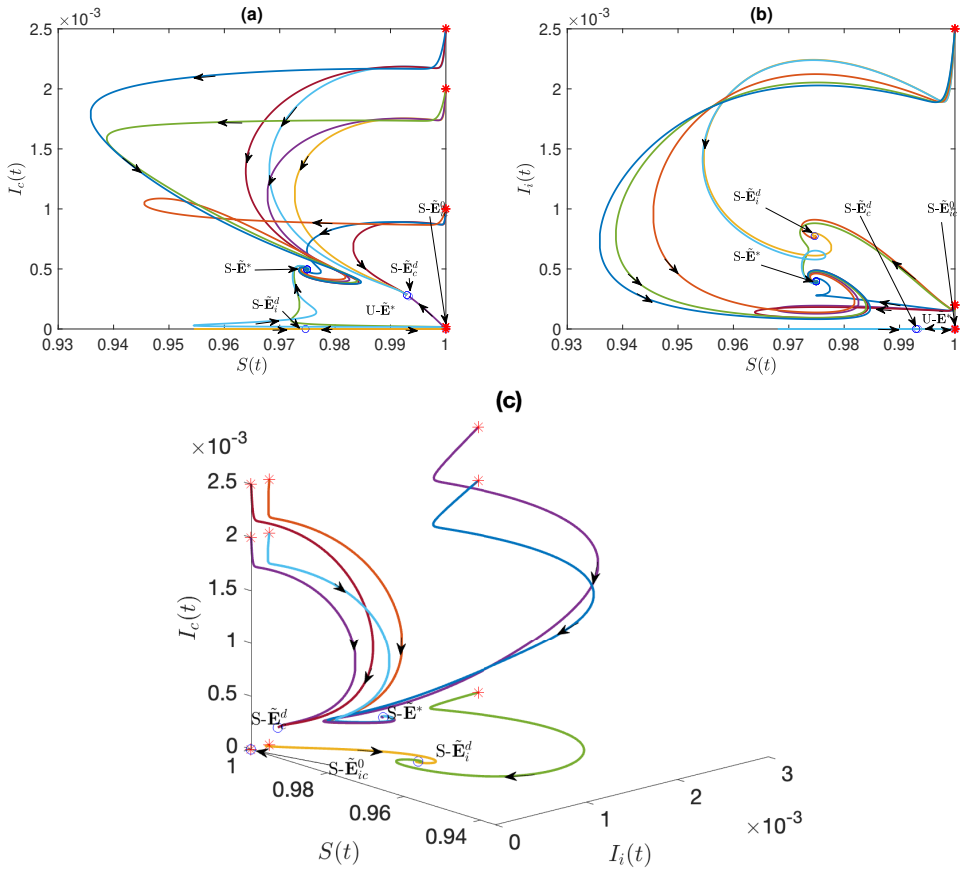

Figure 6.4: Bifurcation diagrams illustrating phase portraits of the susceptible population $S(t)$ versus the infected populations $I_c(t)$ (subplot (a)), $I_i(t)$ (subplot (b)), and both $I_c(t)$ and $I_i(t)$ (subplot (c)) for various initial conditions: $I_i(0) = [0, 0.0002, 0.0025]$ and $I_c(0) = [0, 0.001, 0.002, 0.0025]$. Trajectories begin at red stars and end at blue circles, with stable (S) and unstable (U) equilibrium points marked. In both subplots, the conditions outlined by Equation (6.10) in Theorem 6.5 are satisfied. The system is governed by key epidemiological parameters: $\Lambda = \mu = \frac{1}{365}$, $\beta_i = 0.1468$, $\beta_c = 0.07950$, $\rho_i = \frac{1}{3}$, $\rho_c = \frac{1}{2.3}$, $\alpha_i = 0.058$, $\alpha_c = 0.04$, $\gamma_i = 0.12$, $\gamma_c = 0.07$, $\omega_i = 0.2$, $\omega_c = 0.5$ $\eta_i^c = 0.9$ and $\eta_c^i = 0.1$.

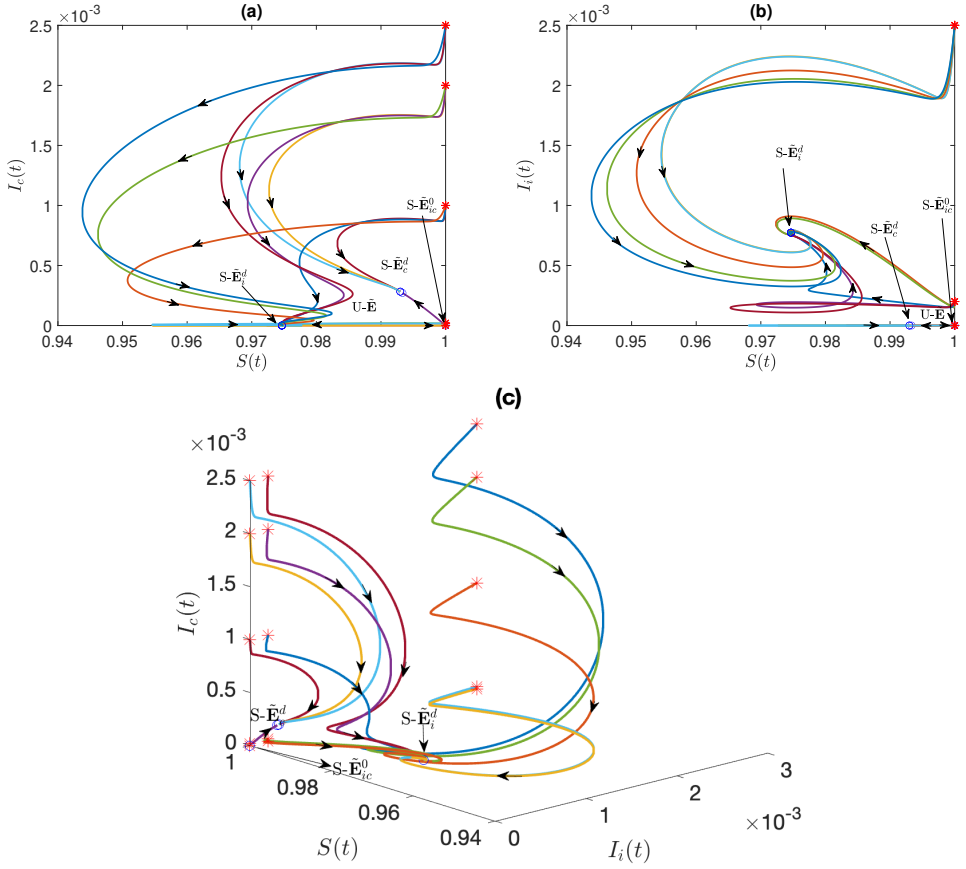

Figure 6.5: Bifurcation diagrams displaying the phase portraits of susceptible individuals versus infected populations, $I_c(t)$ and $I_i(t)$, under the assumption of full immunity ($\eta_i^c = \eta_c^i = 0.0$). The parameters and conditions are consistent with those in Figure 6.4.

tions can co-exist at low levels, with neither strain dominating completely. It is crucial to note that in the system simulated in Figure 6.4, the population had partial cross-immunity, allowing for the continued circulation and interaction of both strains. This partial protection meant that neither strain could fully eradicate the other, leading to the possibility of an endemic co-existence equilibrium, where both strains could co-exist at low levels in the population. However, as described in Figure 6.5, with full cross-immunity ($\eta_i^c = 0.0$ and $\eta_c^i = 0.0$), such co-endemic scenarios are no longer possible and the system tends to stabilize at separate endemic equilibria or a disease-free state.

6.5 Discussion

This chapter explores the dynamics of disease transmission between two pathogens, focusing on scenarios where cross-immunity is present and at least one quarantine reproduction number falls below one. Our findings reveal that if any component of $\tilde{\mathcal{R}}^q$ exceeds one, the model predicts endemic behavior, indicating that the disease persists in the population. In particular, when co-infection is absent and full cross-protection ($\eta_i^c = \eta_c^i = 0$) is in place, the system exhibits subcritical co-existence. This occurs when one quarantine reproduction number is above one, while the other remains below. These results align with previous studies by Andreasen et al. [5], Martcheva et al. [88] and Nuño et al. [96], which also considered pathogens that share the same hosts. Notably, Nuno et al. emphasized that even when one strain's reproductive number is less than one, subthreshold co-existence remains possible. Andreasen et al. argued that the likelihood of co-existence increases when the two diseases differ in virulence and transmission rates. Similarly, Fudolig et al. [50] demonstrated that coexistence can occur in multistrain models even without cross-immunity, with the original and emergent strains co-existing if the new strain's quarantine reproduction number is lower than the original. Martcheva et al. [88] also highlighted that strains can coexist when only one of the quarantine reproduction numbers exceeds one, suggesting that a highly virulent strain can coexist with a less virulent one.

An illustrative example of subcritical co-existence endemic equilibrium can be seen in the co-circulation of influenza and COVID-19. Influenza typically follows a seasonal pattern, with higher transmission rates during the colder months [54]. Even during the ongoing COVID-19 pandemic, influenza continues to circulate seasonally, albeit at reduced levels due to less stringent control measures. Cross-immunity from previous influenza exposure [2] may offer some protection against COVID-19, altering the dynamics of both viruses. In this context, the higher virulence and transmissibility of COVID-19 can result in its persistence and dominance, while influenza continues to circulate at lower levels, highlighting the interaction between the two pathogens.

Furthermore, Theorem 6.5 outlines a critical threshold at which the system's behavior undergoes a qualitative shift, potentially allowing for the coexistence of multiple equilibrium states. If these conditions are not satisfied, the system stabilizes with at least one endemic equilibrium. The key terms in the backward bifurcation condition in Equation (6.6) -such as ρ_i, ρ_c, $1/\mathbf{p}_i$, $1/\mathbf{p}_c$, $1/\mathbf{q}_i$, and $1/\mathbf{q}_c$ - represent the rate of symptom development, the duration of the exposed period, and the duration of the infected period. The ratios $\frac{\rho_i}{\mathbf{p}_i \cdot \mathbf{q}_i}$ and $\frac{\rho_c}{\mathbf{p}_c \cdot \mathbf{q}_c}$ quantify the probability of individuals developing symptoms after exposure to strain-i and strain-c, respectively, reflecting the probability of transitioning to a symptomatic state. In contrast, $\frac{\mathbf{p}_i \cdot \mathbf{q}_i}{\rho_i}$ and $\frac{\mathbf{p}_c \cdot \mathbf{q}_c}{\rho_c}$ represent the

probability of remaining asymptomatic, indicating exposure to the pathogen without showing clinical symptoms.

Conditions $\mathbf{p}_i \cdot \mathbf{q}_i/\rho_i > \beta_i$ and $\mathbf{p}_c \cdot \mathbf{q}_c/\rho_c > \beta_c$ emphasize the need to account for asymptomatic transmission in disease modeling and control strategies. Asymptomatic individuals can still contribute to the spread of infection, playing a crucial role in maintaining transmission within the population. These findings are consistent with previous studies [1, 7, 100], which highlight the importance of asymptomatic carriers in disease dynamics and the unique challenges they present to control efforts.

The results obtained in Figures 6.4 and 6.5 have important implications for understanding and managing multi-strain epidemics. The presence of stable endemic equilibria, $\tilde{\mathbf{E}}^*$ for both strains suggests that, in populations with partial cross-immunity, both infections can persist and coexist at low levels, leading to the possibility of recurrent outbreaks. Partial immunity prevents one strain from fully eradicating the other, which implies that prior exposure to one strain may not fully protect against the other (see Figure 6.4). However, when complete cross-immunity is present, the system tends to stabilize in a disease-free equilibrium or separate endemic equilibria, reducing the probability of simultaneous outbreaks, as shown in Figure 6.5. These findings, obtained near critical quarantine reproduction number thresholds, highlight the role of cross-immunity in shaping disease dynamics and stress the need for comprehensive public health strategies that account for multi-strain interactions. Effective disease control measures, including quarantine, should be designed to manage the quarantine reproduction numbers from both strains to prevent endemicity or promote eradication.

7 Linking the Age-stratified Model with Data

7.1 Introduction

In this chapter, we shift from the theoretical framework discussed in earlier chapters to its practical application in real-world scenarios. Until now, our focus has been on the structure and potential of the model, without going into specific diseases or age groups. We will now demonstrate how this model can be applied to two major contemporary infectious diseases, influenza and COVID-19. The analysis and results discussed here are presented in [48].

7.2 Background

The global outbreak of COVID-19 marked the beginning of a challenging period for public health systems around the world. At the same time, seasonal influenza remained a significant health threat, particularly in temperate regions like Germany. The simultaneous circulation of these two respiratory viruses raised concerns about their potential interactions and their impact on public health resources. Understanding the interplay between influenza and COVID-19 is essential for developing effective control strategies and mitigating their combined burden on healthcare systems [90].

Unlike the predictable seasonal nature of influenza, which typically peakes during the winter months [22], COVID-19 has been characterized by multiple waves of infection driven by new variants of the virus [108], leading to variable transmission rates and outcomes over time. The dynamics of the COVID-19 pandemic have been influenced by factors such as public health interventions, vaccination campaigns, and changes in viral properties [15]. As these diseases share similarities in their transmission routes, primarily through respiratory droplets [119], understanding the individual and combined impacts of these two respiratory viruses is critical to developing effective public health strategies and ensuring that healthcare systems can handle the dual burden of influenza and COVID-19.

The interaction between co-circulating pathogens can occur due to shared host populations, cross-immunity [4], competition for ecological niches [94], or co-infections [137]. Previous studies have examined these dynamics, highlighting the potential for competitive exclusion or co-existence, depending on various factors such as infection rates, immune responses, and public health interventions as we have discussed in Chapter 2. Understanding these dynamics in the context of influenza and COVID-19 is essential to predict outbreak patterns and optimize control measures.

Moreover, by analyzing influenza and COVID-19 co-circulating, understanding the role of age

is crucial for developing effective public health strategies. Age-specific modeling plays a critical role in understanding the transmission dynamics and impact of respiratory infections in different age groups [109]. These models integrate demographic data with disease-specific parameters to predict age-specific susceptibility, severity of illness, and healthcare resource needs [40]. Previous applications have demonstrated the utility of age-specific modeling within the SIR (Susceptible-Infected-Recovered) framework to capture heterogeneity in disease transmission and outcomes, reflecting differences in contact patterns, susceptibility, and health outcomes between age groups [107].

Focusing on age-related vulnerability, COVID-19 has shown significant differences in how the disease affects various age groups. Some studies, such as [78, 109] investigate age-specific transmission dynamics, noting that contact patterns significantly influence transmission rates. The latter find that children and young adults have different contact patterns compared to older adults, affecting the transmission dynamics[109]. Meanwhile, Lee and Raszka (2020) indicate that children, although susceptible to infection, are less likely to be significant transmission drivers compared to adults [78]. Further studies emphasize the differential impacts of COVID-19 between age groups. Atchison et al. (2023) examine long-term symptoms of COVID, showing that younger populations experience significant long-term effects despite older adults being at higher risk of severe initial illness [8]. Wang et al. (2020) and Levin et al. (2020) focus on the severe outcomes faced by elderly populations, highlighting higher hospitalization and mortality rates, longer recovery times, and greater complications, thus emphasizing the need for targeted protective measures for older individuals [79, 127].

However, influenza affects various age groups differently, with significant implications for both morbidity and mortality. Thompson et al. (2003) provided a comprehensive review of national influenza surveillance data, revealing that children and the elderly are particularly vulnerable to severe outcomes, including higher hospitalization and mortality rates during the influenza seasons [124]. Gagnon et al. (2013) further explore age-specific patterns by examining historical and contemporary pandemics, showing that children are often the main spreaders of influenza, while young adults and the elderly suffer more severe effects [51]. Recent studies, such as Wu et al. (2022), have highlighted the need for an age-specific model to improve understanding of influenza dynamics and improve public health responses, ensuring that control measures are effectively tailored to the varying impacts across different age groups [136].

As discussed in Section 1.1.1, quarantine and other non-pharmaceutical interventions (NPIs) have proven to be effective in controlling infectious disease outbreaks, as demonstrated by measures such as lockdowns, travel restrictions, and social distancing during the COVID-19 pandemic. In addition to NPIs, the partial cross-immunity between influenza and COVID-19 - arising from previous infections or vaccinations - plays a key role in shaping the dynamics of these diseases. Cross-immunity can reduce susceptibility to one virus after infection by another, potentially affecting the transmission and severity of both diseases [56, 96]. As highlighted in Section 1.1.2, evidence suggests that previous influenza or coronavirus infections can activate T cells that also target SARS-CoV-2, aiding in virus control [57]. Previous flu infections or vaccinations can enhance the immune response to SARS-CoV-2 [60], and some studies indicate that flu vaccines could reduce the severity of COVID-19, although this is not yet conclusively proven [41]. Furthermore,

previous SARS-CoV-2 infections may influence how the body reacts to other respiratory viruses such as the flu [26]. In general, the interaction between influenza and COVID-19 is complex and requires further research.

Regarding co-infections, a review by [74], which included studies from Asia, Europe, and the Americas, found 749 cases of respiratory viral infections among patients with COVID-19. The global prevalence of these co-infections was 5.01%, with influenza viruses (1.54 %) and enteroviruses (1.32%) being the most common according to 56 studies. They concluded that, although COVID-19 is still widespread, co-infections with a respiratory virus are relatively low. For example, a clinical case in Germany involved a 4-month-old child coinfected with SARS-CoV-2 and influenza A, highlighting the importance of accurate diagnosis and treatment [129]. Similar patterns have been observed in other countries, with two cases in the United States [71], four in Spain [27], and more than ten cases in China [142]. In addition, there were remarkably few reports of other co-infections such as influenza-RSV (respiratory syncytial virus) and Rhinovirus-SARS-CoV-2 [14] between 2020 and 2022. This indicates that although co-infections are present, they are not very common, so it makes sense to focus our analysis on broader trends in viral circulation.

The objective of this chapter is to comprehensively analyze the interactions between influenza and COVID-19 in Germany from January 2020 to December 2022. By incorporating infection data and employing both age-specific and overall SEIQR models, we aim to provide valuable insights into the competitive dynamics and partial cross-immunity between these two pathogens. The refined and validated model, grounded in real-world data, seeks to enhance our understanding of pathogen interactions, inform targeted public health interventions, and offer a clear, replicable framework for future research, ultimately aiding in the effective management of co-circulating respiratory viruses.

7.3 Methodology

This section describes the data sources, model formulation, and analysis techniques. The study uses epidemiological data to develop and calibrate an age-stratified multi-strain model that captures transmission dynamics between age groups. The analysis includes computing the age-specific control reproduction number, performing global sensitivity analysis, and applying data preprocessing techniques to ensure accurate model fitting.

7.3.1 Data source

We utilized officially reported data on SARS-CoV-2 and influenza infections from the Robert Koch Institute, Germany's national health authority [68]. The age distribution of the German population was derived from data provided by the Federal Statistical Office of Germany [53]. This classification captures the critical stages of human development and health, allowing targeted public health analyses and interventions [68]. The dataset includes weekly age-specific reports of SARS-CoV-2 and influenza infections, covering the period from the first week of 2020 to the last week of 2022. Table 7.1 presents a summary of the total infections reported for SARS-CoV-2 and influenza by age group. The time frame in the table provides a basis for examining the long-term effects of COVID-19 on influenza patterns, including potential changes in immunity

Table 7.1: Age distribution and new cases from the first week of 2020 to the last week of 2022, covering the development and administration of COVID-19 vaccines [28]. This period allows assessment of various measures influenced COVID-19 and influenza interactions, including cross-immunity effects.

j	Age of participants (a_j)	Number of Participants (new cases)		Total
		Influenza data	Covid-19 data	
1	0-4 years	44348	1015561	1059909
2	5-14 years	95847	4471306	4567153
3	15-34 years	114777	10940785	11055562
4	35-59 years	117369	14550028	14667397
5	60-79 years	52056	4896335	4948391
6	80+ years	25635	1509503	1535138
	Total	441532	37283918	37725450

and disease prevalence. It also sheds light on how populations have adapted to ongoing public health challenges over time. We chose the period from 2020 to 2022 for the model, including influenza and COVID-19, because it encompasses critical phases of both pandemics, offering a comprehensive view of their interactions. Although the epidemics of influenza and COVID-19 peaked at different times - COVID-19 surged in early 2020 while influenza saw suppression due to public health measures - they overlapped enough to allow for the study of their combined impact on healthcare systems and population health. Sentinel surveillance data highlights these differences, with influenza activity being unusually low during 2020-2021, while COVID-19 cases were high, reflecting the differing dynamics during these years [68]. This period provides a unique opportunity to analyze the interaction between these viruses under varying public health conditions.

Furthermore, we incorporated comprehensive influenza data from 2018 to 2019 to provide a baseline before the pandemic for comparison. Including these data strengthens the analysis by offering essential context for assessing influenza trends before and during the COVID-19 pandemic. This approach improves the formulation of our model, as discussed in Sections 1.1.1 and 1.1.2, allowing a more comprehensive evaluation of the interaction between influenza and SARS-CoV-2.

7.3.2 Age-stratified multi-strain model

In Model (4.2), excluding the compartments for co-infections (E_{ic}, I_{ic}, Q_{ic}, and R_{ic}), each remaining compartment is subdivided into six distinct subcompartments to represent different age groups, as described in Table 7.1. As a result, the total population N_T at any time t consists of fifty-four compartments, which can be expressed as:

$$N_T = \sum_{j=1}^{6} S^{a_j} + \sum_{j=1}^{6} E_i^{a_j} + \sum_{j=1}^{6} E_c^{a_j} + \sum_{j=1}^{6} I_i^{a_j} + \sum_{j=1}^{6} I_c^{a_j} + \sum_{j=1}^{6} Q_i^{a_j} + \sum_{j=1}^{6} Q_c^{a_j} + \sum_{j=1}^{6} R_i^{a_j} + \sum_{j=1}^{6} R_c^{a_j}.$$

For each pathogen-i, pathogen-c, and each age group a_j, we define the number of people in each compartment at time t in Table 7.2. The system of ordinary differential equations (ODEs) is thoroughly detailed in Equation (7.1), capturing the rate of change in the number of individuals within each compartment over time t for $j = 1$. This dynamic process is further illustrated in

Notation	Intepretation
	Represents the number of ...
$S^{a_j}(t)$	susceptible individuals in the age group a_j at time t
$E_i^{a_j}(t)$	individuals in the age group a_j who are exposed to pathogen-i at time t
$E_c^{a_j}(t)$	individuals in the age group a_j who are exposed to pathogen-c at time t
$I_i^{a_j}(t)$	individuals in age group a_j who are infectious with pathogen-i at time t
$I_c^{a_j}(t)$	individuals in age group a_j who are infectious with pathogen-c at time t
$Q_i^{a_j}(t)$	individuals in age group a_j quarantined at time t due to pathogen-i infection
$Q_c^{a_j}(t)$	individuals in age group a_j quarantined at time t due to pathogen-c infection
$R_i^{a_j}(t)$	individuals in age group a_j recovered from pathogen-i at time t
$R_c^{a_j}(t)$	individuals in age group a_j recovered from pathogen-c at time t
$N_T^{a_j}(t)$	of all individuals in each age group a_j at time t
$N_T(t)$	of all individuals in all age groups at time t

Table 7.2: Model variables at time t. The age group a_j where $j = 1, 2, \cdots, 6$ are given in Table 7.1

Figure 7.1, with all parameters defined in Table 7.5.

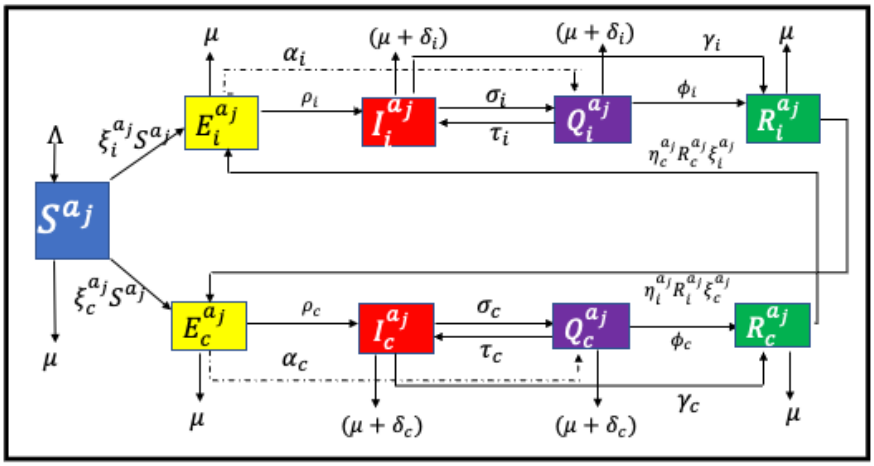

Figure 7.1: Flowcharts depicting the dynamics of a two-strain system within each age group, beginning with age group 1 ($a_{j=1}$). Similar structures are employed for $j = 2, 3, \cdots, 6$, with the exception that there is no inflow rate into the susceptible group.

$$
\begin{aligned}
S'^{a_j}(t) =& \Lambda - \xi_i^{a_j}(t)S^{a_j}(t) - \xi_c^{a_j}(t)S^{a_j}(t) - \mu S^{a_j}(t),\\
E_i'^{a_j}(t) =& \xi_i^{a_j}(t)S^{a_j} + \eta_c^i R_c^{a_j}(t)\xi_i^{a_j}(t) - (\alpha_i + \rho_i + \mu)E_i^{a_j}(t),\\
E_c'^{a_j}(t) =& \xi_c^{a_j}(t)S^{a_j}(t) + \eta_i^c R_i^{a_j}(t)\xi_c^{a_j}(t) - (\alpha_c + \rho_c + \mu)E_c^{a_j}(t),\\
I_i'^{a_j}(t) =& \rho_i E_i^{a_j}(t) + \tau_i Q_i^{a_j}(t) - (\gamma_i + \sigma_i + \delta_i + \mu)I_i^{a_j}(t),\\
I_c'^{a_j}(t) =& \rho_c E_c^{a_j}(t) + \tau_c Q_c^{a_j}(t) - (\gamma_c + \sigma_c + \delta_c + \mu)I_c^{a_j}(t),\\
Q_i'^{a_j}(t) =& \alpha_i E_i^{a_j}(t) - (\phi_i + \tau_i + \delta_i + \mu)Q_i^{a_j}(t) + \sigma_i I_i^{a_j}(t),\\
Q_c'^{a_j}(t) =& \alpha_c E_c^{a_j}(t) - (\phi_c + \tau_c + \delta_c + \mu)Q_c^{a_j}(t) + \sigma_c I_c^{a_j}(t),\\
R_i'^{a_j}(t) =& \phi_i Q_i^{a_j}(t) + \gamma_i I_i^{a_j}(t) - \eta_i^c R_i^{a_j}(t)\xi_c^{a_j}(t) - \mu R_i^{a_j}(t),\\
R_c'^{a_j}(t) =& \phi_c Q_c^{a_j}(t) + \gamma_c I_c^{a_j}(t) - \eta_c^i R_c^{a_j}(t)\xi_i^{a_j}(t) - \mu R_c^{a_j}(t).
\end{aligned}
\tag{7.1}
$$

As detailed in the model formulation and its basic properties (Section 4.2), the model approaches 1 in the long run. This indicates that the system will eventually stabilize, reflecting a steady-state behavior under the given assumptions and parameters. The vectors $\xi_c(t) = (\xi_c^{a_1}(t), \xi_c^{a_2}(t), \cdots, \xi_c^{a_6}(t))'$ and $\xi_i(t) = (\xi_i^{a_1}(t), \xi_i^{a_2}(t), \cdots, \xi_i^{a_6}(t))'$ represent the force of infection rates for COVID-19 and influenza, respectively. Each function predicts the expected number of new infections caused by an infectious individual in a population per unit of time. At a specific age group a_j, the expressions for the terms $\xi_i^{a_j}(t)$ and $\xi_c^{a_j}(t)$ incorporate interactions between distinct age groups within the population and are expressed as follows:

$$
\begin{aligned}
\xi_i^{a_j}(t) &= \sum_{l=1}^{6} c_i^{a_{jl}} \beta_i^{a_j}(t)\Big[I_i^{a_j}(t) + \Omega_i Q_i^{a_j}(t)\Big],\\
&\text{and}\\
\xi_c^{a_j}(t) &= \sum_{l=1}^{6} c_c^{a_{jl}} \beta_c^{a_j}(t)\Big[I_c^{a_j}(t) + \Omega_c Q_c^{a_j}(t)\Big].
\end{aligned}
\tag{7.2}
$$

In Equation (7.2), the terms enclosed in square brackets represent individuals actively transmitting the infection. To incorporate the assumption of imperfect quarantine, we introduce scaling factors Ω_i and Ω_c to denote the effectiveness of quarantine measures in reducing, albeit not completely eliminating, the risk of transmission. Hence, Ω_i and Ω_c are bound within the range $(0, 1]$. The terms $\beta_i^{a_j}(t)$ and $\beta_c^{a_j}(t)$ signify time-dependent transmission probabilities per contact for influenza and SARS-CoV-2, respectively, in age group a_l induced by an infected individual of age a_j (Note: j can be equal to l). Additionally, the formula:

$$
c_k^{a_{jl}} = \frac{M_{a_{jl}}}{N^{a_j}} \quad \text{where } k = i \text{ or } c \tag{7.3}
$$

computes the contact rate matrix or mixing coefficient for age group a_j interacting with age group a_l, with k representing either influenza (i) or SARS-CoV-2 (c). The social contact matrix $M_{a_{jl}}$, shown in Figure 7.2, represents the average daily contacts between age groups. Derived from POLYMOD data for Germany [91], it quantifies interaction patterns essential for modeling disease transmission. The heatmap in Figure 7.2 visualizes these interactions, with the x-axis showing initiating age groups and the y-axis representing their counterparts. The six age categories correspond to those in Table 7.1. Darker shades indicate higher interaction frequency, while the diagonal pattern highlights the tendency for individuals to interact more within their own

age group. These contact patterns play a crucial role in understanding the spread of infections across different demographic groups.

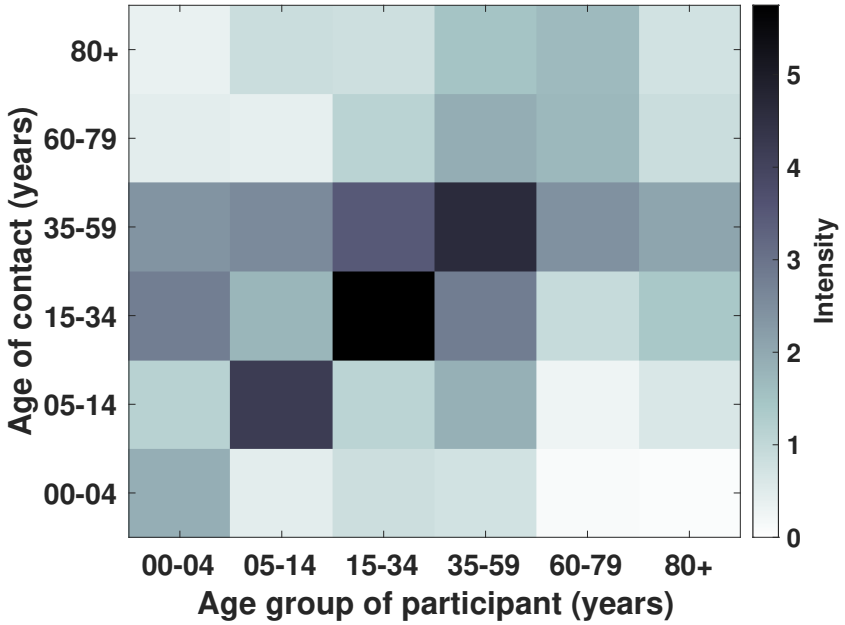

Figure 7.2: Heatmap of interaction intensity between age groups in Germany, as reported by [91]. Participants are shown on the x-axis and their contacts on the y-axis. Darker color indicate higher interaction intensities.

7.3.3 Model analysis and fitting

Age-specific control reproduction number

The control reproduction number $\tilde{\mathcal{R}}^q$ is determined using the next-generation method, as described in Section 3.4.2. For the model (7.1), which includes infected compartments $E_i, E_c, I_i, I_c, Q_i, Q_c$ across age groups $j = 1, 2, \ldots, 6$, the age-specific control reproduction numbers for COVID-19 ($\tilde{\mathcal{R}}_c^{a_j}$) and influenza ($\tilde{\mathcal{R}}_i^{a_j}$) are computed by finding the spectral radius (largest eigenvalue) of the respective blocks of the next generation matrix $\mathbf{K}$:

$$\begin{aligned}\tilde{\mathcal{R}}_c^{a_j} &= \left(\frac{\beta_c^{a_j}(t)c^{a_jl}(t)(\alpha_c\mathbf{q}_c + \rho_c\sigma_c + \alpha_c\tau_c + \mathbf{r}_c\rho_c)}{\mathbf{p}_c((\gamma_c + \delta_c + \mu)\mathbf{r}_c + (\phi_c + \delta_c + \mu)\sigma_c)}\right) S^{a_j}(t),\\ \tilde{\mathcal{R}}_i^{a_j} &= \left(\frac{\beta_i^{a_j}(t)c^{a_jl}(t)(\alpha_i\mathbf{q}_i + \rho_i\sigma_i + \alpha_i\tau_i + \mathbf{r}_i\rho_i)}{\mathbf{p}_i((\gamma_i + \delta_i + \mu)\mathbf{r}_i + (\phi_i + \delta_i + \mu)\sigma_i)}\right) S^{a_j}(t).\end{aligned} \tag{7.4}$$

These expressions provide the age-specific reproduction numbers for each age group a_j. Here

$$\begin{aligned}\mathbf{p}_i &= \alpha_i + \rho_i + \mu, \quad & \mathbf{q}_i &= \gamma_i + \sigma_i + \delta_i + \mu, \quad & \mathbf{r}_i &= \phi_i + \tau_i + \delta_i + \mu,\\ \mathbf{p}_c &= \alpha_c + \rho_c + \mu, \quad & \mathbf{q}_c &= \gamma_c + \sigma_c + \delta_c + \mu, \quad & \mathbf{r}_c &= \phi_c + \tau_c + \delta_c + \mu.\end{aligned}$$

By evaluating the age-specific quarantine reproduction numbers for both COVID-19 and influenza, $\tilde{\mathcal{R}}_c^{a_j}$ and $\tilde{\mathcal{R}}_i^{a_j}$, we assess the expected number of secondary cases generated by an infected individual in each age group, taking into account the control measures in place, such as

quarantine and isolation, across different age groups. Finally, we determine the overall control reproduction number $\tilde{\mathcal{R}}^q$ as the maximum of all age-specific quarantine reproduction numbers for both COVID-19 and influenza:

$$\tilde{\mathcal{R}}^q = \max\{\tilde{\mathcal{R}}_c^{a_j}, \tilde{\mathcal{R}}_i^{a_j} \text{ for all } j\}.$$

This provides a measure of the worst-case potential for disease spread under current control measures across different age groups. If $\tilde{\mathcal{R}}^q$ exceeds 1, it indicates that despite control measures, the disease could continue to spread. Conversely, if it is less than 1, it suggests that the control measures are effective in reducing the spread of the diseases below the threshold where an outbreak could be sustained.

Global sensitivity analysis

An important methodological technique for modeling that helps find the aspects that most affect the outcome of the models is global sensitivity analysis (GSA). GSA techniques have been widely used in epidemiological modeling research to measure the uncertainty of the model between input and output. For example, [95] use the Pearson correlation to capture the impacts of individual parameters and their interactions, whereas [83, 135] utilizes the Sobol sensitivity technique, an alternative GSA method. The Sobol indices are measures used in sensitivity analysis to quantify the contribution of each input variable to the variance of the output of a model [114].

In this section, we apply the Sobol sensitivity technique to the generalized model, concentrating on the important parameters listed in Table 7.5. Through a methodical manipulation of these variables over their potential domains, GSA evaluates the resilience of our model's forecasts and pinpoints the most consequential variables. Furthermore, GSA sheds light on parameter interactions by providing a thorough understanding of how many adjustments might impact the behavior of the model [62, 113, 114]. Recognizing the sensitivity of partial cross-immunity between COVID-19 and influenza parameters can aid in forecasting disease trends and developing management plans. We have included a detailed information on our methods in Appendix 7.A.

After analyzing identifying factors that can be kept constant within their range of variation without altering the variability in pathogen dynamics, in the next section, we delve into the crucial steps of model calibration and data analysis, essential for ensuring the accuracy and reliability of our computational model.

Data pre-processing

The initial stage of data fitting involved managing missing values and rectifying inconsistencies tailored to each data set related to the pathogens, ensuring data integrity. The use of histograms to visualize the distributions provided insight into the spread of data and facilitated the identification of notable patterns or outliers. Following this, a variety of transformation techniques, including logarithmic, square root, and power transformations, were applied to normalize the distribution of data and mitigate the impact of outliers or skewedness. This comprehensive pre-processing phase laid a solid foundation, contributing to the reliability and robustness of subsequent modeling analyses.

Model fitting

The compartmental model was initialized with parameters and fitted to normalized data using the least squares optimization method, utilizing parameter sets sampled from the Sobol analysis. In cases where transformed variables failed to achieve normality, a non-parametric approach was adopted. This involved generating 10,000 bootstrapped samples to estimate the median and confidence intervals, following the methodology outlined by Efron and Tibshirani (1994) [35]. Furthermore, the significance of differences between estimated parameters was evaluated using statistical tests such as the t test or the Mann-Whitney U test, with a significance level set at 0.05 to determine if there were statistical disparities between the means or medians of the compared groups, respectively.

7.4 Findings

This section presents the key results derived from the analysis, focusing on sensitivity analysis, model fitting, and epidemiological insights.

Table 7.3: Sensitivity indices for two output variables, I_i and I_c, individually and collectively, with respect to different input factors. OVI stands for the output variable of interest.

	OVI$= I_i$		**OVI** $= I_c$		**OVI** $= (I_i + I_c)$	
Input factors	$\mathbf{SI}_i^{P_i}$	$\mathbf{SI}_{tot}^{P_i}$	$\mathbf{SI}_i^{P_i}$	$\mathbf{SI}_{tot}^{P_i}$	$\mathbf{SI}_i^{P_i}$	$\mathbf{SI}_{tot}^{P_i}$
$P_1 \equiv c$	0.004	0.044	0.002	0.034	0.004	0.046
$P_2 \equiv \Lambda$	0.000	0.000	0.000	0.000	0.000	0.000
$\vdots \equiv \mu$	0.000	0.000	0.000	0.000	0.000	0.000
Ω_c	0.000	0.000	0.000	0.002	0.000	0.001
Ω_i	0.001	0.008	0.000	0.000	0.000	0.003
β_c	0.012	0.086	0.836	0.936	0.491	0.600
β_i	0.819	0.932	0.005	0.046	0.318	0.408
α_c	0.000	0.000	0.000	0.006	0.000	0.003
α_i	0.000	0.007	0.000	0.000	0.000	0.002
ρ_c	0.002	0.015	0.023	0.062	0.016	0.047
ρ_i	0.013	0.042	0.000	0.020	0.008	0.036
γ_c	0.000	0.001	0.005	0.014	0.003	0.008
γ_i	0.002	0.006	0.000	0.001	0.001	0.003
σ_c	0.001	0.001	0.005	0.013	0.004	0.008
σ_i	0.000	0.001	0.000	0.000	0.001	0.001
δ_c	0.000	0.000	0.000	0.000	0.000	0.000
δ_i	0.000	0.000	0.000	0.000	0.000	0.000
ϕ_c	0.000	0.001	0.002	0.009	0.001	0.005
ϕ_i	0.003	0.011	0.000	0.001	0.001	0.005
τ_c	0.000	0.005	0.000	0.000	0.000	0.002
τ_i	0.000	0.000	0.000	0.010	0.000	0.005
$\vdots \equiv \eta_c^i$	0.005	0.038	0.000	0.001	0.002	0.015
$P_{23} \equiv \eta_i^c$	0.000	0.002	0.001	0.025	0.001	0.015
Sum	0.861	1.198	0.877	1.180	0.849	1.211

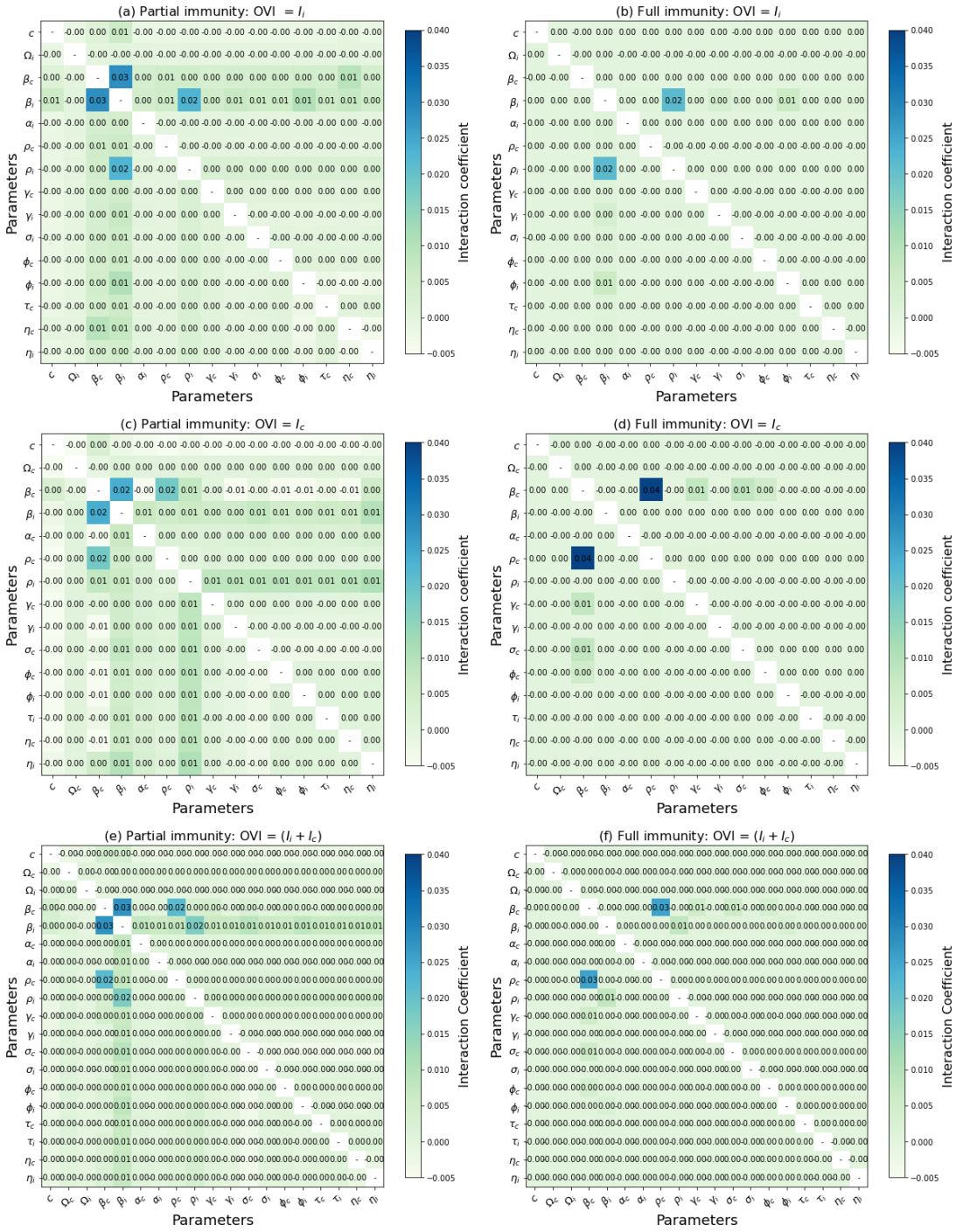

Figure 7.3: Visualization of parameter interactions in infection output variance using a symmetric matrix. Parameters with no interaction, as indicated in Table 7.3, have been omitted. '-' indicates no self-interaction, while positive (negative) coefficients denote positive (inverse) interactions between parameters and output variance.

7.4.1 Output of sensitivity analysis

Table 7.3 highlights β_i and β_c as the most influential parameters within the system. Specifically, β_i contributes 81.9% to the variance of I_i, while β_c contributes 83.6% to the variance of I_c. When considering the combined effect of I_i and I_c, β_i and β_c contribute 31.8% and 49.1%, respectively. Furthermore, marginal influences are observed, such as the effect of β_c on the variance of I_i contributing 1. 2% and the effect of β_i on the variance of I_c contributing 0.5%, attributed to cross-immunity. Depending on the output variable of interest, c, Ω_c, Ω_i, α_c, α_i, ρ_c, ρ_i, γ_c, γ_i, σ_c, σ_i, ϕ_c, ϕ_i, τ_c, τ_i, η_c^i and η_i^c have minimal or no direct influence on either I_i or I_c, but their interactions with other parameters can significantly amplify their impact. In contrast, Λ, μ, δ_c, and δ_i show no direct influence on I_i, I_c, or $I_i + I_c$, and lack significant interactions with other parameters. Thus, they can be identified as common non-influential factors within the model.

In Figure 7.3, we show the interaction between two input factors that influence the outputs I_i, I_c, and $I_i + I_c$. In particular, the interaction between β_i and β_c remains significant, with values of 0.03 and 0.02, particularly in the case of partial cross-immunity, as shown in subplots (a), (c) and (e). Positive values indicate that simultaneous increases in β_i and β_c result in higher levels of I_i, I_c, and $I_i + I_c$. However, in subplots (b), (d), and (f), which assume full cross-immunity, no interaction is observed between β_i and β_c, suggesting that the two factors no longer influence each other under these conditions. Furthermore, interactions such as (β_i, ρ_i) and (β_c, ρ_c) have a comparable significance to the first-order effects of β_i and β_c, showing a substantial impact on the variance of the output. These interactions remain significant even under full cross-immunity conditions.

7.4.2 Fitted model and estimated parameters

We fitted our model to real-world data using parameter sets from sensitivity analysis. This method includes both single- and dual-pathogen models, using age-specific parameters to account for differences in how diseases spread and affect various age groups. The estimated parameters for single-pathogen models help us to understand how each pathogen spreads on its own. This is important for accurately expanding the model to handle interactions between two pathogens, such as competition or co-existence. For example, in subplot (a) of Figure 7.4, each pathogen is modeled separately, and the fit closely matches the observed data. In contrast, in subplot (b), where both pathogens are modeled together, influenza peaks early but then decreases, while COVID-19 becomes more dominant. Although influenza increases slightly toward the end (as observed in subplot (A) Figure 1.2), its numbers remain lower than COVID-19, showing that influenza has overtaken it, as seen in the transition dynamics between the two strains described in Figure 7.9. Furthermore, compared to a model that combines all age groups, our age-specific model shows improved precision in fitting the data, as demonstrated in the Figure subplot 7.4 (c).

Table 7.4 presents the transmission probability parameters (β_i and β_c) estimated for both the single pathogen and multipathogen models. The distributions of these parameters across various time periods and age groups are depicted in Figures 7.5 and 7.6. Specifically, Figure 7.5 illustrates the distribution of transmission parameters (β_i and β_c) for the single pathogen model in different age groups, showing variations within each group. The mean values are highlighted, and the p-values of the t test indicate the significance of the differences between the strains, providing

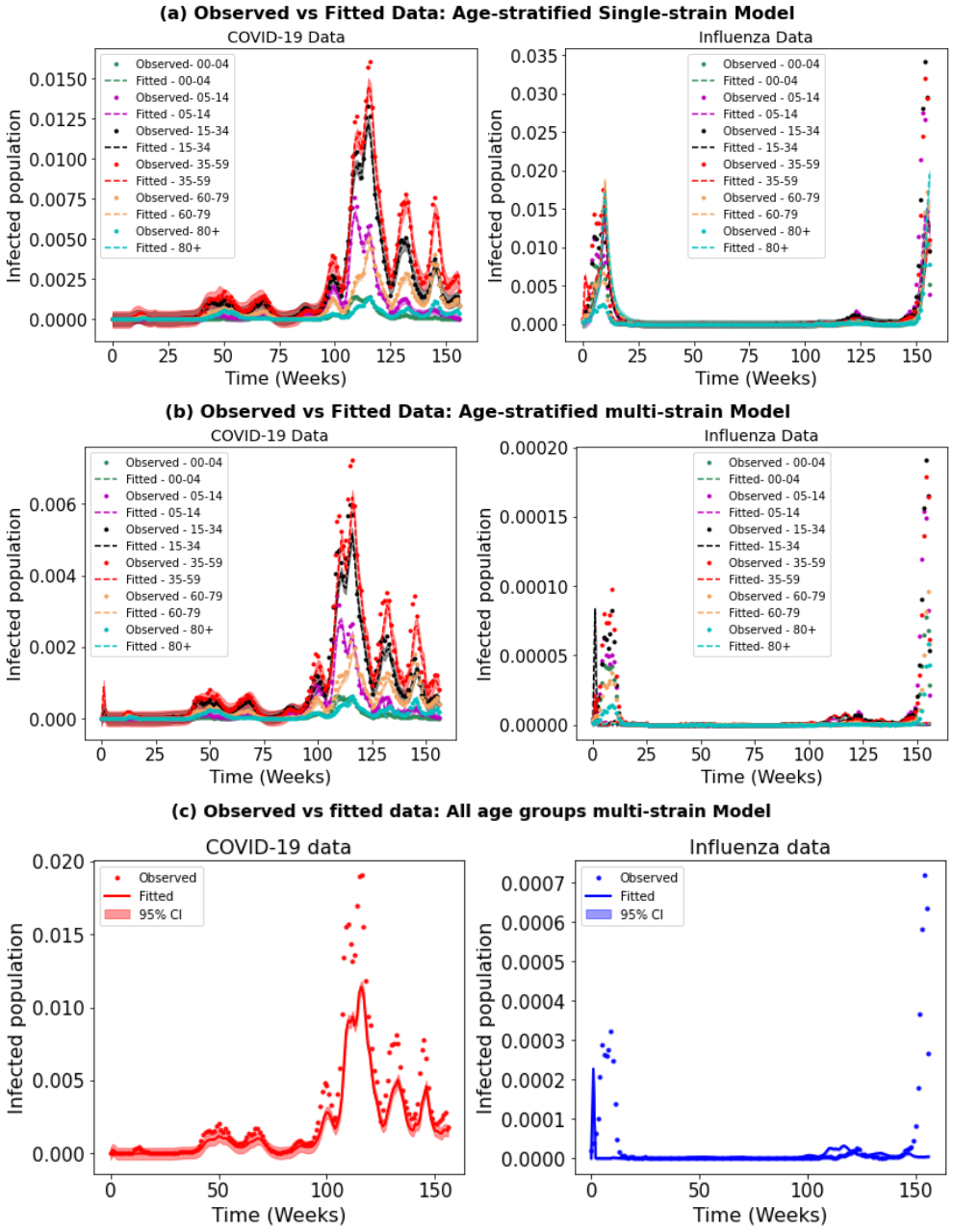

Figure 7.4: Assessing the adequacy of the SARS-CoV-2 and Influenza models by comparing their fit to observed data. The bandwidth illustrates the 95% confidence intervals for the fitted data. On the X-axis, '0' corresponds to the first week of 2020, while '157' indicates the final week of 2022.

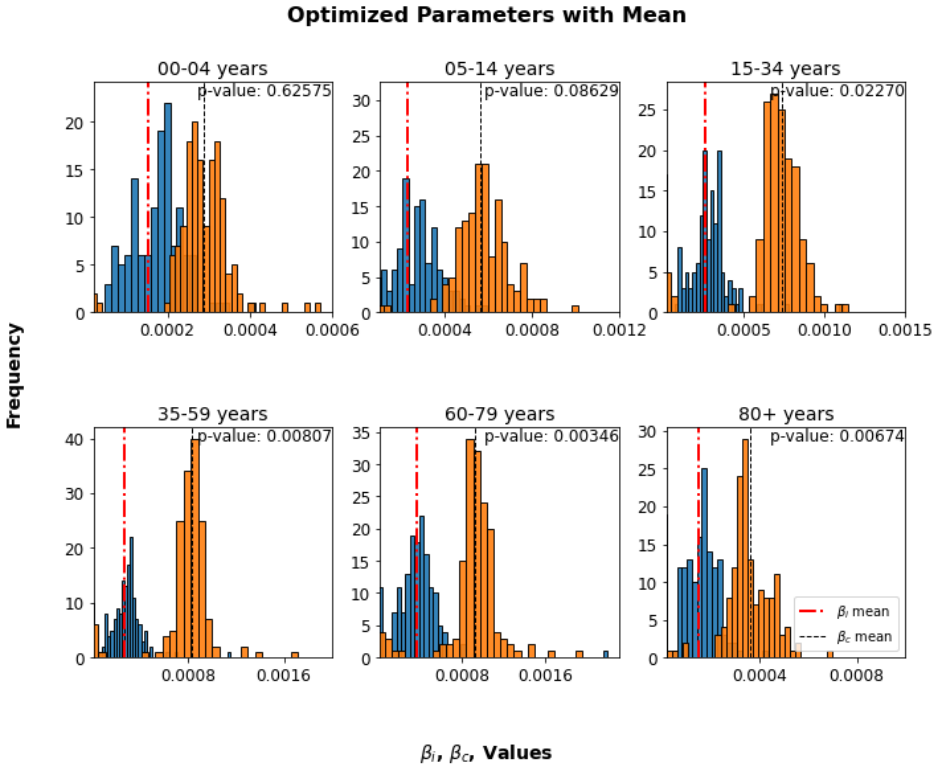

Figure 7.5: Histograms of single-strain model optimized parameters (β_i in blue, β_c in orange) with mean values indicated by dashed-dotted and dashed lines. T-test p-values are included to illustrate differences in transmission dynamics between strains within the same age group. The x-axis represents parameter values, and the y-axis shows frequency.

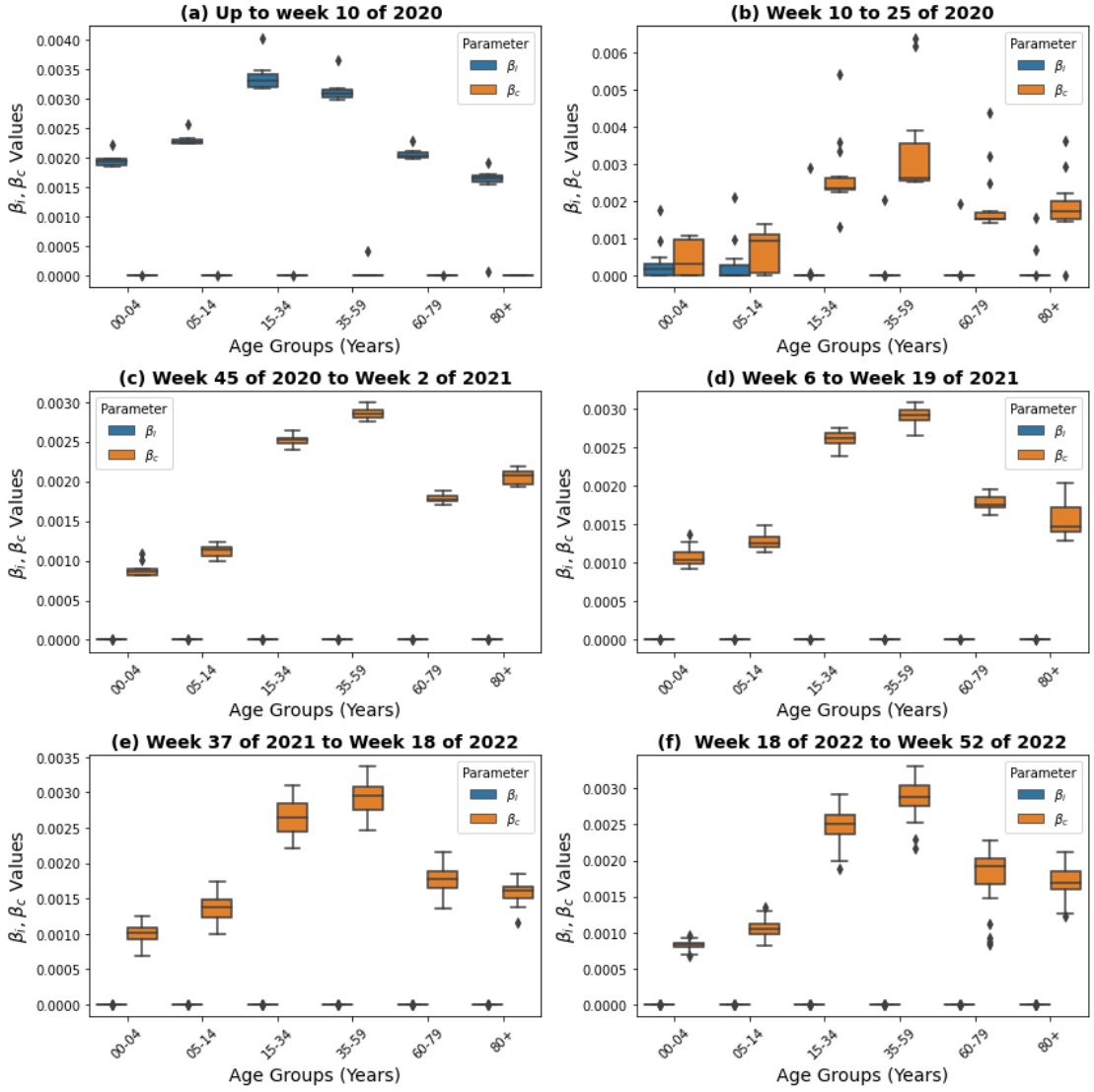

Figure 7.6: Boxplots of β_i and β_c values across age groups in a multi-strain model for each pandemic wave. Each subplot represents a time interval from the first (a) to the sixth and seventh waves (f). The central line in each box is the median, the box represents the interquartile range (IQR), and whiskers extend to 1.5 times the IQR from the box edges, with outliers shown as points.

Table 7.4: The estimated parameters include mean and standard error values for β_i and β_c in the single strain model, and median values along with confidence intervals for β_i and β_c in the multi-strain model.

Single-strain model			
Age (years)	β_i **Mean(SE)**	β_c **Mean(SE)**	**P-values**
0-4	$1.5\times10^{-4}(7.8\times10^{-6})$	$2.8\times10^{-4}(8.2\times10^{-6})$	0.6257
5-14	$2.2\times10^{-4}(1.3\times10^{-5})$	$5.6\times10^{-4}(1.5\times10^{-5})$	0.0862
15-34	$2.5\times10^{-4}(1.1\times10^{-5})$	$7.3\times10^{-4}(2.3\times10^{-5})$	0.0227
35-59	$2.8\times10^{-4}(1.0\times10^{-5})$	$8.3\times10^{-4}(2.8\times10^{-5})$	0.0080
60-79	$3.7\times10^{-4}(1.7\times10^{-5})$	$9.3\times10^{-4}(2.9\times10^{-5})$	0.0034
80+	$1.5\times10^{-4}(8.3\times10^{-6})$	$3.6\times10^{-4}(1.2\times10^{-5})$	0.0067
Multi-strain model			
Age (years)	β_i **Median (CI)**	β_c **Median (CI)**	**P-values**
0-4	$6.2\times10^{-12}(2.3\times10^{-12}\text{-}1.5\times10^{-11})$	$0.0009(8.7\times10^{-4}\text{-}9.7\times10^{-4})$	< 0.0001
5-14	$1.9\times10^{-13}(2.7\times10^{-14}\text{-}4.8\times10^{-13})$	$0.0014(1.2\times10^{-3}\text{-}1.5\times10^{-3})$	< 0.0001
15-34	$3.5\times10^{-15}(1.4\times10^{-16}\text{-}1.8\times10^{-14})$	$0.0024(2.3\times10^{-3}\text{-}2.5\times10^{-3})$	< 0.0001
35-59	$2.7\times10^{-15}(1.5\times10^{-16}\text{-}1.2\times10^{-14})$	$0.0028(2.7\times10^{-3}\text{-}2.9\times10^{-3})$	< 0.0001
60-79	$1.2\times10^{-13}(1.4\times10^{-14}\text{-}7.3\times10^{-13})$	$0.0024(2.3\times10^{-3}\text{-}2.5\times10^{-3})$	< 0.0001
80+	$1.0\times10^{-13}(5.2\times10^{-15}\text{-}4.5\times10^{-13})$	$0.0012(1.1\times10^{-3}\text{-}1.2\times10^{-3})$	< 0.0001

information on how transmission dynamics vary between pathogens and among demographics of age. The findings illustrated in Figure 7.6 shed light on the dynamics of the estimated infection probability rates for both influenza (β_i) and COVID-19 (β_c) in the multipathogen model over a specified time frame. In subplot (a), during the initial phase of the simulation until week 10 of 2020, the median transmission rates of influenza (β_i) remain relatively consistent between age groups, ranging from approximately 1.7×10^{-3} to 3.2×10^{-3}. These values suggest a moderate to high probability of influenza infections in all age groups, with slightly higher transmission rates observed in the age groups 15-34 and 35-59 compared to others. In contrast, the median transmission rates for COVID-19 (β_c) are considerably lower between all age groups during this period, ranging from approximately 1.7×10^{-16} to 7.4×10^{-13}. These values indicate a very low probability of COVID-19 infections, with transmission rates nearly negligible, especially in the 00-04 and 05-14 age groups.

From week 10 to 25 of 2020 (as described in 7.6 subplot (b)), older age groups (05-14, 15-34, 35-59, 60-79, 80+) exhibit lower median influenza infection probability rates compared to the youngest age group, 00-04. The age group 00-04 shows a median transmission rate of approximately 0.0001671, with a confidence interval ranging from 8.33×10^{-8} to 0.0003237. In contrast, for COVID-19 transmission, the 00-04 age group now shows the lowest median transmission rate among all age groups, approximately 0.0003176. However, similar to influenza, the wide confidence interval indicates considerable uncertainty regarding the actual transmission rate within this age group. Generally, the median values for COVID-19 (β_c) show an increase compared to the previous period, ranging from approximately 0.3×10^{-3} to 1.7×10^{-3} across different age groups. Data for week 45 of 2020 to week 52 of 2022 (as shown in subplots 7.6 (c) to (f)) under-

score the increased prevalence of COVID-19 compared to influenza, with COVID-19 exhibiting higher median values and greater certainty in estimates across different age groups. This increase suggests a higher probability of COVID-19 infections during this period, with the highest transmission rates observed in the age groups 15-34 and 35-59. In particular, the confidence intervals for the median values are relatively narrow, indicating more precise estimates compared to the probabilities of influenza transmission.

Estimated number of secondary cases

Utilizing Equation (7.4), estimations of secondary cases associated with specific age groups for each pathogen are provided weekly (see Figures 7.7 and 7.8). These results highlight the different transmission dynamics of influenza and COVID-19 between age groups. In the first week of 2020, no cases of COVID-19 were reported, which aligns with the absence of any recorded secondary cases. In contrast, Influenza exhibited its highest estimated number of quarantine reproductions in the age group 05-14 at 2.31, suggesting potential transmission to approximately 2.31 individuals within the same age group per infected individual. Subsequent transmission rates for other age groups that interact with individuals in the same age group were: 15-34 (2.05), 00-04 (2.00), 35-59 (1.98), 60-79 (1.45) and 80 + (0.65). In Week 10, the estimated number of influenza quarantine reproduction in various age groups was significantly lower, with values ranging from 0.01 to 0.46. In contrast, for COVID-19, the highest estimated number of quarantine reproduction was observed in the 35-59 age group (3.53), followed by the 15-34 age group (2.72), the 60-79 age group (1.92), the 05-14 age group (1.80), the 80 + age group (0.42) and the 00-04 age group (0.30). In Week 13, the estimated number of influenza quarantine reproductions remained consistently low, below 0.2 for most age groups. However, for COVID-19, there was a decrease compared to the previous week, with values ranging from 0.12 to 1.82 across different age groups.

In subsequent selected weeks, ranging from Week 50 of 2020 through Week 41 of 2022, which marks the peak week of other pandemic waves, patterns similar to Figure 7.7 are observed. Throughout these weeks, the highest number of quarantine reproductions is consistently observed in the 35-59 age group, indicating a greater transmission potential within this demographic. However, there is notable variation in the dynamics of interaction within other age groups, suggesting nuanced transmission patterns between different phases of the pandemic. During this period, the dynamics of influenza transmission shows the highest values in the 05-14 age group, followed by the 35-59 and 60-79 age groups, with their values consistently remaining below one (1) in different age groups. This suggests that while some transmission occurs, it remains relatively low in most demographics during this time frame (see Figure 7.8).

7.4.3 Dominance and extinction

Figure 7.9 illustrates the time-dependent infection rates (β_i for influenza and β_c for COVID-19), accompanied by their 95% confidence intervals (CI) shown as shaded regions for each age group. These infection rates were derived from a multipathogen model, providing a detailed comparison of how the transmission patterns of influenza and COVID-19 evolved over time, while accounting for the uncertainties of the estimate. The results shown in Figure 7.9 clearly show a shift from influenza dominance in early 2020 to the rise of the prevalence of COVID-19 in subsequent months. Influenza activity remained consistently low for the remainder of the

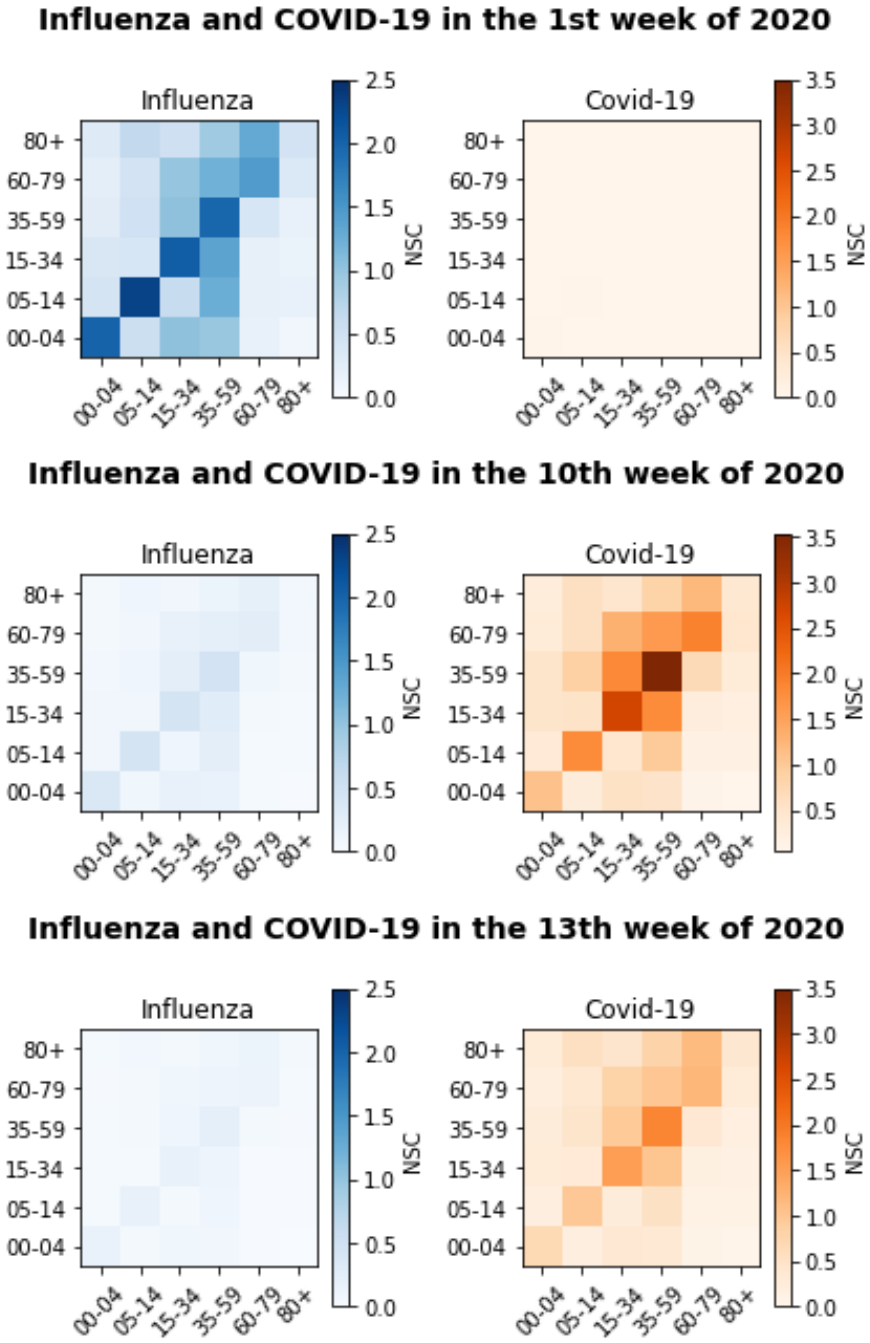

Figure 7.7: Quarantine reproduction number for both Influenza and COVID-19 across different age groups during the initial COVID-19 wave at selected weeks. The x-axis represents the age of individuals (years), while the y-axis represents the age of secondary cases (years). NSC: Number of secondary cases.

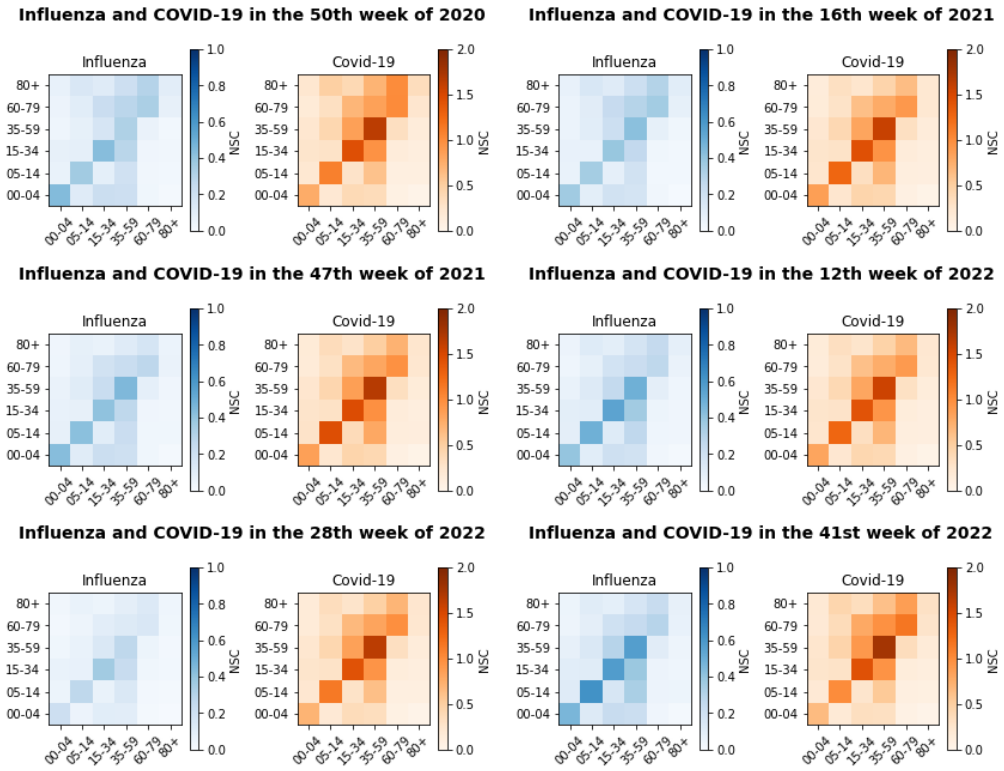

Figure 7.8: Estimates of quarantine reproduction number for Influenza and COVID-19 across age groups during peak weeks from the second to seventh waves. X-axis: Age of individuals (years), Y-axis: Age of secondary cases (years). NSC: Number of secondary cases.

period, while COVID-19 transmission persisted with fluctuating intensity. This trend reflects the dynamic epidemiological landscape during the pandemic, highlighting the importance of sustained monitoring and adaptable public health measures to manage both COVID-19 and influenza outbreaks. The progression of infection rates underscores the complex interaction between these respiratory viruses, highlighting the critical need for targeted proactive strategies to mitigate the impact of seasonal and pandemic outbreaks.

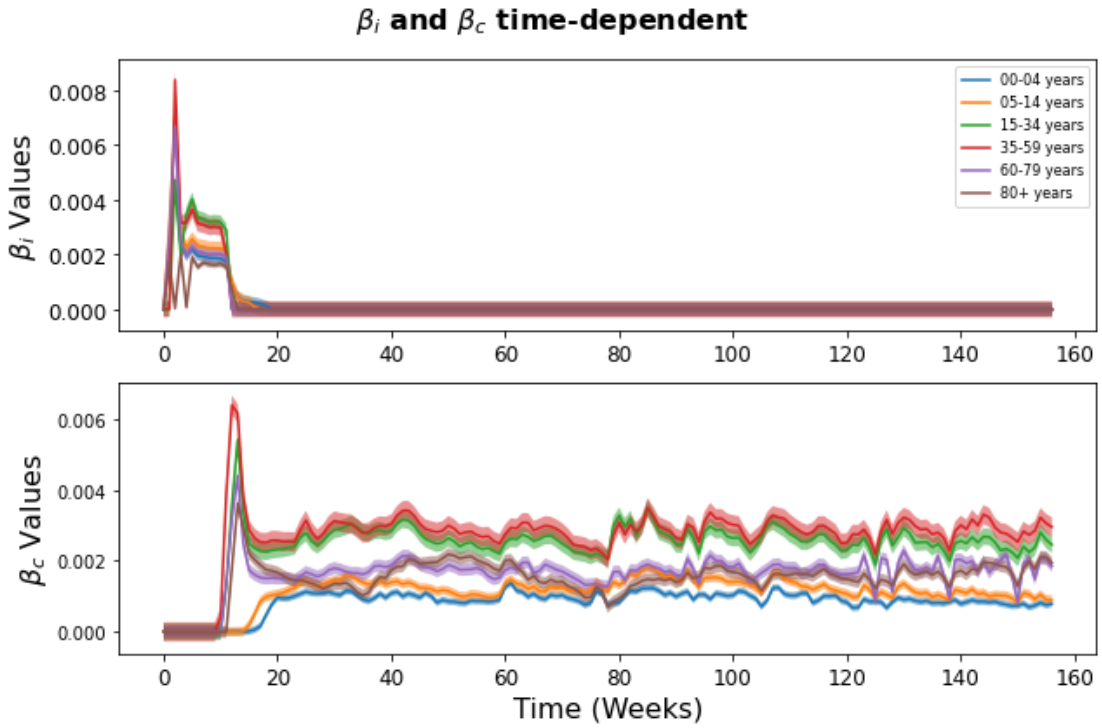

Figure 7.9: Time-dependent estimates of the parameters β_c and β_i in the multi-pathogen model. The X-axis represents time, with '0' marking the first week of 2020 and '157' indicating the final week of 2022. The shaded areas represent the 95% confidence intervals for the parameter estimates.

7.5 Discussion

This chapter investigates the co-existence dynamics of influenza and SARS-CoV-2 using a mathematical model incorporating age-specific parameters. By performing sensitivity analysis and fitting the model to real-world data using sampled parameter sets, we explore transmission patterns and susceptibility variations across different age groups and pandemic waves. The results highlight the importance of age-specific factors in understanding disease dynamics and provide insight into the impact of interactions between key parameters on disease transmission.

Sensitivity analysis emphasizes the critical influence of β_i and β_c on the dynamics of influenza (I_i) and COVID-19 (I_c) infections, respectively, highlighting their substantial role in explaining variations in infection levels and underscoring their importance in understanding disease spread. Furthermore, the complexity of the model is increased by the effects of other parameters and

their interactions, with some factors having minimal direct impact but potentially magnifying their influence through interactions with key parameters. In particular, the interaction between influenza (β_i) and SARS-CoV-2 (β_c) transmission rates remains a key determinant, especially in scenarios involving partial cross-immunity. This aligns with findings from Nuño et al. (2005) [96], who used a $SIRD$ model to investigate the effects of partial cross-immunity on the spread of two co-circulating influenza strains. Their results suggested that partial cross-immunity could result in complex epidemic dynamics, including oscillations in the prevalence of each strain and potential coexistence. Fome et al. (2024) [45] found that robust cross-immunity, where exposure to one strain provides strong protection against the other, reduces susceptibility to the second strain, leading to a dominant peak reflecting the primary outbreak. However, weak cross-immunity increases the likelihood of multiple-strain coexistence, potentially resulting in overlapping or merged peaks. These findings suggest that when there is some degree of immune overlap between diseases, the interaction between their transmission rates becomes a crucial factor in determining the overall dynamics of infection.

Our model fitting to real data revealed that the age-structured model effectively captured the dynamics of both influenza and COVID-19, surpassing the combined model of all age groups (see Figure 7.4). This underscores the importance of integrating age-related factors into epidemic modeling, given their significant influence on disease transmission dynamics, severity patterns, and long-term trends. When comparing the age-structured single and multi-strain models (Table 7.4), notable differences emerged in the estimated probability of infection (β_i and β_c). For example, in the age group 0-4, the median value of β_i was lower in the multi-strain model (6.2×10^{-12}) compared to the mean value in the single-strain model (1.5×10^{-4}), while for β_c, the median in the multi-strain model (0.0009) significantly exceeded the mean in the single-strain model (0.00028). These disparities between age groups indicate that the incorporation of multiple strains leads to notable differences in estimated transmission rates, likely due to complex interactions between pathogen strains and their impacts on transmission dynamics.

Contrasting Transmission Patterns: Analysis of estimated quarantine reproduction numbers highlights clear disparities between influenza and COVID-19. Influenza consistently exhibits lower reproduction numbers across all age groups compared to COVID-19, suggesting relatively less effective transmission dynamics. This observation is consistent with recent findings by [105, 115, 141], indicating that COVID-19 has resulted in lower rates of infection and disease burden among children compared to influenza outbreaks.

Age group transmission dynamics: Both pathogens demonstrate varying transmission rates between different age groups. In the case of influenza, the age group 05-14 consistently emerges with the highest transmission potential, followed by the age groups 35-59 and 60-79 (see Figure 7.6 and Figure 7.7). This implies a significant role for younger people in influenza transmission, aligning with prior research such as [21, 22, 126]. These studies suggest that children and adolescents, particularly those in educational or childcare settings, serve as potential vectors for influenza transmission due to heightened social interactions. In addition, older adults, especially those aged 60 and older, face elevated risks of serious influenza complications [21].

In contrast, the dynamics of COVID-19 transmission demonstrate higher numbers of quarantine reproduction in all age groups compared to influenza, regardless of time periods without (before

December 27, 2020) and with (from December 27, 2020) COVID-19 vaccination, and only periods with influenza vaccination. The 35-59 age group consistently shows the highest transmission potential, followed by the 15-34 and 60-79 age groups, as shown in Figure 7.6. This underscores the critical role of middle-aged adults in the spread of COVID-19, corroborating findings from studies such as [105, 109], which highlight the substantial contribution of contacts to transmission, primarily within young adult and adult demographics.

7.A Appendix: Breakdown of sensitivity evaluation methods

In practical applications these analyzes will be carried out using a computer program; thus, here we only describe the variance-based numerical procedure for computing indices.

Step 1: Define the output function and targeted parameters

Utilizing the notations introduced in [113, 114], we denote the output function of interest as

$$Y = g(P_1, P_2, \cdots, P_k), \tag{7.5}$$

over the domain

$$\Gamma = [0,1]^k = \{(P_1, P_2, \cdots, P_k) | 0 \leq P_i \leq 1 \text{ for } i = 1, 2, \cdots, k\},$$

which represents the k-dimensional unit hypercube. P_i where $i = 1, 2, \cdots, k$ are input factors, each of which is uniformly distributed within the specified ranges, as indicated in Table 7.5. For each range of variation P_i, we want to determine what would happen to the uncertainty of Y if we could fix a factor.

We consider a function Y as an integral over time derived from the model output of interest. Sobol considers an expansion of g in terms of increasing dimensions:

$$g = g_0 + \sum_i g_i + \sum_i \sum_{j>i} + \cdots + g_{12\cdots k}.$$

Each individual term is also square integrable in the domain of existence and is a function of only the factors in its index, that is,

$$g_i = g_i(P_i), \; g_{ij} = g_{ij}(P_i, P_j)$$

and so on for a total of 2^k terms including g_0.

Given $Y = g(P)$, the total variance $V(Y)$ can be decomposed as:

$$V(Y) = \sum_{i=1}^{k} V_i + \sum_{i<j} V_{ij} + \cdots + V_{12\cdots k}$$

where: V_i is the variance contribution of parameter P_i (first-order effect). V_{ij} is the variance contribution due to the interaction between the parameters P_i and P_j (second order effect). Higher-order terms represent interactions among more parameters.

Step 2: Sample generation

We start by generating a random number sample matrix with dimensions $(N, 2k)$, where k represents the number of input parameters and N is the number of samples. Next, we split this

Table 7.5: Description of model parameters with their definitions, distributions, ranges, and units

Symbol	Definition	Distribution	Range	Unit	Source
c	Contact rate	Uniform	$[0, 1]$	day^{-1}	[109]
Λ	Birth rate	Uniform	$(0,\ 1/365]$	year^{-1}	[96]
μ	Natural death rate	Uniform	$(0,\ 1/365]$	year^{-1}	[96]
Ω_c	Scaling factor in Q_c	Uniform	$[0, 1]$	-	[45]
Ω_i	Scaling factor in Q_i	Uniform	$[0, 1]$	-	[45]
β_c	strain-c transmission probabilities per contact	Uniform	$[0,\ 1]$	day^{-1}	to be estimated
β_i	strain-i transmission probabilities per contact	Uniform	$[0,\ 1]$	day^{-1}	to be estimated
ρ_c	Rate of developing strain-c symptoms	Uniform	$[1/4.3, 1/2.3]$	day^{-1}	[109]
ρ_i	Rate of developing strain-i symptoms	Uniform	$[1/5, 1/2]$	day^{-1}	[37]
α_c	rate of isolating E_c	Uniform	$[0.89, 1.51]$	day^{-1}	[123]
α_i	rate of isolating E_i	Uniform	$[0.89, 1.51]$	day^{-1}	[123]
σ_c	Isolation rate I_c	Uniform	[0.02,0.1]	day^{-1}	[37]
σ_i	isolation rate I_i	Uniform	[0.02,0.1]	day^{-1}	[96]
τ_c	progression rate from Q_c to I_c	Uniform	$(0, 0.5]$	day^{-1}	[140]
τ_i	progression rate from Q_i to I_i	Uniform	$(0, 0.5]$	day^{-1}	[140]
ϕ_c	Q_c recovery rate	Uniform	$[0.08, 0.14]$	day^{-1}	[140]
ϕ_i	Q_i recovery rate	Uniform	$[0.08, 0.14]$	day^{-1}	[96]
γ_c	I_c recovery rate	Uniform	$[0.28, 0.38]$	day^{-1}	[123]
γ_i	I_i recovery rate	Uniform	$[1/6, 1/4]$	day^{-1}	[120]
δ_c	Death rate due to strain-c	Uniform	$[0.001, 0.1]$	day^{-1}	[45]
δ_i	Death rate due to strain-i	Uniform	$[0.001, 0.1]$	day^{-1}	[37]
η_c	Cross-immunity against strain-c	Uniform	$[0, 1]$	-	[122]
η_i	Cross-immunity against strain-i	Uniform	$[0, 1]$	-	[122]

sample matrix into two main sample matrices, $\mathbf{A}$ and $\mathbf{B}$, each of size $N \times k$. These matrices contain half of the samples each. We then define a matrix $\mathbf{B}_{\mathbf{A}}^{(i)}$, where each column is taken from matrix $\mathbf{B}$ except for the i-th column, which is replaced with the corresponding column from matrix $\mathbf{A}$. This results in a set of matrices, each representing a specific interaction scenario between the parameters of matrices $\mathbf{A}$ and $\mathbf{B}$.

Step 3: Computation of the model output

For each set of input values in the sample matrices $\mathbf{A}$, $\mathbf{B}$ and $\mathbf{B}_{\mathbf{A}}^{(i)}$, we compute the corresponding model outputs. This results in three vectors of model outputs, each of dimension $N \times 1$:

$$Y_{\mathbf{A}} = g(\mathbf{A}), \quad Y_{\mathbf{B}} = g(\mathbf{B}), \quad Y_{\mathbf{B}_{\mathbf{A}}^{(i)}} = g(\mathbf{B}_{\mathbf{A}}^{(i)})$$

These vectors represent the model output for the samples in matrices $\mathbf{A}$, $\mathbf{B}$, and the modified matrix $\mathbf{B}_{\mathbf{A}}^{(i)}$, respectively.

Step 4: Estimation of the sensitivity indices for each P_i on Y

First-order Sobol index $\mathbf{SI}_i^{P_i}$: Measures the contribution of P_i alone to the output variance.

$$\mathbf{SI}_i^{P_i} = \frac{V(E(Y|P_i))}{V(Y)} = \frac{\frac{1}{N}\sum_{i=1}^{N} Y_{\mathbf{A}}^{(i)} Y_{\mathbf{B}_{\mathbf{A}}^{(i)}}^{(i)} - g_0^2}{\frac{1}{N}\sum_{i=1}^{N} (Y_{\mathbf{A}}^{(i)})^2 - g_0^2}$$

Sobol index of total order $\mathbf{SI}_{tot}^{P_i}$: Measures the contribution of P_i, including all its interactions

with other variables.

$$\mathbf{SI}_{tot}^{P_i} = 1 - \frac{V(E(Y|P_{\sim i}))}{V(Y)} = \frac{\frac{1}{N}\sum_{i=1}^{N} Y_{\mathbf{B}}^{(i)} Y_{\mathbf{B}_{\mathbf{A}}^{(i)}}^{(i)} - g_0^2}{\frac{1}{N}\sum_{i=1}^{N} (Y_{\mathbf{A}}^{(i)})^2 - g_0^2}$$

Here, the term g_0, is computed as:

$$g_0 = \frac{1}{N}\sum_{i=1}^{N} Y_{\mathbf{A}}^{(i)}$$

Step 5: Simulating the model

In this stage, we calculate sensitivity indices to assess how individual parameters, their collective impact, and their interactions contribute to the variability observed in model results. To generate combinations of parameters, we used Saltelli sampling, leveraging the *saltelli.sample* function provided by the SALib library [63, 99]. Model simulations were conducted using the Python programming language (version 3.10.11) using the *sobol.analyze* function. The sample size, denoted as N, was set to 2^{15}. Each simulation run took approximately 0.001 seconds to complete. The total computational cost of executing the model for $k = 23$ factors amounted to $(2k + 2)N$. A summary of the results obtained is presented in Table 7.3, and visual representations are provided in Figure 7.3.

7.B Appendix: Pathogen interaction

In multipathogen scenarios, competition means that different infectious agents in the same host or population affect each other. An infectious agent can make it harder for another to survive, reproduce, or spread. Coexistence, on the other hand, means that infectious agents can live and spread in the same population over time, although they can compete with each other [92].

Various viruses coexist within the human respiratory system, contributing to acute respiratory infections. This common habitat allows for interactions between viruses, which can alter the risk of infection for individuals and subsequently influence infection patterns throughout the population. For example, Nickbakhsh et al. (2019) discuss the concept of viral interference, where the presence of one respiratory virus can inhibit the infection and spread of another. Provides information on how influenza and COVID-19 might interact [94]. Figure 1.2 illustrates how COVID-19 and influenza, both occupying the respiratory tract niche, interact and affect the dynamics of infectious diseases within this shared environment. The sharp increase in COVID-19 cases followed by a notable reduction in influenza cases during the same period suggests competitive interactions between these two viruses. This competition likely arises from shared host resources and immune responses, where the introduction and rapid spread of COVID-19 may have suppressed influenza transmission. The timing of key interventions, such as public restrictions and the face mask mandate, further influenced the prevalence of both viruses, demonstrating how changes in the shared niche can significantly alter the dynamics of co-circulating respiratory pathogens.

8 Conclusion

The $SEIQR$ models that have been developed and analyzed in this thesis significantly advance our understanding of multipathogen dynamics by including important factors such as cross-immunity, imperfect quarantine, and co-infection in populations. We provide an overview of the results in this chapter and discuss how they may influence public health policy and practice, particularly as they relate to the management of infectious disease outbreaks. We also discuss possible ways to extend this work to improve our understanding of pathogen interactions and resistance.

8.1 Reflections

Our results in Section 4.3, particularly Lemma 4.8, highlight that effective quarantine measures are crucial for infection control, even when the quarantine reproduction numbers fall below one. We showed that having both strain-i and strain-c with quarantine reproduction numbers less than 1 isn't enough to ensure the stability of the disease-free state. Additional conditions, especially those related to the degree to which quarantine measures are implemented, must be met to keep the disease-free state stable (Section 4.3.1). Another key outcome of this section is the identification of challenges posed by co-infections, especially under imperfect quarantine measures, as shown in Proposition 4.11. Our findings suggest that while quarantine can slow the transmission of individual strains, the persistence of co-infections can extend the outbreak, complicating containment efforts. In contrast, as demonstrated in Proposition 4.12, in the absence of co-infections, perfect quarantine measures can more effectively curb the spread when the reproduction numbers for each strain are kept below one. Given the difficulties associated with co-infections, public health strategies should focus on controlling multiple pathogens simultaneously, rather than addressing each one individually. To overcome the limitations of imperfect quarantine, policies could focus on stricter enforcement, providing adequate support to quarantined individuals, and educating the public on the importance of adherence to quarantine measures.

The analysis in Sections 4.4 and 4.5 sheds light on the dynamics of multiple pathogens, focusing on competitive exclusion (Section 4.4.1), co-existence (Section 4.4.3) and co-infection (Section 4.5) under quarantine measures. Our investigation of cross-immunity reveals its significant role in shaping epidemic outcomes. We find that a strain with a quarantine reproduction number greater than 1 will outcompete and eventually drive to extinction a strain with a reproduction number less than 1, especially under complete immunity. However, introducing partial cross-immunity allows the weaker strain to persist and transmit, although at a reduced rate (Figure 6.1). Furthermore,

when all reproduction numbers exceed 1, the strain with the higher value dominates, leading to the extinction of the other. With partial cross-immunity, more complex dynamics arise, such as the possibility of multiple stable endemic equilibria and alternating dominance (Figure 6.2). These findings highlight the intricate interactions between pathogens and demonstrate the importance of public health interventions in influencing the long-term coexistence or eradication of diseases.

The numerical investigation of co-infections and cross-immunity, as illustrated in Figures 4.5 and 4.6, reveals the significant impact of cross-immunity on epidemic patterns. Strong cross-immunity can effectively suppress secondary outbreaks, resulting in a single peak in infection prevalence. However, weakened cross-immunity can lead to more complex dynamics, such as multiple infection waves or merging outbreaks, as immunity diminishes. This highlights the crucial role of robust immunity, through natural recovery or vaccination, in controlling diseases with multiple strains. The findings underscore the importance of achieving high levels of population immunity through vaccination, as supported by the World Health Organization (WHO), to prevent unnecessary cases and deaths [132]. Effective vaccination programs or natural immunity that enhance cross-immunity are essential to manage the spread of multiple strains. In contrast, low levels of cross-immunity require more rigorous surveillance and intervention to prevent widespread outbreaks. This analysis emphasizes the need for continuous monitoring of immunity levels to adapt public health strategies and mitigate the impact of infections involving multiple strains.

Furthermore, we noticed that when control measures bring the quarantine reproduction number ($\tilde{\mathcal{R}}_i^q$ or $\tilde{\mathcal{R}}_c^q$) below 1, it suggests that we could potentially wipe out the disease. However, because of something called backward bifurcation, diseases with a quarantine reproduction number below one might still hang around at a low level. Moreover, even if both strains have reproduction numbers below 1, we still need to ensure that quarantine measures are working well to keep the disease-free state stable (Section 4.3.1). If we relax or fail to properly implement these control measures, as often happens with imperfect quarantine, the disease could return to this low level. This underscores the importance of consistently implementing and maintaining control measures to prevent disease resurgence. An example of this is tuberculosis. Even after implementing measures such as treatments and vaccination, the reproduction number can be reduced below one. Although it has a reproduction number below one, tuberculosis can persist within a subpopulation with latent infections. When control measures are relaxed, these latent cases can become active, leading to a recurrence of tuberculosis [20].

Chapter 5 highlights the crucial role of quarantine and isolation in the management of early-stage epidemics, demonstrating that timely and effective implementation can significantly reduce disease transmission, as seen in Figure 5.2. However, perfect quarantine is often unrealistic [84], making a combination of strategies, as shown in Figure 5.5, more effective than relying on a single measure. The figure shows that integrating quarantine, isolation, and public information campaigns not only reduces peak infections, but also shortens the time to reach peak. Maximizing quarantine and isolation rates is shown to be most effective in controlling the epidemic, emphasizing the need for early and strong interventions.

Policymakers are encouraged to prioritize these strategies to reduce the severity of the epidemic

and ease pressure on healthcare systems. Although public information campaigns have a smaller effect, they still improve compliance and reinforce the benefits of quarantine and isolation. Varying maximum infection times according to different strategies, as shown in Figure 5.5, suggests that adaptive responses are essential. Furthermore, analysis and visualization in Figure5.1 suggest that faster recovery among quarantined individuals highlights the importance of providing support during isolation to improve compliance and health outcomes. A coordinated approach that combines quarantine, effective isolation, public outreach, and support for quarantined individuals is critical to controlling disease spread and minimizing socioeconomic impacts. Optimizing quarantine in conjunction with other public health measures can significantly mitigate the health and socioeconomic consequences of an epidemic, ensuring a more resilient public health system for future outbreaks.

In Chapter 7, the theoretical framework is applied to real-world scenarios, demonstrating how the model can be used to understand the transmission dynamics of influenza and COVID-19 across different age groups. This highlights the practical relevance of the model in the treatment of contemporary infectious diseases. The findings, as shown in Figure 7.4, emphasize the importance of adjusting for age-specific factors to accurately model the transmission dynamics of coexisting pathogens. Sensitivity analyzes further reveal that the interaction between disease transmission rates for each virus is significantly influenced by partial cross-immunity, as observed in Figure 7.3. This analysis shows that when there is some overlap in immunity between COVID-19 and influenza, the way their transmission rates interact plays a critical role in determining how both diseases spread.

Figure 1.2 highlights that public health measures, such as mask mandates and restrictions, helped reduce the transmission of both viruses in 2020. However, COVID-19, which is more contagious, became the dominant virus, while influenza remained at lower levels, as seen in Figure 1.2 (B). At the end of 2022, influenza cases started to increase again (see Figure 1.2 (A)), even as COVID-19 declined. This suggests that factors such as immunity and health interventions influence how the two viruses interact. It also points to the need for strategies that address both diseases simultaneously to effectively manage their spread.

Strategies that address both COVID-19 and influenza simultaneously are essential for managing the co-circulation of these viruses, particularly in settings where they overlap seasonally. Effective approaches to preventing the spread of both pathogens in high-risk environments such as hospitals, schools, and long-term care facilities include targeted quarantine and isolation protocols. Implementing isolation policies that account for both COVID-19 and influenza can significantly reduce transmission in these settings, where the impact of an outbreak is more severe. Specific guidelines that consider both viruses help minimize disruptions while maintaining control over infection rates.

In addition to quarantine and isolation strategies, integrated public health messaging is crucial. By promoting preventive measures, such as mask use, hand hygiene, and maintaining social distancing, public health campaigns can reduce the transmission of both viruses. Coordinating messaging ensures that people are aware of how to protect themselves from both COVID-19 and influenza, which often share similar modes of transmission. This strategy is particularly important during periods of increased viral activity, such as the winter months, when both

diseases are more likely to spread.

Finally, combined vaccination campaigns that administer both COVID-19 and influenza vaccines together play a vital role in enhancing cross-immunity between these two respiratory pathogens. As more people achieve immunity through vaccination or prior infection, the spread of the diseases diminishes or ceases entirely [86, 132]. Therefore, delivering both vaccines at the same time can activate the immune system to create a more robust defense, potentially improving its ability to respond effectively to either virus.

8.2 Future directions

Despite advances, our models continue to fall short of fully capturing the complexities of co-infection and cross-immunity, highlighting crucial areas requiring more study. More research is required, although [74] points out that co-infections between respiratory viruses and SARS-CoV-2 are not very common. Circumstances such as the co-infection of SARS-CoV-2 and influenza A in a German infant aged 4 months [129] emphasize how important a precise diagnosis is. By improving data collection and focusing on scenarios where co-infections are more common, we can better understand the dynamics and implications for public health. In addition, better diagnostic methods can uncover latent patterns that help public health officials recognize threats and formulate targeted countermeasures.

Cross-immunity has been among the areas of our focus in this study, yet more research is needed, particularly regarding age-specific partial cross-immunity. For example, [130] found that adults generally exhibit a stronger antibody response to SARS-CoV-2 compared to children, who show reduced protective responses. This variation implies that adults may possess stronger cross-immunity than children, making the latter more susceptible to co-circulating pathogens. Future models should incorporate age-specific cross-immunity parameters; in our model, where 0 signifies full protection while 1 means no protection, children could be assigned higher cross-immunity values, while adults could be assigned lower values reflecting their stronger immunity. Investigating the strength and duration of immunity across different age groups will enhance the refinement of vaccination and intervention strategies.

Although our model successfully identified backward bifurcation phenomena, future research should focus on a more detailed exploration of the underlying factors that trigger backward bifurcation, particularly in multipathogen settings involving co-infections. Investigating how co-infections influence the stability of disease-free and endemic equilibria could provide critical insights into the complex dynamics at play. This deeper understanding would allow public health officials to anticipate potential disease resurgence, especially in scenarios with imperfect quarantine measures, thus improving epidemic control strategies.

Our model assumes that disease-induced deaths are rare, reflecting a scenario in which interventions are highly effective in reducing mortality. However, we acknowledge that this simplification might not fully account for the elevated risks faced by certain age groups. According to previous research, 65-year-olds and older people, as well as children under 5, are at a higher risk of severe complications and death from influenza [22, 124]. Similarly, during the COVID-19 pandemic, numerous studies have shown that older adults and young children are significantly more vul-

nerable to severe outcomes, with higher rates of hospitalization and mortality reported among the elderly [127]. These limitations highlight areas for future research and underscore the need for caution when interpreting our results within the context of these constraints.

Although our current models concentrate primarily on respiratory viruses, there is significant potential for expanding the framework to encompass interactions between other co-circulating pathogens, such as RSV, rhinoviruses, and bacteria like Streptococcus pneumonia. Extending the model to include these additional pathogens would enable a more comprehensive understanding of the multipathogen landscape. This could improve predictions in high-risk environments, including hospitals, schools, and long-term care facilities, where co-infections may be more frequent and have different transmission dynamics. Such an approach would enhance public health strategies by considering a wider range of potential co-infections and their impact on disease management in these diverse settings.

Bibliography

[1] M. Ali, S. T. H. Shah, M. Imran, **and** A. Khan. *The role of asymptomatic class, quarantine and isolation in the transmission of COVID-19. Journal of biological dynamics*, 14: 389–408, 2020. doi: 10.1080/17513758.2020.1773000 (see pp. 13, 85)

[2] N. M. Almazán, A. Rahbar, M. Carlsson, T. Hoffman, L. Kolstad, B. Rönnberg, M. R. Pantalone, I. L. Fuchs, A. Nauclér, M. Ohlin, **and** others. *Influenza A H1N1–mediated pre-existing immunity to SARS-CoV-2 predicts COVID-19 outbreak dynamics. medRxiv*, 2021–12, 2021. doi: 10.1101/2021.12.23.21268321 (see p. 84)

[3] B. Alosaimi, A. Naeem, M. E. Hamed, H. S. Alkadi, T. Alanazi, S. S. Al Rehily, A. Z. Almutairi, **and** A. Zafar. *Influenza co-infection associated with severity and mortality in COVID-19 patients. Virology journal*, 18: 1–9, 2021. doi: 10.1186/s12985-021-01594-0 (see pp. 4, 5, 9)

[4] V. Andreasen, J. Lin, **and** S. A. Levin. *The dynamics of cocirculating influenza strains conferring partial cross-immunity. Journal of mathematical biology*, 35: 825–842, 1997. doi: 10.1007/s002850050079 (see pp. 11, 12, 27, 87)

[5] V. Andreasen **and** A. Pugliese. *Pathogen coexistence induced by density-dependent host mortality. Journal of theoretical biology*, 177: 159–165, 1995. doi: 10.1016/S0022-5193(19)30172-9 (see p. 84)

[6] J. Arino, R. Jordan, **and** P. Van den Driessche. *Quarantine in a multi-species epidemic model with spatial dynamics. Mathematical biosciences*, 206: 46–60, 2007. doi: 10.1016/j.mbs.2005.09.002 (see pp. 9, 13)

[7] M. S. Aronna, R. Guglielmi, **and** L. M. Moschen. *A model for COVID-19 with isolation, quarantine and testing as control measures. Epidemics*, 34: 100437, 2021. doi: 10.1016/j.epidem.2021.100437 (see pp. 2, 49, 71, 85)

[8] C. J. Atchison, B. Davies, E. Cooper, A. Lound, M. Whitaker, A. Hampshire, A. Azor, C. A. Donnelly, M. Chadeau-Hyam, G. S. Cooke, **and** others. *Long-term health impacts of COVID-19 among 242,712 adults in England. Nature Communications*, 14: 6588, 2023. doi: 10.1038/s41467-023-41879-2 (see p. 88)

[9] S. Bhowmick, I. M. Sokolov, **and** H. H. Lentz. *Decoding the double trouble: A mathematical modelling of co-infection dynamics of SARS-CoV-2 and influenza-like illness. Biosystems*, 104827, 2023. doi: 10.1016/j.biosystems.2023.104827 (see p. 11)

[10] A. Blut **and** others. *Influenza virus. Transfusion Medicine and Hemotherapy*, 36: 32, 2009. doi: 10.1159/000197314 (see p. 49)

[11] M. M. Böhmer, U. Buchholz, V. M. Corman, M. Hoch, K. Katz, D. V. Marosevic, S. Böhm, T. Woudenberg, N. Ackermann, R. Konrad, **and** others. *Investigation of a COVID-19 outbreak in Germany resulting from a single travel-associated primary case: a case series. The Lancet Infectious Diseases*, 20: 920–928, 2020. doi: 10.1016/S1473-3099(20)30314-5 (see p. 49)

[12] M. Braun **and** M. Golubitsky. *Differential equations and their applications.* **volume** 2 Springer, 1983. (see pp. 18, 19)

[13] H. J. Bremermann **and** H. Thieme. *A competitive exclusion principle for pathogen virulence. Journal of mathematical biology*, 27: 179–190, 1989. doi: 10.1007/BF00276102 (see pp. 9, 55)

[14] U. Buchholz, A.-S. Lehfeld, K. Tolksdorf, W. Cai, J. Reiche, B. Biere, R. Dürrwald, **and** S. Buda. *Respiratory infections in children and adolescents in Germany during the COVID-19 pandemic. Journal of health monitoring*, 8: 20, 2023. doi: 10.25646/11437 (see p. 89)

[15] Bundeszentrale für gesundheitliche Aufklärung (BZgA) *Coronavirus* https://www.infektionsschutz.de/coronavirus/ [Accessed 19-Jun-2024] 2024 (see pp. 1, 87)

[16] C. Castillo-Chavez, C. W. Castillo-Garsow, **and** A.-A. Yakubu. *Mathematical models of isolation and quarantine. Jama*, 290: 2876–2877, 2003. doi: 10.1001/jama.290.21.2876 (see p. 13)

[17] C. Castillo-Chavez, Z. Feng, **and** W. Huang. *On the Computation of R 0 and its Role on Global Stability. Mathematical Approaches for Emerging and Reemerging Infectious Diseases: An Introduction*, 229–250, 2002. (see p. 38)

[18] C. Castillo-Chavez, H. W. Hethcote, V. Andreasen, S. A. Levin, **and** W. M. Liu. *Epidemiological models with age structure, proportionate mixing, and cross-immunity. Journal of mathematical biology*, 27: 233–258, 1989. doi: 10.1007/BF00275810 (see p. 10)

[19] C. Castillo-Chavez, W. Huang, **and** J. Li. *Competitive exclusion and coexistence of multiple strains in an SIS STD model. SIAM Journal on Applied Mathematics*, 59: 1790–1811, 1999. doi: 10.1137/S0036139997325862 (see p. 9)

[20] C. Castillo-Chavez **and** B. Song. *Dynamical models of tuberculosis and their applications. Math. Biosci. Eng*, 1: 361–404, 2004. doi: 10.3934/mbe.2004.1.361 (see pp. 21, 22, 73, 75, 76, 112)

[21] S. Cauchemez, A. Bhattarai, T. L. Marchbanks, R. P. Fagan, S. Ostroff, N. M. Ferguson, D. Swerdlow, P. H. W. Group, S. V. Sodha, M. E. Moll, **and** others. *Role of social networks in shaping disease transmission during a community outbreak of 2009 H1N1 pandemic influenza. Proceedings of the National Academy of Sciences*, 108: 2825–2830, 2011. doi: 10.1073/pnas.1008895108 (see p. 106)

[22] S. Cauchemez, N. M. Ferguson, C. Wachtel, A. Tegnell, G. Saour, B. Duncan, **and** A. Nicoll. *Closure of schools during an influenza pandemic. The Lancet infectious diseases*, 9: 473–481, 2009. doi: 10.1016/S1473-3099(09)70176-8 (see pp. 87, 106, 114)

[23] Centers for Disease Control and Prevention *Types of Influenza Viruses* https://www.cdc.gov/flu/about/viruses/types.htm [Accessed 19-Jun-2024] 2024 (see p. 1)

[24] T. Chotpitayasunondh, T. K. Fischer, J.-M. Heraud, A. C. Hurt, A. S. Monto, A. Osterhaus, Y. Shu, **and** J. S. Tam. *Influenza and COVID-19: What does co-existence mean? Influenza and Other Respiratory Viruses*, 15: 407–412, 2021. doi: 10.1111/irv.12824 (see pp. 5, 28)

[25] M. Ciotti, M. Ciccozzi, A. Terrinoni, W.-C. Jiang, C.-B. Wang, **and** S. Bernardini. *The COVID-19 pandemic. Critical reviews in clinical laboratory sciences*, 57: 365–388, 2020. doi: 10.1080/10408363.2020.1783198 (see p. 1)

[26] B. J. Cowling **and** G. M. Leung. *Epidemiological research priorities for public health control of the ongoing global novel coronavirus (2019-nCoV) outbreak. Eurosurveillance*, 25: 2000110, 2020. doi: 10.2807/1560-7917.ES.2020.25.6.2000110 (see pp. 4, 89)

[27] E. Cuadrado-Payán, E. Montagud-Marrahi, M. Torres-Elorza, M. Bodro, M. Blasco, E. Poch, A. Soriano, **and** G. J. Piñeiro. *SARS-CoV-2 and influenza virus co-infection. Lancet (London, England)*, 395: e84, 2020. doi: 10.1016/S0140-6736(20)31052-7 (see p. 89)

[28] Deutschland.de *Coronavirus in Germany: information* Accessed: 2023-07-21 2023 (see p. 90)

[29] O. Diekmann **and** J. A. P. Heesterbeek. *Mathematical epidemiology of infectious diseases: model building, analysis and interpretation.* **volume** 5 John Wiley & Sons, 2000. (see p. 10)

[30] K. Dietz. *Epidemiologic interference of virus populations. Journal of mathematical biology*, 8: 291–300, 1979. doi: 10.1007/BF00276314 (see p. 10)

[31] E. C. for Disease Prevention **and** Control *Guidelines for the use of non-pharmaceutical measures to delay and mitigate the impact of COVID-19* https://www.ecdc.europa.eu/en/publications-data/covid-19-guidelines-non-pharmaceutical-interventions Accessed: 2024-06-22 2020 (see p. 2)

[32] J. DiStefano III. *Dynamic systems biology modeling and simulation.* Academic Press, 2015. (see pp. 24, 26)

[33] J. R. Dormand **and** P. J. Prince. *A family of embedded Runge-Kutta formulae. Journal of computational and applied mathematics*, 6: 19–26, 1980. doi: 10.1016/0771-050X(80)90013-3 (see p. 25)

[34] S. Q. Du **and** W. Yuan. *Mathematical modeling of interaction between innate and adaptive immune responses in COVID-19 and implications for viral pathogenesis. Journal of medical virology*, 92: 1615–1628, 2020. doi: 10.1002/jmv.25866 (see p. 9)

[35] B. Efron **and** R. J. Tibshirani. *An introduction to the bootstrap.* CRC press, 1994. (see p. 95)

[36] K. U. Egeonu, A. Omame, **and** S. C. Inyama. *A co-infection model for two-strain malaria and cholera with optimal control. International Journal of Dynamics and Control*, 9: 1612–1632, 2021. doi: 10.1007/s40435-020-00748-2 (see p. 41)

[37] S. E. Eikenberry, M. Mancuso, E. Iboi, T. Phan, K. Eikenberry, Y. Kuang, E. Kostelich, **and** A. B. Gumel. *To mask or not to mask: Modeling the potential for face mask use by the general public to curtail the COVID-19 pandemic. Infectious disease modelling*, 5: 293–308, 2020. (see pp. 49, 108)

[38] M. Erdem, M. Safan, **and** C. Castillo-Chavez. *Mathematical analysis of an SIQR influenza model with imperfect quarantine. Bulletin of Mathematical Biology*, 79: 1612–1636, 2017. doi: 10.1007/s11538-017-0301-6 (see p. 70)

[39] Z. Feng, C. Castillo-Chavez, **and** A. F. Capurro. *A model for tuberculosis with exogenous reinfection. Theoretical population biology*, 57: 235–247, 2000. doi: 10.1006/tpbi.2000.1451 (see p. 74)

[40] N. M. Ferguson, D. Laydon, G. Nedjati-Gilani, N. Imai, K. Ainslie, M. Baguelin, S. Bhatia, A. Boonyasiri, Z. Cucunubá, G. Cuomo-Dannenburg, **and** others. *Report 9: Impact of non-pharmaceutical interventions (NPIs) to reduce COVID19 mortality and healthcare demand*. **volume** 16 Imperial College London London, 2020. (see p. 88)

[41] G. Fink, N. Orlova-Fink, T. Schindler, S. Grisi, A. P. S. Ferrer, C. Daubenberger, **and** A. Brentani. *Inactivated trivalent influenza vaccination is associated with lower mortality among patients with COVID-19 in Brazil. BMJ evidence-based medicine*, 26: 192–193, 2021. doi: 10.1136/bmjebm-2020-111549 (see pp. 4, 88)

[42] S. Flaxman, S. Mishra, A. Gandy, H. J. T. Unwin, T. A. Mellan, H. Coupland, C. Whittaker, H. Zhu, T. Berah, J. W. Eaton, **and** others. *Estimating the effects of non-pharmaceutical interventions on COVID-19 in Europe. Nature*, 584: 257–261, 2020. doi: 10.1038/s41586-020-2405-7 (see p. 2)

[43] A. D. Fome, H. Rwezaura, M. L. Diagne, S. Collinson, **and** J. M. Tchuenche. *A deterministic Susceptible-Infected-Recovered model for studying the impact of media on epidemic dynamics. Healthcare Analytics*, 100189, 2023. doi: 10.1016/j.health.2023.100189 (see pp. 31, 71)

[44] A. D. Fome, W. Bock, **and** A. Klar. *Analysis of a competitive respiratory disease system with quarantine. arXiv preprint arXiv:2307.05044*, 2023. doi: 10.48550/arXiv.2307.05044 (see p. 27)

[45] A. D. Fome, W. Bock, **and** A. Klar. *Analysis of a competitive respiratory disease system with quarantine: Epidemic thresholds and cross-immunity effects. Applied Mathematics and Computation*, 485: 128968, 2024. doi: 10.1016/j.amc.2024.128968 (see pp. 73, 106, 108)

[46] A. D. Fome, W. Bock, **and** A. Klar. *Conditions for Backward Bifurcation in a Multi-Pathogen Model with Imperfect Quarantine and Cross-Immunity*. under-review, 2024. (see p. 73)

[47] A. D. Fome, W. Bock, **and** A. Klar. *Equilibria Dynamics in Competitive Respiratory Disease Systems with Quarantine. ECMI2023 Proceedings*, Accepted, 2024. (see p. 27)

[48] A. D. Fome, I. Rodiah, W. Bock, B. Lange, **and** A. Klar. *The Interplay of Influenza and COVID-19 in Germany, January 2020 - December 2022: A Study of Competitive Disease Dynamics with Quarantine Measures and Partial Cross-Immunity. manuscript in preparation*, 2024. (see p. 87)

[49] A. D. Fome, I. Rodiah, W. Bock, B. Lange, **and** A. Klar. *The Interplay of Influenza and Covid-19 in Germany, January 2020-December 2022: A Study of Competitive Disease Dynamics with Quarantine Measures and Partial Cross-Immunity. Available at SSRN 5019051*, 2024. doi: 10.2139/ssrn.5019051 (see p.)

[50] M. Fudolig **and** R. Howard. *The local stability of a modified multi-strain SIR model for emerging viral strains. PloS one*, 15: e0243408, 2020. doi: 10.1371/journal.pone.0243408 (see pp. 11, 12, 27, 84)

[51] A. Gagnon, M. S. Miller, S. A. Hallman, R. Bourbeau, D. A. Herring, D. J. Earn, **and** J. Madrenas. *Age-specific mortality during the 1918 influenza pandemic: unravelling the mystery of high young adult mortality. PloS one*, 8: e69586, 2013. doi: 10.1371/journal.pone.0069586 (see p. 88)

[52] G. F. Gause. *The struggle for existence: a classic of mathematical biology and ecology*. Courier Dover Publications, 2019. (see p. 10)

[53] F. S. O. of Germany (Destatis) *GENESIS-Online Database* Accessed: 2025-01-27 2025 (see p. 89)

[54] E. Goka, P. Vallely, K. Mutton, **and** P. Klapper. *Influenza A viruses dual and multiple infections with other respiratory viruses and risk of hospitalisation and mortality. Influenza and other respiratory viruses*, 7: 1079–1087, 2013. doi: 10.1111/irv.12020 (see p. 84)

[55] T. Götz, W. Bock, R. Rockenfeller, **and** M. Schäfer. *A two-strain SARS-COV-2 model for Germany–Evidence from a Linearization. arXiv preprint arXiv:2102.11333*, 2021. doi: 10.48550/arXiv.2102.11333 (see p. 9)

[56] A. J. Greaney, A. N. Loes, K. H. Crawford, T. N. Starr, K. D. Malone, H. Y. Chu, **and** J. D. Bloom. *Comprehensive mapping of mutations in the SARS-CoV-2 receptor-binding domain that affect recognition by polyclonal human plasma antibodies. Cell host & microbe*, 29: 463–476, 2021. doi: 10.1016/j.chom.2021.02.003 (see p. 88)

[57] A. Grifoni, D. Weiskopf, S. I. Ramirez, J. Mateus, J. M. Dan, C. R. Moderbacher, S. A. Rawlings, A. Sutherland, L. Premkumar, R. S. Jadi, **and** others. *Targets of T cell responses to SARS-CoV-2 coronavirus in humans with COVID-19 disease and unexposed individuals. Cell*, 181: 1489–1501, 2020. doi: 10.1016/j.cell.2020.05.015 (see pp. 3, 88)

[58] J. Guckenheimer **and** P. Holmes. *Nonlinear oscillations, dynamical systems, and bifurcations of vector fields*. **volume** 42 Springer Science & Business Media, 2013. (see p. 18)

[59] A. B. Gumel. *Causes of backward bifurcations in some epidemiological models. Journal of Mathematical Analysis and Applications*, 395: 355–365, 2012. doi: 10.1016/j.jmaa.2012.04.077 (see p. 74)

[60] A. Gupta, M. V. Madhavan, K. Sehgal, N. Nair, S. Mahajan, T. S. Sehrawat, B. Bikdeli, N. Ahluwalia, J. C. Ausiello, E. Y. Wan, **and** others. *Extrapulmonary manifestations of COVID-19. Nature medicine*, 26: 1017–1032, 2020. doi: 10.1038/s41591-020-0968-3 (see pp. 4, 88)

[61] S. Gupta, N. Ferguson, **and** R. Anderson. *Chaos, persistence, and evolution of strain structure in antigenically diverse infectious agents. Science*, 280: 912–915, 1998. doi: 10.1126/science.280.5365.912 (see p. 73)

[62] D. Hamby. *A comparison of sensitivity analysis techniques. Health physics*, 68: 195–204, 1995. (see pp. 25, 26, 94)

[63] J. Herman **and** W. Usher. *SALib: An open-source Python library for sensitivity analysis. Journal of Open Source Software*, 2: 97, 2017. doi: 10.21105/joss.00097.pdf (see p. 109)

[64] H. W. Hethcote. *Three basic epidemiological models*. Springer, 1989. 119–144 (see p. 28)

[65] M. W. Hirsch, S. Smale, **and** R. L. Devaney. *Differential equations, dynamical systems, and an introduction to chaos*. Academic press, 2013. (see pp. 16, 24)

[66] M. E. Hochberg **and** R. D. Holt. *The coexistence of competing parasites. I. The role of cross-species infection. The American Naturalist*, 136: 517–541, 1990. eprint: https://www.journals.uchicago.edu/doi/abs/10.1086/285111 (see p. 9)

[67] P.-F. Hsieh **and** Y. Sibuya. *Basic theory of ordinary differential equations*. Springer Science & Business Media, 2012. (see p. 17)

[68] R. K. Institute *Robert Koch Institute Homepage* 2025 (see pp. 89, 90)

[69] N. Jebril. *World Health Organization declared a pandemic public health menace: a systematic review of the coronavirus disease 2019 "COVID-19". Available at SSRN 3566298*, 2020. doi: 10.2139/ssrn.3566298 (see p. 1)

[70] W. O. Kermack **and** A. G. McKendrick. *A contribution to the mathematical theory of epidemics. Proceedings of the royal society of london. Series A, Containing papers of a mathematical and physical character*, 115: 700–721, 1927. doi: 10.1098/rspa.1927.0118 (see p. 9)

[71] V. M. Konala, S. Adapa, V. Gayam, S. Naramala, S. R. Daggubati, C. B. Kammari, **and** A. Chenna. *Co-infection with Influenza A and COVID-19. European journal of case reports in internal medicine*, 7: 2020. doi: 10.12890/2020_001656 (see pp. 4, 89)

[72] B. W. Kooi, M. Aguiar, **and** N. Stollenwerk. *Bifurcation analysis of a family of multi-strain epidemiology models. Journal of computational and applied mathematics*, 252: 148–158, 2013. doi: 10.1016/j.cam.2012.08.008 (see p. 41)

[73] C. M. Kribs-Zaleta **and** J. X. Velasco-Hernández. *A simple vaccination model with multiple endemic states. Mathematical biosciences*, 164: 183–201, 2000. doi: 10.1016/S0025-5564(00)00003-1 (see p. 74)

[74] H. Krumbein, L. S. Kümmel, P. C. Fragkou, C. Thölken, B. L. Hünerbein, R. Reiter, K. A. Papathanasiou, H. Renz, **and** C. Skevaki. *Respiratory viral co-infections in patients with COVID-19 and associated outcomes: A systematic review and meta-analysis. Reviews in Medical Virology*, 33: e2365, 2023. doi: 10.1002/rmv.2365 (see pp. 89, 114)

[75] N. C. Kyriakidis, A. López-Cortés, E. V. González, A. B. Grimaldos, **and** E. O. Prado. *SARS-CoV-2 vaccines strategies: a comprehensive review of phase 3 candidates. npj Vaccines*, 6: 28, 2021. doi: 10.1038/s41541-021-00292-w (see p. 4)

[76] C.-C. Lai, C.-Y. Wang, **and** P.-R. Hsueh. *Co-infections among patients with COVID-19: The need for combination therapy with non-anti-SARS-CoV-2 agents? Journal of Microbiology, Immunology and Infection*, 53: 505–512, 2020. doi: 10.1016/j.jmii.2020.05.013 (see p. 5)

[77] T. Lazebnik **and** S. Bunimovich-Mendrazitsky. *Generic approach for mathematical model of multi-strain pandemics. PloS one*, 17: e0260683, 2022. doi: 10.1371/journal.pone.0260683 (see pp. 9, 11)

[78] B. Lee **and** W. V. Raszka. *COVID-19 transmission and children: the child is not to blame. Pediatrics*, 146: 2020. doi: 10.1542/peds.2020-004879 (see p. 88)

[79] A. T. Levin, W. P. Hanage, N. Owusu-Boaitey, K. B. Cochran, S. P. Walsh, **and** G. Meyerowitz-Katz. *Assessing the age specificity of infection fatality rates for COVID-19: systematic review, meta-analysis, and public policy implications. European journal of epidemiology*, 35: 1123–1138, 2020. doi: 10.1007/s10654-020-00698-1 (see p. 88)

[80] J. Liang, Y. Wang, Z. Lin, W. He, J. Sun, Q. Li, M. Zhang, Z. Chang, Y. Guo, W. Zeng, **and** others. *Influenza and COVID-19 co-infection and vaccine effectiveness against severe cases: a mathematical modeling study. Frontiers in Cellular and Infection Microbiology*, 14: 1347710, 2024. doi: 10.3389/fcimb.2024.1347710 (see p. 11)

[81] A. M. Liapunov. *Stability of Motion by AM Liapunov.* **volume** 30 Elsevier, 2000. (see p. 23)

[82] X. Liu, Y. Peng, Z. Chen, F. Jiang, F. Ni, Z. Tang, X. Yang, C. Song, M. Yuan, Z. Tao, **andothers**. *Impact of non-pharmaceutical interventions during COVID-19 on future influenza trends in Mainland China. BMC Infectious Diseases*, 23: 632, 2023. doi: 10.1186/s12879-023-08594-1 (see p. 3)

[83] X. Lu **and** E. Borgonovo. *Global sensitivity analysis in epidemiological modeling. European journal of operational research*, 304: 9–24, 2023. doi: 10.1016/j.ejor.2021.11.018 (see p. 94)

[84] B. A. Ly, M. A. A. Ahmed, F. B. Traore, N. H. Diarra, M. Dembele, D. Diarra, I. F. Kandé, H. Sangho, **and** S. Doumbia. *Challenges and difficulties in implementing and adopting isolation and quarantine measures among internally displaced people during the COVID-19 pandemic in Mali (161/250). Journal of Migration and Health*, 5: 100104, 2022. doi: 10.1016/j.jmh.2022.100104 (see pp. 59, 70, 112)

[85] D. Marciniuk, T. Ferkol, A. Nana, M. M. de Oca, K. Rabe, N. Billo, **and** H. Zar. *Respiratory diseases in the world. realities of today–opportunities for tomorrow. African Journal of Respiratory Medicine Vol*, 9: 2014. eprint: https://www.openaccessjournals.com/articles/AJRM%20Mar%2014%20pp%204-13.pdf (see p. 1)

[86] M. Martcheva. *An introduction to mathematical epidemiology*. **volume** 61 Springer, 2015. (see pp. 4, 10, 19, 20, 23, 34, 36, 43, 46, 114)

[87] M. Martcheva. *Methods for deriving necessary and sufficient conditions for backward bifurcation. Journal of biological dynamics*, 13: 538–566, 2019. doi: 10.1080/17513758.2019.1647359 (see p. 29)

[88] M. Martcheva, S. S. Pilyugin, **and** R. D. Holt. *Subthreshold and superthreshold coexistence of pathogen variants: the impact of host age-structure. Mathematical biosciences*, 207: 58–77, 2007. doi: 10.1016/j.mbs.2006.09.010 (see p. 84)

[89] L. Mitchell **and** J. V. Ross. *A data-driven model for influenza transmission incorporating media effects. Royal Society open science*, 3: 160481, 2016. doi: 10.1098/rsos.160481 (see pp. 31, 67)

[90] M. Moriyama, W. J. Hugentobler, **and** A. Iwasaki. *Seasonality of respiratory viral infections. Annual review of virology*, 7: 83–101, 2020. doi: 10.1146/annurev-virology-012420-022445 (see p. 87)

[91] J. Mossong, N. Hens, M. Jit, P. Beutels, K. Auranen, R. Mikolajczyk, M. Massari, S. Salmaso, G. S. Tomba, J. Wallinga, **and** others. *Social contacts and mixing patterns relevant to the spread of infectious diseases. PLoS medicine*, 5: e74, 2008. doi: 10.1371/journal.pmed.0050074 (see pp. 92, 93)

[92] J. D. Murray. *Mathematical biology: I. An introduction. Interdisciplinary applied mathematics*. **volume** 17 Mathematical Biology, Springer, 2002. (see pp. 19, 109)

[93] R. Musa, O. J. Peter, **and** F. A. Oguntolu. *A non-linear differential equation model of COVID-19 and seasonal influenza co-infection dynamics under vaccination strategy and immunity waning. Healthcare Analytics*, 4: 100240, 2023. doi: 10.1016/j.health.2023.100240 (see p. 11)

[94] S. Nickbakhsh, C. Mair, L. Matthews, R. Reeve, P. C. Johnson, F. Thorburn, B. Von Wissmann, A. Reynolds, J. McMenamin, R. N. Gunson, **and** others. *Virus–virus interactions impact the population dynamics of influenza and the common cold. Proceedings of the National Academy of Sciences*, 116: 27142–27150, 2019. doi: 10.1073/pnas.1911083116 (see pp. 87, 109)

[95] E. O. Nsoesie, R. J. Beckman, **and** M. V. Marathe. *Sensitivity analysis of an individual-based model for simulation of influenza epidemics. PloS one*, 7: e45414, 2012. doi: 10.1371/journal.pone.0045414 (see p. 94)

[96] M. Nuño, Z. Feng, M. Martcheva, **and** C. Castillo-Chavez. *Dynamics of two-strain influenza with isolation and partial cross-immunity. SIAM Journal on Applied Mathematics*, 65: 964–982, 2005. doi: 10.1137/S003613990343882X (see pp. 3, 11–13, 27, 49, 55, 73, 84, 88, 106, 108)

[97] M. M. Ojo, T. O. Benson, O. J. Peter, **and** E. F. D. Goufo. *Nonlinear optimal control strategies for a mathematical model of COVID-19 and influenza co-infection. Physica A: Statistical Mechanics and its Applications*, 607: 128173, 2022. doi: 10.1016/j.physa.2022.128173 (see pp. 9, 11, 13)

[98] D. Okuonghae. *Backward bifurcation of an epidemiological model with saturated incidence, isolation and treatment functions. Qualitative theory of dynamical systems*, 18: 413–440, 2019. doi: 10.1007/s12346-018-0293-0 (see p. 71)

[99] T. E. Oliphant. *Python for scientific computing. Computing in science & engineering*, 9: 10–20, 2007. doi: 10.1109/MCSE.2007.58 (see p. 109)

[100] D. P. Oran **and** E. J. Topol. *Prevalence of asymptomatic SARS-CoV-2 infection: a narrative review. Annals of internal medicine*, 173: 362–367, 2020. doi: 10.7326/M20-3012 (see p. 85)

[101] W. H. Organization **and** others *Considerations for quarantine of contacts of COVID-19 cases: interim guidance, 19 August 2020* techreport World Health Organization, 2020 doi: https://apps.who.int/iris/bitstream/handle/10665/333901/WHO-2019-nCoV-IHRQuarantine-2020.3-eng.pdf (see pp. 2, 31)

[102] R. Ozaras, R. Cirpin, A. Duran, H. Duman, O. Arslan, Y. Bakcan, M. Kaya, H. Mutlu, L. Isayeva, F. Kebanli, **and** others. *Influenza and COVID-19 coinfection: report of six cases and review of the literature. Journal of medical virology*, 92: 2657–2665, 2020. doi: 10.1002/jmv.26125 (see p. 13)

[103] J. S. Peiris, K. Y. Yuen, A. D. Osterhaus, **and** K. Stöhr. *The severe acute respiratory syndrome. New England Journal of Medicine*, 349: 2431–2441, 2003. doi: 10.1056/NEJMra032498 (see p. 1)

[104] L. Perko. *Differential equations and dynamical systems.* **volume** 7 Springer Science & Business Media, 2013. (see p. 32)

[105] E. Petersen, M. Koopmans, U. Go, D. H. Hamer, N. Petrosillo, F. Castelli, M. Storgaard, S. Al Khalili, **and** L. Simonsen. *Comparing SARS-CoV-2 with SARS-CoV and influenza pandemics. The Lancet infectious diseases*, 20: e238–e244, 2020. doi: 10.1016/S1473-3099(20)30484-9 (see pp. 2, 106, 107)

[106] L. Pinky **and** H. M. Dobrovolny. *SARS-CoV-2 coinfections: Could influenza and the common cold be beneficial? Journal of Medical Virology*, 92: 2623–2630, 2020. doi: 10.1002/jmv.26098 (see p. 13)

[107] K. Prem, A. R. Cook, **and** M. Jit. *Projecting social contact matrices in 152 countries using contact surveys and demographic data. PLoS computational biology*, 13: e1005697, 2017. doi: 10.1371/journal.pcbi.1005697 (see p. 88)

[108] Robert Koch Institute *Coronavirus SARS-CoV-2 (COVID-19)* https://www.rki.de/DE/Content/InfAZ/N/Neuartiges_Coronavirus/nCoV.html [Accessed 19-Jun-2024] 2024 (see p. 87)

[109] I. Rodiah, P. Vanella, A. Kuhlmann, V. K. Jaeger, M. Harries, G. Krause, A. Karch, W. Bock, **and** B. Lange. *Age-specific contribution of contacts to transmission of SARS-CoV-2 in Germany. European Journal of Epidemiology*, 38: 39–58, 2023. doi: 10.1007/s10654-022-00938-6 (see pp. 30, 88, 107, 108)

[110] R. Ross. *The prevention of malaria*. Dutton, 1910. (see p. 10)

[111] M. A. Safi **and** A. B. Gumel. *Dynamics of a model with quarantine-adjusted incidence and quarantine of susceptible individuals. Journal of Mathematical Analysis and Applications*, 399: 565–575, 2013. doi: 10.1016/j.jmaa.2012.10.015 (see p. 13)

[112] M. A. Safi **and** A. B. Gumel. *Qualitative study of a quarantine/isolation model with multiple disease stages. Applied Mathematics and Computation*, 218: 1941–1961, 2011. doi: 10.1016/j.amc.2011.07.007 (see pp. 9, 13)

[113] A. Saltelli, P. Annoni, I. Azzini, F. Campolongo, M. Ratto, **and** S. Tarantola. *Variance based sensitivity analysis of model output. Design and estimator for the total sensitivity index. Computer physics communications*, 181: 259–270, 2010. doi: 10.1016/j.cpc.2009.09.018 (see pp. 94, 107)

[114] A. Saltelli, M. Ratto, T. Andres, F. Campolongo, J. Cariboni, D. Gatelli, M. Saisana, **and** S. Tarantola. *Global sensitivity analysis: the primer*. John Wiley & Sons, 2008. (see pp. 26, 94, 107)

[115] B. Salzberger, T. Glück, **and** B. Ehrenstein. *Successful containment of COVID-19: the WHO-Report on the COVID-19 outbreak in China. Infection*, 48: 151–153, 2020. doi: 10.1007/s15010-020-01409-4 (see p. 106)

[116] A. Sette **and** S. Crotty. *Adaptive immunity to SARS-CoV-2 and COVID-19. Cell*, 184: 861–880, 2021. doi: 10.1016/j.cell.2021.01.007 (see p. 4)

[117] B. Singh, P. Kaur, R.-J. Reid, F. Shamoon, **and** M. Bikkina. *COVID-19 and influenza co-infection: report of three cases. Cureus*, 12: 2020. doi: 10.7759/cureus.9852 (see p. 4)

[118] G. J. Smith, D. Vijaykrishna, J. Bahl, S. J. Lycett, M. Worobey, O. G. Pybus, S. K. Ma, C. L. Cheung, J. Raghwani, S. Bhatt, **and** others. *Origins and evolutionary genomics of the 2009 swine-origin H1N1 influenza A epidemic. Nature*, 459: 1122–1125, 2009. doi: 10.1038/nature08182 (see p. 1)

[119] J. Stowe, E. Tessier, H. Zhao, R. Guy, B. Muller-Pebody, M. Zambon, N. Andrews, M. Ramsay, **and** J. Lopez Bernal. *Interactions between SARS-CoV-2 and influenza, and the impact of coinfection on disease severity: a test-negative design. International journal of epidemiology*, 50: 1124–1133, 2021. doi: 10.1093/ije/dyab081 (see pp. 1, 4, 13, 87)

[120] T. Suess, C. Remschmidt, S. B. Schink, B. Schweiger, A. Heider, J. Milde, A. Nitsche, K. Schroeder, J. Doellinger, C. Braun, **and** others. *Comparison of shedding characteristics of seasonal influenza virus (sub) types and influenza A (H1N1) pdm09; Germany, 2007–2011. PloS one*, 7: e51653, 2012. doi: 10.1371/journal.pone.0051653 (see pp. 49, 108)

[121] J. Sultana, G. Mazzaglia, N. Luxi, A. Cancellieri, A. Capuano, C. Ferrajolo, C. de Waure, G. Ferlazzo, **and** G. Trifirò. *Potential effects of vaccinations on the prevention of COVID-19: rationale, clinical evidence, risks, and public health considerations. Expert review of vaccines*, 19: 919–936, 2020. doi: 10.1080/14760584.2020.1825951 (see p. 71)

[122] L. Taber, A. Paredes, W. Glezen, **and** R. Couch. *Infection with influenza A/Victoria virus in Houston families, 1976. Epidemiology & Infection*, 86: 303–313, 1981. doi: 10.1017/S0022172400069059 (see pp. 29, 108)

[123] B. Tang, N. L. Bragazzi, Q. Li, S. Tang, Y. Xiao, **and** J. Wu. *An updated estimation of the risk of transmission of the novel coronavirus (2019-nCov). Infectious disease modelling*, 5: 248–255, 2020. doi: 10.1016/j.idm.2020.02.001 (see pp. 49, 108)

[124] W. W. Thompson, D. K. Shay, E. Weintraub, L. Brammer, N. Cox, L. J. Anderson, **and** K. Fukuda. *Mortality associated with influenza and respiratory syncytial virus in the United States. Jama*, 289: 179–186, 2003. doi: 10.1001/jama.289.2.179 (see pp. 88, 114)

[125] P. Van den Driessche **and** J. Watmough. *Reproduction numbers and sub-threshold endemic equilibria for compartmental models of disease transmission. Mathematical biosciences*, 180: 29–48, 2002. doi: 10.1016/S0025-5564(02)00108-6 (see pp. 20, 34, 46, 73)

[126] C. Viboud, P.-Y. Boëlle, S. Cauchemez, A. Lavenu, A.-J. Valleron, A. Flahault, **and** F. Carrat. *Risk factors of influenza transmission in households. British Journal of General Practice*, 54: 684–689, 2004. doi: https://bjgp.org/content/54/506/684 (see p. 106)

[127] L. Wang, W. He, X. Yu, D. Hu, M. Bao, H. Liu, J. Zhou, **and** H. Jiang. *Coronavirus disease 2019 in elderly patients: characteristics and prognostic factors based on 4-week follow-up. Journal of infection*, 80: 639–645, 2020. doi: 10.1016/j.jinf.2020.03.019 (see pp. 88, 115)

[128] N. R. Waterlow. *Mathematical Modelling of Cross-protection Between Respiratory Viruses.* phdthesis. London School of Hygiene & Tropical Medicine, 2022. (see pp. 11, 12)

[129] G. Wehl, M. Laible, **and** M. Rauchenzauner. *Co-infection of SARS CoV-2 and influenza A in a pediatric patient in Germany. Klinische Pädiatrie*, 232: 217–218, 2020. doi: 10.1055/a-1163-7385 (see pp. 89, 114)

[130] S. P. Weisberg, T. J. Connors, Y. Zhu, M. R. Baldwin, W.-H. Lin, S. Wontakal, P. A. Szabo, S. B. Wells, P. Dogra, J. Gray, **and** others. *Distinct antibody responses to SARS-CoV-2 in children and adults across the COVID-19 clinical spectrum. Nature immunology*, 22: 25–31, 2021. doi: 10.1038/s41590-020-00826-9 (see p. 114)

[131] World Health Organization *Coronavirus Disease (COVID-19)* https://www.who.int/news-room/fact-sheets/detail/coronavirus-disease-(covid-19) [Accessed 19-Jun-2024] 2024 (see p. 1)

[132] World Health Organization *Herd immunity, lockdowns and COVID-19* https://www.who.int/news-room/questions-and-answers/item/herd-immunity-lockdowns-and-covid-19 Accessed: 2024-08-14 2020 (see pp. 112, 114)

[133] World Health Organization *Influenza (Seasonal)* https://www.who.int/news-room/fact-sheets/detail/influenza-(seasonal) [Accessed 19-Jun-2024] 2024 (see p. 1)

[134] World Health Organization, Eastern Mediterranean Regional Office *COVID-19 and Influenza* https://www.emro.who.int/health-topics/influenza/covid-19-and-influenza.html [Accessed 19-Jun-2024] 2024 (see pp. 1, 2)

[135] J. Wu, R. Dhingra, M. Gambhir, **and** J. V. Remais. *Sensitivity analysis of infectious disease models: methods, advances and their application. Journal of The Royal Society Interface*, 10: 20121018, 2013. doi: 10.1098/rsif.2012.1018 (see p. 94)

[136] L. Wu, X. Guo, J. Liu, X. Ma, Z. Huang, **and** X. Sun. *Evaluation of influenza vaccination coverage in Shanghai city during the 2016/17 to 2020/21 influenza seasons. Human Vaccines & Immunotherapeutics*, 18: 2075211, 2022. doi: 10.1080/21645515.2022.2075211 (see p. 88)

[137] X. Wu, Y. Cai, X. Huang, X. Yu, L. Zhao, F. Wang, Q. Li, S. Gu, T. Xu, Y. Li, **and** others. *Co-infection with SARS-CoV-2 and influenza A virus in patient with pneumonia, China. Emerging infectious diseases*, 26: 1324, 2020. doi: 10.3201/eid2606.200299 (see pp. 4, 5, 87)

[138] X. Yan **and** Y. Zou. *Optimal and sub-optimal quarantine and isolation control in SARS epidemics. Mathematical and computer modelling*, 47: 235–245, 2008. doi: 10.1016/j.mcm.2007.04.003 (see p. 70)

[139] J. Yang, X. Shi, X. Song, **and** Z. Zhao. *Threshold dynamics of a stochastic SIQR epidemic model with imperfect quarantine. Applied Mathematics Letters*, 136: 108459, 2023. doi: 10.1016/j.aml.2022.108459 (see pp. 49, 71)

[140] W. Yang. *Modeling COVID-19 pandemic with hierarchical quarantine and time delay. Dynamic Games and Applications*, 11: 892–914, 2021. doi: 10.1007/s13235-021-00382-3 (see p. 108)

[141] B. Yu **and** T. Xiaonan. *Comparison of COVID-19 and influenza characteristics. Journal of Zhejiang University. Science. B*, 22: 87, 2021. doi: 10.1631/jzus.B2000479 (see pp. 28, 106)

[142] X. Zhu, Y. Ge, T. Wu, K. Zhao, Y. Chen, B. Wu, F. Zhu, B. Zhu, **and** L. Cui. *Co-infection with respiratory pathogens among COVID-2019 cases. Virus research*, 285: 198005, 2020. doi: 10.1016/j.virusres.2020.198005 (see p. 89)

[143] C. M. Zipfel, V. Colizza, **and** S. Bansal. *The missing season: the impacts of the COVID-19 pandemic on influenza. Vaccine*, 39: 3645–3648, 2021. doi: 10.1016/j.vaccine.2021.05.049 (see p. 4)

List of Figures

List of Tables

Akademischer Lebenslauf

2021 Annahme als Doktorand am Fachbereich Mathematik an der Technischen Universität Kaiserslautern.

2017 Master of Science in Mathematischen Wissenschaften, Afrikanisches Institut für Mathematische Wissenschaften
Thema der Master-Arbeit: Der Einfluss der Wahl der Medienfunktionen auf die Krankheitsmodellierung.

2014 Bachelor of Science mit Pädagogik am Fachbereich Physik, Mathematik und Informatik, Pädagogische Hochschule der Universität Dar Es Salaam
Thema der Bachelor-Arbeit: Anmeldesystem für Lehramtsstudierende.

Academic curriculum vitae

2021 Accepted as a PhD student at the Department of Mathematics, Rheinland-Pfälzische Technische Universität Kaiserslautern-Landau, Kaiserslautern.

2017 Master of Science in Mathematical Sciences, African institute for Mathematical Science
Thesis: The Influence of Choice of Media Function on Disease Modeling.

2014 Bachelor of Science with Education, Department of Physics, Mathematics, and Informatics, Dar Es Salaam University College of Education
Thesis: Teachers Trainee Registration System.